DYNAMIC COUPLING OF MULTIPLE STRUCTURES THROUGH SOIL

by

Artur Luna Pais

Diplome in Civil Engineering
Ecole Polytechnique Federale de Lausanne
Switzerland (1980)

S.M., Massachusetts Institute of Technology
(1985)

SUBMITTED TO THE DEPARTMENT OF CIVIL
ENGINEERING IN PARTIAL FULFILLMENT OF THE
REQUIREMENTS FOR THE DEGREE OF

DOCTOR OF PHILOSOPHY

at the

MASSACHUSETTS INSTITUTE OF TECHNOLOGY

June 1988

Signature of Author ______________________________
Department of Civil Engineering
May 13, 1988

Certified by ______________________________
Eduardo E. Kausel
Thesis Supervisor

Accepted by ______________________________
Ole S. Madsen
Chairman, Departmental Committee on Graduate Students

DYNAMIC COUPLING OF MULTIPLE STRUCTURES THROUGH SOIL

by

Artur Luna Pais

Submitted to the Department of Civil Engineering
on May 13th, 1988, in partial fulfillment of the
requirements for the Degree of Doctor of Philosophy

ABSTRACT

A two–dimensional Boundary Element formulation is developed to study dynamic problems involving several rigid foundations and tunnels embedded in a layered halfspace. This formulation is applied in the frequency domain, and uses very efficient approximate Green's functions which can be evaluated in closed form without the need of numerical integrations. The approximation consists in subdividing each layer of soil into several sublayers and assuming a linear variation of the displacements across each sublayer.

The possible existence of noncausal solutions while considering nonconvex domains is investigated with the method developed, and some comparisons with time–domain results are performed. It is found that the frequency–domain results using the discrete Green's functions obey causality in every case.

The boundary element code is used to assess the influence of underground structures, such as a tunnel, in the seismic motion observed at the surface. A particular situation examined is that of downtown Mexico City during the earthquakes of September 1985, with focus on the effects that the underground tunnel may have had on the motion in its vicinity. However, no significant effects were observed since the low frequency contents of the seismic waves produced essentially translations on large structures.

An approximate procedure to evaluate the effects of the interaction between multiple foundations subjected to seismic excitations is presented. This method is relatively simple to implement and can be used in fairly general situations involving several cylindrical and rectangular foundations embedded in a halfspace. Some comparisons with more accurate methods show a good agreement, at least as far as the qualitative effect of the interaction is concerned.

Thesis Supervisor: Dr. Eduardo Kausel

Title: Associate Professor of Civil Engineering

ACKNOWLEDGEMENTS

In first place, I would like to express my most sincere gratitude to Prof. Eduardo Kausel whose invaluable guidance and suggestions made my work in this thesis very pleasant and profitable. Prof. Kausel introduced me to the field of soil dynamics and I owe him all the expertise I have acquired. Foremost, I appreciated very much his friendship and trustful attitude which will certainly remain one of the most precious rewards of my stay at MIT.

To the many friends, students, professors and staff, who I have known during these years, especially in the Civil Engineering Department, I would like to show my special thanks. They gave me the sensation of being part of a big family with all members helping each other and contributing to the common goal of an enjoyable life during this period. I would like to mention in particular, Raymond, Tommaso, Massoud, Manuel, Luc, Fouad, Fadi, Mounir, Cemal, Jaideep, Nabil, Luis, Hayat, Otto, Thomas, ..., who despite far away geographically in a recent future, will remain in my memories for ever.

Many thanks to Otto Estorff who performed the necessary computations in the time domain used in section 3.3.2.

Finally and most of all, I would like to thank very much my dear wife Maria Eduarda who besides typing this thesis gave me all the support necessary during these years at MIT.

DEDICATION

To Maria Eduarda

TABLE OF CONTENTS

1. INTRODUCTION

Seismic ground motions are, in general, highly variable in space and time. Although the variability in time is easily quantified from seismograms, less is known about the spatial variability, which depends substantially on the type of waves present and their paths. For extended structures, or structures founded on several foundations, the spatial variability of the seismic motion can be very important and should not be neglected.

When the seismic waves impinge on an extended foundation having a rigidity much higher than the surrounding soil, the foundation cannot accomodate the spatial variation of the motion; as a result, the free–field motion is distorted by the effect of the waves scattered by the foundation as well as those generated by its vibration. This phenomenon is usually called soil–structure interaction. On the other hand, when a structure is founded on several foundations placed at some distance, the free–field ground motion will be different under each foundation, and since they are connected through the structure, some interaction takes place.

The exact solution for soil–structure interaction problems is very complex, analytical solutions being available only for very special situations such as strip or disk foundations bonded to an elastic halfspace and subjected to either forced vibrations or seismic waves. For more general cases, numerical methods such as finite elements and boundary elements have been used. Since these problems deal, in general, with infinite domains, the Boundary Element Method (BEM) seems very advantageous, because it only requires discretization of the boundary separating the foundation from the soil. However, the BEM is based in the validity of the superposition principle and, hence can only be used efficiently for linear problems. The BEM requires the use of certain fundamental solutions referred to as Green's functions, which represent the free–field dynamic displacements observed when a unit load is applied at some point in the domain. These fundamental solutions are usually very difficult to obtain in closed form, which limits the applicability of the BEM.

Although an homogeneous halfspace represents the simplest soil model of practical importance, it is rather limited since most subgrades present a stratification into horizontal layers due to the geological process of sedimentation. To account for the variability along the vertical direction, a great effort has been made in the evaluation of the Green's functions for the case of horizontally layered media. Exact solutions in closed form are not available and most methods require the numerical integration of infinite integrals. Another approach, developed by Kausel and Peek [22], discretizes each layer into several sublayers assuming that the displacements vary linearly across each sublayer along the vertical direction. This procedure is restricted to a stratum of finite depth but it is very efficient as the Green's functions do not require the numerical evaluation of integral transforms. The solution is expressed in the frequency domain but results in the time domain can easily be obtained by Fourier transformation, using the fast Fourier algorithm. Seale [39] extended this formulation to incorporate a halfspace by using approximate expressions for the dynamic impedances of the halfspace. This approximation, named paraaxial, works well if the vibration near the halfspace interface is originated by waves travelling close to a vertical path (small values of the wave–number). However, even in other cases, good results can be obtained if a series of sublayers are added underneath the zone of interest before the halfspace is considered. A very efficient Boundary Element code can be developed by using the procedure just described to evaluate the Green's functions.

The problem of dynamic coupling between several structures through the soil, sometimes referred to as structure–soil–structure interaction, has been receiving some attention recently. However, most of the studies up to date consider only surface foundations, or two foundations embedded in a homogeneous stratum; also, past efforts have concentrated almost exclusively on theory and code development. For 3–dimensional modelling, supercomputers have been used extensively in order to be able to analyse several foundations.

In this work, a boundary element code is developed for studying the dynamic interaction between multiple structures. The code is implemented in a microcomputer in a modular way, to take maximum advantage of the memory available. Since the analysis focuses mainly on demonstrating in a qualitative sense the implications of structure to structure interaction, the code will be restricted to a 2–dimensional analysis, considering both in–plane and anti–plane motions. The Green's functions used are based on the algorithm developed by Kausel and Seale. Some effort is made in showing the accuracy of such idealizations by comparing the results with other numerical solutions obtained using finite elements and time–domain boundary elements; special attention is given to the verification of causality constraints of the response in non–convex domains, since in these cases the BEM does not insure that the response perceived at a given point is null until the time it takes the fastest wave to reach that point travelling along the shortest path.

The influence of underground structures on the surrounding ground motion as well as the interaction between underground structures and surface or embedded foundations is investigated in relation to the earthquakes that hit Mexico City in September 1985. The presence of underground structures, such as the subway tunnel, has been thought as a possible cause of the contrasting pattern of structural damages observed in downtown Mexico City during the earthquakes. Severely affected zones alternate with zones where the buildings hardly suffered any damages, even though the geological characteristics essentially did not change from one site to the other. Results obtained by a 2–dimensional amplification analysis using the code developed are compared with actual recorded motions at the surface, and the potential for deleterious effects caused by the tunnel is assessed. Emphasis is made on the effects of the in–plane rotation of the subway tunnel elicited by incident SV seismic waves.

Finally, an approximate procedure is suggested which may be used to assess in a qualitative sense the effects of dynamic coupling of multiple structures through the soil. This approximation is based on Iguchi's method, which was shown to provide very good estimates of soil–structure interaction for the case of a single embedded foundation subjected to seismic excitations. The method presented can be used in the case of several rectangular and/or cylindrical foundations embedded into a halfspace subjected to seismic waves travelling obliquely in any direction. Some examples and comparisons with more exact solutions are shown.

2. REVIEW OF PREVIOUS WORK

2.1 Wave Propagation in Layered Media

The solution of problems involving forced vibrations of foundations or the response of underground structures to seismic excitations requires the analysis of wave propagation by the soil. As widely recognized, soil is a very complex medium composed in general, of three different phases (air, water and skeleton), and exhibiting a highly non–linear behavior. In addition, the soil characteristics can only be determined with some accuracy near the surface or at discrete intervals by means of borings. Hence, several assumptions must be made when describing the soil behavior, even for static problems. Dynamic analysis, on the other hand, presents another degree of complexity, in that the soil is thought of in most cases as an homogeneous linear elastic material. Although such simplifications are clearly limiting, these models describe with acceptable accuracy the main features of the dynamic problem analyzed.

It is often the case that the soil exhibits distinct horizontal layers due to the process of sedimentation; in such case the idealization of the soil as a homogeneous halfspace or stratum is unacceptable. Even though such layering is never perfectly horizontal, due to the geological movements and faulting of the soil mass, the idealization of the subgrade as being composed of several horizontal layers welded to one another is necessary in order for the mathematical model to remain solvable.

Thomson [41] and Haskell [17] developed some 30 years ago a transfer matrix approach to study wave propagation in layered media. This problem can be divided into two uncoupled motions in a 2–dimensional domain: one motion is produced by SV (shear) and P (longitudinal) waves, and the displacements are contained in a vertical plane (in–plane case); the other motion results from SH (shear) waves propagating along the vertical plane, with the ground displacements being perpendicular to that plane (anti–plane case). Figure 2.1 shows the geometry and axis orientation chosen.

in–plane case

The dynamic equilibrium equations for waves propagating in a layer j are

$$(\lambda_m+2G_m)\frac{\partial^2 u_x}{\partial x^2}+\lambda_m\frac{\partial^2 u_z}{\partial x\partial z}+G_m\left[\frac{\partial^2 u_x}{\partial z^2}+\frac{\partial^2 u_z}{\partial x\partial z}\right]-\rho_m\frac{\partial^2 u_x}{\partial t^2}=0 \tag{2.1 a}$$

$$(\lambda_m+2G_m)\frac{\partial^2 u_z}{\partial z^2}+\lambda_m\frac{\partial^2 u_x}{\partial x\partial z}+G_m\left[\frac{\partial^2 u_z}{\partial x^2}+\frac{\partial^2 u_x}{\partial x\partial z}\right]-\rho_m\frac{\partial^2 u_z}{\partial t^2}=0 \tag{2.1 b}$$

where u_x and u_z represent the displacements in the x and z directions respectively; λ_m and G_m are the Lame constants of layer m and ρ_m is its mass density.

Fourier transforming these equations with respect to time ($t \rightarrow \omega$) and horizontal coordinate ($x \rightarrow k$), one obtains

$$k^2(\lambda_m+2G_m)\bar{U}_x + ik(\lambda_m+G_m)\frac{d\bar{U}_z}{dz} - G_m\frac{d^2\bar{U}_z}{dz^2} - \omega^2\rho_m\bar{U}_x = 0 \tag{2.2 a}$$

$$k^2G_m\bar{U}_z + ik(\lambda_m+G_m)\frac{d\bar{U}_z}{dz} - (\lambda_m+2G_m)\frac{d^2\bar{U}_z}{dz^2} - \omega^2\rho_m\bar{U}_z = 0 \tag{2.2 b}$$

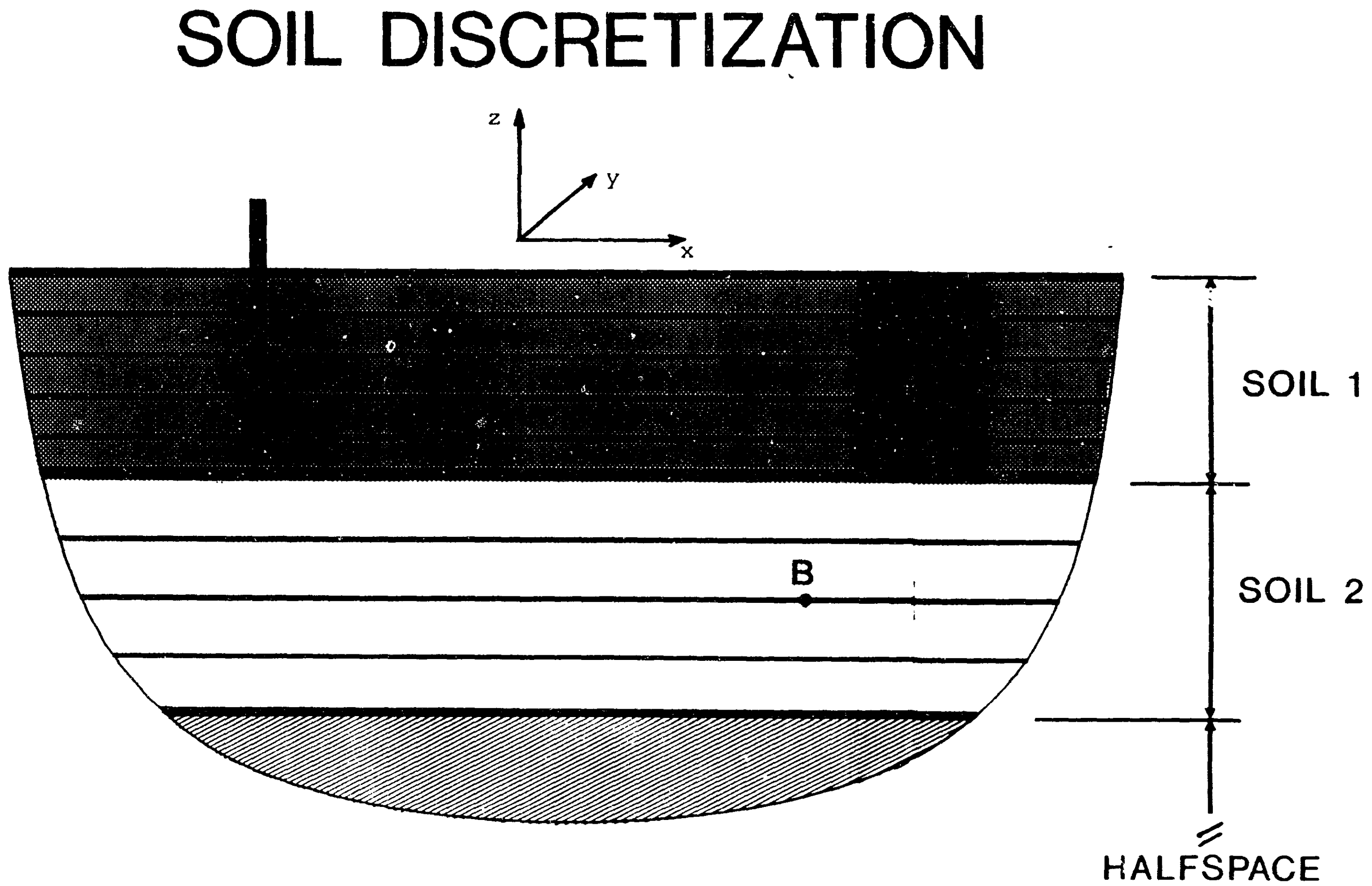

Fig.2.1 - Layered halfspace

Equations 2.2 a,b can be uncoupled with the introduction of two potential functions ϕ and ψ such that

$$u_x = \frac{\partial \phi}{\partial x} - \frac{\partial \psi}{\partial z} \rightarrow \bar{U}_x = -ik\Phi - \frac{d\Psi}{dz} \qquad (2.3\ a)$$

$$u_z = \frac{\partial \phi}{\partial z} - \frac{\partial \psi}{\partial x} \rightarrow \bar{U}_z = \frac{d\Phi}{dz} - ik\Psi \qquad (2.3\ b)$$

and the equations of motion become

$$\frac{d^2\Phi}{dz^2} - k^2\Phi + \frac{\omega^2}{C_{pm}}\Phi = 0 \qquad (2.4\ a)$$

$$\frac{d^2\Psi}{dz^2} - k^2\Psi + \frac{\omega^2}{C_{sm}}\Psi = 0 \qquad (2.4\ b)$$

where $C_{pm} = \sqrt{\frac{\lambda_m + 2G_m}{\rho_m}}$ and $C_{sm} = \sqrt{\frac{G_m}{\rho_m}}$ are, respectively, the longitudinal and shear wave velocities. Defining $r_m = \sqrt{1-(\omega/kC_{pm})^2}$ and $s_m = \sqrt{1-(\omega/kC_{sm})^2}$, the solution of equations 2.4 can be written as

$$\Phi(z) = A_m \cos(kr_m z) + B_m \sin(kr_m z) \qquad (2.5\ a)$$

$$\Psi(z) = C_m \cos(ks_m z) + D_m \sin(ks_m z) \qquad (2.5\ b)$$

and the displacements $\bar{U}_x$ and $\bar{U}_z$ can then be obtained by substituting these expressions into equations 2.3. To find the integration constants A_m, B_m, C_m and D_m, boundary conditions must be imposed at the upper and lower interfaces of the layer m, where either traction or displacements are prescribed. In the transfer matrix method developed by Thompson and Haskell, the tractions and displacements at one interface of the layer can be expressed in terms of the same quantities at the other interface through a matrix H_m called the transfer matrix or propagator matrix:

$$\begin{pmatrix} \bar{U}_2 \\ \bar{S}_2 \end{pmatrix} = H_m \cdot \begin{pmatrix} \bar{U}_1 \\ \bar{S}_1 \end{pmatrix} \tag{2.6}$$

anti–plane case

For anti–plane motion the displacements are in the y direction (u_y) and the differential equation of motion in a layer m is

$$G_m\left(\frac{\partial^2 u_y}{\partial x^2} + \frac{\partial^2 u_y}{\partial z^2}\right) - \rho_m \frac{\partial^2 u_y}{\partial t^2} = 0 \tag{2.7}$$

which after Fourier transformation becomes

$$k^2 G_m \bar{U}_y - G_m \frac{d^2 \bar{U}_y}{dz^2} - \omega^2 \rho_m \bar{U}_y = 0 \tag{2.8}$$

with solution

$$\bar{U}_y = E_m \cos(ks_m z) + F_m \sin(ks_m z) \tag{2.9}$$

As in the in–plane case, the constants E_m and F_m are obtained from the boundary conditions at the interfaces (traction or displacement) and a transfer matrix

H_m can be constructed in order to obtain a relation similar to that in equation (2.6).

2.1.1 Stiffness Matrix Approach

Kausel and Roesset [21] extended the transfer matrix algorithm by manipulating equation (2.6) in such a way so that the tractions at the interfaces are expressed in terms of the boundary displacements. Recognizing that in the upper interface the external loads $\bar{P}_1$ are equal to the corresponding traction $\bar{S}_1$ while at the bottom interface $\bar{P}_2=-\bar{S}_2$, a relation is obtained between external loads and displacements

$$\begin{Bmatrix} \bar{P}_1 \\ \bar{P}_2 \end{Bmatrix} = K_m \cdot \begin{Bmatrix} \bar{U}_1 \\ \bar{U}_2 \end{Bmatrix} \tag{2.10}$$

The matrix K_m can be thought of as a stiffness matrix for layer m, and if a factor i ($i=\sqrt{-1}$) is introduced in the vertical loads and displacements, then K_m is also symmetric. The global stiffness matrix of a stack of layers can be obtained by overlaying the individual layers stiffnesses at the corresponding degrees of freedom as is usual in structural analysis.

Kausel and Roesset presented expressions for the stiffness matrices of layers corresponding to in–plane and anti–plane motions for zero and non–zero values of the frequency ω and the wave–number k. Such expressions involve transcendental functions of the parameters r_m and s_m defined previously. The stiffnesses of a halfspace relating the loads applied to the surface of the halfspace and the corresponding displacements were also included. This approach can be used to solve in an exact and very elegant way problems related to wave propagation.

2.2 Thin–layer Method

2.2.1 Description

As pointed out in the previous section, the terms of the stiffness matrices of each layer have complex terms, so that the inverse Fourier transformation required to express the solution in terms of the horizontal coordinate x must be evaluated numerically. Even if efficient procedures are used to perform these transformations (see Apsel [4]) they are very time consuming since the integrations extend to infinity and the kernels of the integrals have an oscillating behavior. A quite different approach was undertaken by Waas [45], who used instead a finite element approximation to model the stack of layers. Each layer is divided into several sublayers, and the displacements are assumed to vary linearly across the thickness of each sublayer. Waas used this procedure to obtain consistent boundaries in a 2–D domain, and Kausel [20] extended it to the axisymmetric case. In this method, the stiffness matrix of each sublayer is an algebraic expression in terms of the wave–number k

$$K_m = A_m k^2 + B_m k + G_m - \omega^2 M_m \tag{2.11}$$

For purposes of completness, the derivation of the expression for K_m and the matrices A_m, B_m, G_m and M_m are described in appendix A. These matrices depend only on the thickness h of the sublayer and its material properties (G, λ and ρ). This thickness shall be chosen in such a way that the system models properly waves travelling in a vertical direction; this implies a maximum value of h equal to 1/4 the wavelength λ ($\lambda = \frac{2\pi C_s}{\omega}$).

2.2.2 Green's Functions in a Layered Stratum

Kausel and Peek [22] used the approximate stiffness matrices given by equation 2.11 to develop a closed form solution for the Green's functions corresponding to dynamic loads in a horizontally layered stratum. The procedure was as follows: the stiffness matrix of each sublayer (in the frequency–wave number domain) was assembled into a global stiffness matrix. The resulting algebraic system of equations was solved by a spectral decomposition of the stiffness matrix (which implied solving a quadratic eigenvalue problem for the wave–numbers) and the solution in the frequency–spatial coordinates domain was then obtained by inverse Fourier transformation, which could be performed in closed form. The displacements were then computed as a summation over all the natural modes of the system.

Although the formulation for the Green's functions described above is completely general and can be applied to three–dimensional geometries, this study focuses on a two–dimensional implementation of this method, and the Green's functions are evaluated for in–plane and anti–plane line loads. Appendix B describes in detail the steps necessary for the computation of the Green's functions for both of these (plane) cases. The final result is a matrix relating the displacements at any interface to the external loads applied (equations B19 and B20). If the loads are applied within the interior of a sublayer, then the load can be replaced by the consistent "nodal" loads at the interfaces as described in [21]. Also, if the displacements are required at the interior of a sublayer, then they can be obtained by linear interpolation of the displacements at the corresponding interfaces (at the same x location), since the model assumes a linear variation of displacements across each sublayer.)

2.2.3 Extension to Layered Halfspaces – Paraaxial Approximation

The Green's functions developed by Kausel and Peek [22] and described above are extremely efficient, especially for problems involving several layers with distinct characteristics. As shown in [22], the accuracy obtained is also very good when considering just a reduced number of sublayers. However, the formulation assumes that the stack of layers rest on top of firm rock and cannot be extended directly to the cases where a halfspace is present. The reason is that since the halfspace has an infinite depth, a linear variation of displacements is certainly not possible. One way to cope with this problem is to extend the stratum to a greater depth so that any reflections at the bottom attenuate sufficiently (because of internal damping) before they reach and influence the response in the region of interest. However, this approach increases the number of sublayers required and does not eliminate the reflected waves at the bottom of the stratum. To extend this formulation to layered halfspaces, Seale [39] developed a paraaxial approximation by expanding the dynamic stiffnesses of the halfspace in Taylor series with respect to the wave–number k. This solution is very convenient since the quadratic eigenvalue problem in k is still quadratic and the algorithm to compute the Green's function remains exactly the same, the only difference being the introduction of the extra degrees of freedom in the stiffness matrix corresponding to the displacements at the top of the halfspace.

The exact halfspace impedances given in Kausel and Roesset [21] are, for the in–plane case

$$\mathbf{K} = 2kG\left(\frac{1-s^2}{2(1-rs)}\begin{bmatrix} r & 1 \\ 1 & s \end{bmatrix} - \begin{bmatrix} 0 & 1 \\ 1 & 0 \end{bmatrix}\right) \tag{2.12}$$

and for the anti–plane case

$$\mathbf{K} = ksG \tag{2.13}$$

where $r = \sqrt{1-(\omega/kC_p)^2}$ and $s = \sqrt{1-(\omega/kC_s)^2}$; ω being the frequency of the motion.

For the in–plane case, the approximate stiffness matrix of the halfspace becomes

$$\mathbf{K}(k) \approx i\omega\rho C_s\begin{bmatrix} 1 & 0 \\ 0 & 1/\alpha \end{bmatrix} + G\frac{(1-2\alpha)}{\alpha}k\begin{bmatrix} 0 & 1 \\ 1 & 0 \end{bmatrix} + i\frac{GC_s}{2\,\alpha\omega}k^2\begin{bmatrix} -(2-\alpha) & 0 \\ 0 & (1-2\alpha)/\alpha^2 \end{bmatrix} \tag{2.14}$$

and for the anti–plane case it becomes

$$\mathbf{K}(k) \approx i\frac{G\omega}{C_s} - i\frac{GC_s}{2\,\omega}k^2 \tag{2.15}$$

where $\alpha = C_s/C_p$, the ratio between the shear wave and longitudinal wave velocities. It can be seen that the exact stiffnesses have terms involving square roots which imply that those expressions have branch points in the complex k–plane. As it is widely known, Taylor series are only valid up to the nearest singularity so that for values of $k>\omega/C_p$ the values given by the approximations are not valid anymore (even if more terms were taken in the Taylor series). Hence, it is important to model the layered halfspace in such a way that high values of k do not contribute significantly to the response. One possibility is to always have a sufficient number of sublayers (10 to 12) between the deepest concentrated load and the top of the halfspace, so that the load gets diffused along the horizontal coordinate at the top of the halfspace. As a result, its spatial Fourier transform (in the x coordinate) does not contain high values of the wave number k.

Seale showed that the paraxial approximation is similar to the absorbing boundaries developed by Clayton and Engquist (see [39]). Waves traveling nearly vertically are well transmitted into the halfspace, while shallow waves are in part reflected back. Hence, in the special cases when the halfspace is softer than the overlying layers the paraxial approximation does not work very well for obliquely incident waves.

3. BOUNDARY ELEMENT SOLUTION

3.1 Formulation of the Method

The dynamic equilibrium equation for wave propagation in homogeneous media can be written as

$$\sigma_{ij,j} + b_i - \rho u_{i,tt} = 0 \qquad i,j = 1,2,3 \tag{3.1}$$

where the comma defines differentiation, and a repeated index means summation over its range; b_i represents the distributed external load in the direction i and ρ is the specific mass of the soil.

Consider another displacement field, denominated u_i^*, which is virtual in nature but also satisfies the wave equation. Multiplying equation (3.1) by u_i^* and integrating the resulting equality over the entire domain under consideration gives

$$\iiint_v u_i^* (\sigma_{ij,j} + bi - \rho u_{i,tt})\, dV = 0 \quad i,j = 1,2,3 \tag{3.2}$$

After integration by parts of the term in $\sigma_{ij,j}$, the above equation is transformed into

$$\iint_S t_i u_i^* dS - \iiint_v \sigma_{ij} \epsilon_{ij}^* d_V + \iiint_v (b_i - \rho u_{i,tt})\, u_i^*\, dV = 0 \tag{3.3}$$

in which $t_i = \alpha_{\nu j} \sigma_{ij}$ represent the tractions along the boundary S ($\alpha_{\nu j}$ is the direction cosine for the angle formed by the outward normal and the axis j).

The term $\sigma_{ij}\overset{*}{\epsilon}_{ij}$ can be expressed in terms of ϵ_{ij}, using the stress–strain tensor for the soil D

$$\sigma_{ij}\overset{*}{\epsilon}_{ij} = (D\epsilon_{ij})\,\overset{*}{\epsilon}_{ij} \tag{3.4}$$

Taking into account the symmetry of D, eq. 3.4 can be transformed into

$$(D\epsilon_{ij})\,\overset{*}{\epsilon}_{ij} = (D\overset{*}{\epsilon}_{ij})\,\epsilon_{ij} = \overset{*}{\sigma}_{ij}\epsilon_{ij} \tag{3.5}$$

so that

$$\iiint_v \sigma_{ij}\overset{*}{\epsilon}_{ij}dV = \iiint_v \overset{*}{\sigma}_{ij}\epsilon_{ij}dV \tag{3.6}$$

Integrating by parts the right hand side of the expression above, one obtains

$$\iiint_v \overset{*}{\sigma}_{ij}\epsilon_{ij}dV = \iint_S \overset{*}{t}_i u_i ds - \iiint_v \overset{*}{\sigma}_{ij,j}u_i dV \tag{3.7}$$

But the virtual displacement field also satisfies the equilibrium equations, hence

$$\overset{*}{\sigma}_{ij,j} = -\overset{*}{b}_i + \rho\overset{*}{u}_{i,tt} \tag{3.8}$$

Combining the results of equations 3.4–3.8 with equation 3.3, the basic relation for the boundary element formulation is obtained

$$\iint_S t_i\overset{*}{u}_i dS + \iiint_v (b_i - \rho u_{i,tt})\overset{*}{u}_i dV = \iint_S \overset{*}{t}_i u_i dS + \iiint_v (\overset{*}{b}_i - \rho\overset{*}{u}_{i,tt})u_i dV \tag{3.9}$$

Equation 3.9 can also be expressed in the frequency domain. Assuming an harmonic motion with frequency ω, $u_{i,tt} = -\omega^2 u_i$ and $\overset{*}{u}_{i,tt} = -\omega^2 \overset{*}{u}_i$. Hence, $u_{i,tt}\overset{*}{u}_i = \overset{*}{u}_{i,tt}u_i = -\omega^2 u_i \overset{*}{u}_i$. Furthermore, assuming that there are no external distributed loads, $b_i = 0$, and equation (3.9) becomes

$$\iint_S t_i \overset{*}{u}_i dS = \iint_S \overset{*}{t}_i u_i dS + \iiint_v \overset{*}{b}_i u_i dV \tag{3.10}$$

If $\overset{*}{b}_i$ corresponds to a unit load in direction i at point $\underline{x}_0$, $\overset{*}{b}_i = \delta(\underline{x}-\underline{x}_0)$ (δ being the Dirac delta function), the volume integral reduces to the value of the displacement in direction i at point $\underline{x}_0$, $u_i(\underline{x}_0)$. Thus, the displacement in any direction at any point inside the domain can be expressed in terms of the displacements and tractions at the boundary,

$$u_i(\underline{x}_0) = \iint_S (t_i \overset{*}{u}_i - \overset{*}{t}_i u_i) dS \tag{3.11}$$

For problems involving a halfspace or a stratum over rigid rock, the only finite boundary where the product of the boundary tractions and displacements do not vanish is the boundary of the structure being analysed (foundation, tunnel, cavity, etc.). Along, the free surface, since t_i and $\overset{*}{t}_i$ vanish, the products $t_i \overset{*}{u}_i$ and $\overset{*}{t}_i u_i$ are zero. Hence, the surface integral in equation 3.11 only needs to be evaluated at the interface between the structure or cavity being analyzed and the soil.

When the ficticious point load is applied on the boundary ($\underline{x}_0 \in S$), equation 3.11 will involve only unknown displacements and tractions at the boundary. However, the integral will exhibit singularities near the loading, which need to be integrated with caution. This procedure leads to an integral equation, which in most cases cannot be solved in closed form. Hence, to generalize the method, one has to use numerical approximations.

In the Direct Boundary Element Method, the boundary tractions and displacements are expressed as a function of their values at a few discrete points (nodes), usually using polynomial interpolations. The integral in equation 3.11 is, therefore, approximated by a summation having as unknowns either the tractions, or the displacements at each node (but not both, since in a well posed problem, one of them must be prescribed at every point on the boundary). Imposing virtual displacement fields corresponding to virtual loads at each node and for each direction, a system of linear equations is obtained. Defining U as the vector of displacements at the boundary nodes, some of which are known, and P the vector of the tractions, the system of equations can be written as

$$\mathbf{A}\cdot\mathbf{U} = \mathbf{B}\cdot\mathbf{P} \tag{3.12}$$

where the element a_{ij} of A represents the traction in node–direction j due to a unit load in node–direction i and the element b_{ij} of B corresponds to the displacement in node–direction j due to a unit load in node–direction i. The system above can be rearranged so that all unknowns are transferred to the same side and the resulting system can be solved using standard algorithms. It should be noted, however, that the matrices obtained are not symmetric and are fully populated.

A two–dimensional boundary element code was developed using the Green's functions described in the previous chapter. The type of elements used are linear in vertical planes and constant in horizontal planes. The details of the computation of the resulting tractions and displacements at the nodes are described in Appendix C. It should be emphasized that in this case, due to the constraint of having the displacements varying piecewise linearly with depth, the singularities near a concentrated load are just Dirac delta functions, which are easy to integrate. In a continuous and isotropic formulation, the singularities are of the logarithmic type and special integration quadratures need to be used. Both in–plane and anti–plane motions are analyzed, and since they are completely uncoupled, two separate programs were developed, one for each situation. The code can be used to obtain the dynamic stiffness matrices of embedded rigid foundations or tunnels, as well as their response to seismic waves. These waves are prescribed at the base of the stratum or at the top of the halfspace and can consist of SH (anti–plane), P or SV (in–plane) waves arriving obliquely. The solution is computed for different frequencies of the motion and the response in time can then be obtained by Fourier transformation using the fast Fourier transform algorithm. The programs were implemented in a 'AT' type microcomputer and all the computations in this work were performed in that system.

Response to Ground Motions

In order to study the response of a rigid foundation or tunnel to incident seismic waves, the solution can be divided into two steps. First, using the free–field motion due to the incident waves, the corresponding tractions and displacements along the "imaginary" boundary of the structure are computed (P^* and U^* respectively). In a second step, the boundary element equations are solved for the incremental tractions ($P-P^*$), and displacements ($U-U^*$). These incremental values must correspond to changes on the boundary conditions at the interface soil–structure and hence, they must satisfy the boundary element equation 3.12

$$\mathbf{A}\cdot(\mathrm{U}-\mathrm{U}^*) = \mathbf{B}\cdot(\mathrm{P}-\mathrm{P}^*) \tag{3.13}$$

When the structures are very stiff in comparison to the soil, it can be assumed that they displace rigidly, so that the displacements along the boundary can be obtained from the rigid body motions through a transformation matrix T, which only depends on the relative coordinates of the boundary nodes with respect to a reference point

$$\mathrm{U} = \mathrm{T}\mathrm{u}_o \tag{3.14}$$

Assuming the reference point has zero coordinates and using the axis convention shown in figure 3.1, each submatrix of T, corresponding to each node j, is given by

$$\text{in-plane motion} \qquad \mathrm{T}_j = \begin{bmatrix} 1 & 0 & -z_j \\ 0 & 1 & x_j \end{bmatrix} \tag{3.15}$$

for $\mathrm{u}_o^T = \left[\mathrm{u}_x^1\ \mathrm{u}_z^1\ \mathrm{u}_\theta^1\ \mathrm{u}_x^2\ \mathrm{u}_z^2\ \mathrm{u}_\theta^2 \ldots\right]$ where the superscript indicates to the structure under consideration

$$\text{anti-plane motion} \qquad \mathrm{T}_j = [1] \tag{3.16}$$

for $\mathrm{u}_o^T = \left[\mathrm{u}_y^1\ \mathrm{u}_y^2 \ldots\right]$

Introducing equation 3.14 into equation 3.13 and rearranging some terms, gives

$$\mathrm{ATu}_o = \mathrm{A}\cdot\mathrm{U}^* + \mathrm{B}\cdot(\mathrm{P}-\mathrm{P}^*) \tag{3.17}$$

Premultiplying equation 3.17 by $\mathrm{T}^T\mathrm{B}^{-1}$ results in

$$T^TB^{-1}ATu_0 = T^TB^{-1}A\cdot U^* + T^TP - T^TP^* \tag{3.18}$$

Defining $K = T^TB^{-1}AT$ and $H = B^{-1}A$, equation 3.18 can be written as

$$Ku_0 - T^TP = T^T(H\cdot U^* - P^*) \tag{3.19}$$

The term T^TP represents the resulting forces and moments on the soil around each structure. Since no external loads are applied to the structures, these resulting forces must equal the inertial loads

$$T^TP = \omega^2Mu_0 \tag{3.20}$$

where M stands for the mass matrix of the structures considered and is explicitly given by

in–plane case

$$M = \begin{bmatrix} m_1 & 0 & -z_1m_1 & & & & \\ & m_1 & x_1m_1 & & 0 & & \\ & & J_1 & & & & \\ & & & m_2 & 0 & -z_2m_2 & \\ & \text{symm.} & & & m_2 & x_2m_2 & \\ & & & & & J_2 & \\ & & & & & & \ddots \end{bmatrix} \tag{3.21}$$

anti–plane case $$M = \begin{bmatrix} m_1 & 0 & \\ 0 & m_2 & \\ & & \ddots \end{bmatrix} \tag{3.22}$$

where m_i represents the mass of structure i and J_i its mass moment of inertia ($J_i = J_{0i} + (x_i^2+z_i^2)m_i$; J_{0i}=mass moment of inertia w.r.t. the center of mass); (x_i, z_i) are the relative coordinates of the center of mass of structure i with respect to its reference point.

Substitution from equation 3.20 into equation 3.19 leads to

$$(K-\omega^2 M)u_0 = T^T(H \cdot U^* - P^*) \tag{3.23}$$

Equation 3.23 can be solved for u_0, the rigid motions of each structure, considering different seismic motions (defined by U^* and P^*). Figure 3.1 shows an example of a model that this formulation can solve. After obtaining the rigid motions of each structure, the resulting displacements at points within the domain can be computed by applying a ficticious load at the location and direction of the desired displacement. Designating by A^I the row matrix of the resulting tractions on the boundary nodes of the structures, and B^I the row matrix of the resulting displacements, the unknown displacement u_i is given by (referring to equation 3.11)

$$u_i - u_i^* = -A^I(Tu_0 - U^*) + B^I(P - P^*) \tag{3.24}$$

where u_i^* represents the displacement due to the incident seismic waves at the point and direction chosen. Since from equation 3.13, $P-P^* = B^{-1}A(Tu_0 - U^*) = H(Tu_0 - U^*)$, equation 3.24 can be transformed into

$$u_i = (B^I H - A^I)\cdot(Tu_0 - U^*) + u_i^* \tag{3.25}$$

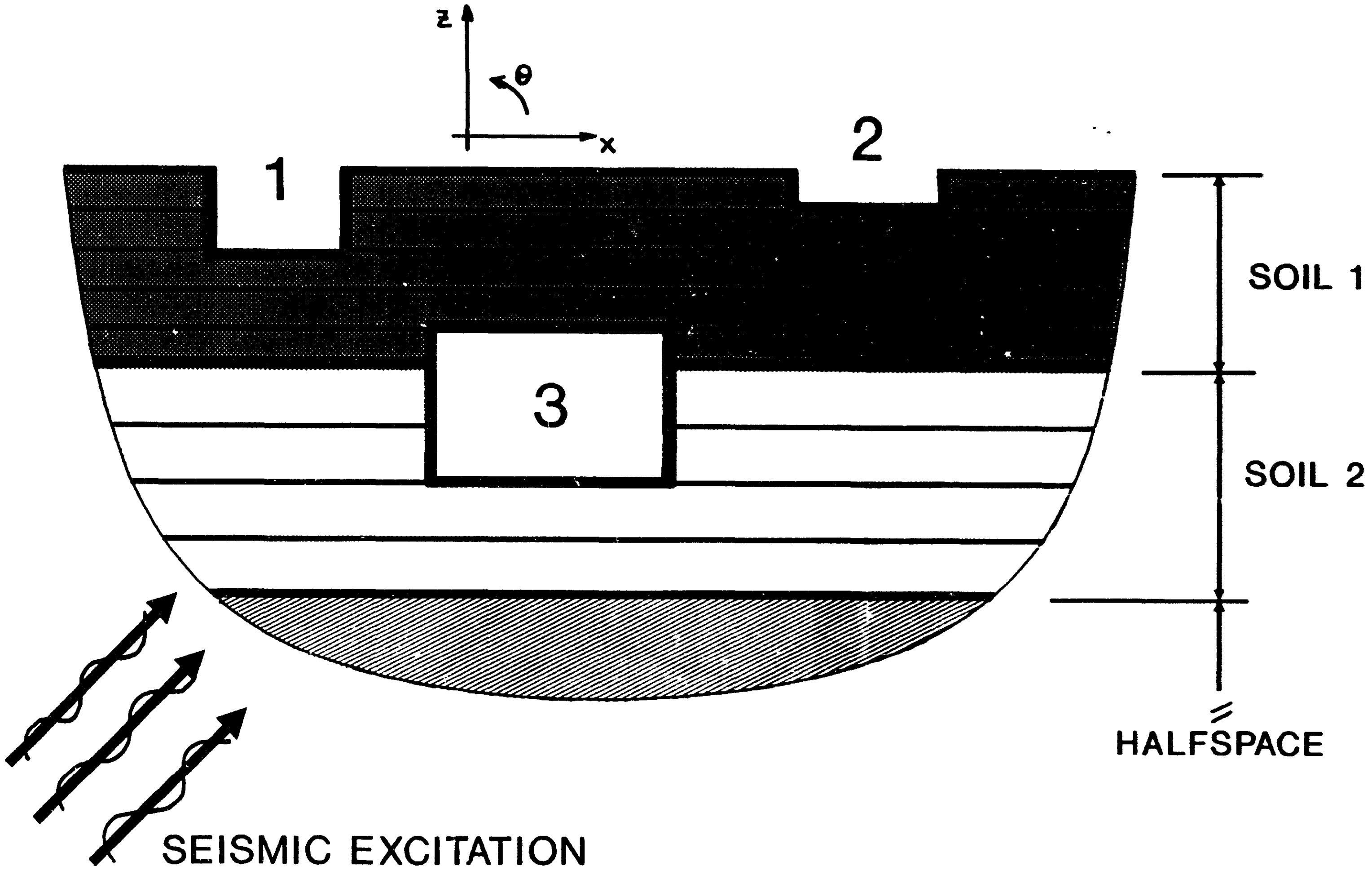

MULTIPLE STRUCTURE ANALYSIS

Figure 3.1

3.2 Comparison with Numerical Results

3.2.1 Dynamic Response of Strip Foundations Embedded in a Stratum

To test the Boundary Element code developed, some comparisons with other numerical results were performed. First, the dynamic compliances of a rigid embedded strip foundation were evaluated and compared with the results obtained by Chang–Liang [9], who used for this purpose the finite element method. Figure 3.2 shows the geometry of the model chosen. The soil was taken as linearly viscoelastic with an internal damping of the hysteretic type, which was incorporated using the Correspondence Principle as explained in Appendix A. The stratum thickness was taken equal to the total width of the foundation (H/B=2), since with these dimensions the soil–structure interaction effects are important at frequencies close to the lowest natural frequencies of the stratum. The embeddement of the foundation was taken equal to 2/3 its halfwidth (E/B=2/3), the deepest case analyzed by Chang–Liang. A Poisson's ratio of 0.30 and internal damping coefficient β=10% were chosen in accordance with the values used in [9]. A massless foundation was analyzed and the results were computed for several values of the dimensionless frequency a_o, defined as $a_o = \omega H/C_s$. In the boundary element analysis, the stratum was divided into 9 equal sublayers and the bottom of the foundation was discretized into 5 constant elements. Some comparisons with a finer discretization, halving each sublayer, were also undertaken for the static case. The dynamic compliances for the in–plane horizontal displacement and rocking were normalized with respect to the corresponding static values and their variations with frequency are displayed in figures 3.3–3.5, where both the real and the (negative of the) imaginary parts are plotted. It can be seen that the results of the two methods agree extremely well in the entire frequency range analyzed, the largest differences being of the order of only a few percent.

RIGID EMBEDDED STRIP FOUNDATION

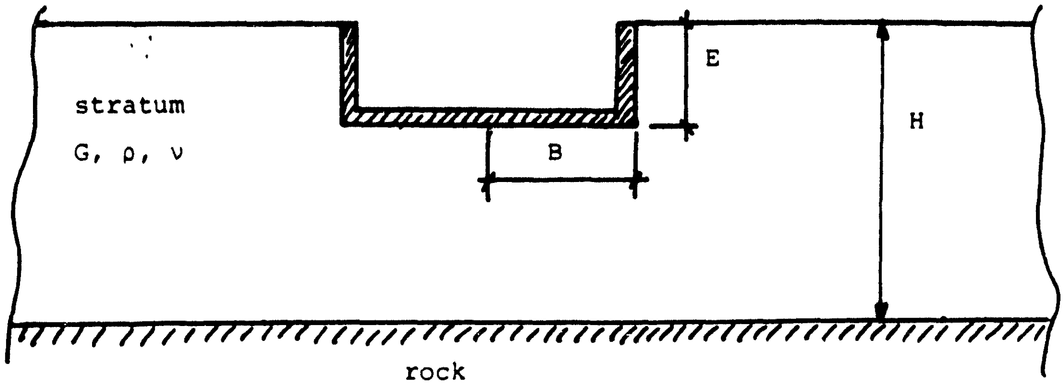

Fig.3.2 - Geometry

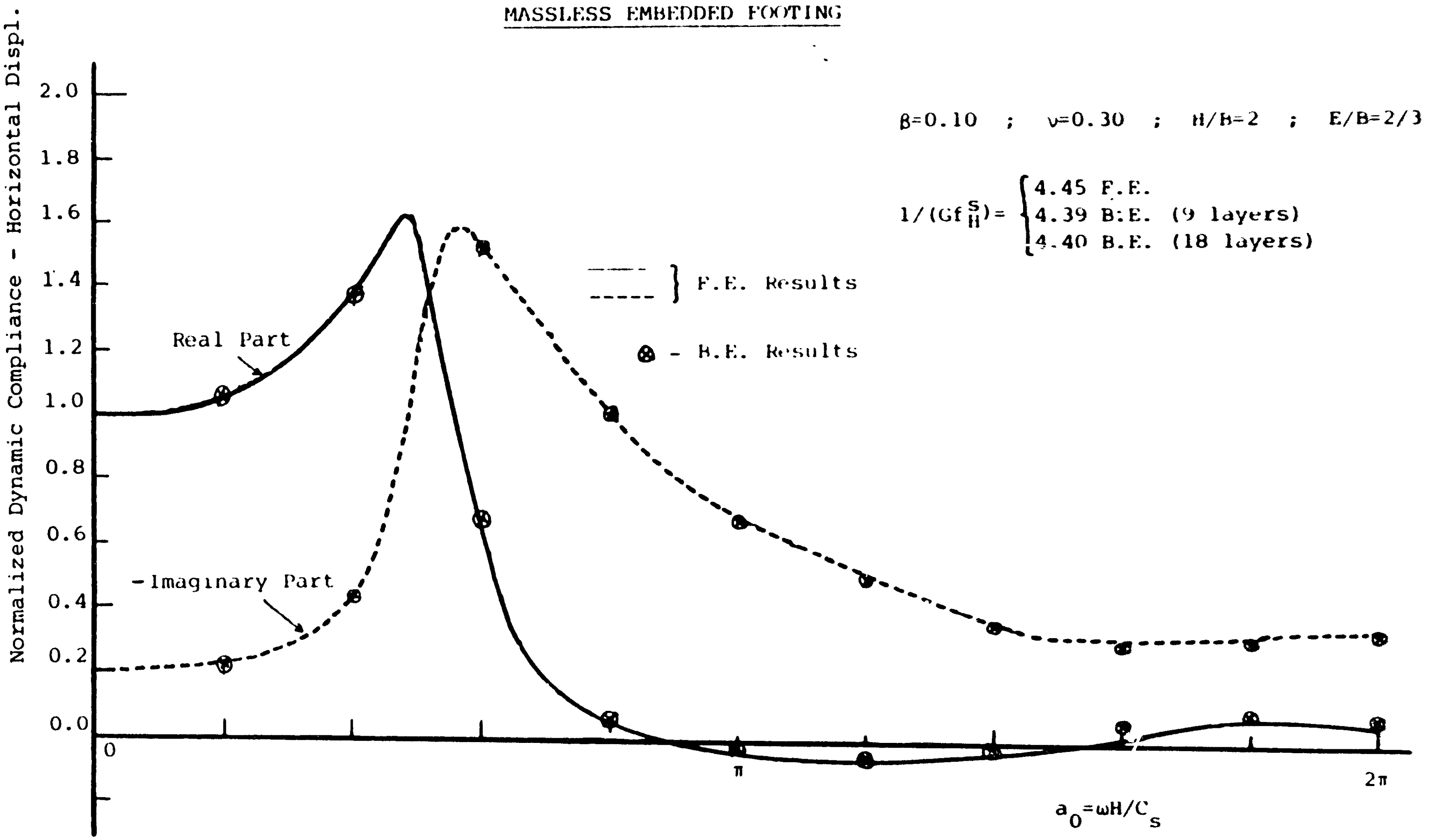
MASSLESS EMBEDDED FOOTING
β=0.10 ; ν=0.30 ; H/B=2 ; E/B=2/3
$1/(Gf^S_H) = \begin{cases} 4.45 \text{ F.E.} \\ 4.39 \text{ B.E. (9 layers)} \\ 4.40 \text{ B.E. (18 layers)} \end{cases}$
F.E. Results
⊗ - B.E. Results
Real Part
- Imaginary Part
Normalized Dynamic Compliance - Horizontal Displ.
2.0
1.8
1.6
1.4
1.2
1.0
0.8
0.6
0.4
0.2
0.0
0
π
2π
$a_0=\omega H/C_s$

Figure 3.3

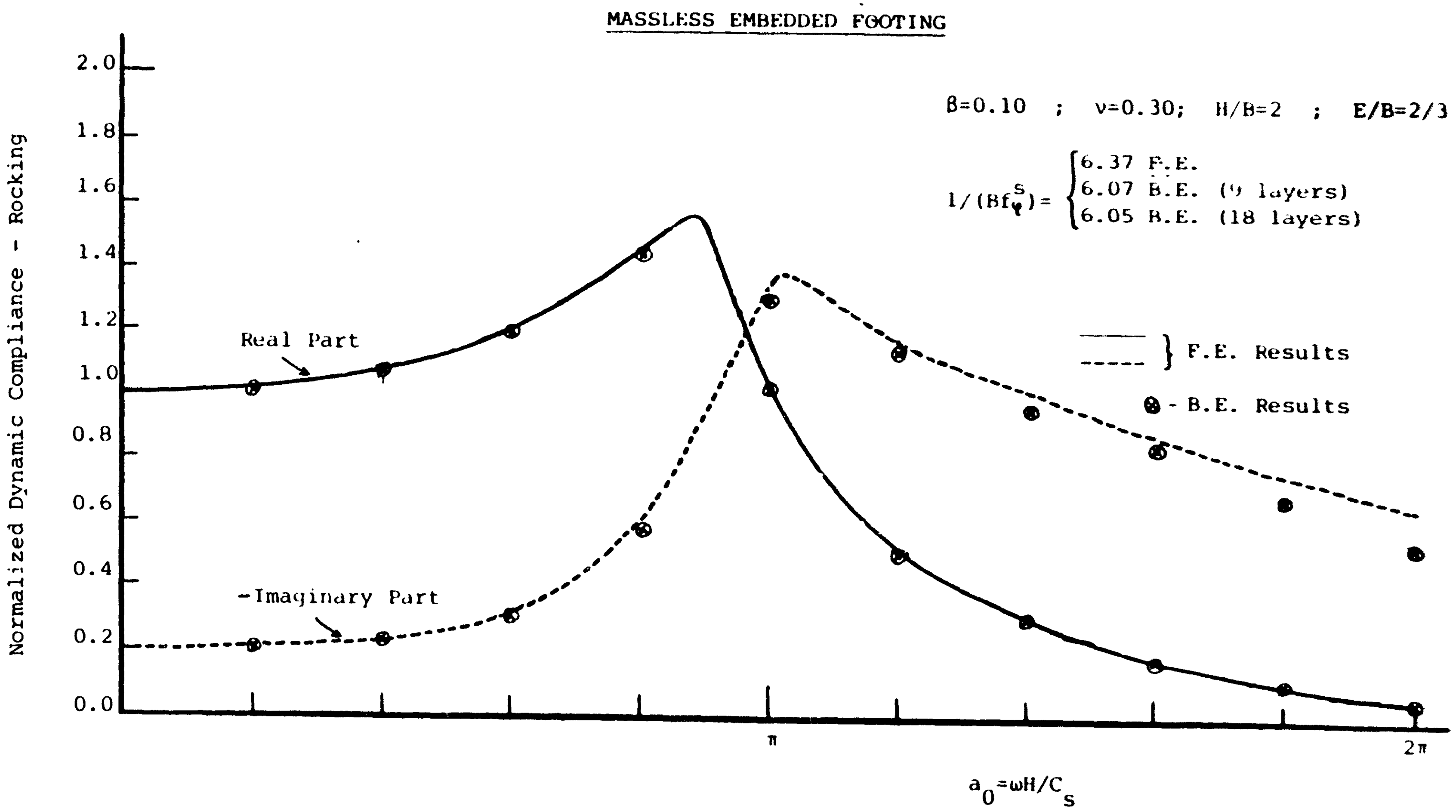
MASSLESS EMBEDDED FOOTING
β=0.10 ; ν=0.30; H/B=2 ; E/B=2/3
$1/(Bf_{\psi}^{s}) = \begin{cases} 6.37 \text{ F.E.} \\ 6.07 \text{ B.E. (9 layers)} \\ 6.05 \text{ B.E. (18 layers)} \end{cases}$
} F.E. Results
⊗ - B.E. Results
Real Part
-Imaginary Part
Normalized Dynamic Compliance - Rocking
2.0
1.8
1.6
1.4
1.2
1.0
0.8
0.6
0.4
0.2
0.0
π
2π
$a_0 = \omega H / C_s$

Figure 3.4

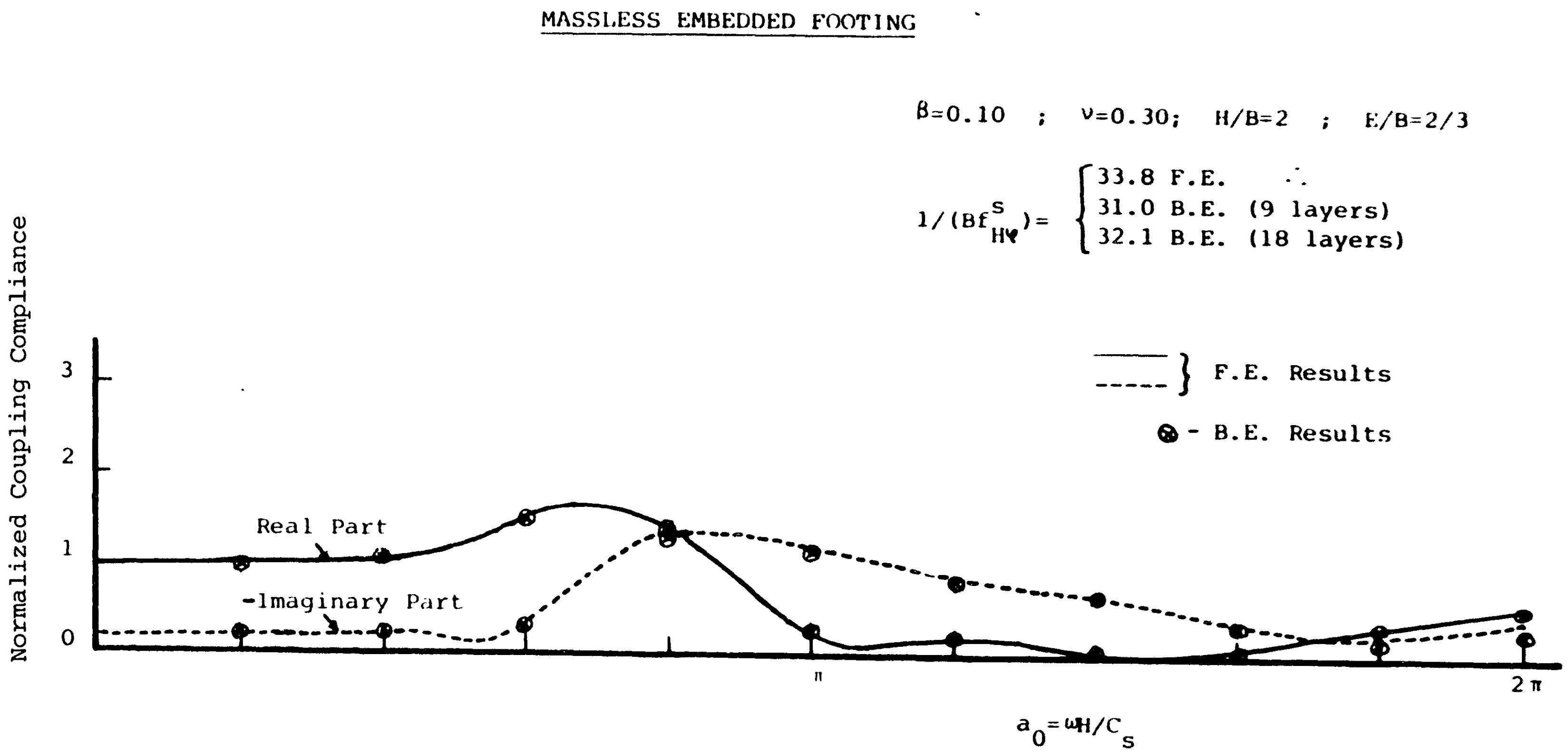
MASSLESS EMBEDDED FOOTING
β=0.10 ; ν=0.30; H/B=2 ; E/B=2/3
$1/(Bf^{s}_{H\psi}) = \begin{cases} 33.8 \text{ F.E.} \\ 31.0 \text{ B.E. (9 layers)} \\ 32.1 \text{ B.E. (18 layers)} \end{cases}$
} F.E. Results
⊗ - B.E. Results
Normalized Coupling Compliance
3
2
1
0
Real Part
-Imaginary Part
π
2π
$a_0=\omega H/C_s$

Figure 3.5

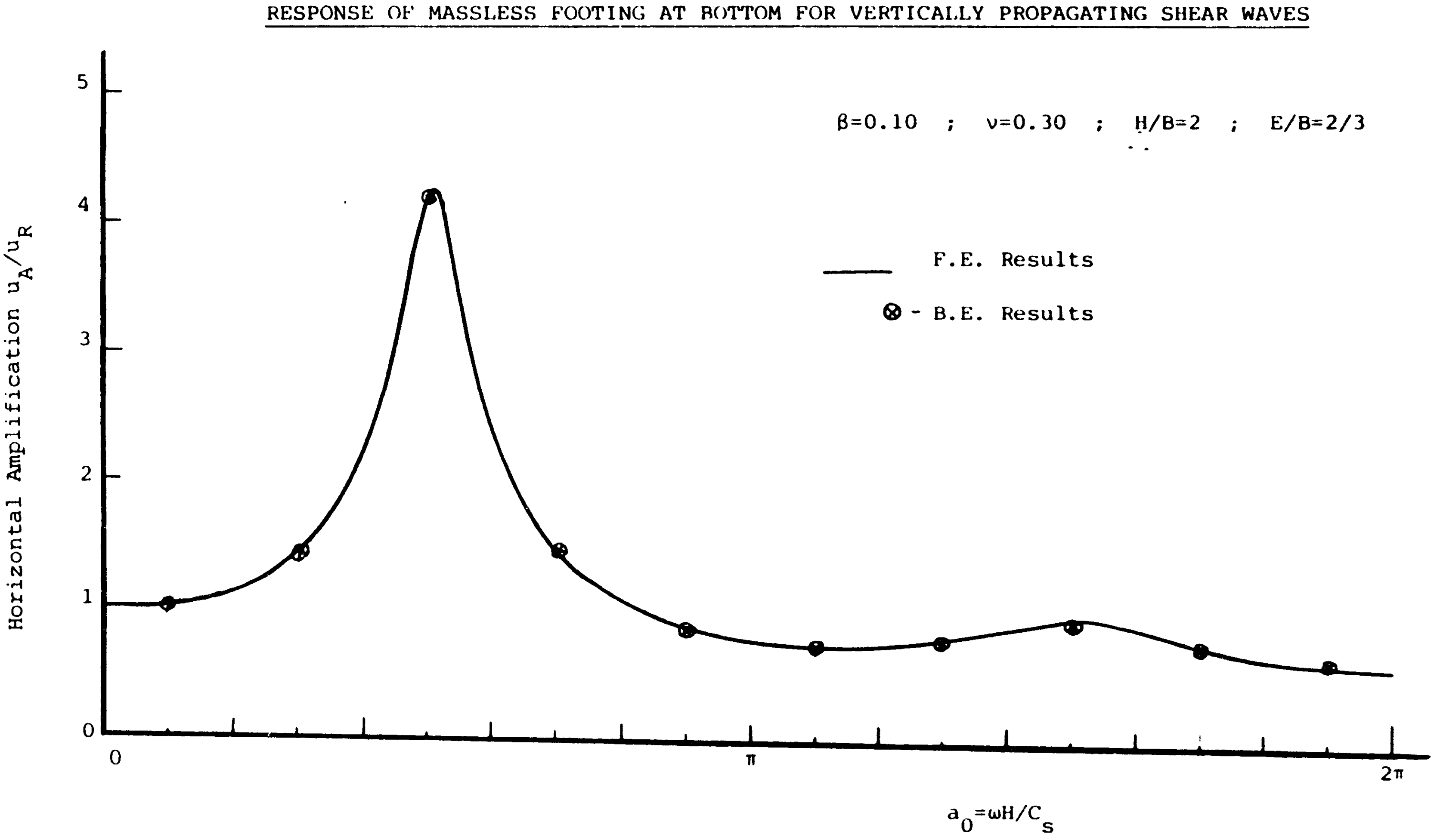

RESPONSE OF MASSLESS FOOTING AT BOTTOM FOR VERTICALLY PROPAGATING SHEAR WAVES

Figure 3.6

RESPONSE OF MASSLESS FOOTING AT BOTTOM FOR VERTICALLY PROPAGATING SHEAR WAVES

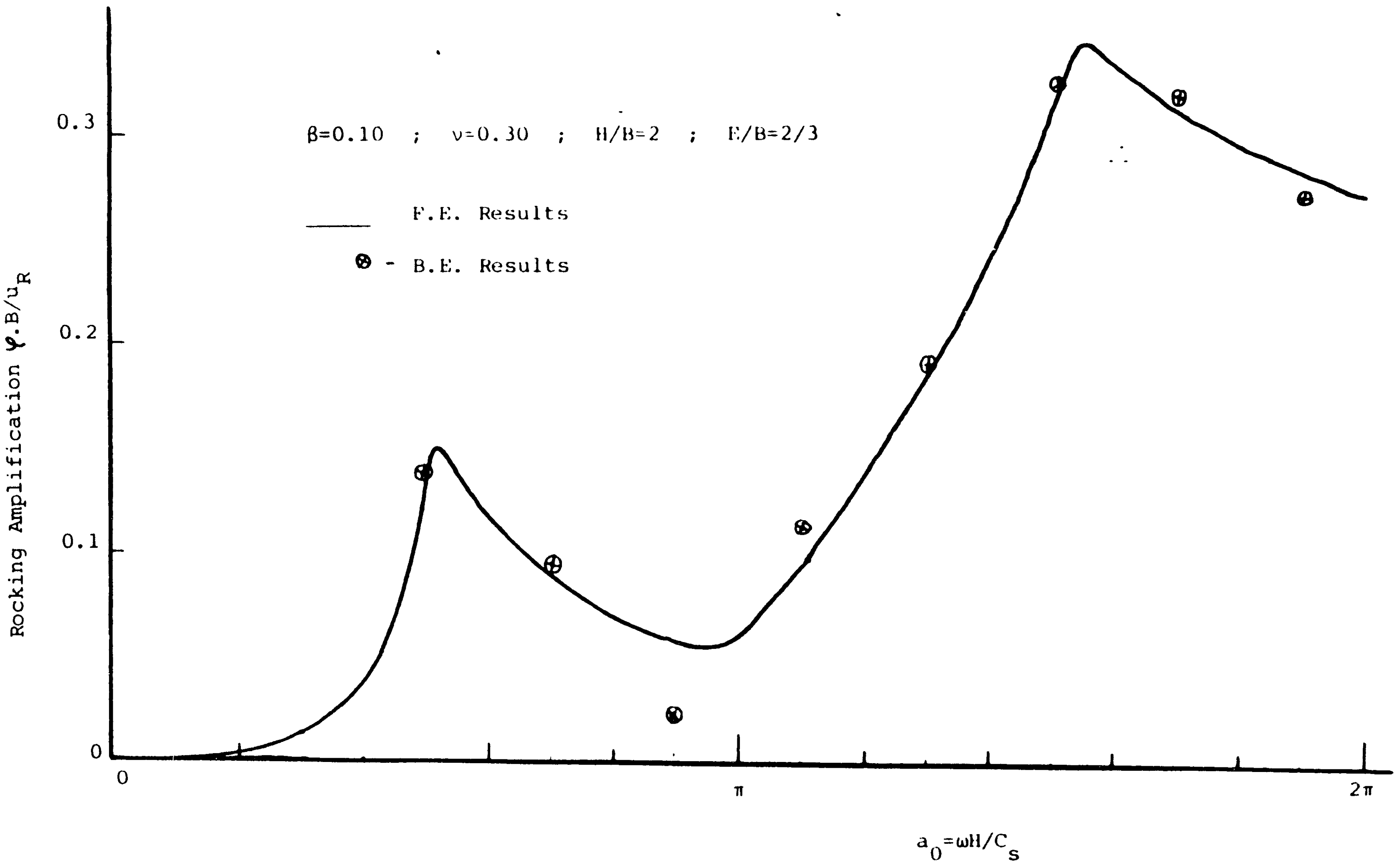

Figure 3.7

RESPONSE OF MASSLESS FOOTING AT BOTTOM FOR VERTICALLY PROPAGATING SHEAR WAVES - PHASE ANGLES

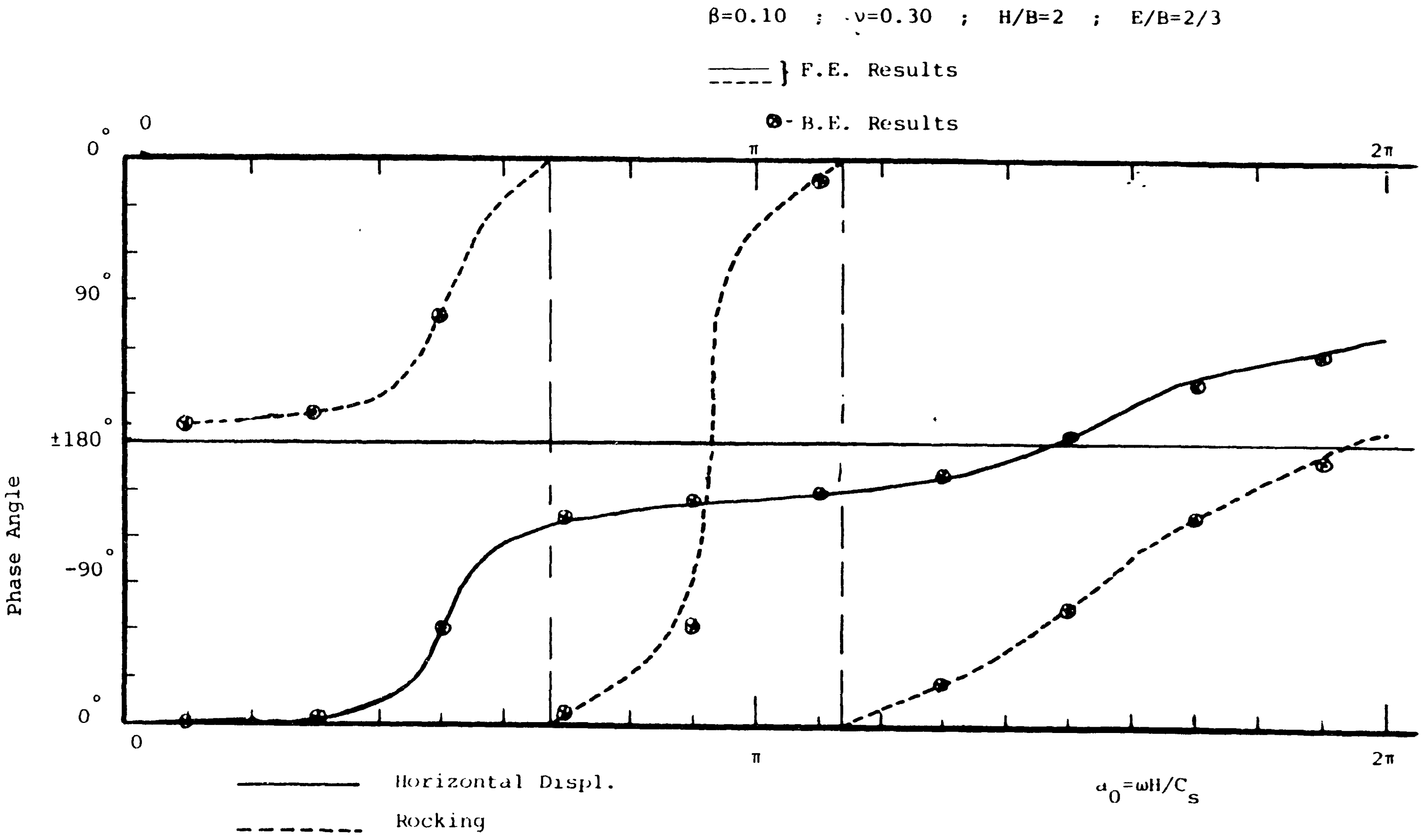

Figure 3.8

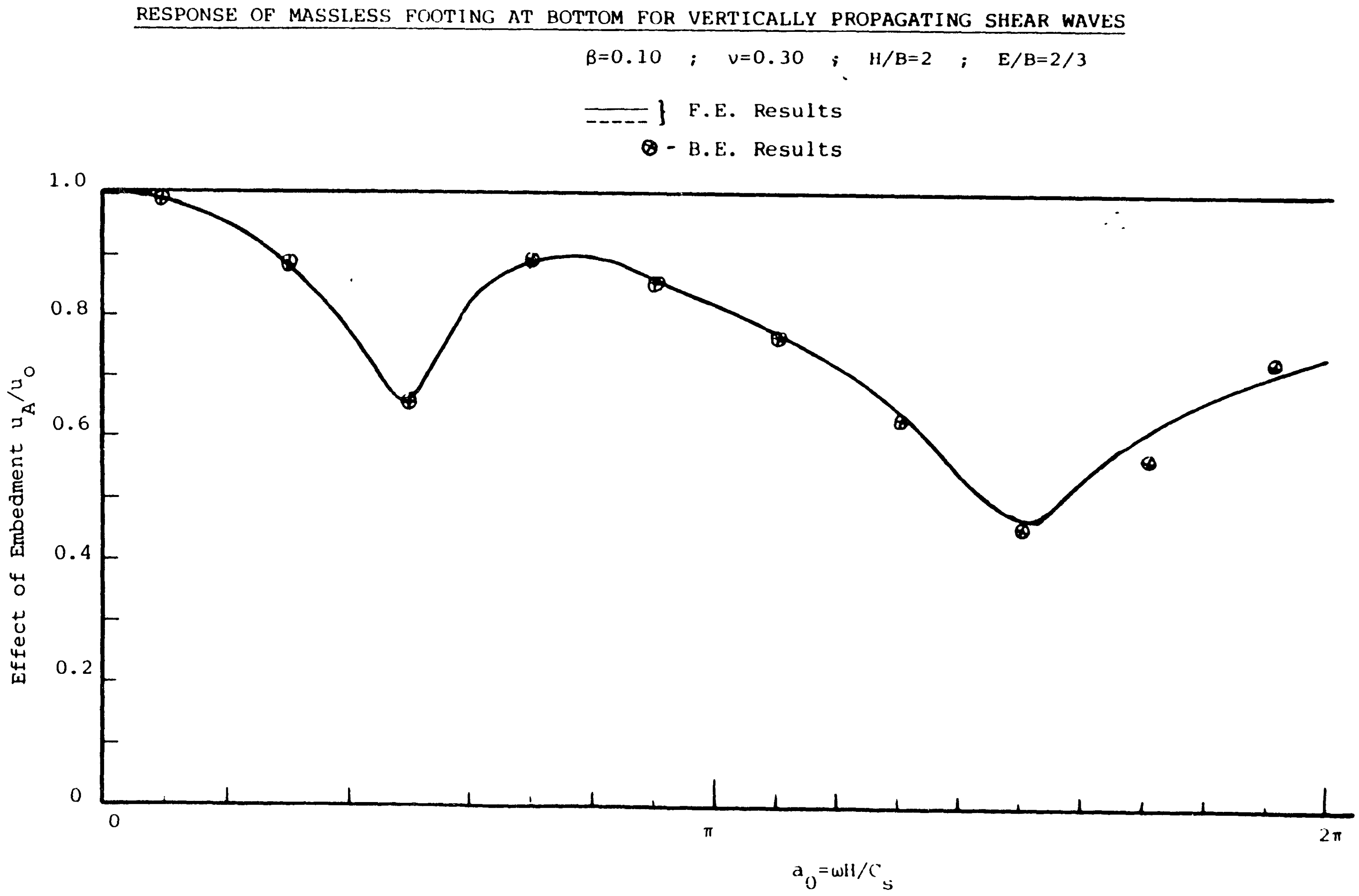
RESPONSE OF MASSLESS FOOTING AT BOTTOM FOR VERTICALLY PROPAGATING SHEAR WAVES
β=0.10 ; ν=0.30 ; H/B=2 ; E/B=2/3
F.E. Results
⊗ - B.E. Results
1.0
0.8
0.6
0.4
0.2
0
Effect of Embedment u_A/u_o
0
π
2π
$a_0=\omega H/C_s$

Figure 3.9

Afterwards, the response of the rigid foundation to vertically incident in–plane shear waves was computed. The displacements of the foundation are referred to the centroid of its bottom, and were normalized with respect to the free–field horizontal displacement at rock level, u_R. The results corresponding to the absolute value of the horizontal displacement and rocking are displayed, respectively, in figures 3.6 and 3.7 as a function of the dimensionless frequency a_o. Figure 3.8 shows the phase angle of the input motions. The ratio of the horizontal displacement of the foundation and the free–field motion at the surface can be seen in figure 3.9. As before, an extremely good agreement between both methods is found in all cases.

These results are very satisfactory if it is noted that while in the Finite Element method the whole stratum depth needs to be discretized (even incorporating consistent boundaries at each side of the foundation) while in the Boundary Element approach only (4+4+5)*2=26 degrees of freedom were needed.

3.2.2 Dynamic Stiffnesses of Surface Strip Foundations Bonded to a Halfspace

As explained in section 2.2.3, the extension of the Green functions used to the case of a layered halfspace can only be done directly in an approximate way by using a paraaxial approximation for the dynamic stiffnesses of the halfspace. In order to check the accuracy and convergence of such procedure, the dynamic stiffnesses of a rigid strip foundation bonded to the surface of an homogeneous halfspace were computed and compared with accurate numerical solutions given in Gazetas [13], which were computed by a semi–analytical procedure. Figure 3.10 shows the geometry and parameters chosen for this problem. The boundary element results were obtained using constant elements and modelling the halfspace with a top layer having 100 m (=2B) and divided into 24 sublayers.

The theoretical static stiffness for rocking of a strip footing is

$$K_{\varphi} = \frac{\pi G B^2}{2(1-\nu)} \left\{ 1 + \left[\frac{\ln(3-4\nu)}{\pi} \right]^2 \right\} \tag{3.26}$$

while the static stiffnesses for in–plane horizontal and vertical displacements of strip footings are zero.

Figure 3.11 shows a comparison of the results using the Boundary Element (B.E.) method with several discretizations (10,20 and 40 nodes) and the value given by equation 3.26 (for a Poisson's ratio of 0.33 and unit shear modulus). The horizontal axis represents a measure of the discretization size and it can be seen that the B.E. results converge almost in a linear way to the exact stiffness. Moreover, if the results corresponding to 20 and 40 nodes are extrapolated linearly, a very accurate estimate of the static rocking stiffness is obtained.

In figures 3.12–3.14, the absolute value of the dynamic stiffnesses for horizontal displacement, rocking and vertical displacement are displayed for a dimensionless frequency a_0=1.5 ($a_0=\omega B/C_s$). Again the B.E. results seem to converge linearly to the more accurate values, except for the rocking mode in which a linear extrapolation gives an error of about 5%.

Overall it can be said that constant elements turn out not to be very accurate for this problem, in particular for rocking, since the extremeties of the foundations have an

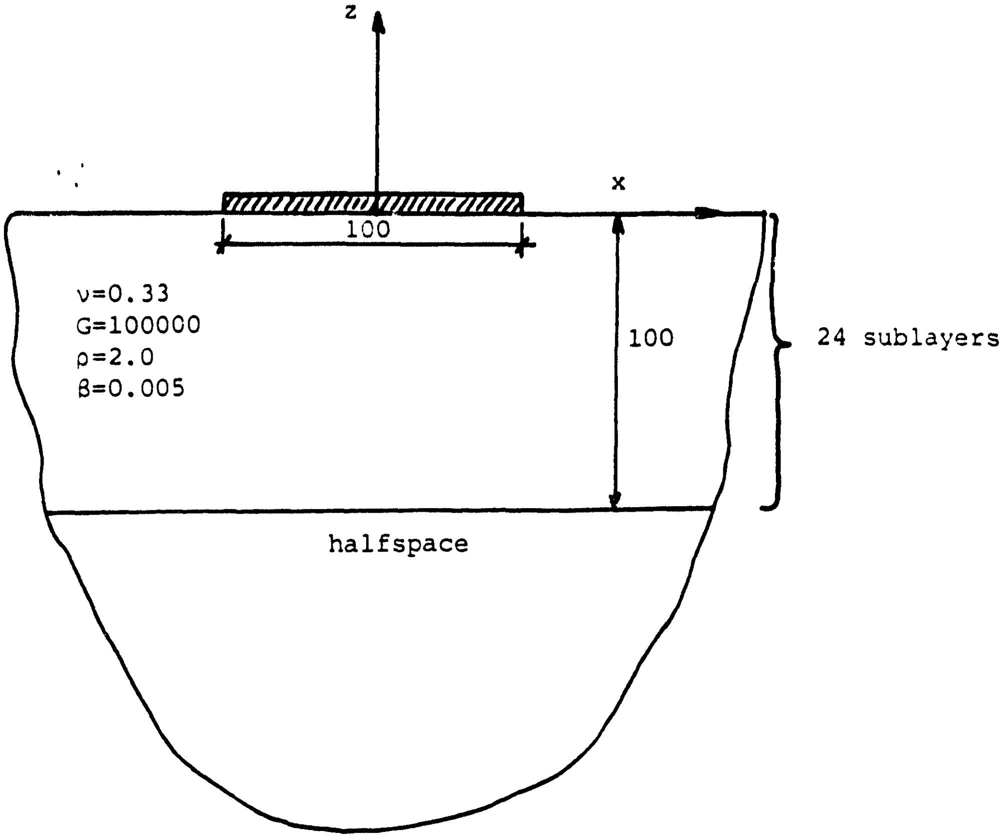

Fig. 3.10- Strip foundation

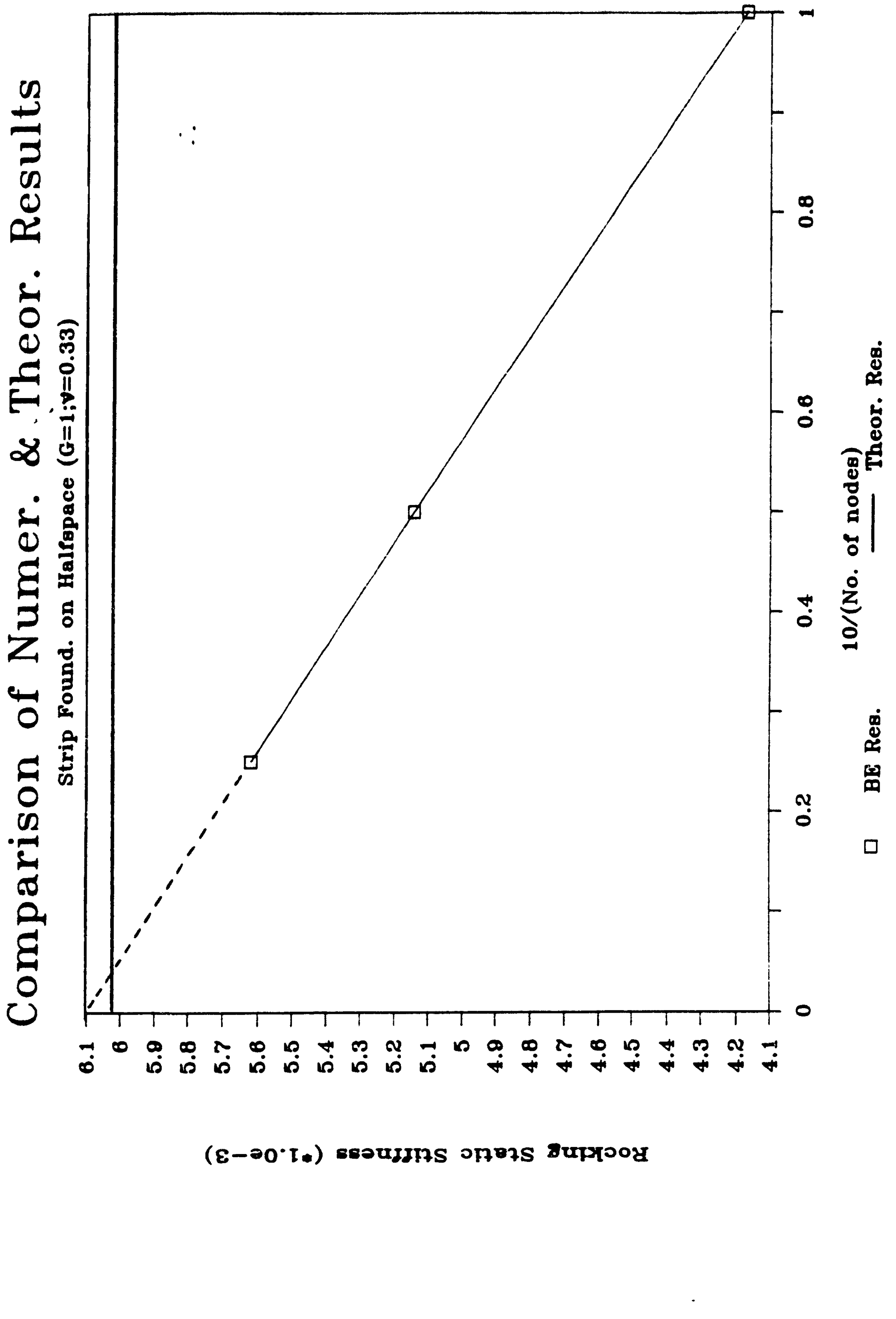
Comparison of Numer. & Theor. Results
Strip Found. on Halfspace (G=1;ν=0.33)
Rocking Static Stiffness (*1.0e-3)
6.1
6
5.9
5.8
5.7
5.6
5.5
5.4
5.3
5.2
5.1
5
4.9
4.8
4.7
4.6
4.5
4.4
4.3
4.2
4.1
0
0.2
0.4
0.6
0.8
1
10/(No. of nodes)
□ BE Res.
Theor. Res.

Figure 3.11

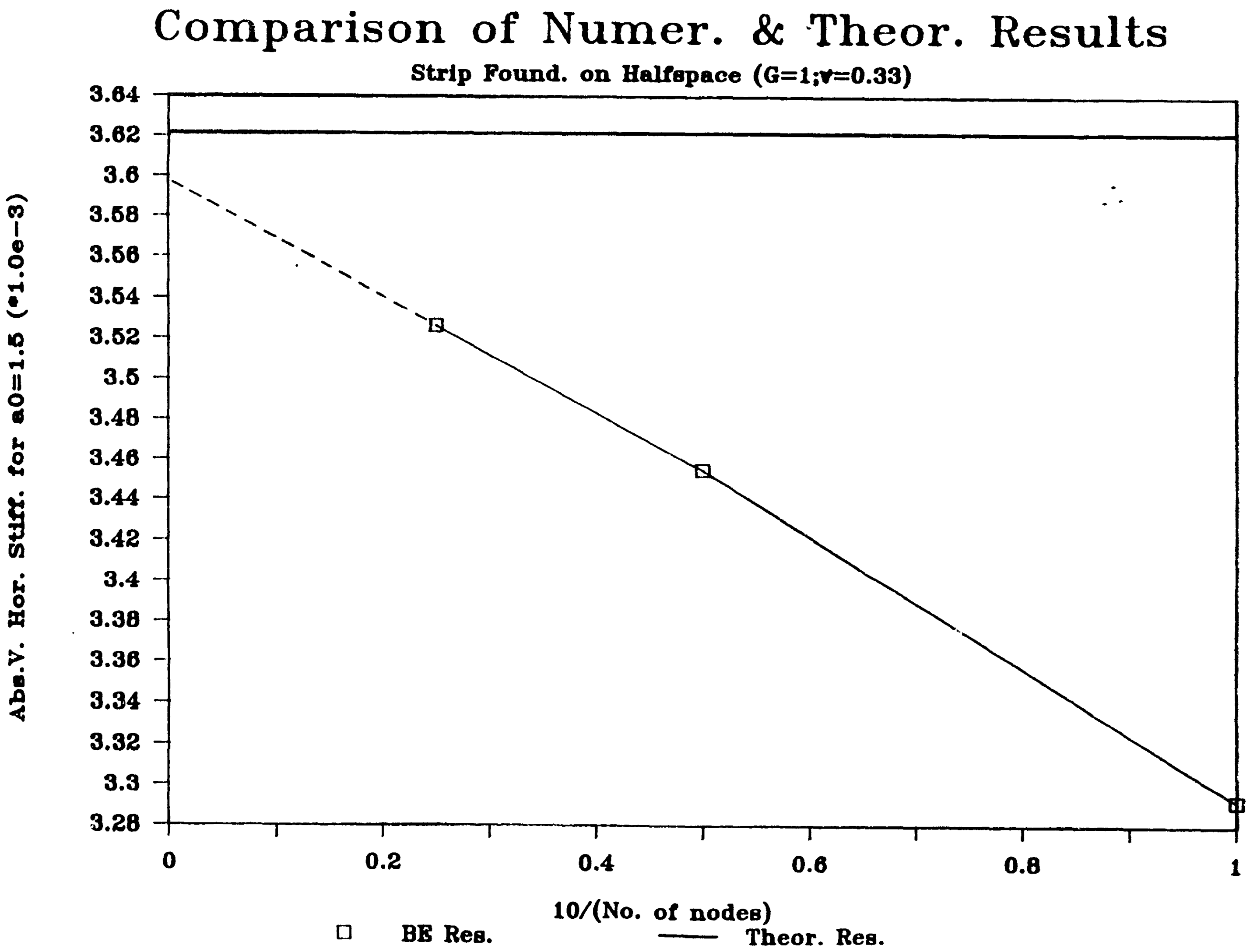
Comparison of Numer. & Theor. Results
Strip Found. on Halfspace (G=1;ν=0.33)
Abs.V. Hor. Stiff. for a0=1.5 (*1.0e-3)
3.64
3.62
3.6
3.58
3.56
3.54
3.52
3.5
3.48
3.46
3.44
3.42
3.4
3.38
3.36
3.34
3.32
3.3
3.28
0
0.2
0.4
0.6
0.8
1
10/(No. of nodes)
□ BE Res.
—— Theor. Res.

Figure 3.12

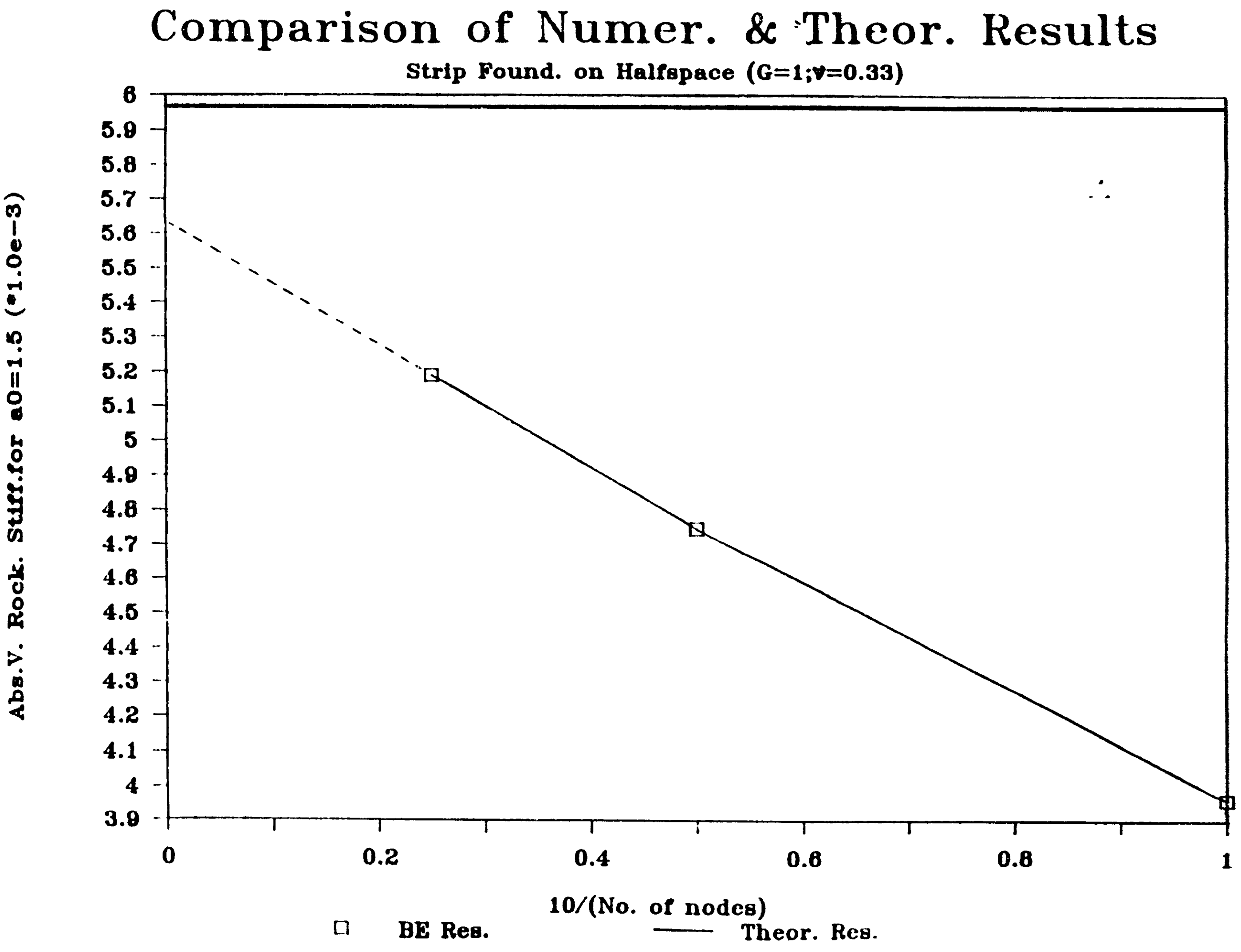
Comparison of Numer. & Theor. Results
Strip Found. on Halfspace (G=1;ν=0.33)
Abs.V. Rock. Stiff.for a0=1.5 (*1.0e−3)
6
5.9
5.8
5.7
5.6
5.5
5.4
5.3
5.2
5.1
5
4.9
4.8
4.7
4.6
4.5
4.4
4.3
4.2
4.1
4
3.9
0
0.2
0.4
0.6
0.8
1
10/(No. of nodes)
□ BE Res.
—— Theor. Res.

Figure 3.13

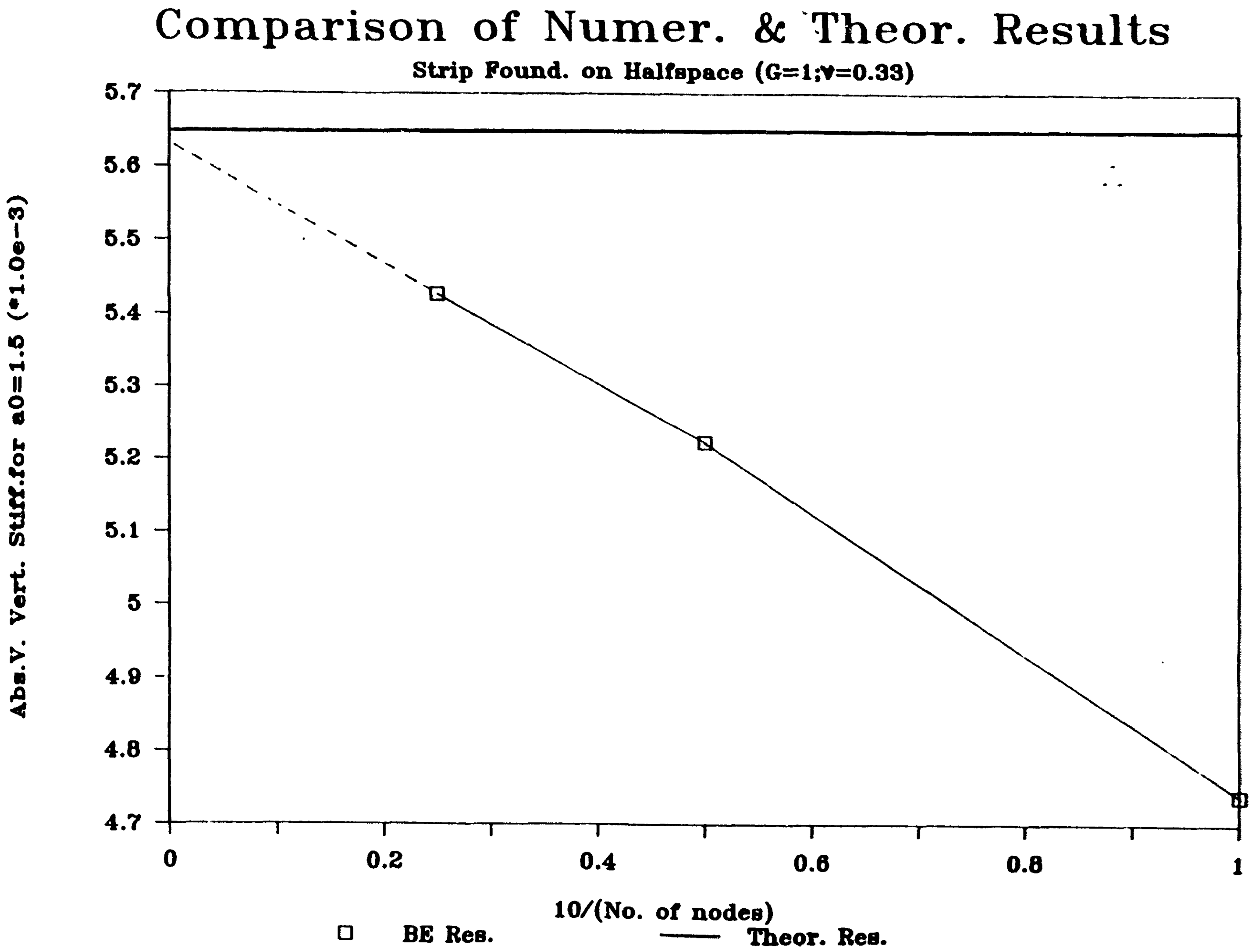
Comparison of Numer. & Theor. Results
Strip Found. on Halfspace (G=1;ν=0.33)
Abs.V. Vert. Stiff.for a0=1.5 (*1.0e-3)
5.7
5.6
5.5
5.4
5.3
5.2
5.1
5
4.9
4.8
4.7
0
0.2
0.4
0.6
0.8
1
10/(No. of nodes)
□ BE Res.
Theor. Res.

Figure 3.14

important effect on the response and are not well modelled with constant elements. However, the results are still acceptable, specially if they are corrected for discretization errors. Finally, the paraaxial approximation seems to work well.

3.3 Causality of the Response

When analysing a dynamic problem in the time domain, the response must satisfy the causality relations between any two points. These relations stipulate that the response at an arbitrary point B due to an excitation at point A can only be received (assuming zero initial conditions) after the shortest period of time it takes the fastest wave to travel from A to B, where the travelling path must be contained inside the domain considered. Since the longitudinal waves have the highest speed C_p, and assuming that the only loading is at point A, it can be stated that $u_B=0$ for $t<|B-A|/C_p$ where $|B-A|$ represents the shortest distance between A and B. These causality relations are very important because they follow directly from basic physical considerations, so that any accurate solution must satisfy causality.

This problem has recently received much attention as can be seen in the works of Antes and von Estorff [2] and Triantafyllidis et al [43]. In particular, when the domains considered are non–convex, it is important to insure that direct waves travelling in a path passing outside the domain, are not present in the solution. Non–convex domains arise when considering open trenches, tunnels, embedded foundations or even hills as is illustrated in figure 3.15. Antes and von Estorff used a boundary element formulation in the time domain and showed that if the method is applied directly to non–convex domains, the causality condition is not satisfied. However, by dividing the domain into convex subdomains and ensuring compatibility and equilibrium at each new boundary, the results obtained improve substantially. Another possibility to ensure causality of

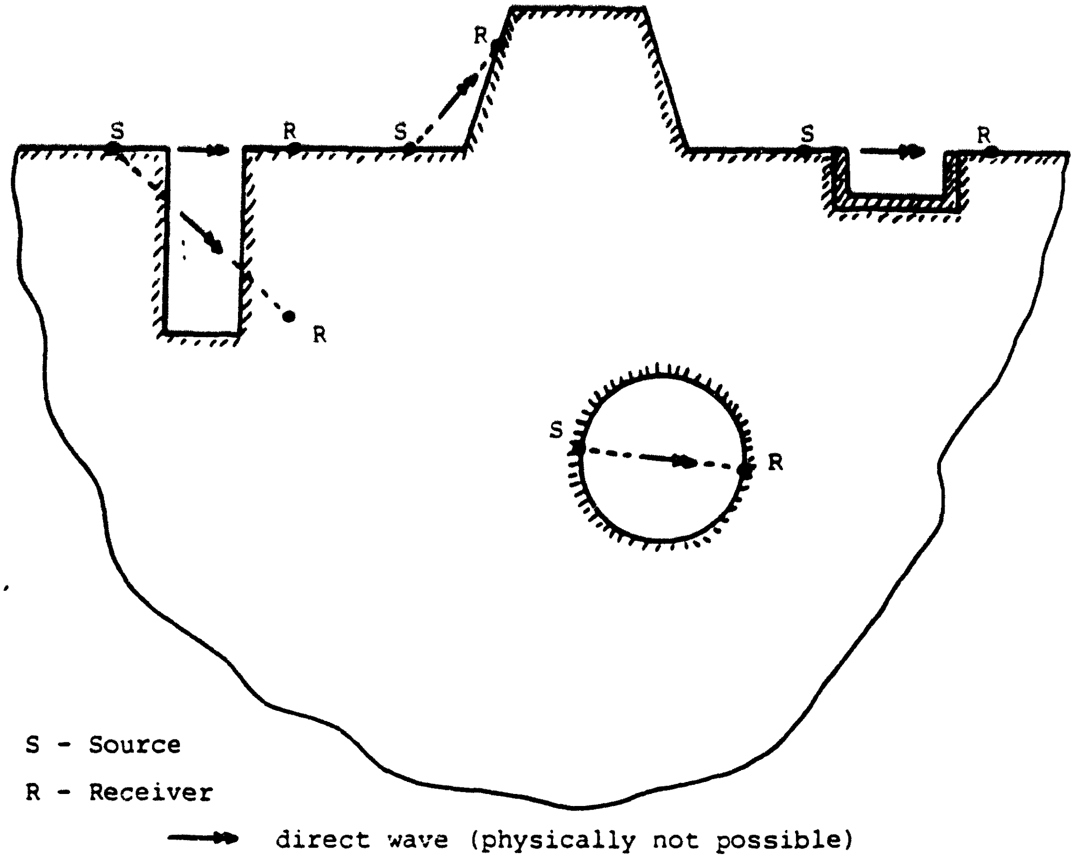

Fig. 3.15 - Non-convex domains

the response in time domain B.E. is to check the real shortest travel time between boundary nodes and set automatically the Green's function to zero for lower times and correct them to eliminate the contribution of "direct" waves.

The contribution of "direct" waves in non–convex domains can be associated with the approximations that need to be made in the exact boundary conditions (tractions and displacements). Since the B.E.M. only satisfies these boundary conditions in an integral sense, there are remaining "sources" along the boundary corresponding to the difference between the exact and approximate boundary conditions. These "sources" produce waves which can travel outside the domain and influence directly other points. If finer discretizations of the boundary are used, then the "errors" on the boundary decrease, and consequently, so does the contribution of direct waves. The B.E.M. approximation errors are intrinsic to the method and exist in all boundaries and at all times; however, their effects are particularly relevant in situations where, because of the causality constraint, the response observed should be null. Hence, a measure of the accuracy of the method can be given by verifying if the solution using the boundary element formulation satisfies causality. In particular, when analyzing non–convex domains with stress–free boundaries (open trench or excavation), the boundary element results tend to present higher errors since, the stresses being obtained by differentiation of the displacements, they are less accurately represented by the polynomial expansions of the displacements.

Triantafyllidis investigated the causality effects in the boundary element solution to dynamic problems formulated both in the time domain and in the frequency domain. He compared the results obtained in the frequency domain for an harmonic loading in a non–convex domain using a direct approach, with the corresponding solution given by a division of the global domain into convex subdomains, and requiring continuity at their interfaces. The time lag required by the causality constraint translates into a phase delay for the frequency domain solutions. It was found once more that both solutions have important differences, the latter approach giving more accurate results.

3.3.1 Evaluation of the Response to a Ricker Wavelet

The causality constraint was investigated for solutions obtained by the boundary element formulation described in chapter 2. Since the computations are performed in the frequency domain, results in the time–domain were obtained by Fourier transformation using the fast Fourier transform algorithm. The example chosen consists of an open trench 50 m deep and 10 m wide in a halfspace, and the results were compared to the case in which no trench is present. Figure 3.16 a,b show the geometry of both models and the soil properties. The halfspace was modelled as a stratum with 100 m in depth, divided into 24 sublayers and the paraaxial approximation for the halfspace was added below the stratum. A small internal damping was prescribed (β=0.005) to prevent numerical overflows for the natural modes of the system.

Since the Green's functions used take into account the stress–free condition at the surface, the only boundary discretized consisted of the trench walls and bottom. The boundary element equation 3.13 was modified as follows

$$A\cdot(U-U^*) = B\cdot(P-P^*) = -B\cdot P^* \tag{3.27}$$

where U^* and P^* represent the free–field displacements and tractions of the imaginary boundary of the trench caused by the applied loading; and P=0 because the walls and bottom of the trench are stress–free. Hence, the displacements of the trench are obtained as

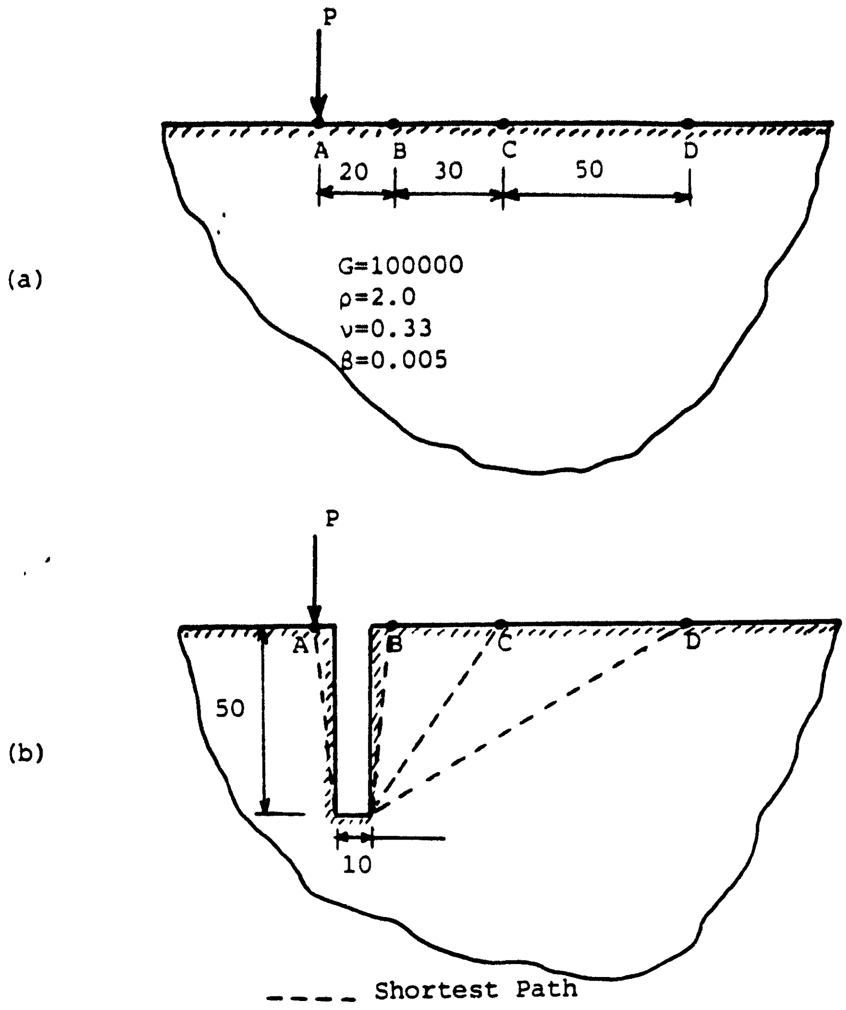

Fig. 3.16 - Source and receiver points. (a) No trench; (b) With trench

$$U = U^{*} - A^{-1}B \cdot P^{*} \tag{3.28}$$

Knowing the displacements of the trench, displacements at other points in the domain can be computed using a derived form of equation 3.24.

$$u_i = u_i^{*} - A^{I}(U - U^{*}) - B^{I}P^{*} \tag{3.29}$$

u_i^{*} representing the displacements at point i in a free–field situation due to the loading.

The dynamic excitation was idealized as a point load with a time variation of a Ricker wavelet. The Ricker wavelet was chosen, since it decays very rapidly both in time and frequency, thus reducing the number of frequencies to be analyzed. Its equation in time is

$$f(t) = a(1-2\tau^2)\, e^{-\tau^2} \tag{3.30}$$

where $\tau = (t-t_s)/t_0$; t_s is the time at which the maximum occurs, 'a' is the amplitude, and t_0 corresponds to the dominant period of the wavelet. Figure 3.17 displays a graph of f(t).

The Fourier transform of f(t), F(ω), is given by

$$F(\omega) = a\left[2\sqrt{\pi}\, t_0 (e^{-i\omega t_s})\right] \Omega^2 e^{-\Omega^2} \tag{3.31}$$

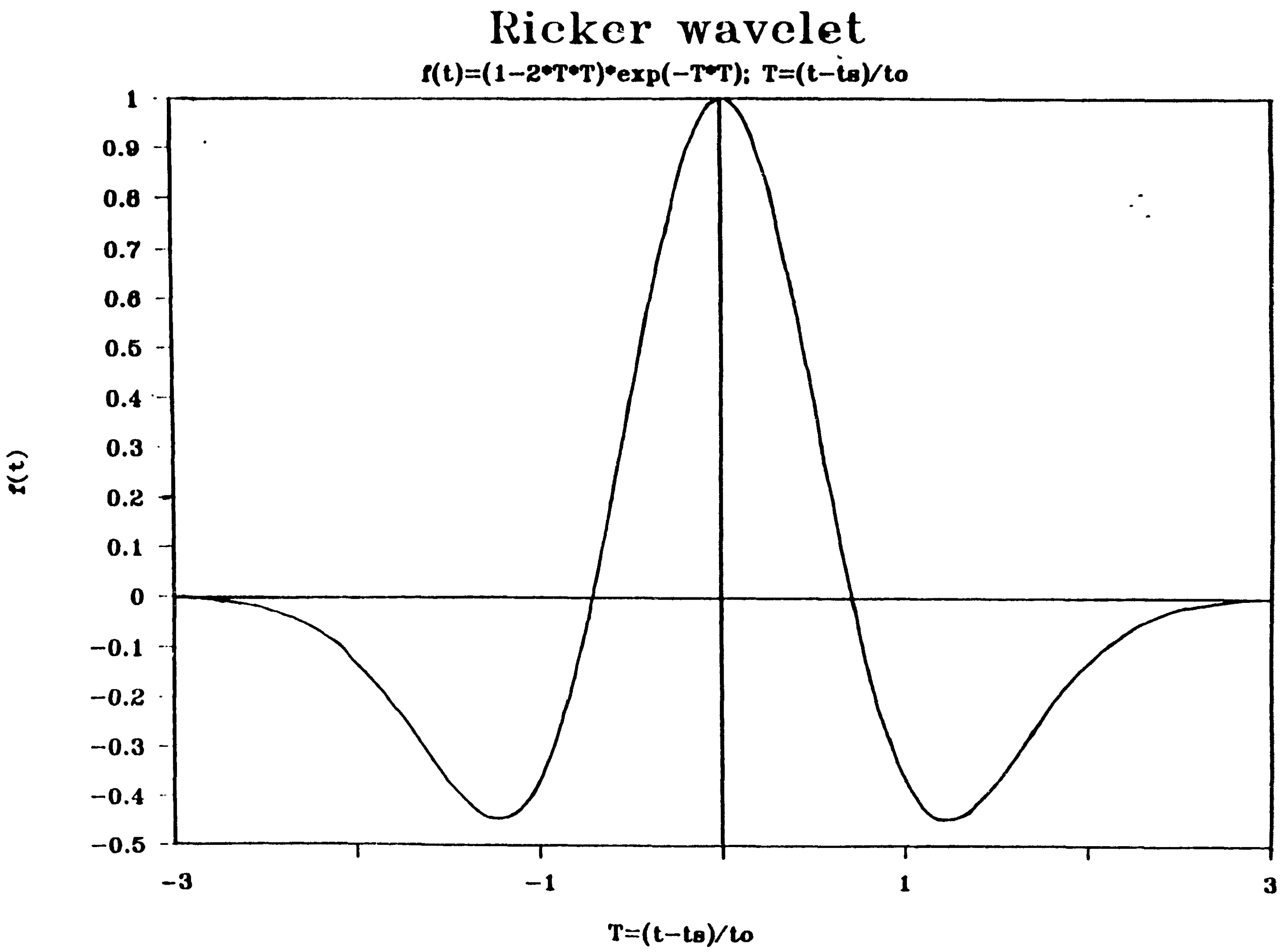
Ricker wavelet
f(t)=(1-2*T*T)*exp(-T*T); T=(t-ts)/to
f(t)
1
0.9
0.8
0.7
0.6
0.5
0.4
0.3
0.2
0.1
0
-0.1
-0.2
-0.3
-0.4
-0.5
-3
-1
1
3
T=(t-ts)/to

Figure 3.17

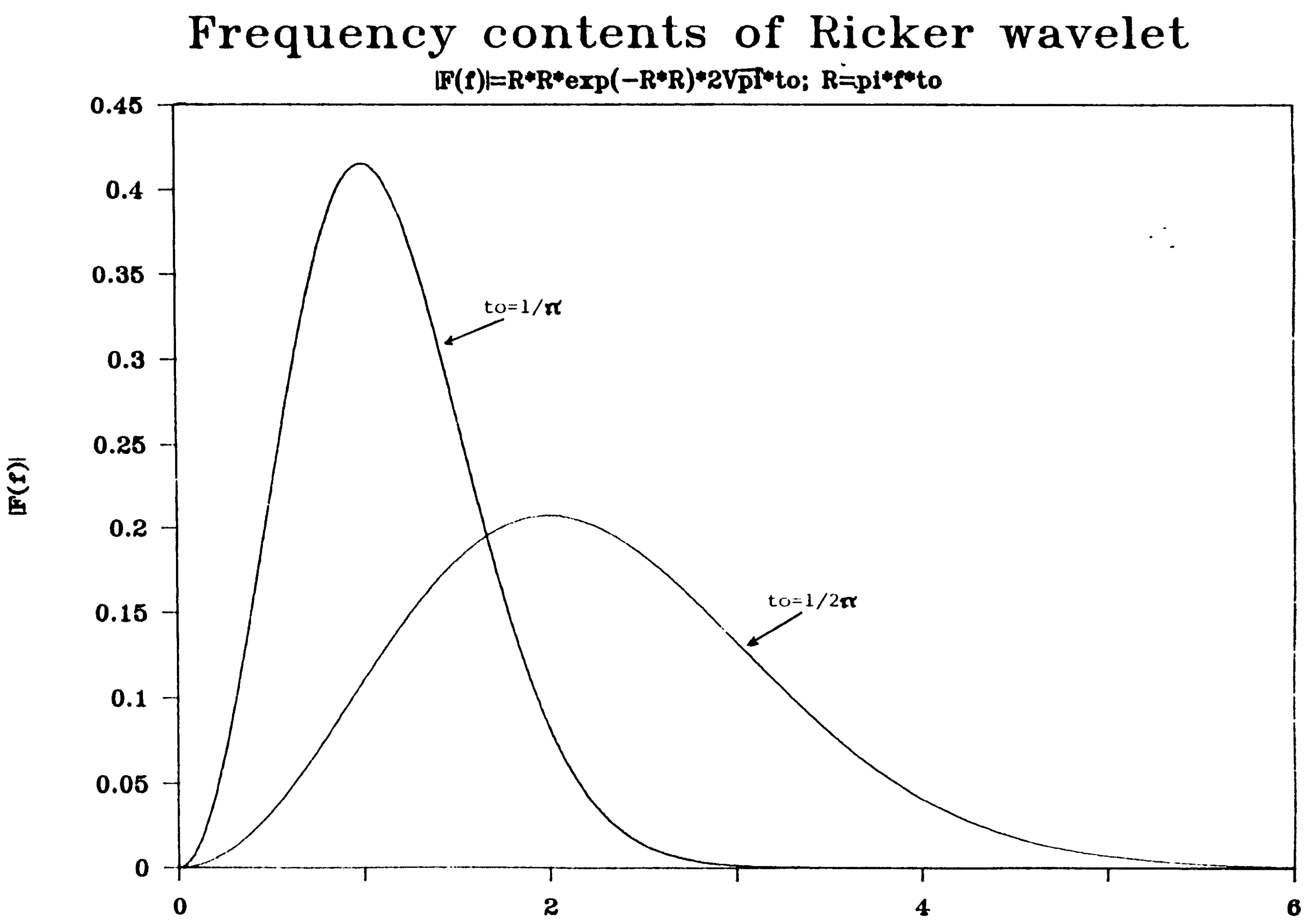
Frequency contents of Ricker wavelet
|F(f)|=R*R*exp(-R*R)*2√pi*to; R=pi*f*to
|F(f)|
0.45
0.4
0.35
0.3
0.25
0.2
0.15
0.1
0.05
0
to=1/π
to=1/2π
0
2
4
6
Frequency f [Hertz]

Figure 3.18

where $\Omega=\omega t_0/2$ and ω is the angular frequency in rads/sec. A graph of $F(\omega)$ is shown in figure 3.18 for two different values of t_0. For this study, t_0 was set to $1/\pi$, which corresponds to a dominant frequency of the wavelet near 1 Hz. The time lag t_s was taken equal to t_0 ($t_s=1/\pi$) which means that it takes about 0.95 sec for the loading to attain its maximum.

The solutions in the time domain were obtained multiplying $F(\omega)$ by the transfer function corresponding to the displacement observed, and Fourier inverting the result (using 8192 points). These transfer functions were computed up to 5 Hz at intervals of 0.10 Hz, and the intermediate values were computed by polynomial interpolation (using Newton's quadrature). The solution in time was obtained at intervals of 0.035 sec.

Figures 3.19–3.21 show a comparison of the results obtained at a point 20 m apart from the loading (point B) for the cases with trench, and without trench. These figures also indicate the shortest time that it would take a shear S or compressional P wave to reach point B. In figure 3.19, the load and displacement considered are vertical. It can be seen that without the trench, the maximum displacement at B is delayed with respect to the maximum loading by about the time it takes a shear wave to travel from A to B, reflecting the fact that for this direction of loading, the perturbation is transmitted along the surface essencially as shear waves. In the case with trench, the maximum displacement is observed later and corresponds very closely to the extra time it takes the shear waves to contour the trench. Also, at the beginning, the displacement at B is zero for a longer period, reflecting the impossibility for the waves to cross the trench directly. According to these results, it seems that the boundary element formulation adopted satisfies quite accurately the causality constraint of the response.

The horizontal displacement at B corresponding to a vertical load at A is shown

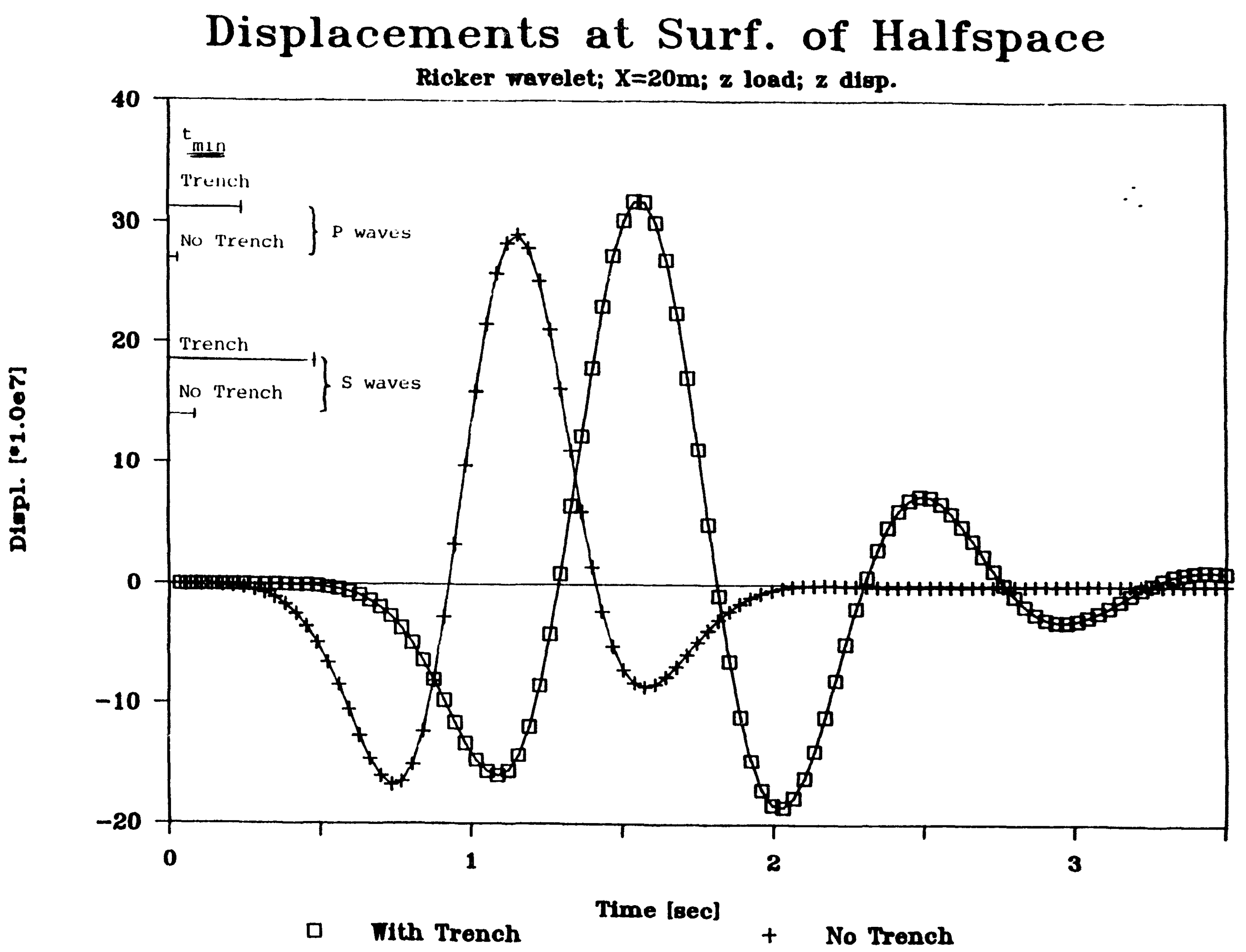
Displacements at Surf. of Halfspace
Ricker wavelet; X=20m; z load; z disp.
t_{min}
Trench
No Trench
P waves
Trench
No Trench
S waves
Displ. [*1.0e7]
40
30
20
10
0
-10
-20
0
1
2
3
Time [sec]
□ With Trench
+ No Trench

Figure 3.19

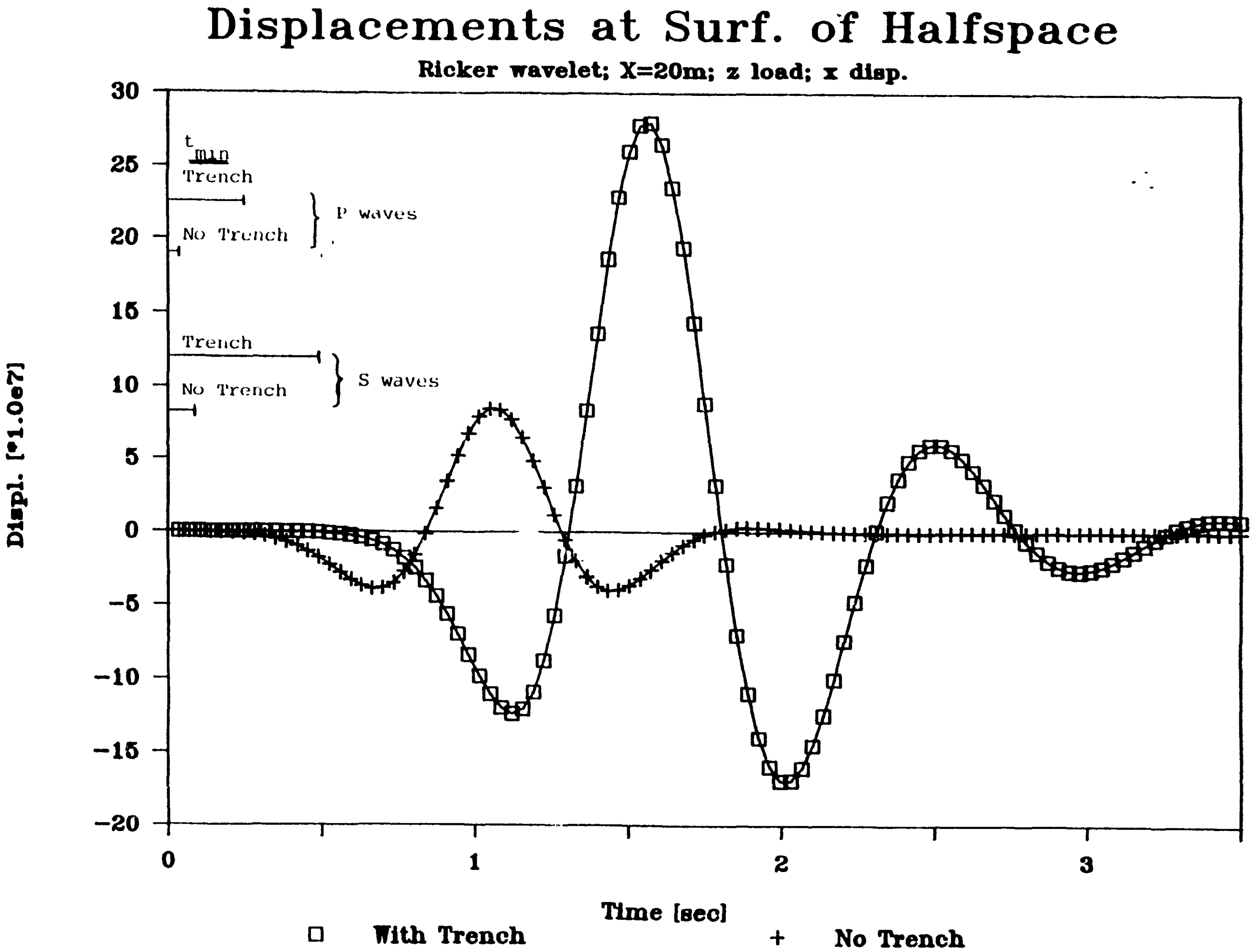
Displacements at Surf. of Halfspace
Ricker wavelet; X=20m; z load; x disp.
Displ. [*1.0e7]
30
25
20
15
10
5
0
−5
−10
−15
−20
t_{min}
Trench
No Trench
P waves
Trench
No Trench
S waves
0
1
2
3
Time [sec]
□ With Trench
+ No Trench

Figure 3.20

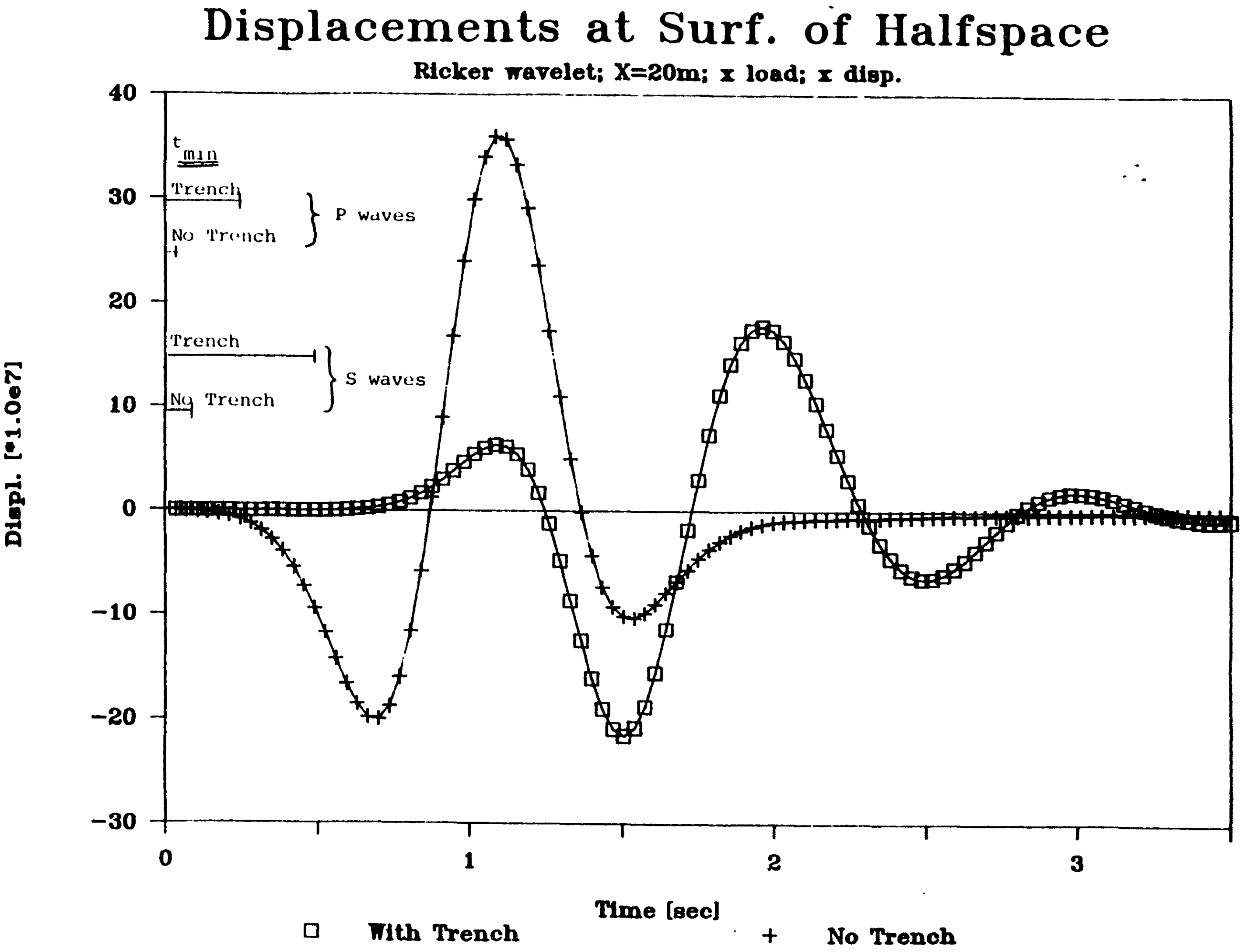
Displacements at Surf. of Halfspace
Ricker wavelet; X=20m; x load; x disp.
Displ. [*1.0e7]
40
30
20
10
0
−10
−20
−30
0
1
2
3
Time [sec]
t_min
Trench
No Trench
P waves
Trench
No Trench
S waves
□ With Trench
+ No Trench

Figure 3.21

in figure 3.20. Again, there is a delay in the time when the maximum response is observed when the trench is present, and this delay is somewhat longer then the difference in travelling times of the fastest shear waves. This may be caused by intermediate reflexions at the walls of the trench. It should be noted that the presence of the trench induces much more important horizontal displacement than would otherwise be observed.

Another interesting observation concerns the comparison of the horizontal displacement at B due to a vertical load at A and the vertical displacement at A due to a horizontal load at B. According to Betti–Maxwell's reciprocity theorem, both should be equal; however, the B.E.M. does not ensure this theorem because of the approximations used at the boundary. Only if the boundary conditions were exactly satisfied could the B.E. solution satisfy the reciprocity relationship. This implies that another test on the accuracy of the B.E. results is to check the reciprocity of the load and displacement in two solutions. Since the domain and reference points considered are symmetric, the vertical displacement at A due to a horizontal load at B is equal to the negative of the vertical displacement at B due to a horizontal load at A. Hence, comparing the results in figure 3.20 with the ones corresponding to a horizontal load at A (in the negative direction) and a vertical displacement at B, a good measure of the accuracy of the solution is obtained. For the case without trench, both results are identical since the Green's functions used satisfy reciprocity; in the case with trench, although some differences were found, they were minimal, less than 1%.

Figure 3.21 corresponds to the case of a horizontal load at A and displacement at B. The displacements at B in the case with trench are very different to the corresponding ones for the halfspace. Instead of the displacements varying in time like the loading function, they are affected by waves reflected at the trench's bottom; this also explains the change in sign of the solution during the initial period. Also, the difference in arrival time of the two peaks observed (one negative and the other positive) approaches the difference in travel time between P and S waves. Therefore, it seems that the motion at B is first caused by P waves and later by S waves.

3.3.2 Comparison with Time–Domain Solution

The results shown in figures 3.19–3.21 were compared with corresponding solutions obtained using a time–domain B.E. formulation presented by Antes and von Estorff [1]. Von Estorff also performed the computations in the time domain for the same cases referred to previously, using either constant or linear elements to model the halfspace and the trench. In his solution, the halfspace surface had to be discretized as well, since the Green's functions used by him correspond to the full 2–D space. The concentrated loading was idealized as an uniformly distributed load over one element.

Figures 3.22–3.30 show a comparison of the displacements observed at various locations using the two approaches. It can be seen that the solutions agree very well for both vertical and horizontal loads and displacements. The more important differences arise for horizontal displacements due to a vertical load, in particular after the maximum is attained. These comparisons, although corresponding to a very simple problem, served to establish a common ground for the more complex situation with a trench.

The displacements obtained for the case with trench are compared in figures 3.31–3.36. Figures 3.31 and 3.32 correspond to the vertical displacement at B and C respectively, caused by a vertical load. It can be seen that the frequency domain solution seems to satisfy the causality principle more closely, and that in the

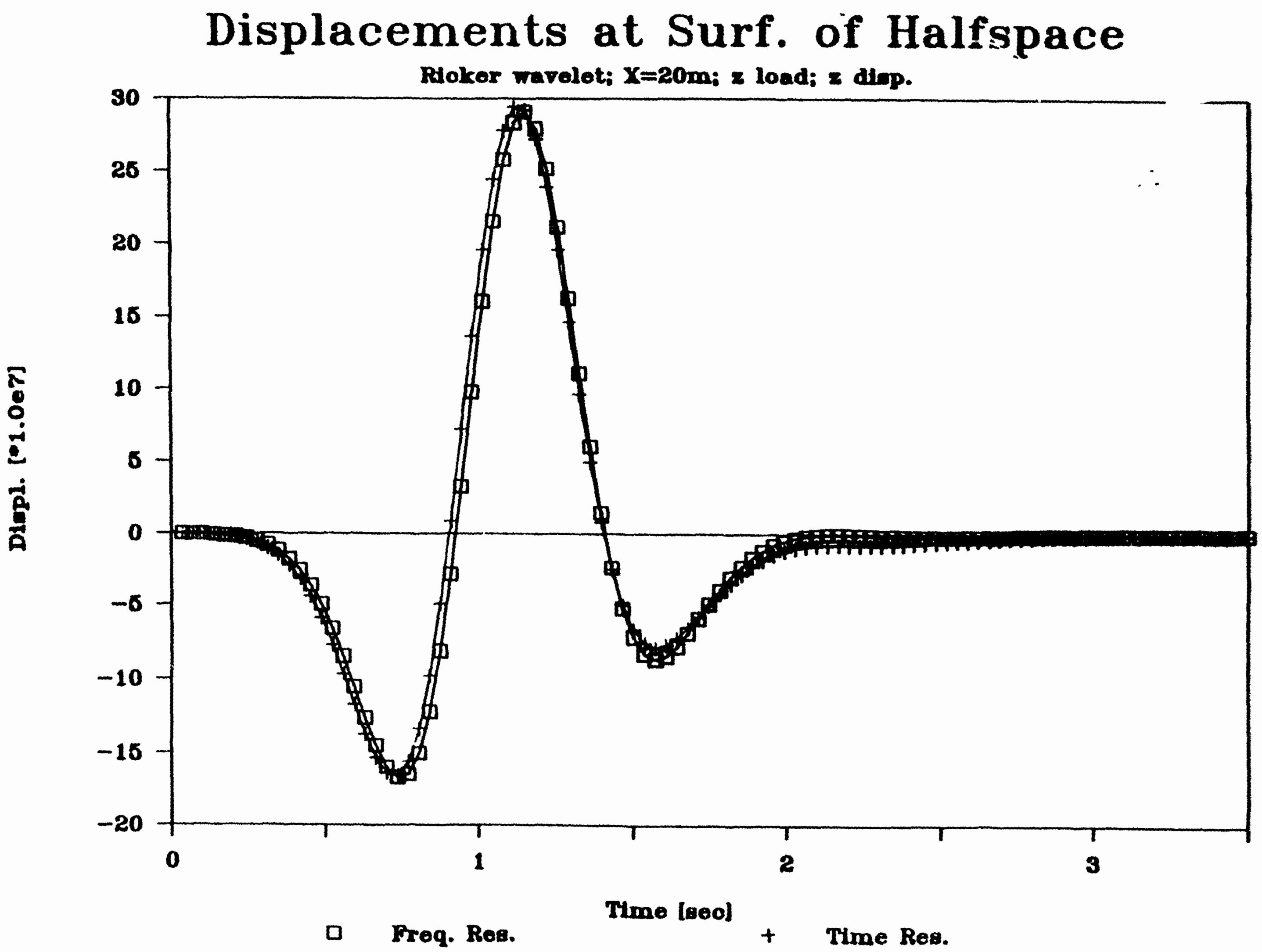
Displacements at Surf. of Halfspace
Ricker wavelet; X=20m; z load; z disp.
Displ. [*1.0e7]
30
25
20
15
10
5
0
−5
−10
−15
−20
0
1
2
3
Time [sec]
□ Freq. Res.
+ Time Res.

Figure 3.22

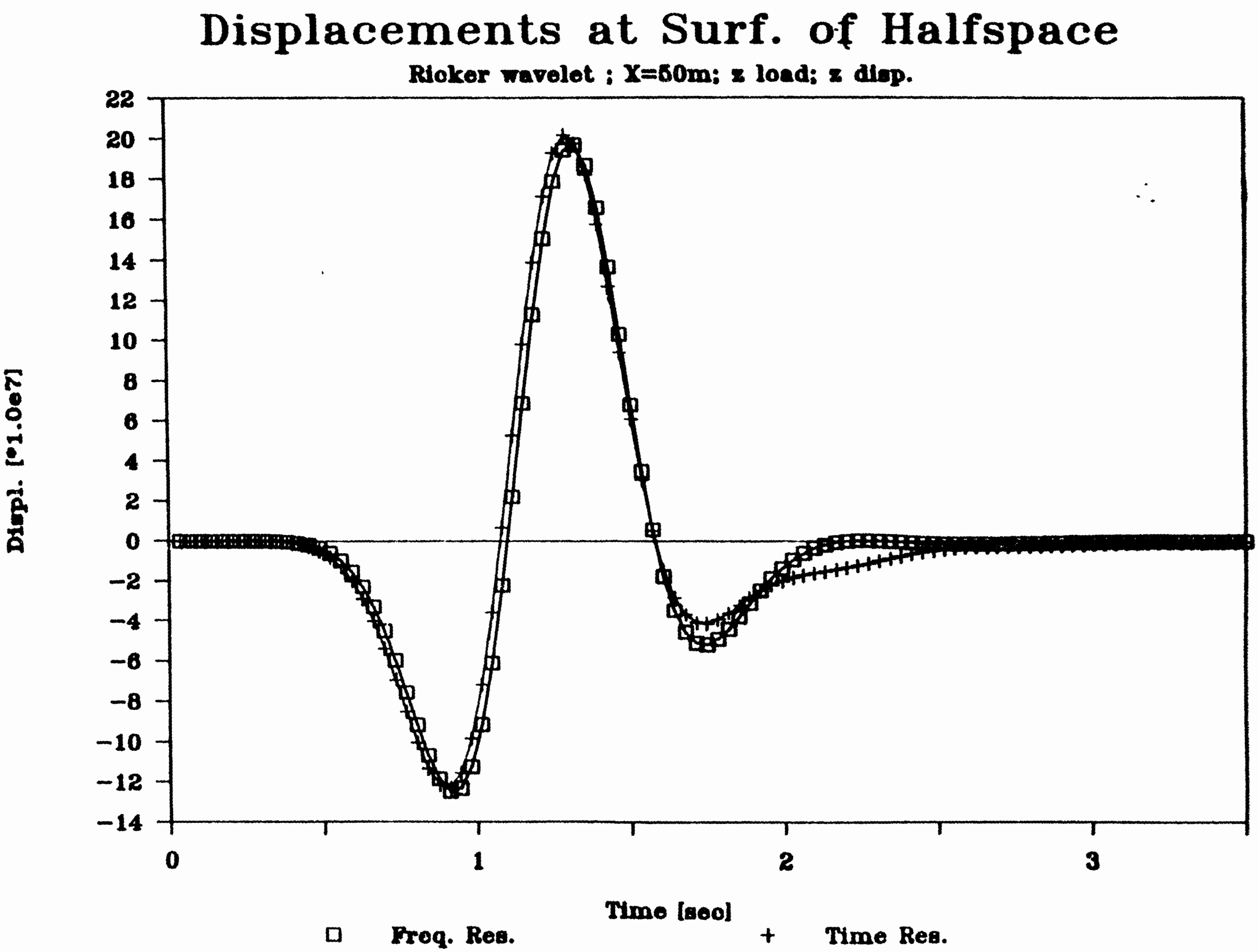
Displacements at Surf. of Halfspace
Ricker wavelet ; X=50m; z load; z disp.
Displ. [*1.0e7]
22
20
18
16
14
12
10
8
6
4
2
0
−2
−4
−6
−8
−10
−12
−14
0
1
2
3
Time [sec]
□ Freq. Res.
+ Time Res.

Figure 3.23

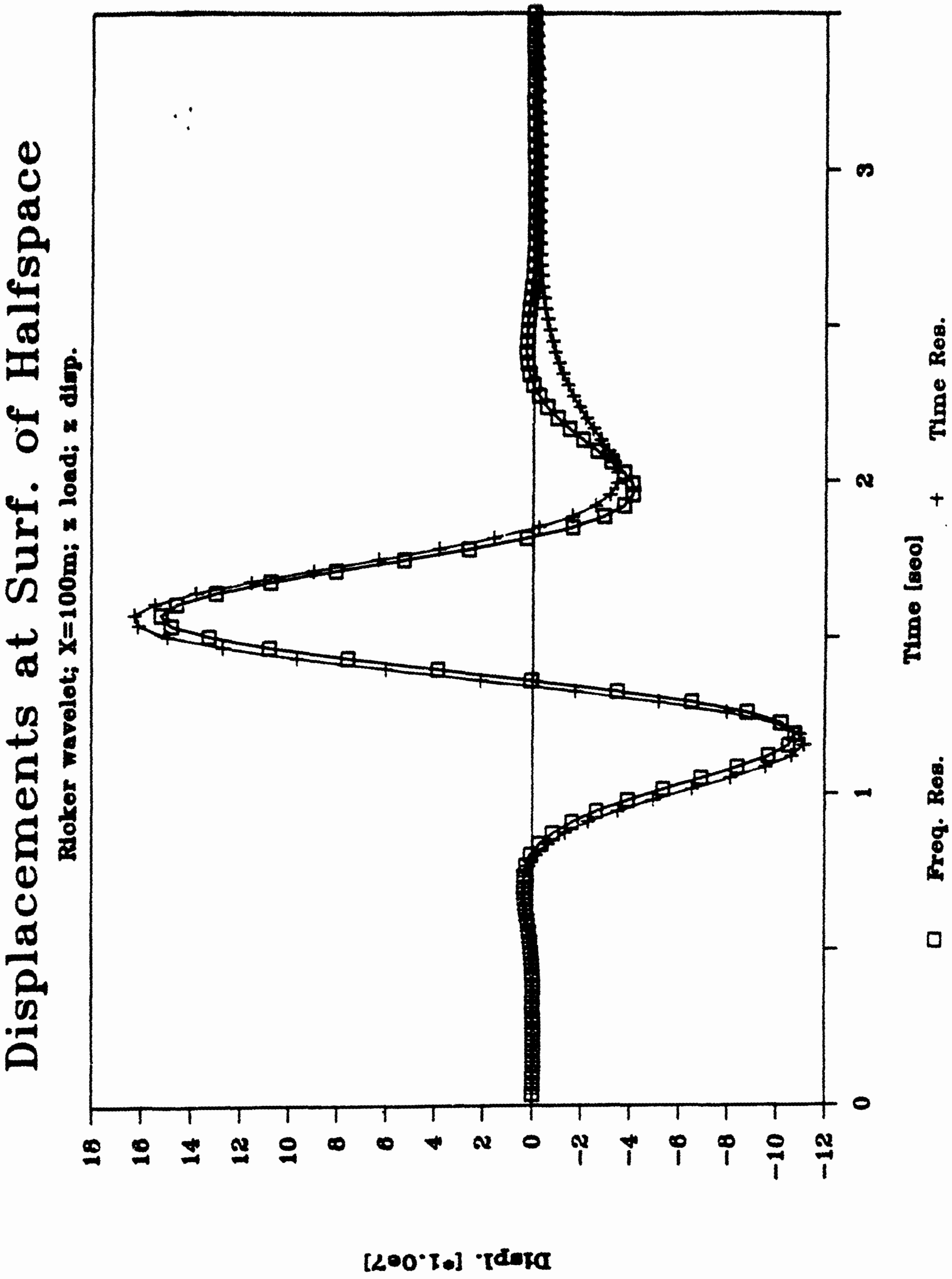
Displacements at Surf. of Halfspace
Ricker wavelet; X=100m; z load; z disp.
Displ. [*1.0e7]
18
16
14
12
10
8
6
4
2
0
−2
−4
−6
−8
−10
−12
0
1
2
3
Time [sec]
□ Freq. Res.
+ Time Res.

Figure 3.24

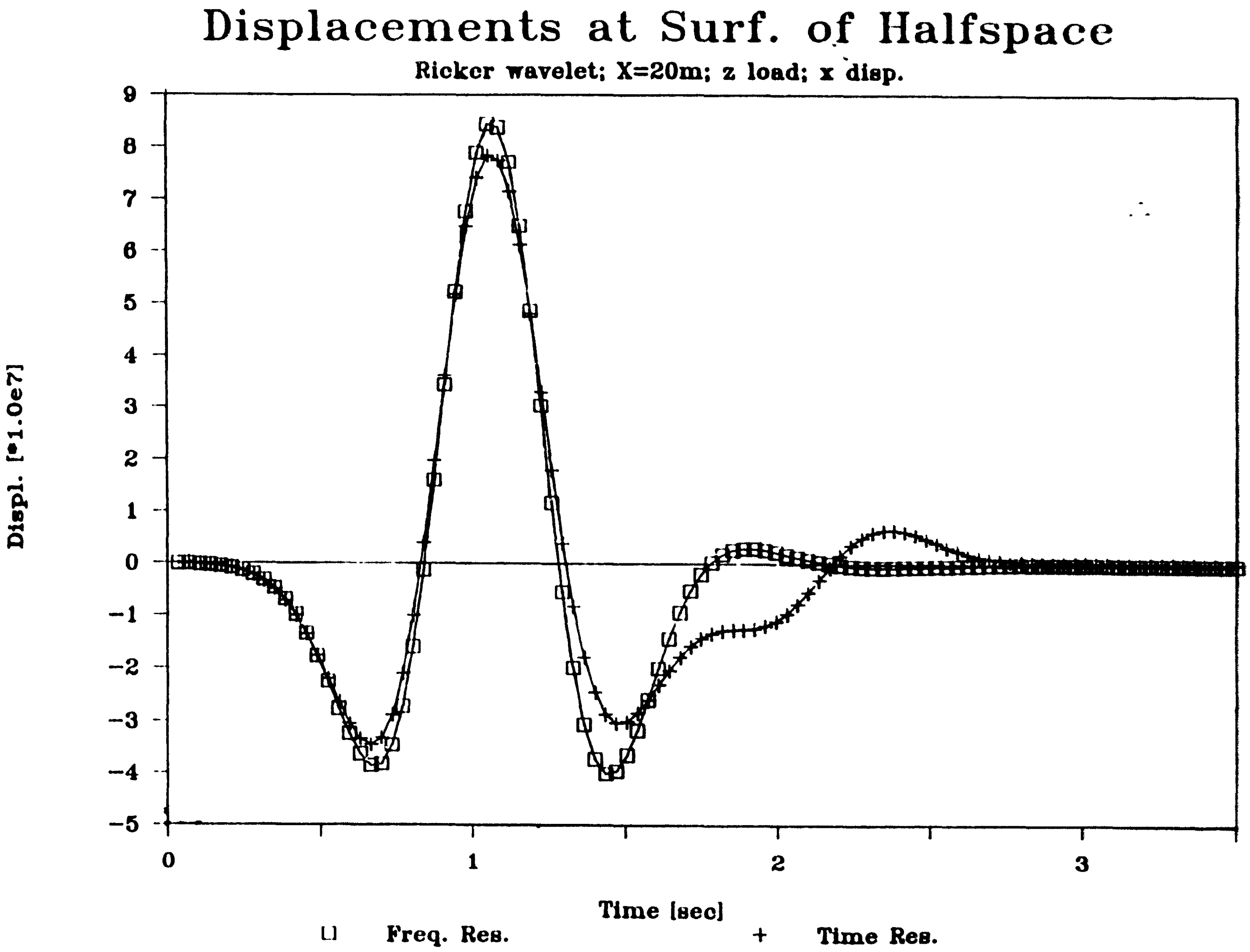
Displacements at Surf. of Halfspace
Ricker wavelet; X=20m; z load; x disp.
Displ. [*1.0e7]
9
8
7
6
5
4
3
2
1
0
−1
−2
−3
−4
−5
0
1
2
3
Time [sec]
□ Freq. Res.
+ Time Res.

Figure 3.25

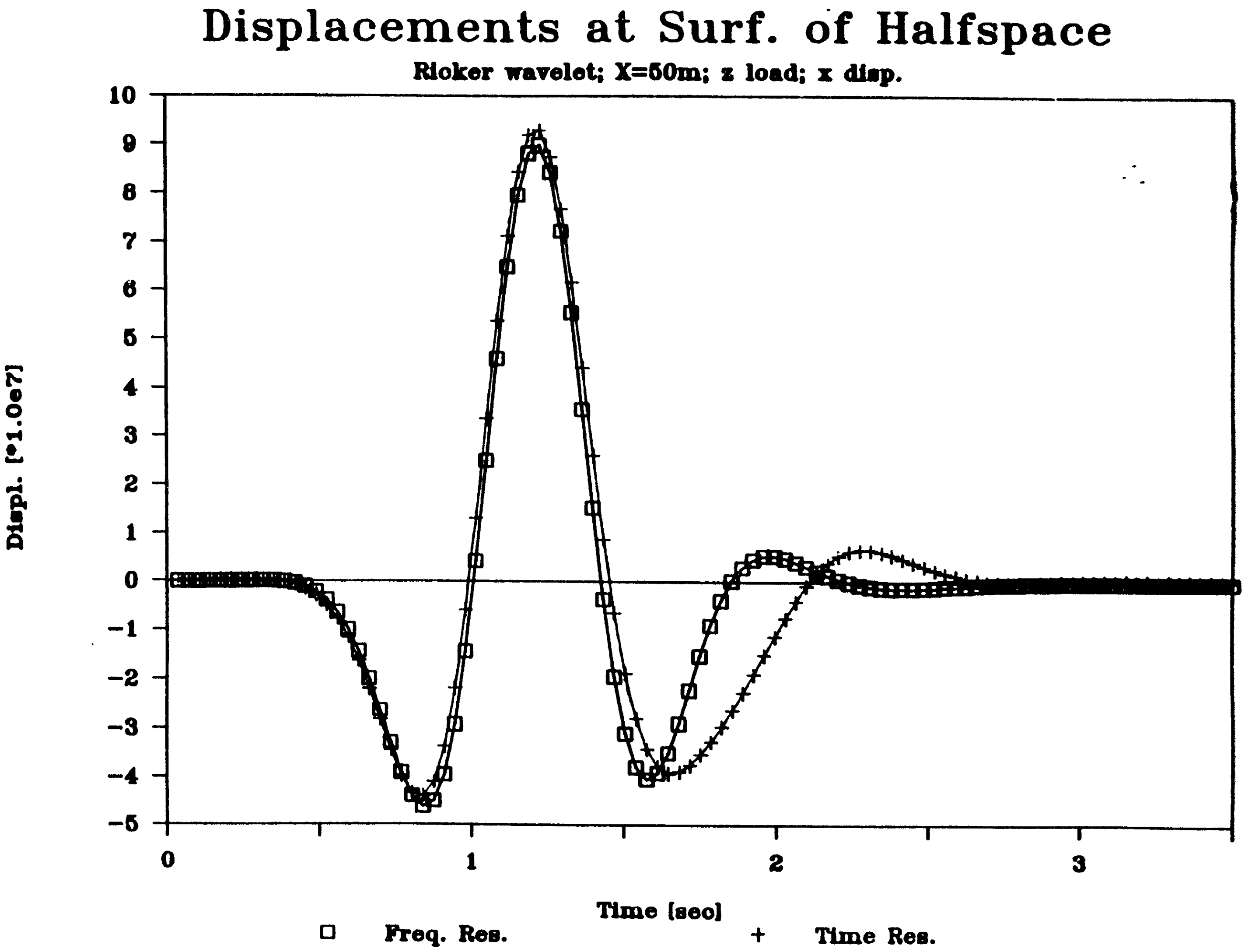
Displacements at Surf. of Halfspace
Ricker wavelet; X=50m; z load; x disp.
Displ. [*1.0e7]
10
9
8
7
6
5
4
3
2
1
0
−1
−2
−3
−4
−5
0
1
2
3
Time [sec]
□ Freq. Res.
+ Time Res.

Figure 3.26

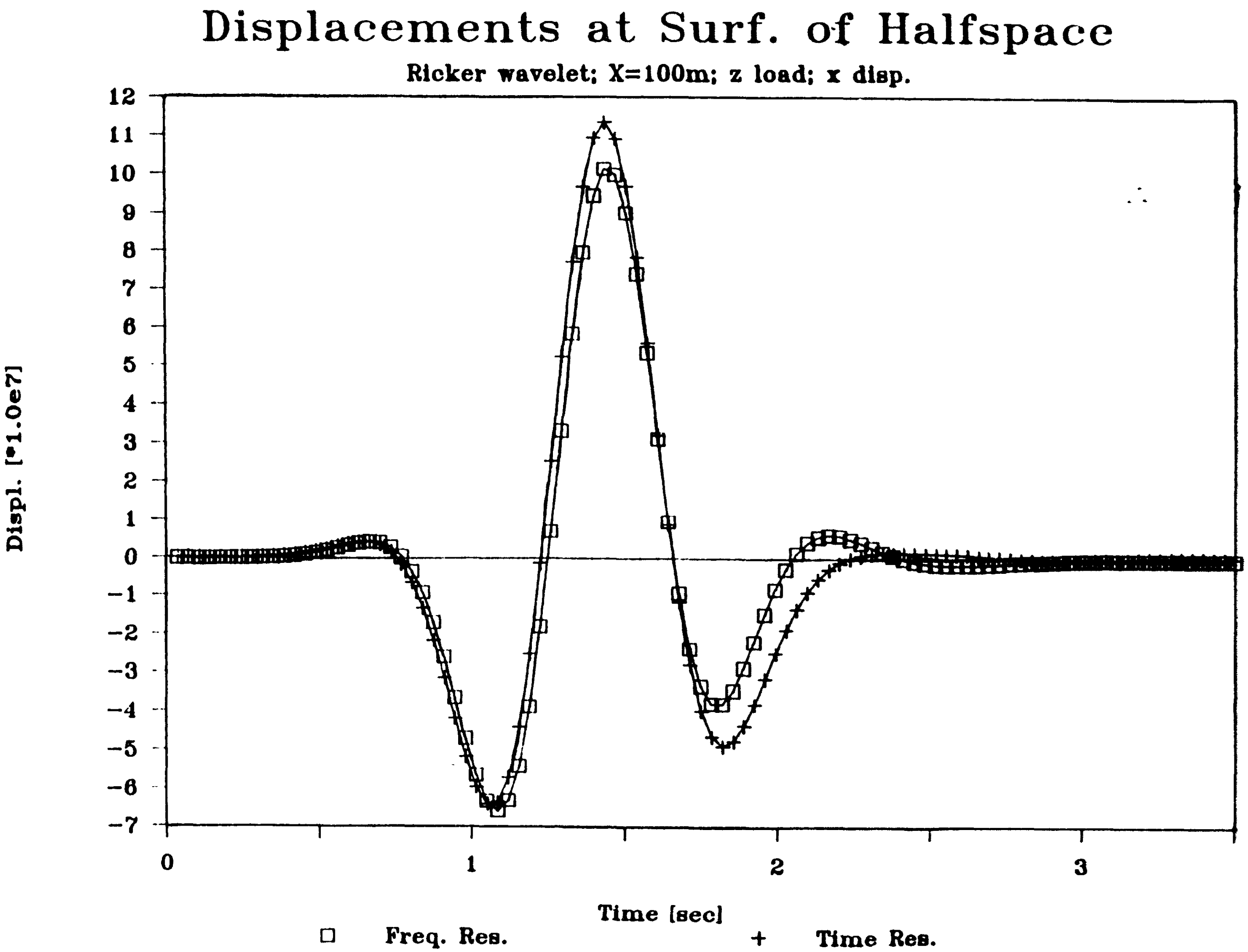
Displacements at Surf. of Halfspace
Ricker wavelet; X=100m; z load; x disp.
Displ. [*1.0e7]
12
11
10
9
8
7
6
5
4
3
2
1
0
−1
−2
−3
−4
−5
−6
−7
0
1
2
3
Time [sec]
□ Freq. Res.
+ Time Res.

Figure 3.27

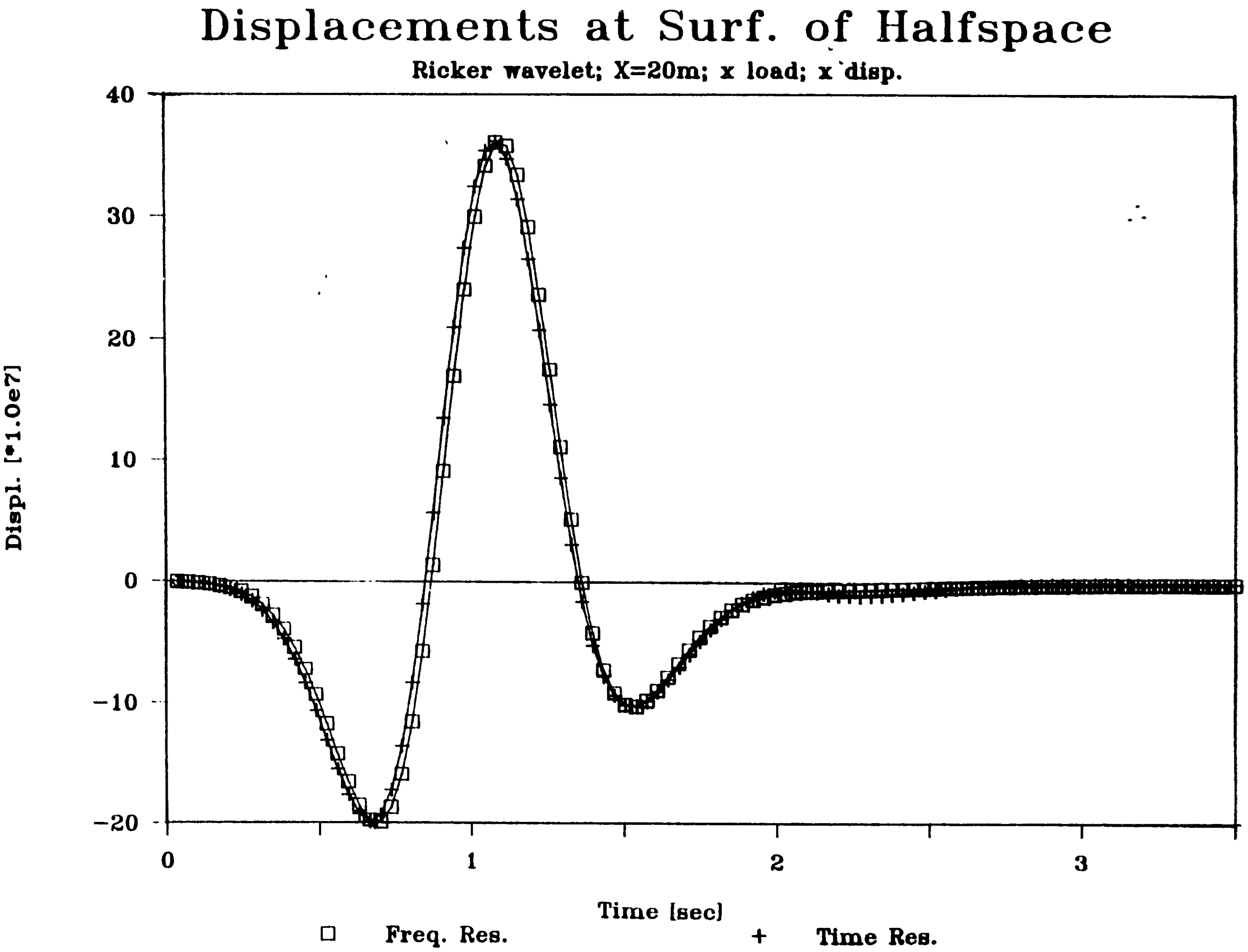
Displacements at Surf. of Halfspace
Ricker wavelet; X=20m; x load; x disp.
40
30
20
10
0
−10
−20
Displ. [*1.0e7]
0
1
2
3
Time [sec]
□ Freq. Res.
+ Time Res.

Figure 3.28

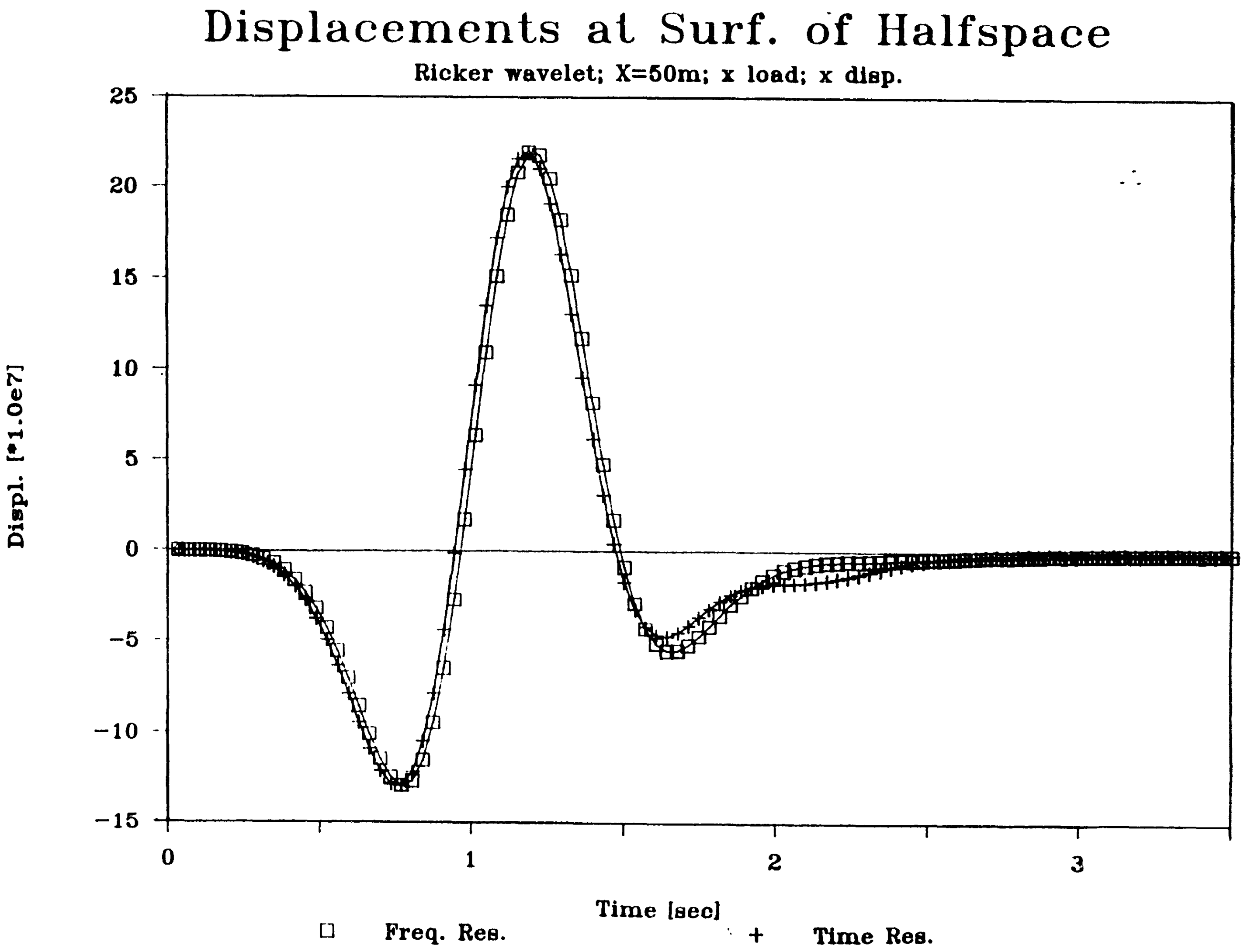
Displacements at Surf. of Halfspace
Ricker wavelet; X=50m; x load; x disp.
Displ. [*1.0e7]
25
20
15
10
5
0
−5
−10
−15
0
1
2
3
Time [sec]
□ Freq. Res.
+ Time Res.

Figure 3.29

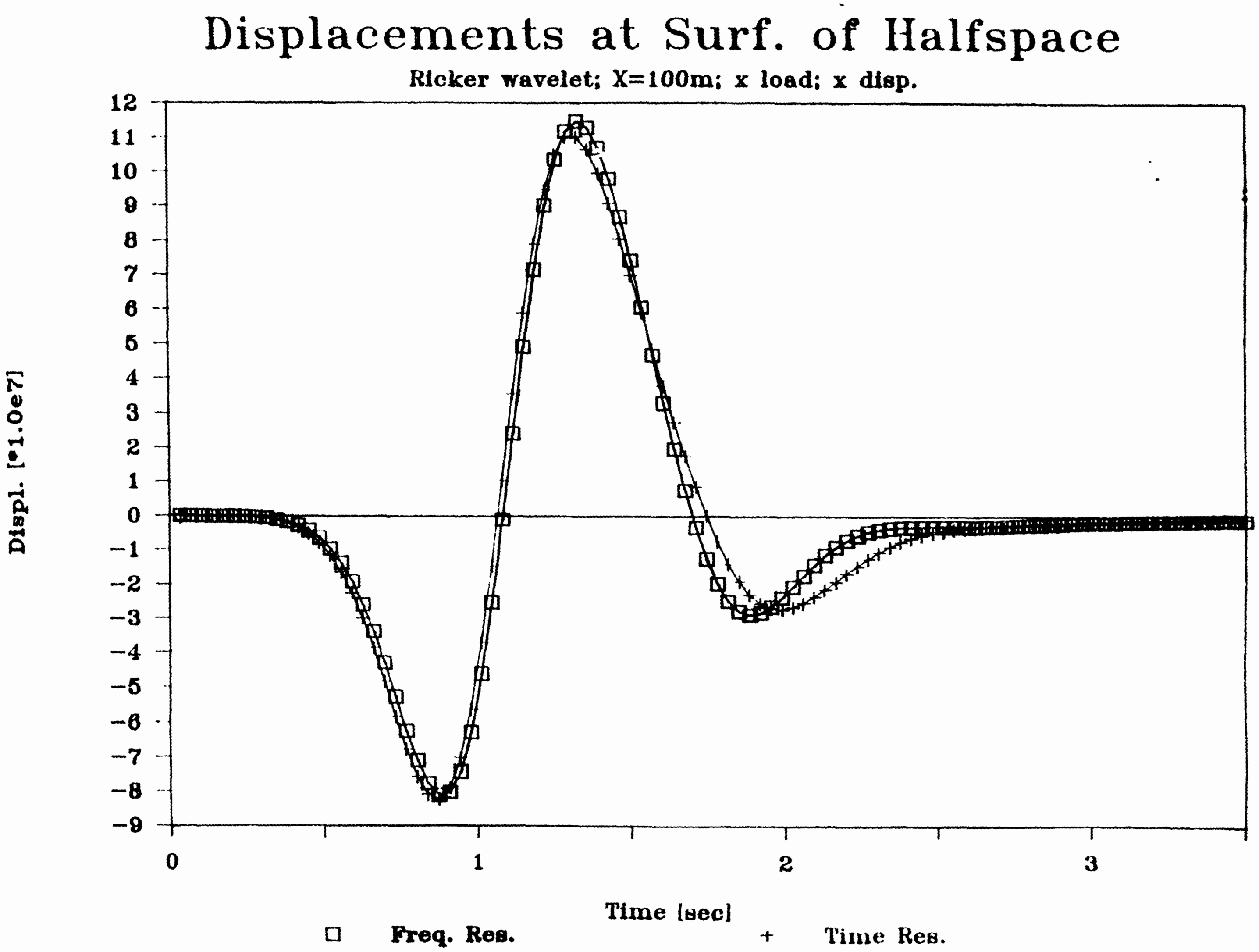
Displacements at Surf. of Halfspace
Ricker wavelet; X=100m; x load; x disp.
Displ. [*1.0e7]
12
11
10
9
8
7
6
5
4
3
2
1
0
-1
-2
-3
-4
-5
-6
-7
-8
-9
0
1
2
3
Time [sec]
□ Freq. Res.
+ Time Res.

Figure 3.30

time–domain approach, linear elements are more accurate than constant elements. These same conclusions are valid for the horizontal displacements due to a vertical load shown in figures 3.33 and 3.34, except that in this case, larger differences can be observed between the various solutions. In figures 3.35 and 3.36, corresponding to horizontal displacements due to a horizontal load, the time–domain results clearly violate the causality condition, since a response is perceived at the control point before the fastest waves have time to arrive there.

These results seem to verify that the thin–layer method gives very accurate results, even for layered halfspaces. The reason that the B.E.M. solutions using the discrete Green's functions obey the causality principle, while the time domain solution using Stoke's tensor does not can be explained as follows: when using the thin–layer method, the upper part of the halfspace is approximated by several sublayers, and the displacements there are constrained to vary linearly across each sublayer. Since the boundary element formulation developed uses linear elements on vertical boundaries, the boundary displacements are completely consistent with the Green's functions used and the boundary conditions on vertical walls are satisfied exactly. Hence, the B.E. method developed seems especially appropriate for this type of problems involving non–convex regions with vertical boundaries.

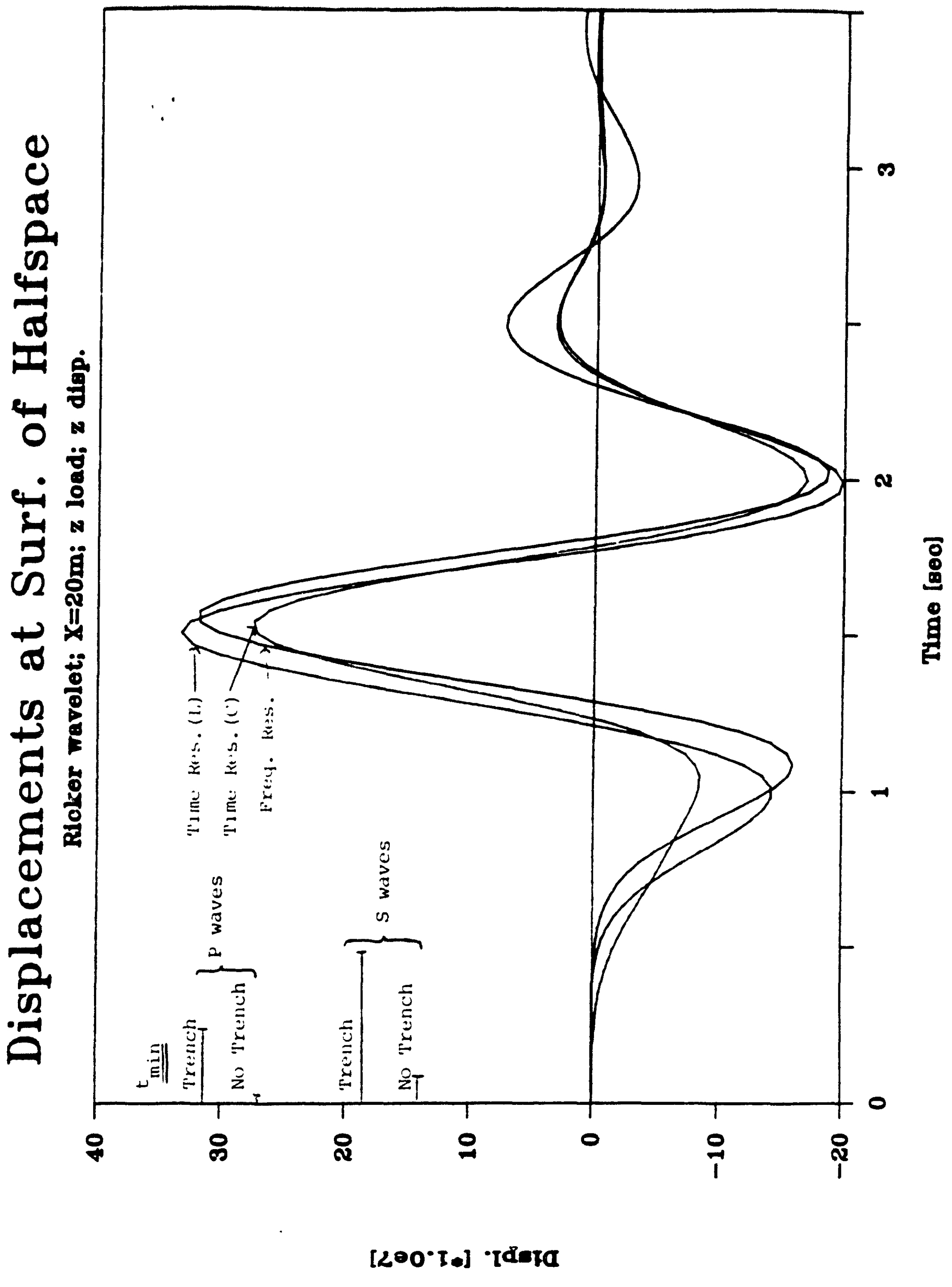
Displacements at Surf. of Halfspace
Ricker wavelet; X=20m; z load; z disp.
t_min
Trench
No Trench
P waves
Trench
No Trench
S waves
Time Res. (L)
Time Res. (C)
Freq. Res.
40
30
20
10
0
−10
−20
Displ. [*1.0e7]
0
1
2
3
Time [sec]

Figure 3.31

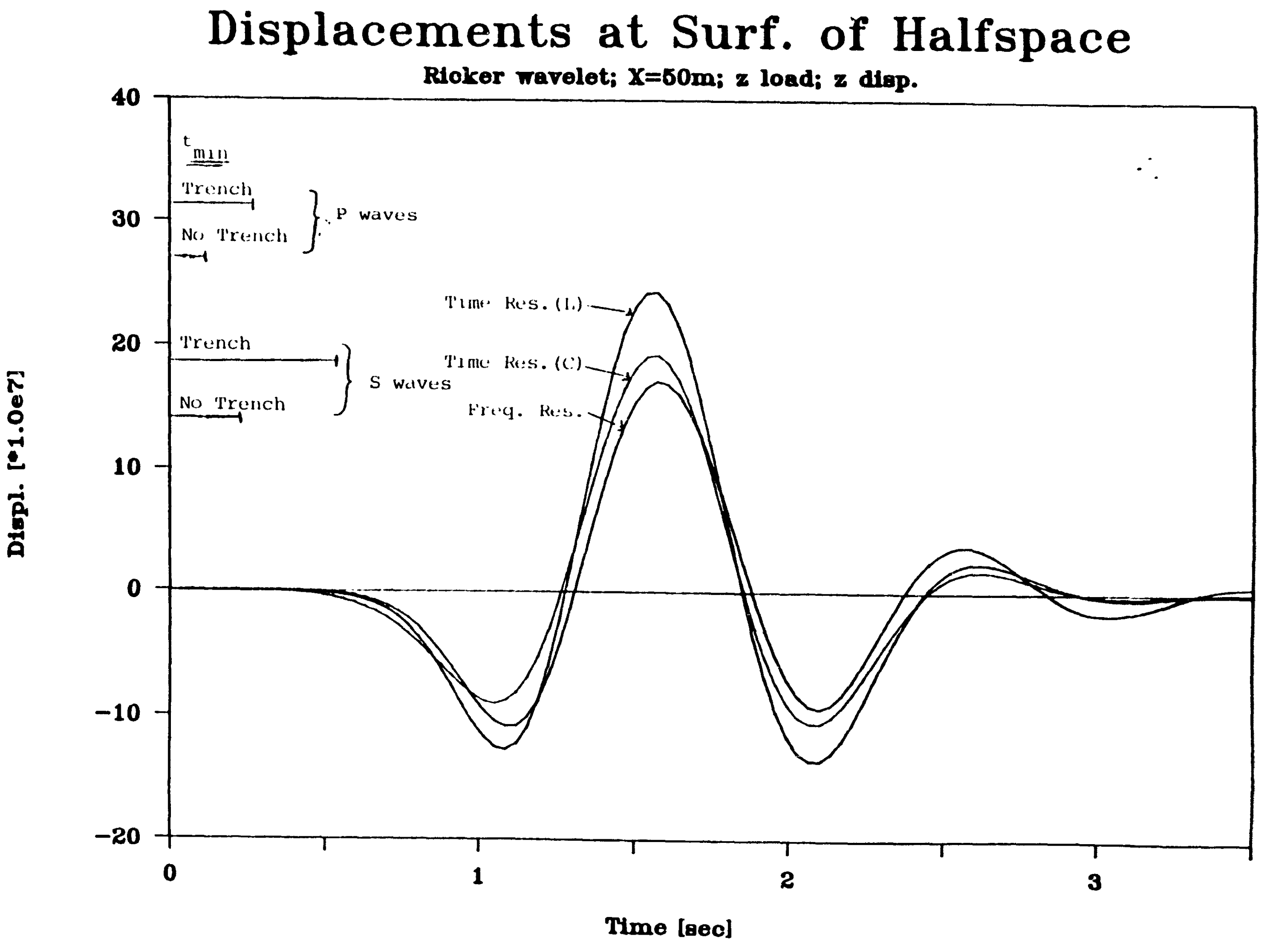
Displacements at Surf. of Halfspace
Ricker wavelet; X=50m; z load; z disp.
t min
Trench
No Trench
P waves
Trench
No Trench
S waves
Time Res. (L)
Time Res. (C)
Freq. Res.
40
30
20
10
0
−10
−20
Displ. [*1.0e7]
0
1
2
3
Time [sec]

Figure 3.32

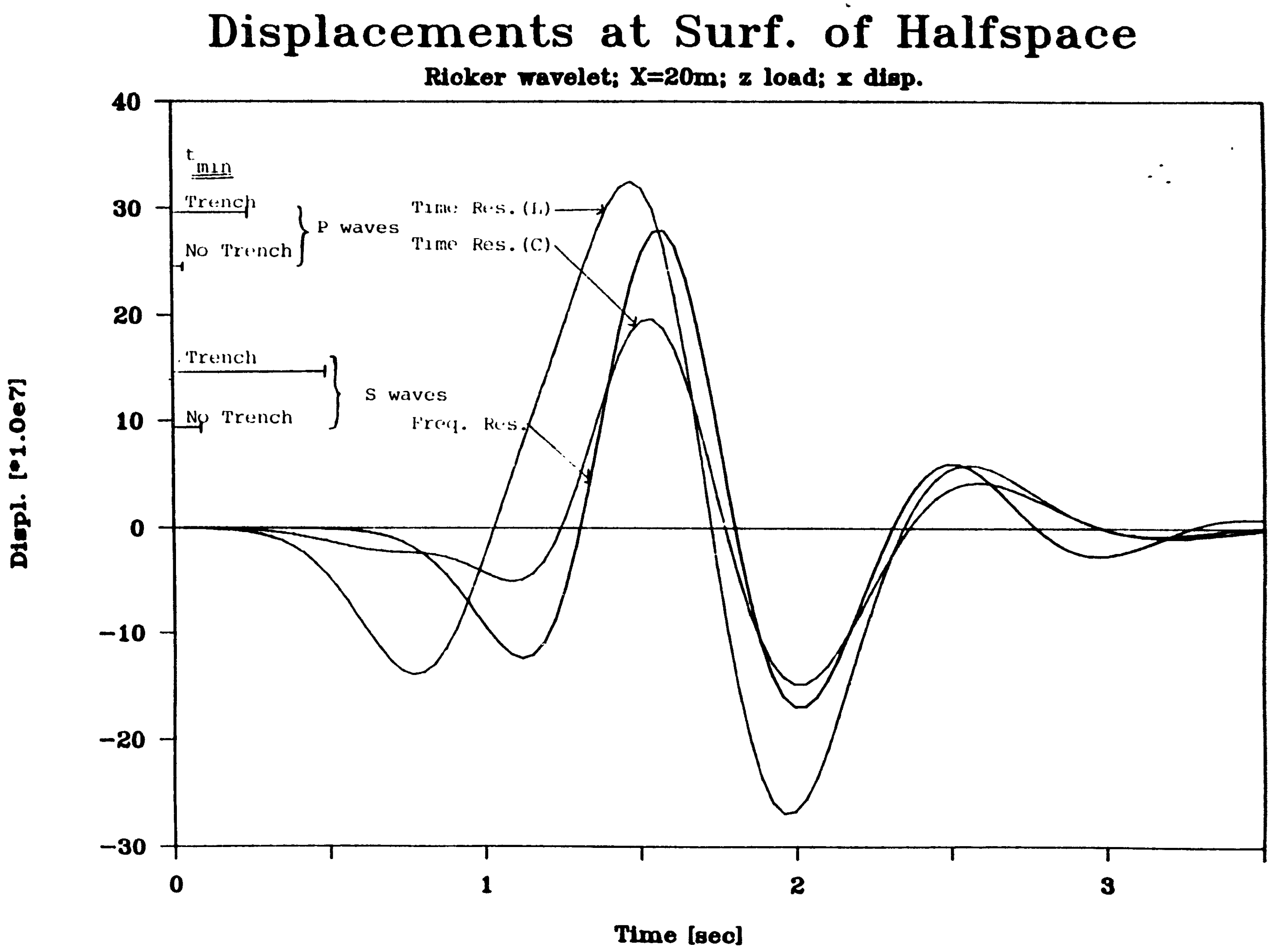
Displacements at Surf. of Halfspace
Ricker wavelet; X=20m; z load; x disp.
t min
Trench
No Trench
P waves
Trench
No Trench
S waves
Time Res. (L)
Time Res. (C)
Freq. Res.
Displ. [*1.0e7]
40
30
20
10
0
−10
−20
−30
0
1
2
3
Time [sec]

Figure 3.33

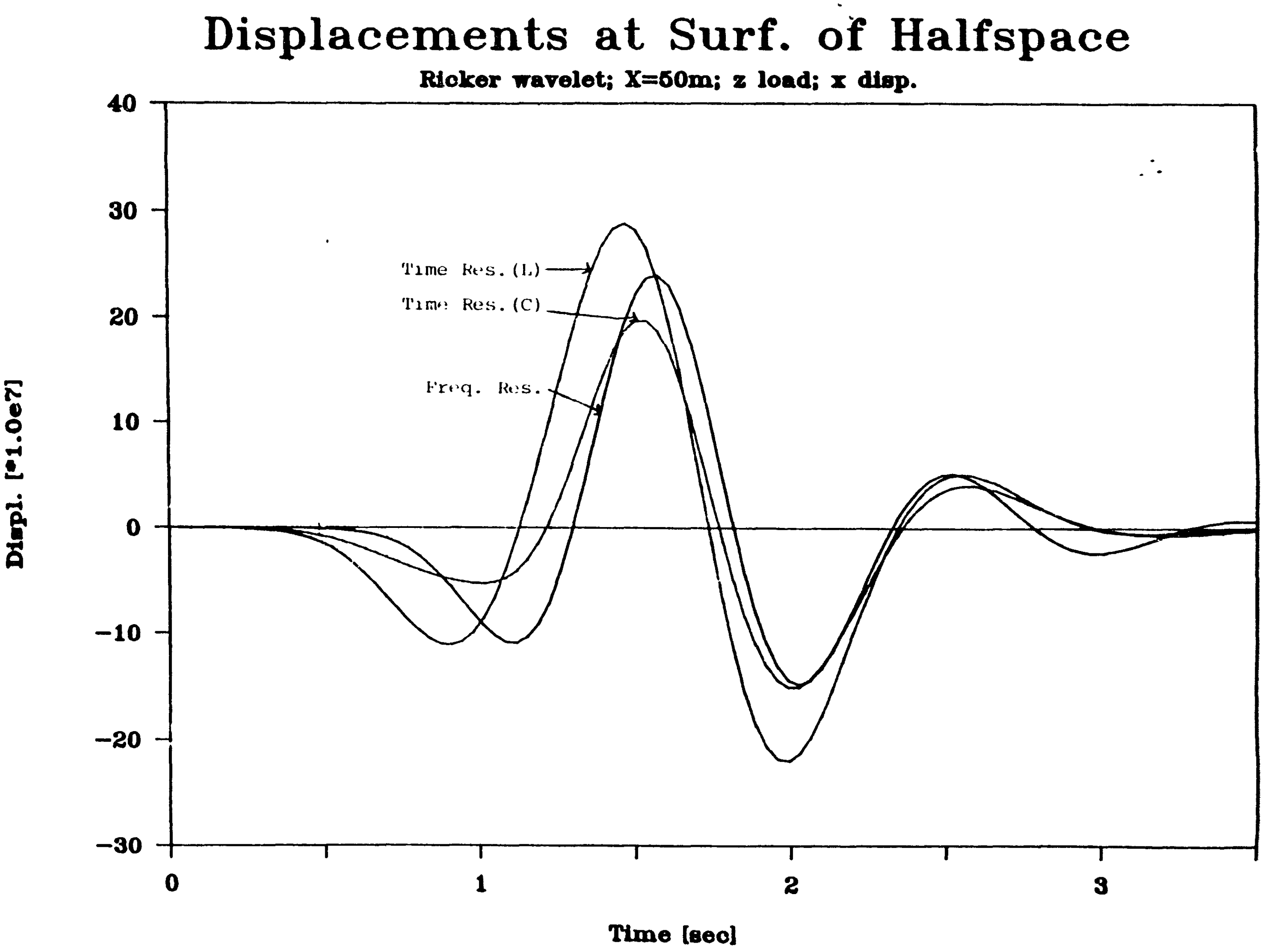
Displacements at Surf. of Halfspace
Ricker wavelet; X=50m; z load; x disp.
Displ. [*1.0e7]
40
30
20
10
0
−10
−20
−30
0
1
2
3
Time [sec]
Time Res. (L)
Time Res. (C)
Freq. Res.

Figure 3.34

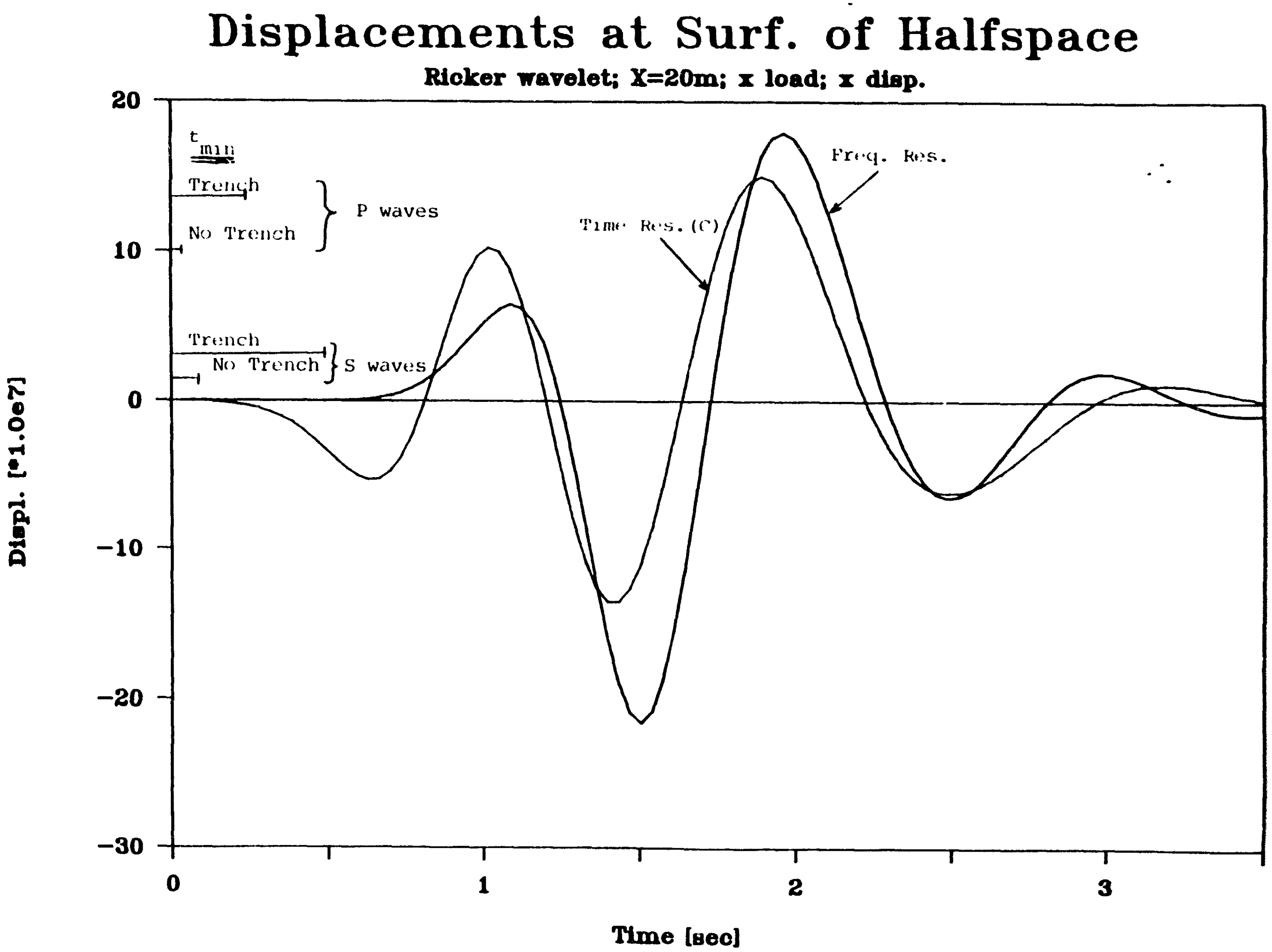
Displacements at Surf. of Halfspace
Ricker wavelet; X=20m; x load; x disp.
Displ. [*1.0e7]
20
10
0
-10
-20
-30
0
1
2
3
Time [sec]
t_{min}
Trench
No Trench
P waves
Trench
No Trench
S waves
Time Res. (C)
Freq. Res.

Figure 3.35

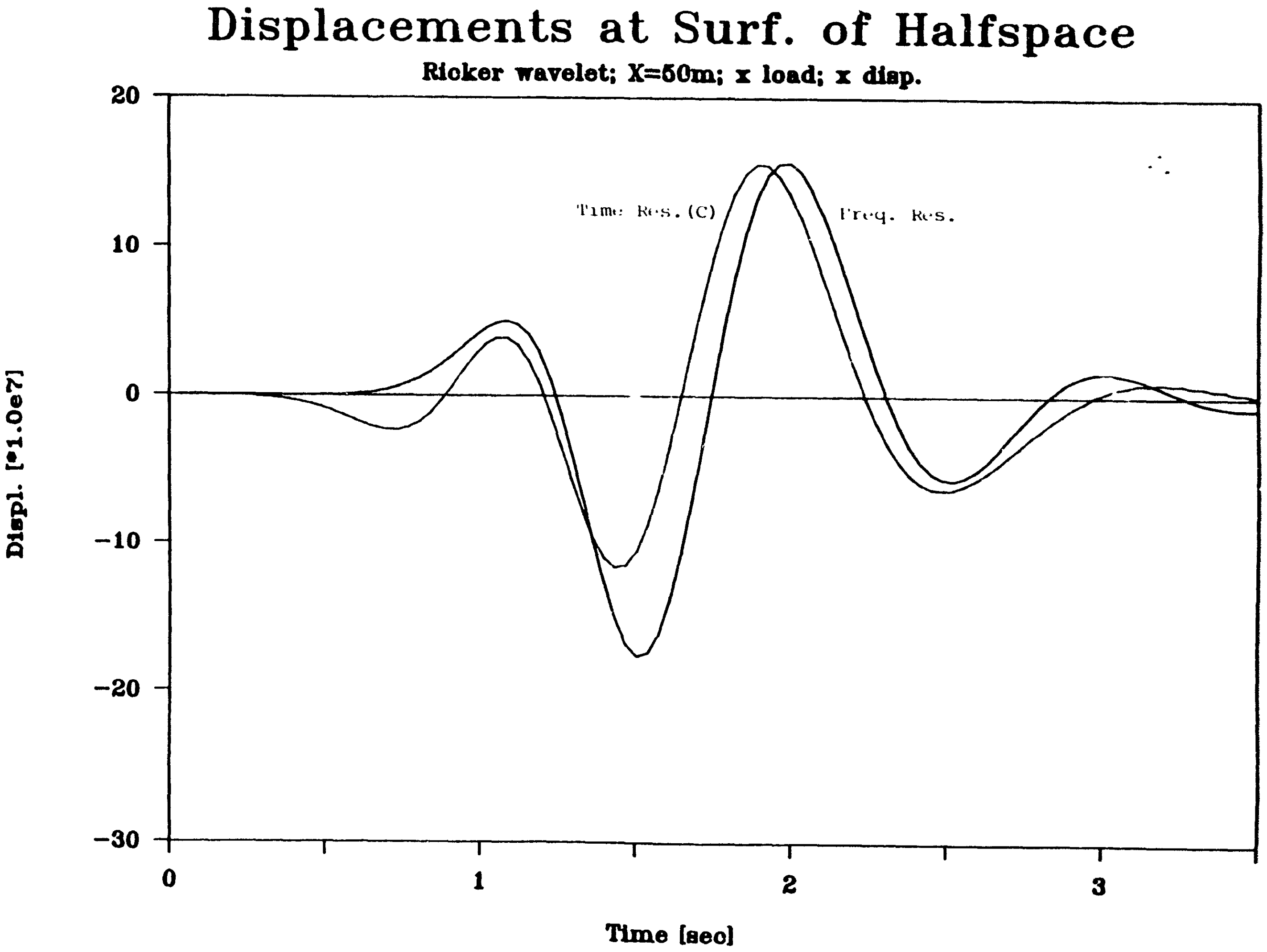
Displacements at Surf. of Halfspace
Ricker wavelet; X=50m; x load; x disp.
Time Res.(C)
Freq. Res.
Displ. [*1.0e7]
20
10
0
−10
−20
−30
0
1
2
3
Time [sec]

Figure 3.36

4. INFLUENCE OF UNDERGROUND STRUCTURES ON THE SEISMIC MOTION AT THE SURFACE – APPLICATION TO THE 1985 EARTHQUAKES IN MEXICO CITY

4.1. Introduction

On September 19, 1985, Mexico City was hit by a strong earthquake causing the loss of several thousands human lifes and great damage to existing constructions. The earthquake, with a magnitude of 8.1, had its epicenter located about 370 km West of Mexico City, at the subducting zone of the Cocos plate near the town of Lazaro Cardenas, Michoacan, on the Pacific Coast. The earthquake originated from two main pulses separated by about 25 sec. This accounts for the unexpected long duration of the ground motion felt in Mexico City. Due to the city's relatively large distance from the fault, the dispersion of the seismic waves resulted in a ground motion in Mexico City which seemed the result of a single event and exhibited a long duration.

Mexico City has been expanding in recent times at a rapid rate, increasing its population from 1.7 millions in 1940 to more than 17 millions today. Most of this expansion took place over lands on Lake Texcoco, which once surrounded the city. Mexico City also became a modern city with tall buildings, large avenues and polluted air. The majority of the downtown area is located on the lake bed, which is composed of very soft clays extending to a depth of 35–40 meters. In past years, to accommodate the water needs of a growing population, water was extensively pumped from the subsoil and, as a result, the city suffered considerable subsidence. Such pumping of water is no longer allowed, and as a result the settlement rate has decreased to about 7–10 cm/year.

Although Mexico City is not located in the immediate vicinity of any important seismic fault, nevertheless it is exposed to major earthquakes. The severity of certain earthquake events in Mexico City is due to the considerable amplification suffered by seismic waves originating at moderate distances, as they pass through the soft clay layers under the city. This results in large seismic intensities observed on the surface in the downtown area.

While the city has experienced several important earthquakes during this century, the September 1985 tremor was one of the most violent and resulted in the greatest damage to date. This damage was, however, concentrated within a few square kilométers, in the lake bed zone, and affected mainly buildings with 8–14 stories, public service buildings, and hospitals, schools and telephone centers.

A detailed study of the damages suffered by a big city during a major earthquake provides lessons for researchers and designers alike. Mexico City, in particular exhibits unique characteristics which make it a specially interesting target for study. Indeed, nowhere else in the world can one find a city of such size standing on deposits as soft as those and located at only moderate distances from major faults.

While the largest damage was confined to certain areas in downtown Mexico City, it was certainly not uniform within such areas, as buildings collapsed next to buildings which sustained little or no damage. One possible cause for this could be the dynamic coupling through the soil of several structures, commonly called structure–soil–structure interaction. Such interaction is indeed important in Mexico City, since the soft sediments there have unusually low shear wave velocities (about 60–80 m/s); as a result, the characteristic wavelength of the seismic motions in the sediment basin are of the same order of magnitude as the physical dimensions of some of the structures standing there. Since these structures are rigid and cannot accommodate the variations in soil motion, interaction takes place (this is normally referred to as kinematic interaction).

As mentioned above, Mexico City is built on the bed of Lake Texcoco, a valley surrounded by basaltic hills belonging to old volcanoes. This valley can be divided into 3 zones according to the subsoil stratigraphy : the zone on the lake bed, containing thick deposits of soft clay with a water content between 100% and 500%, having a depth around 35 m and laying on top of more firm materials; the zone of the hills, exhibiting a rough topography and being composed of hard soils with a relatively high shearing strength; and a zone of transition with variable depth deposits connecting the lake bed to the hard soils.

The soft clay deposits exhibit peculiar dynamic characteristics in the sense that they behave essentially as an elastic material with very little internal damping (2–3%) for large strain values. This behavior contributed to the important amplification of the motion passing through the clay deposits for frequencies equal to the natural frequencies of the stratum. Such amplifications produced an essentially harmonic ground motion which, together with its long duration, was responsible for most of the damage seen in some parts of Mexico City.

One of the most striking facts in the pattern of earthquake's damage in Mexico City was that the more severely affected zones alternated with zones where the buildings hardly suffered any damages. The cause of such irregularities is not well understood, and is presumed to be the result of local soil effects as well as the interaction between multiple structures through the soil. This study presents an investigation on one possible reason for the variability of seismic severity over short distances, namely the influence of massive underground structures (such as the subway tunnel) on the motion observed on the ground surface in their vicinity, and on the interaction between underground structures and surface or embedded foundations. The objective is to understand whether the presence of the tunnel increases or decreases the dynamic response of buildings located in the vicinity, and whether they are more or less prone to seismic damage. The findings are also correlated with actual field evidence concerning the presence or absence of damage. In order to maintain the model simple and make parametric studies possible, a 2–D idealization was used, the soil being modelled as a horizontally stratified stratum. This model can be analyzed using the boundary element code developed.

4.2 Data Available

4.2.1 Seismic Records

Mexico City has an extensive installation of accelerographs with stations located on various types of soils within the valley. Most of these stations registered the September 1985 earthquake, and provided valuable data for the characterization of the seismic motion. However, only one set of records was obtained in the damaged zone, at a station located near the Ministry of Communication and Transportation (abbreviated as SCT) in the southern part of the region. Ground motion records were also obtained at four stations located on hard soil, of which three are in the campus of the National University of Mexico (CUMV, CUIP and CUO1) and one at the Tacubaya site (TACY). On the other hand, the seismic motion experienced in the transition zone was registered by one station placed in the Viveros region (SXVI). In addition, two other stations registered the ground motion above the deeper clay deposits at the Central de Abastos site (CDAO and CDAF). Figure 4.1 shows the location of each of these stations. The seismic records were promptly processed at the Instituto de Ingenieria of the National University of Mexico, using standard procedures for baseline correction and filtering. These data were promptly made available on magnetic tapes.

4.2.2 Soil Profile and Characteristics

In order to carry out this study, it is necessary to obtain a good description of the soil profile near the SCT station as well as the stratification pattern for the soft soil deposits in the damaged region. Reliable soil properties, in particular density and shear wave velocity, are needed to study wave propagation phenomena. A stratigraphy of the subsoil near the SCT station is shown in fig. 4.2.

As can be seen, a layer of much stiffer soil is found at a depth of 41 m; hence, the subsoil can be modelled as a stratum resting over rigid rock. The stratum is divided into three distinct layers: the one on top is composed of very soft soil deposits having a shear wave velocity of about 76 m/sec; it then follows an intermediate 3 m thick layer of a harder soil, which in turn is underlaid by a third layer having a soil with a shear wave velocity of about 94 m/sec. The density of all the materials in the stratum is small, close to the water density, reflecting the high water content of the soil (which can be as high as 500%).

Tests on the dynamic properties of the soft soil deposits showed that they behave essentially as elastic materials for shear strains up to 5–10%, the shear modulus remaining almost constant in this range. However, with further increases in deformation, the shear modulus decays rapidly (see Ref [36]). At the same time, the

STRONG-MOTION ACCELEROGRAPHS IN MEXICO CITY

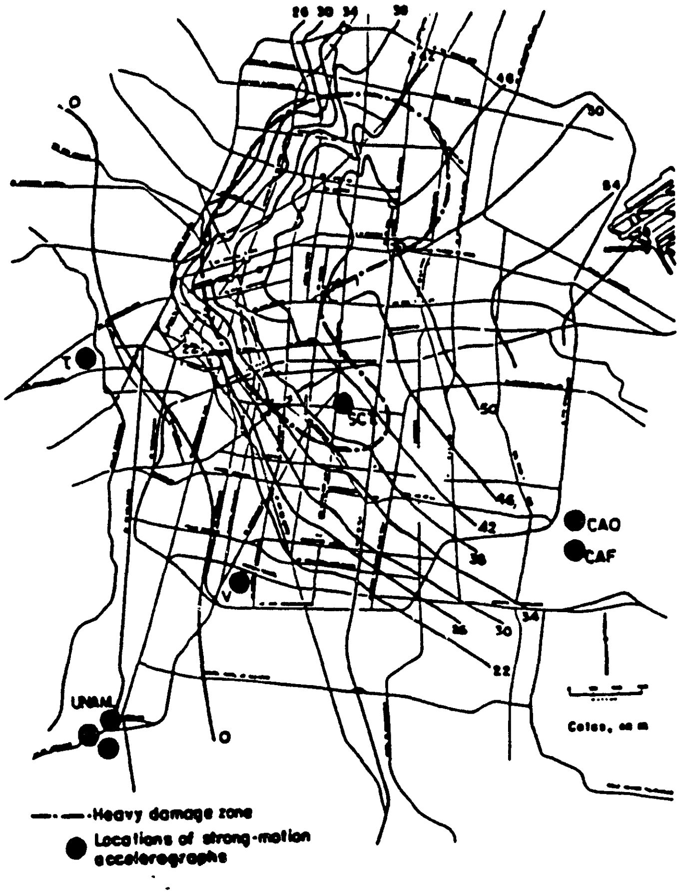

Figure 4.1

STRATIGRAPHY OF THE SUBSOIL NEAR THE SCT STATION

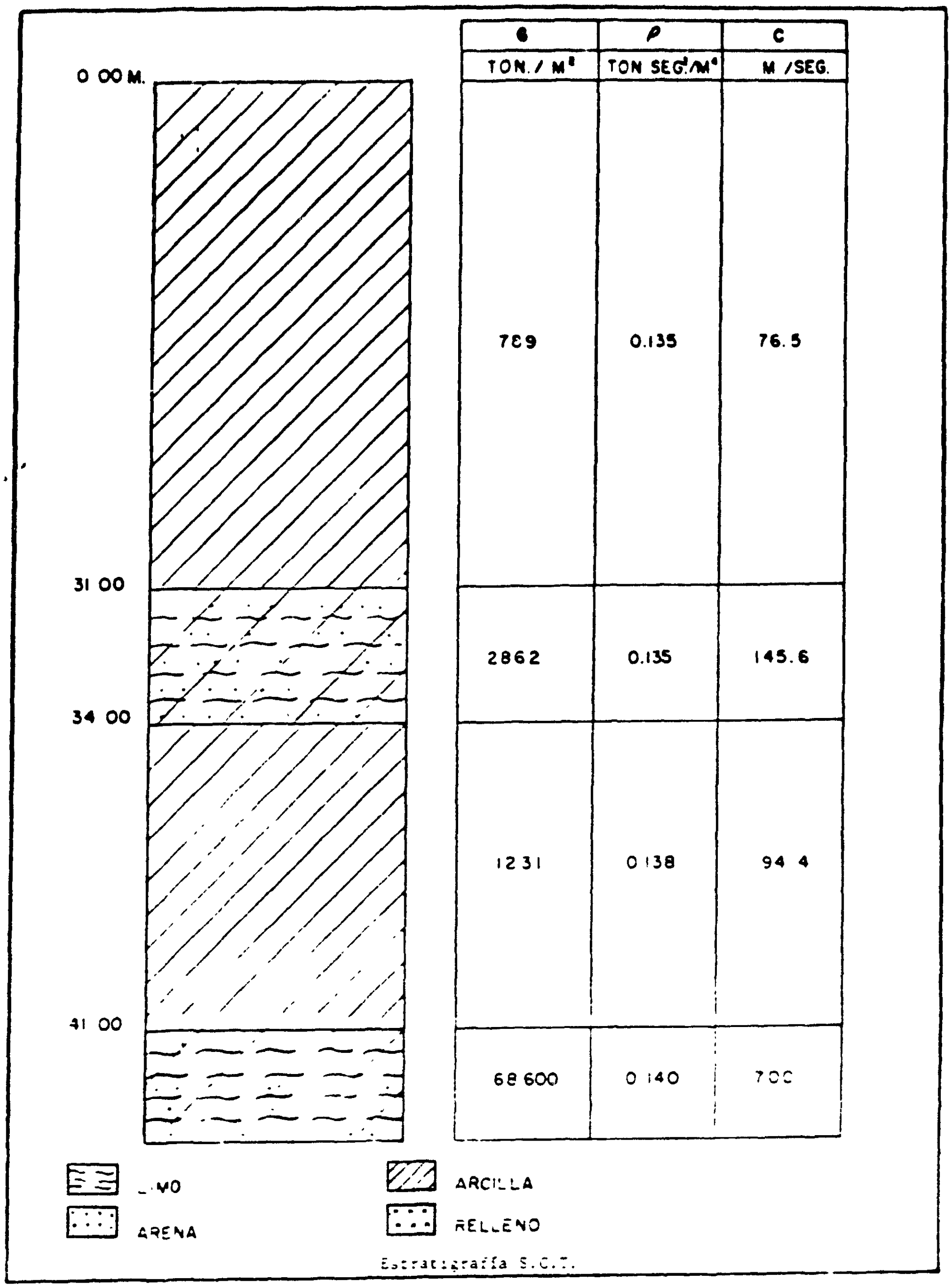

Estratigrafía S.C.T.

Figure 4.2

internal damping is very small, on the order of 2–3% for shear strain values up to 10%; this implies that seismic motions will be subjected to only very small attenuation, and that amplification effects could be important.

4.2.3 Metropolitan Subway Tunnel

Mexico City has a vast system of subway lines extending over the entire urban area (see Fig. 4.3). Its construction began 20 years ago and has since extended to form a network of more than 100 km in total length. Figure 4 shows two typical cross–sections of the subway tunnel. This tunnel has been constructed by excavation from the surface, using for this purpose dug–out walls on each side of the tunnel. The ceiling was subsequently covered with an earth cap of about 1–3 m.

The subway system sustained very well the earthquake, the service being interrupted only momentarily for a global check–up. Some stations, however, became inoperative due to debris formed by collapsed buildings which made their use risky.

4.3. Results

4.3.1 Analysis of Motion Data

The seismic records obtained during the September 1985 earthquake at several stations in Mexico City are valuable in identifying the principal causes of the great damage suffered by some structures. Although only one station (SCT) was active in the heavily damaged zone, the results that it provided give good indications of the characteristics of the seismic motion in that region. Figures 4.5 and 4.6 show the time history of the two components of the horizontal acceleration (after correction)

SUBWAY SYSTEM IN MEXICO CITY

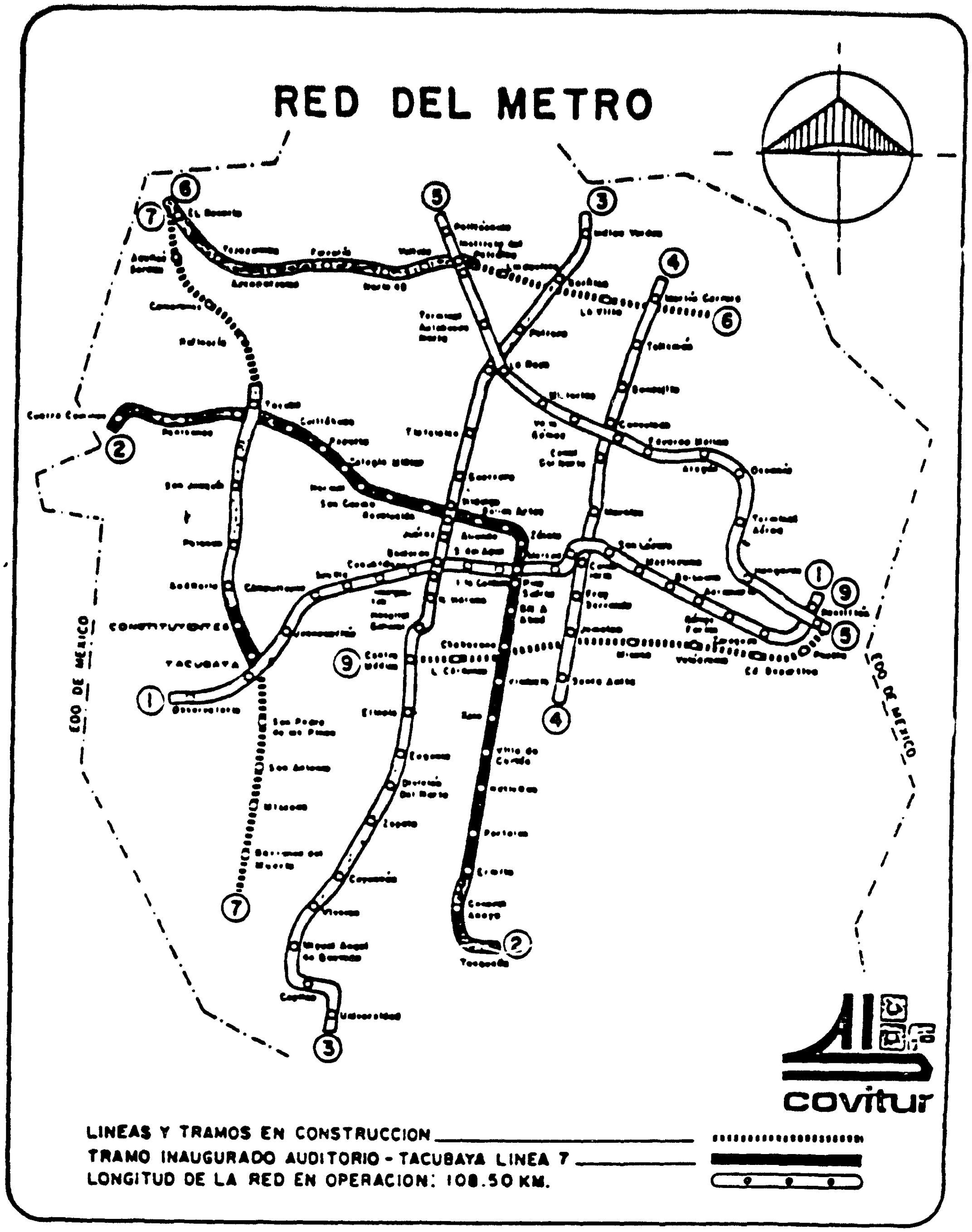

Figure 4.3

TYPICAL CROSS-SECTIONS OF SUBWAY TUNNEL IN MEXICO CITY

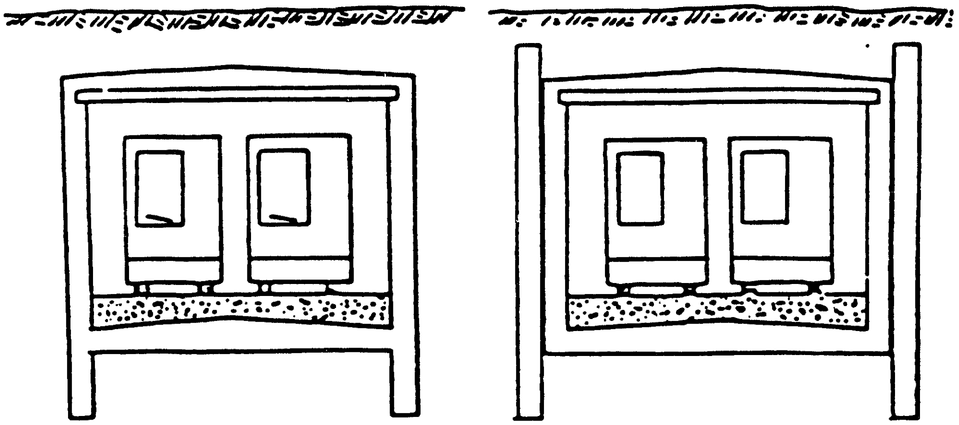

Figure 4.4

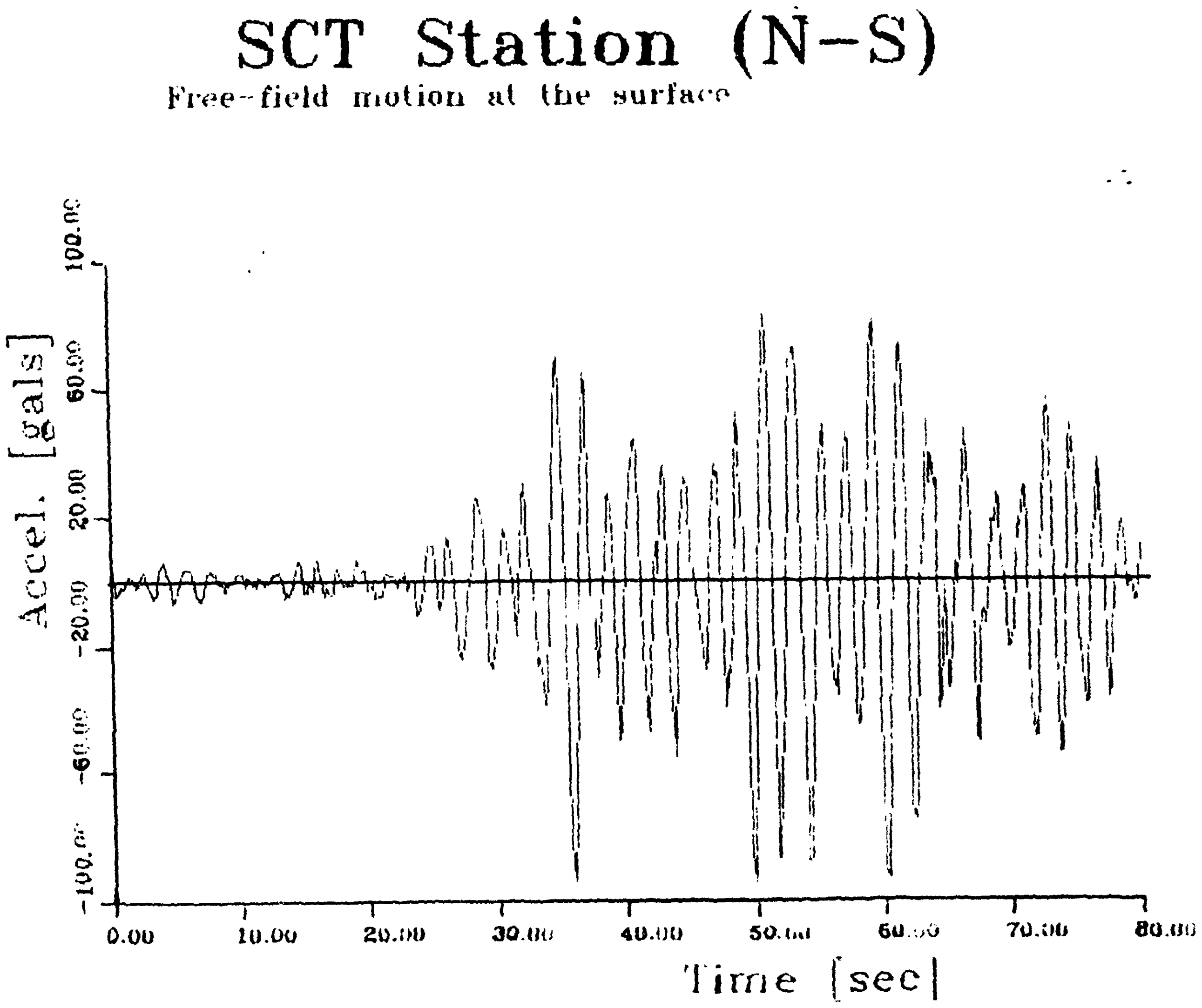
SCT Station (N-S)
Free-field motion at the surface
Accel. [gals]
100.00
60.00
20.00
-20.00
-60.00
-100.00
0.00
10.00
20.00
30.00
40.00
50.00
60.00
70.00
80.00
Time [sec]

Figure 4.5

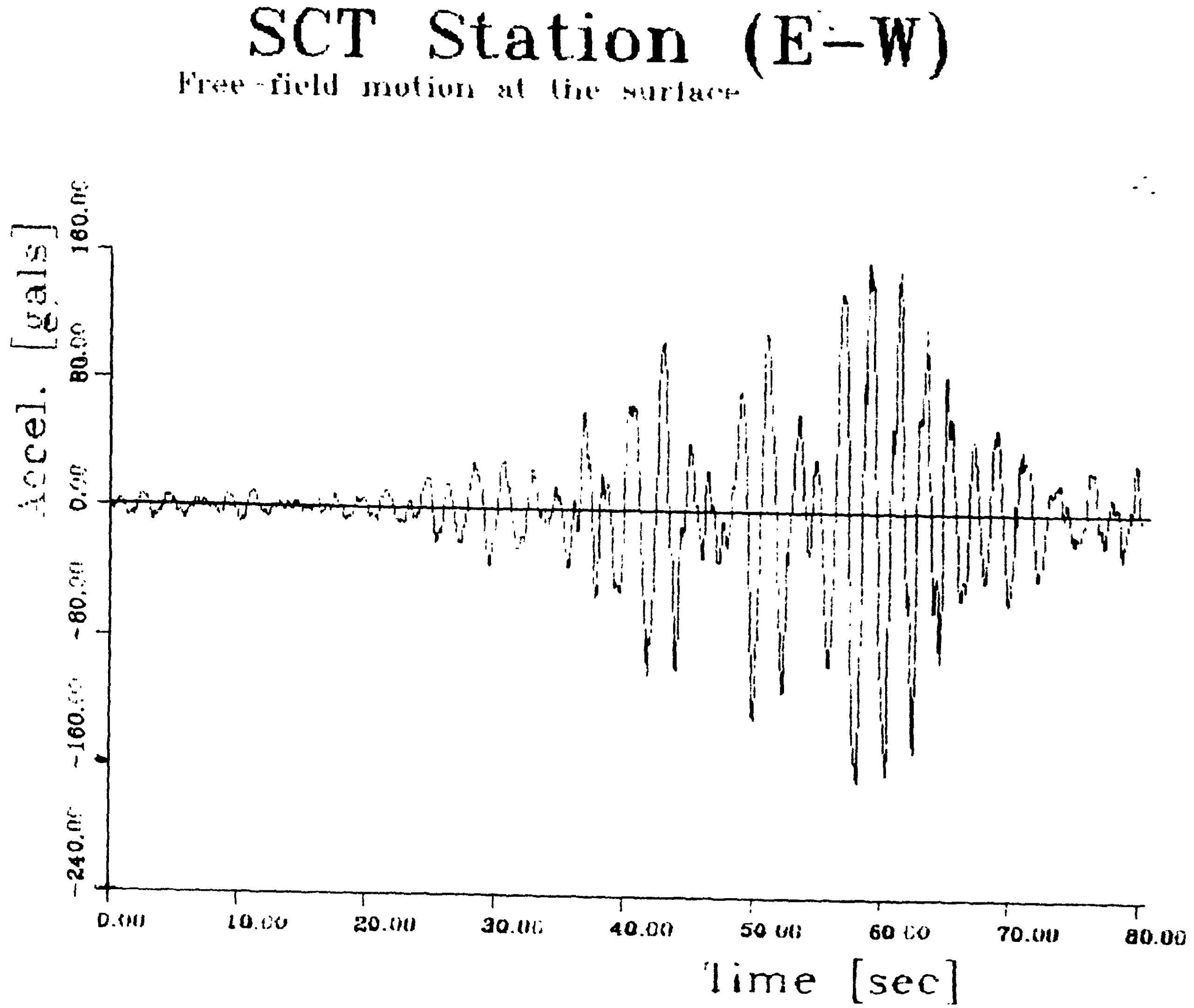
SCT Station (E-W)
Free-field motion at the surface
Accel. [gals]
160.00
80.00
0.00
-80.00
-160.00
-240.00
0.00
10.00
20.00
30.00
40.00
50.00
60.00
70.00
80.00
Time [sec]

Figure 4.6

registered at that station. As can be seen, the strong phase of the motion had a duration of more than 40 s and exhibited an almost pure sinusoidal characteristic, with the E–W component attaining higher amplitudes than the N–S component. Performing Fourier transforms on these time histories, the frequency contents can be analyzed (see figs. 4.7 a,b and 4.8 a,b). The motion has a predominant frequency of 0.5 Hz, and frequencies higher than 1.0 Hz are almost non–existent. This peak concentration of energy at a single frequency is responsible for the concentration of damage in buildings having natural frequencies in this range, and explains why the majority of the collapsed buildings had 6 to 16 stories while short and very tall buildings behaved well during the earthquake. A good approximation for the first natural period of concrete buildings on fixed base in Mexico City is n/10, where n represents the number of stories. Hence, a building with 20 stories has a fundamental period of approximately 2 secs, which coincides with the dominant period of the motion. However, when the elasticity of the foundation and nonlinear behavior of the structural members is taken into account, it is found that buildings most prone to collapse have less than 20 stories.

To understand the peak in the frequency content at 0.5 Hz, the motion amplification for a shear wave travelling vertically through the stratum was analyzed. The result is shown in figures 4.9 and 4.10, which represent the transfer function between the motion at the base of the stratum and at the free surface. An internal damping ratio of 2% was chosen, in accordance with experimental data, and a Poisson's coefficient equal to 0.45, which can be justified by the high water content of the soil. The absolute value of the transfer function exhibits several peaks coincident with the natural frequencies of the stratum. The first peak occurs for a frequency close to 0.5 Hz, which agrees with the Fourier transform of the observed motion at the surface, the amplification value at this frequency exceeding 6.0. It is interesting to

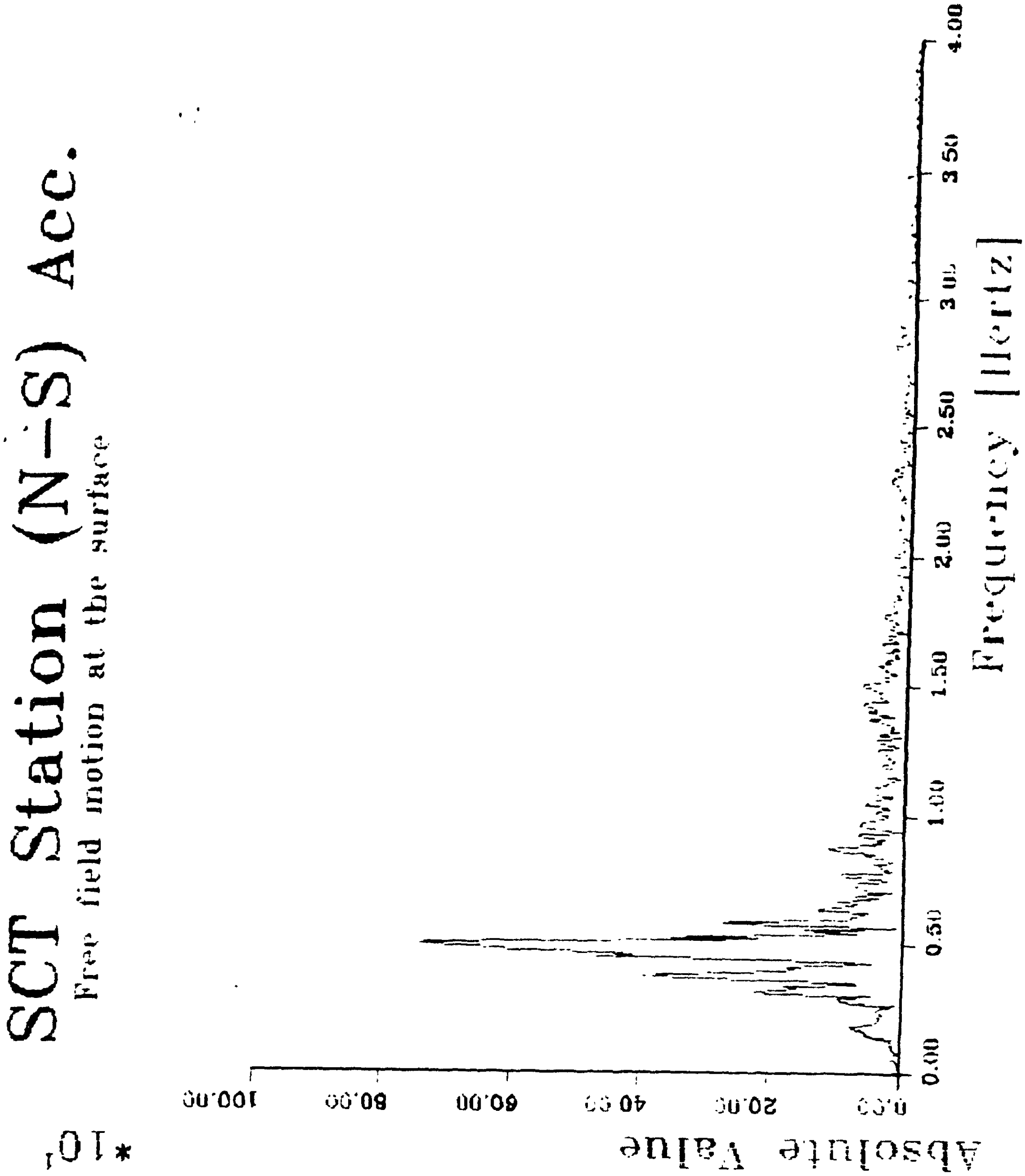
SCT Station (N-S) Acc.
Free field motion at the surface
Absolute Value
*10^1
0.00
20.00
40.00
60.00
80.00
100.00
0.00
0.50
1.00
1.50
2.00
2.50
3.00
3.50
4.00
Frequency [Hertz]

Figure 4.7a

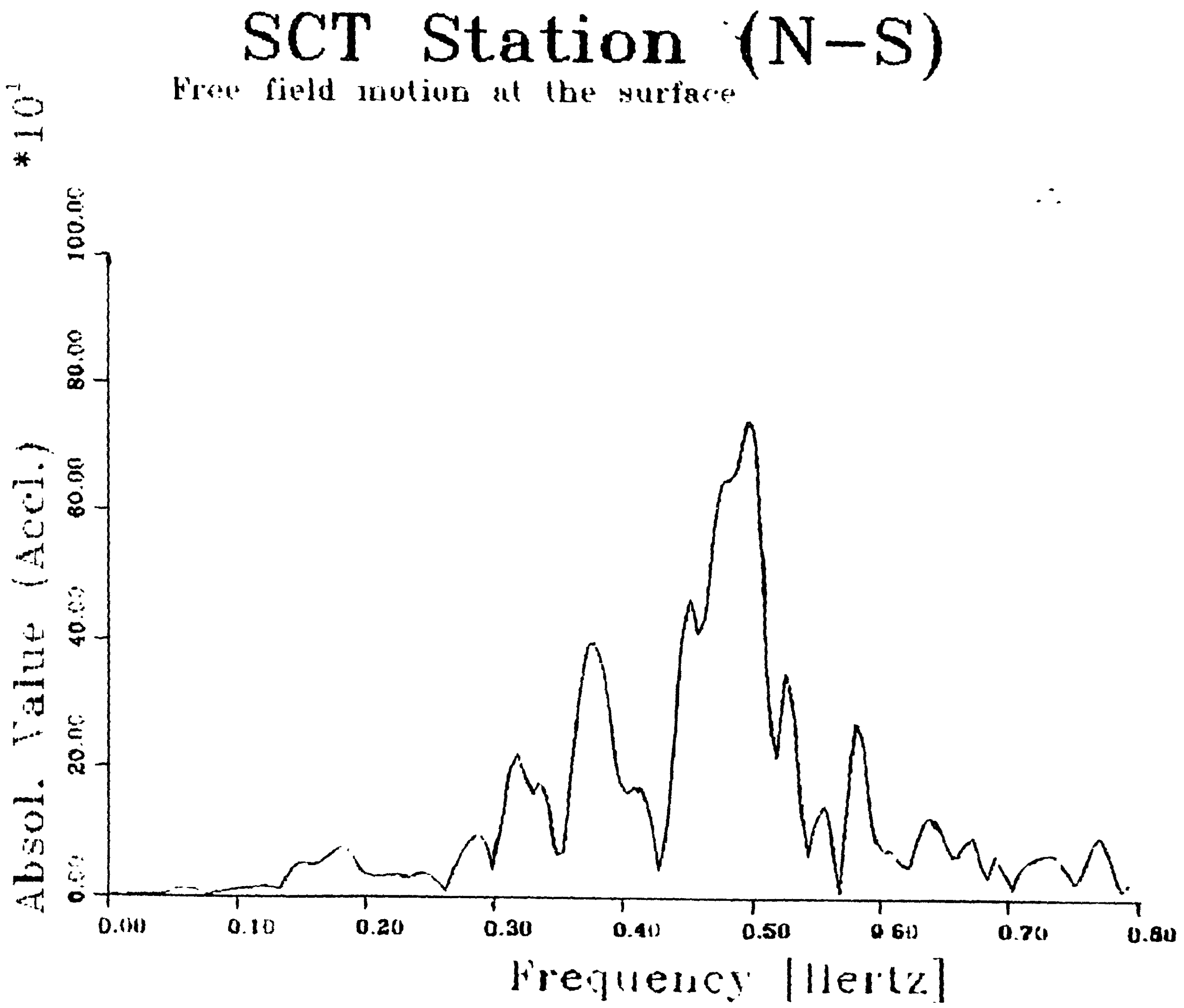
SCT Station (N-S)
Free field motion at the surface
*10^1
Absol. Value (Accl.)
100.00
80.00
60.00
40.00
20.00
0.00
0.00
0.10
0.20
0.30
0.40
0.50
0.60
0.70
0.80
Frequency [Hertz]

Figure 4.7b

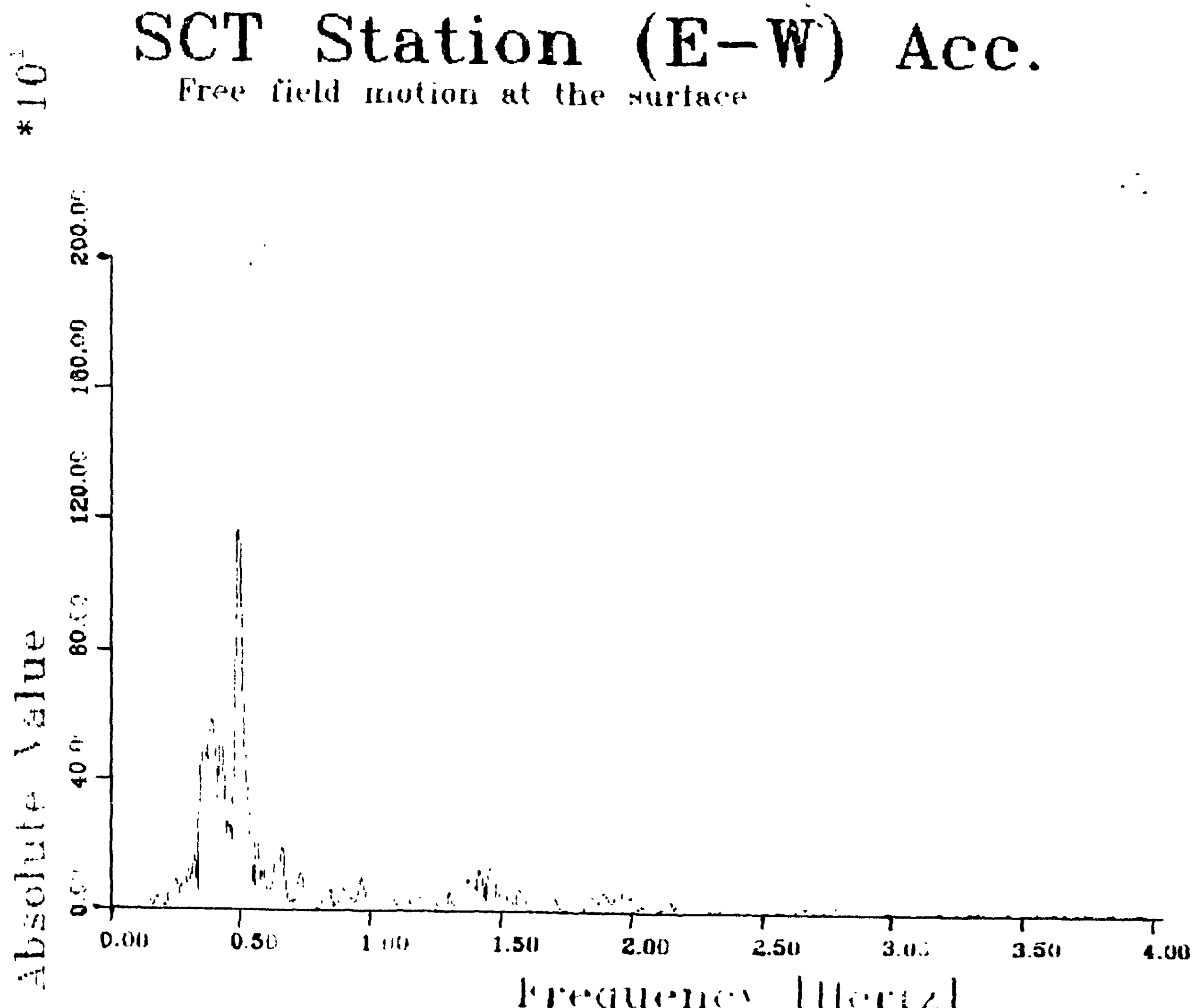
SCT Station (E-W) Acc.
Free field motion at the surface
*10
Absolute Value
0.00
40.00
80.00
120.00
160.00
200.00
Frequency [Hertz]
0.00
0.50
1.00
1.50
2.00
2.50
3.00
3.50
4.00

Figure 4.8a

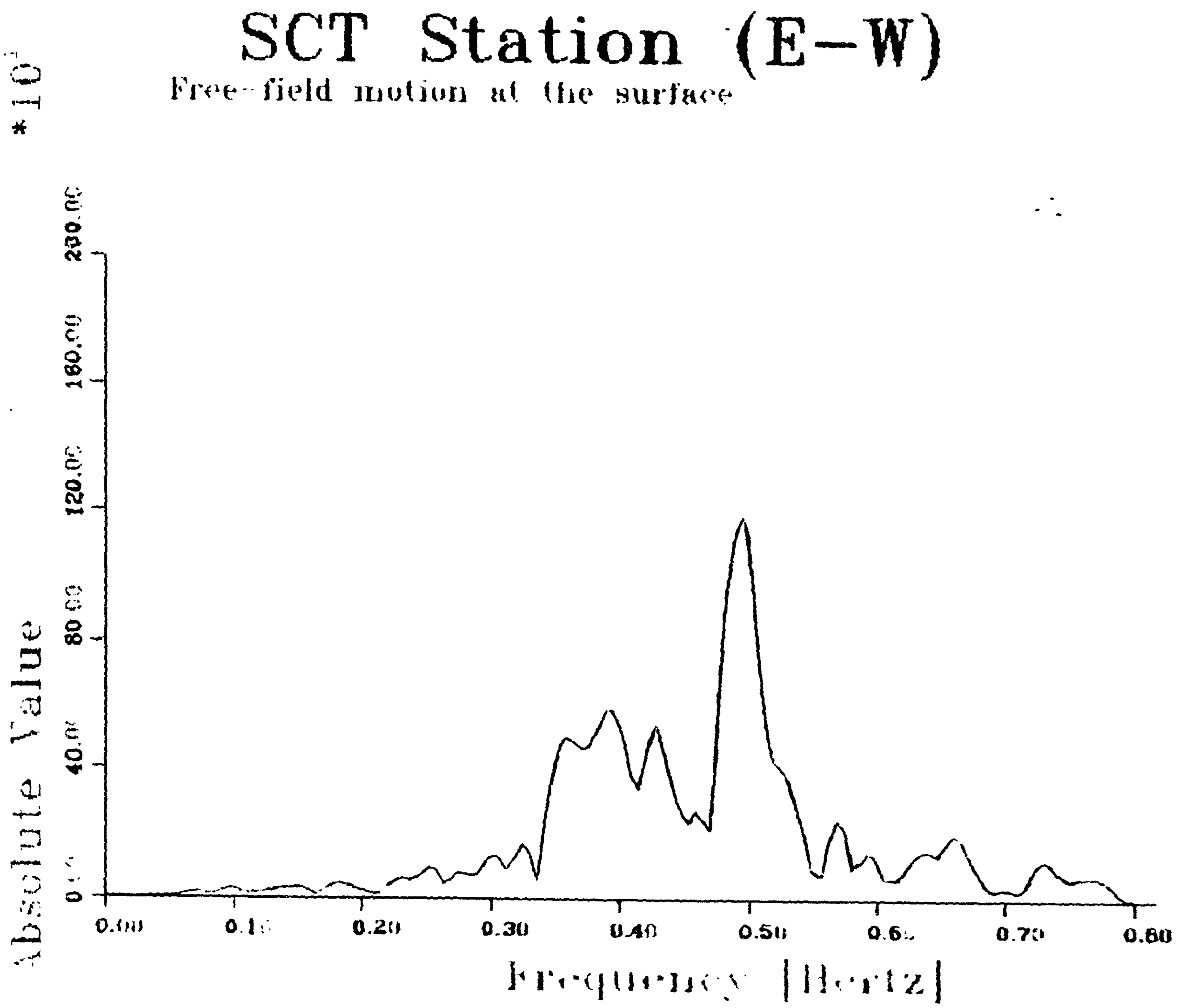
SCT Station (E-W)
Free-field motion at the surface
*10
Absolute Value
0.00
40.00
80.00
120.00
160.00
200.00
0.00
0.10
0.20
0.30
0.40
0.50
0.60
0.70
0.80
Frequency [Hertz]

Figure 4.8b

Transfer Function Rock-Surf.

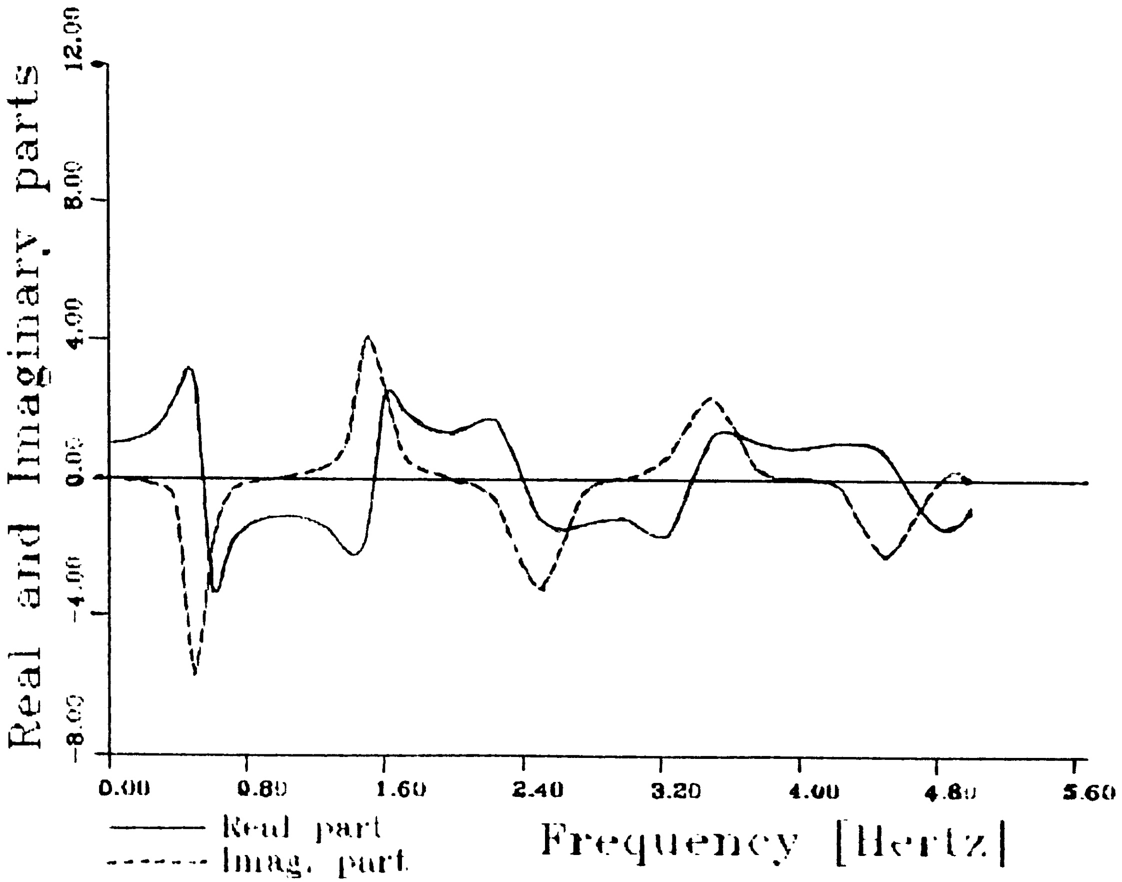

Figure 4.9

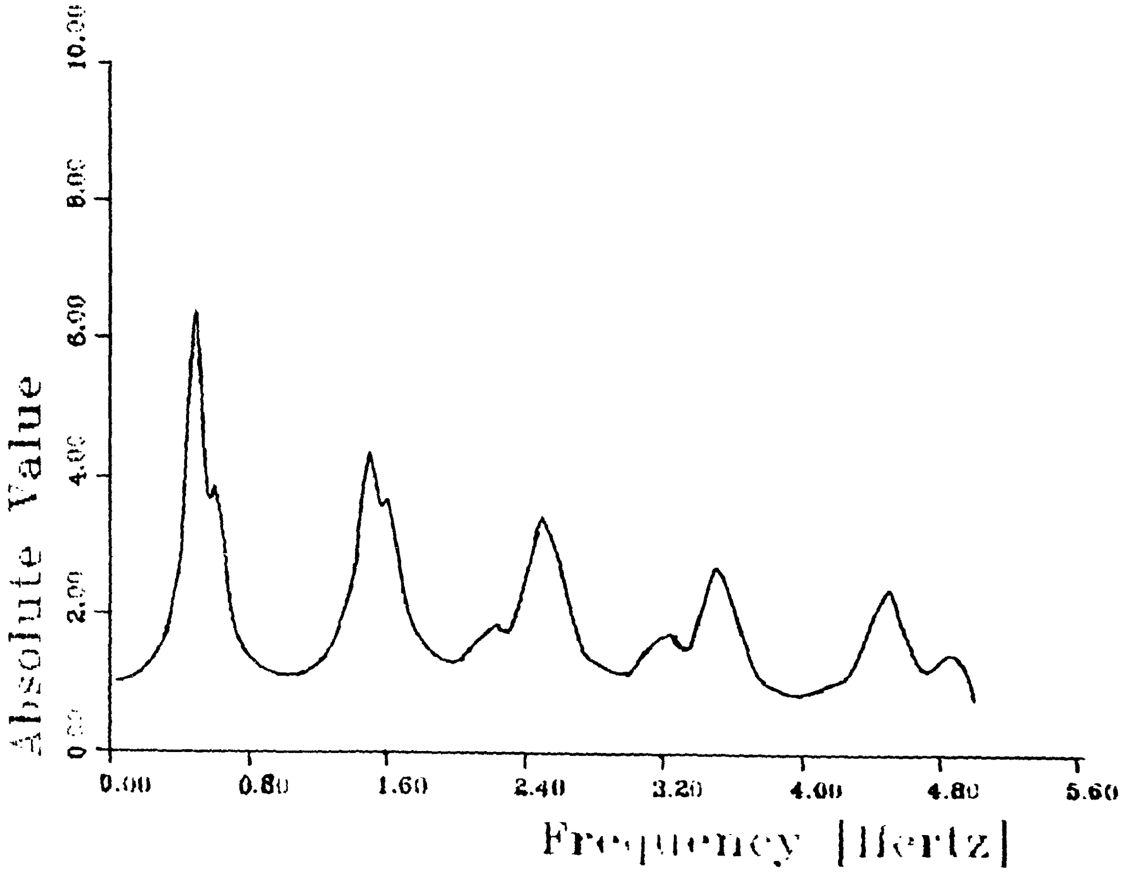

Transfer Function Rock-Surf.

Figure 4.10

note that the other peaks in the transfer function, for higher frequencies, are not present at all in the frequency spectrum of the motion recorded at the surface. Hence, either the motion arriving at the base of the stratum does not contain frequencies higher than about 1.0 Hz or the damping effect is more important for those frequencies.

It is helpful to filter through the stratum the motion observed in a region with firm soil outcropping and compare the resulting motion with the one observed at the SCT station. This was done using the acceleration of the motion recorded at the Tacubaya Station (TACY), whose frequency content is shown in figures 4.11 and 4.12. The absolute value of the Fourier Transform of the corresponding filtered motion at the surface is plotted in figures 4.13 and 4.14. Comparing these figures with figures 4.7a and 4.8a (taking into account the different scales) it can be seen that the amplitude of the filtered motion for a frequency of 0.5 Hz is about one third the amplitude of the real motion while at higher frequencies the opposite occurs, with the amplitude of the filtered motion showing a much greater amplitude than the real motion. This seems to indicate that internal damping is of a viscous nature and increases with frequency; since the saturation of the soil is nearly 300–500%, it is not surprising that viscous effects should be observable.

The acceleration of the motion registered in the transition region at the Viveros Station (SXVI) was also analyzed; the time history and frequency spectrum are displayed in figures 4.15–4.18, which show that this motion is rich in frequencies up to 2.5 Hz. Although the peaks corresponding to the natural frequencies of the stratum at that location are not clearly discernible, it can still be guessed that the lower natural frequencies should be around 0.4 Hz, 1.2 Hz and 2.0 Hz. These values are lower than the natural frequencies at the SCT station, which agrees with the larger depth of the stratum in the Viveros region.

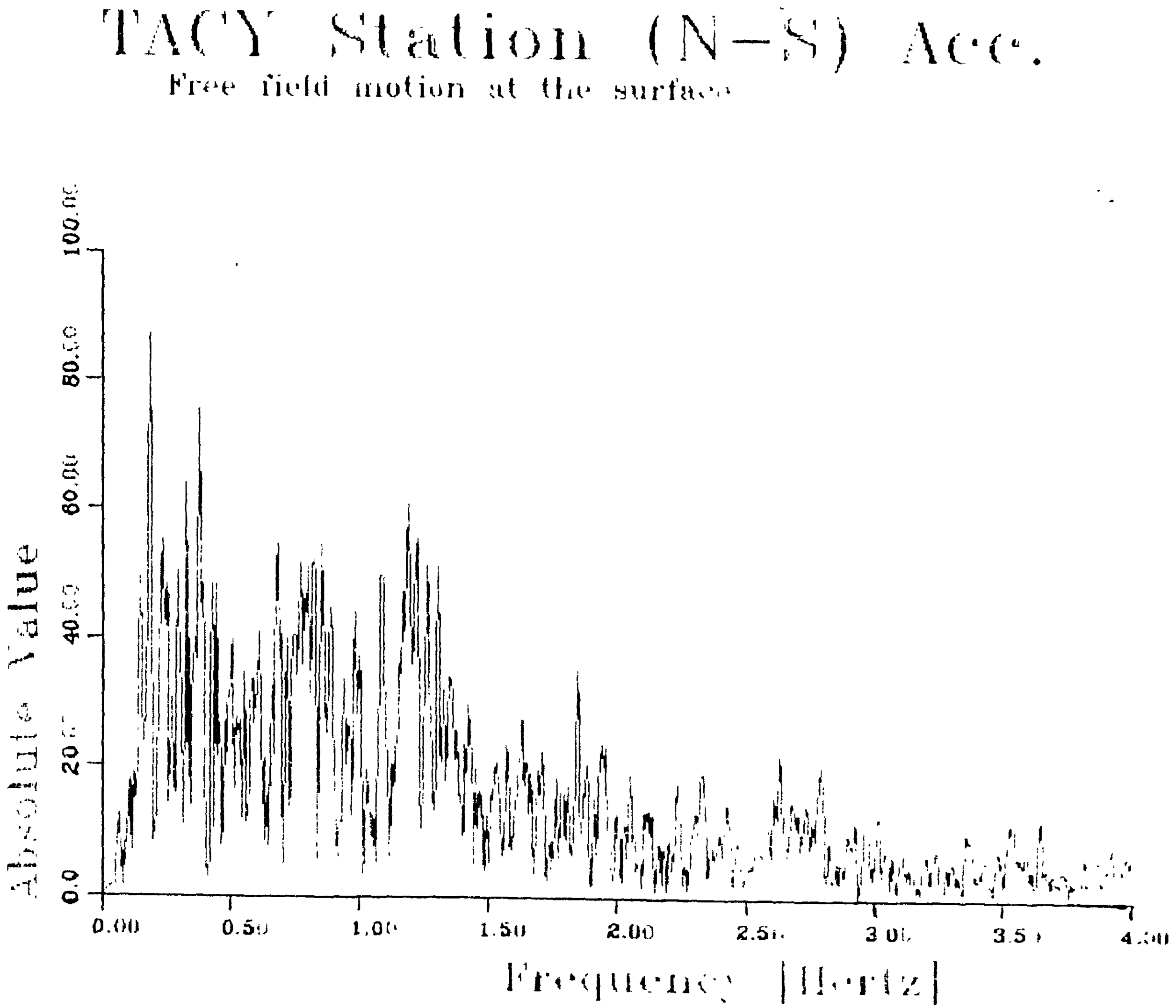
TACY Station (N-S) Acc.
Free field motion at the surface
Absolute Value
0.0
20.00
40.00
60.00
80.00
100.00
0.00
0.50
1.00
1.50
2.00
2.50
3.00
3.50
4.00
Frequency [Hertz]

Figure 4.11

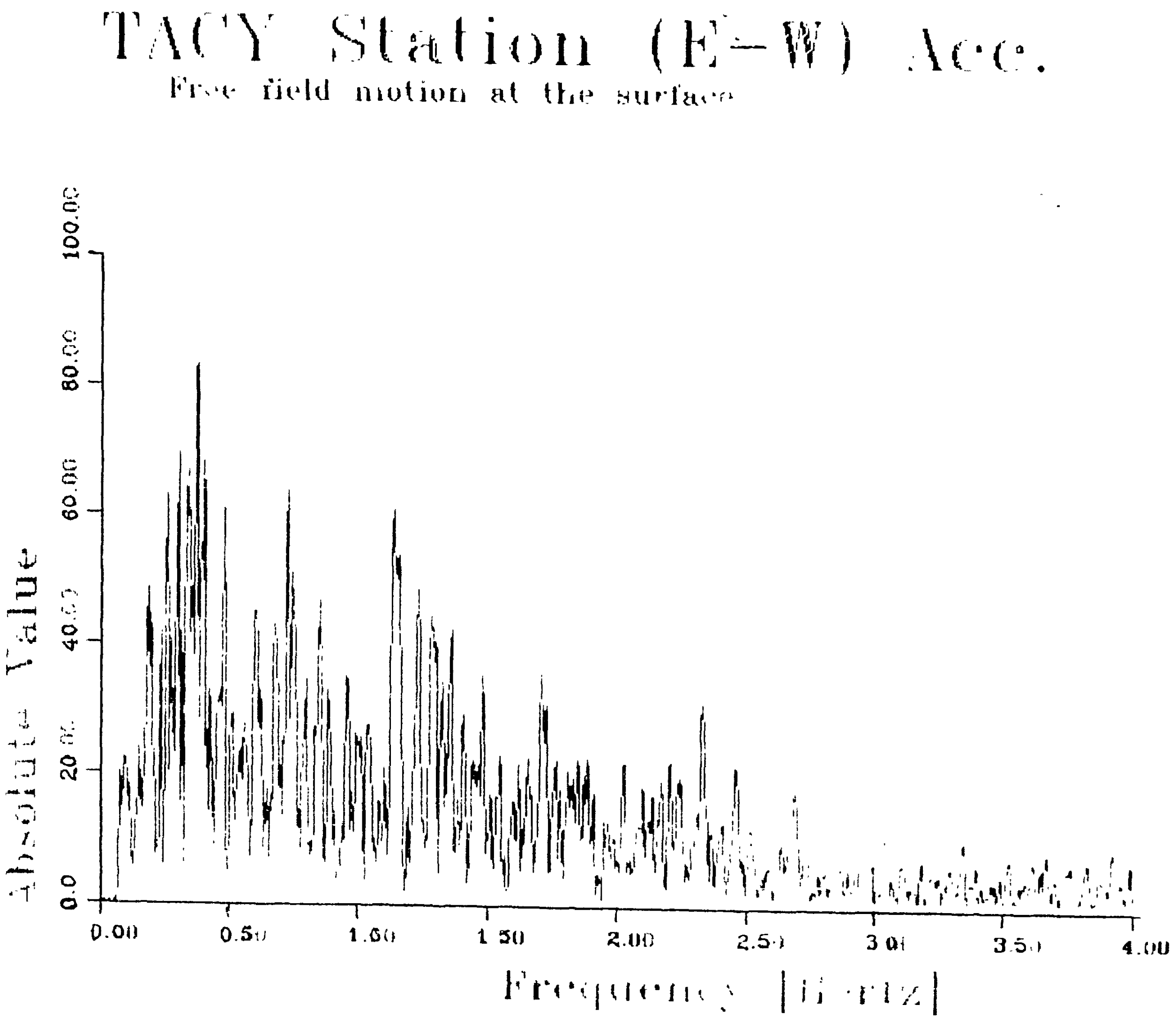
TACY Station (E-W) Acc.
Free field motion at the surface
Absolute Value
0.0
20.00
40.00
60.00
80.00
100.00
0.00
0.50
1.00
1.50
2.00
2.50
3.00
3.50
4.00
Frequency [Hertz]

Figure 4.12

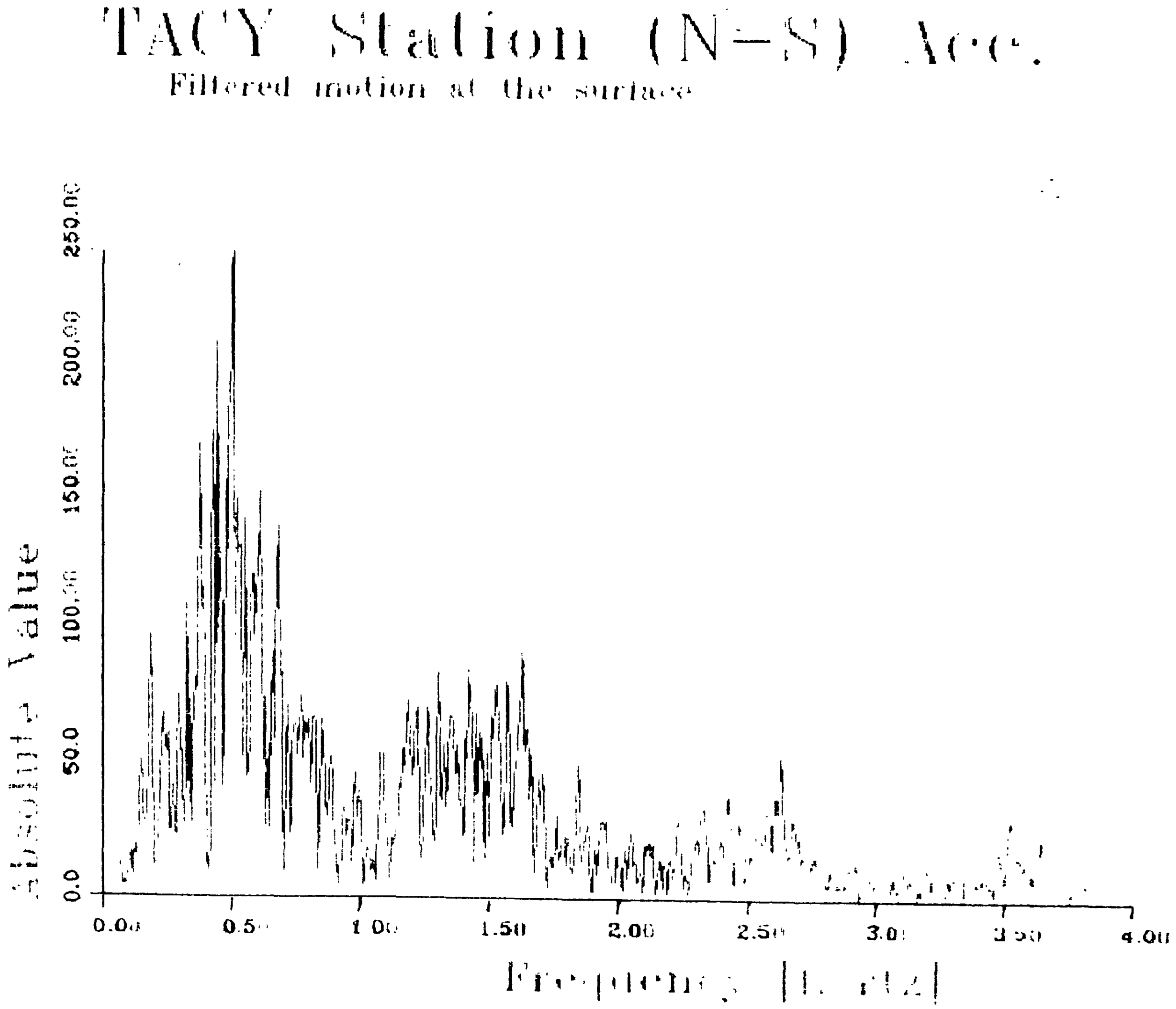
TACY Station (N-S) Acc.

Filtered motion at the surface

Figure 4.13

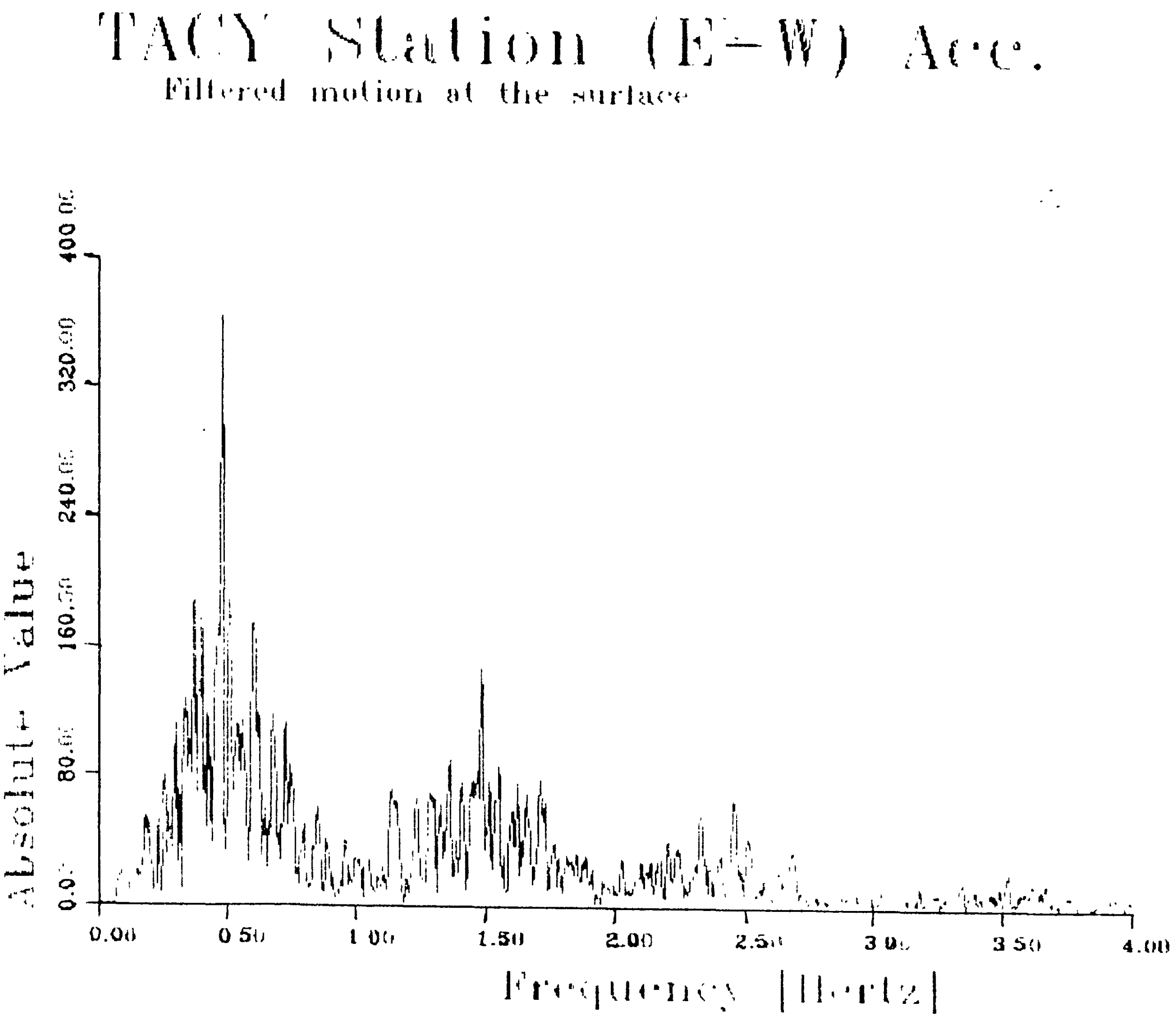
TACY Station (E-W) Acc.
Filtered motion at the surface
Absolute Value
0.0
80.00
160.00
240.00
320.00
400.00
0.00
0.50
1.00
1.50
2.00
2.50
3.00
3.50
4.00
Frequency [Hertz]

Figure 4.14

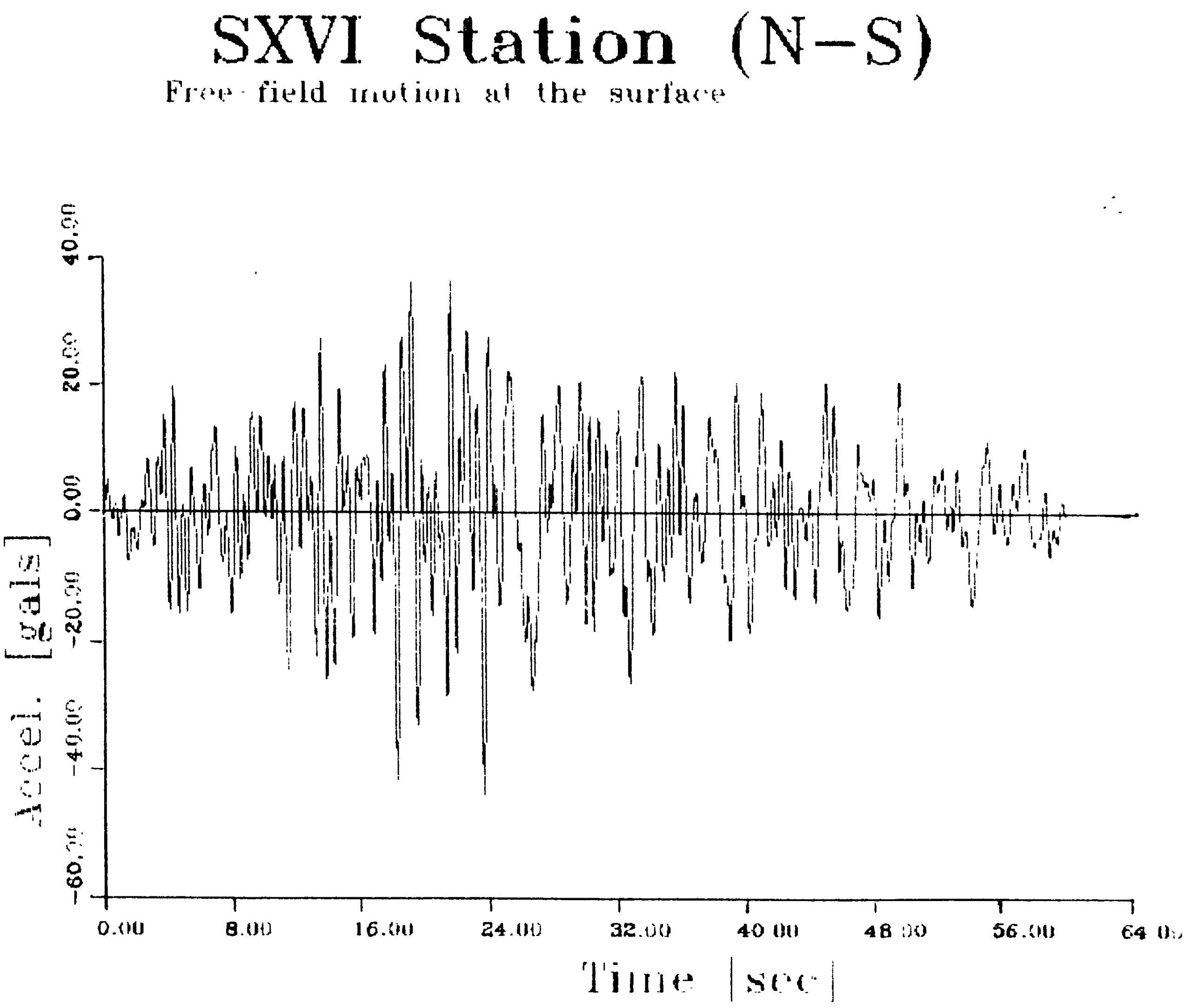

SXVI Station (N–S)

Free-field motion at the surface

Figure 4.15

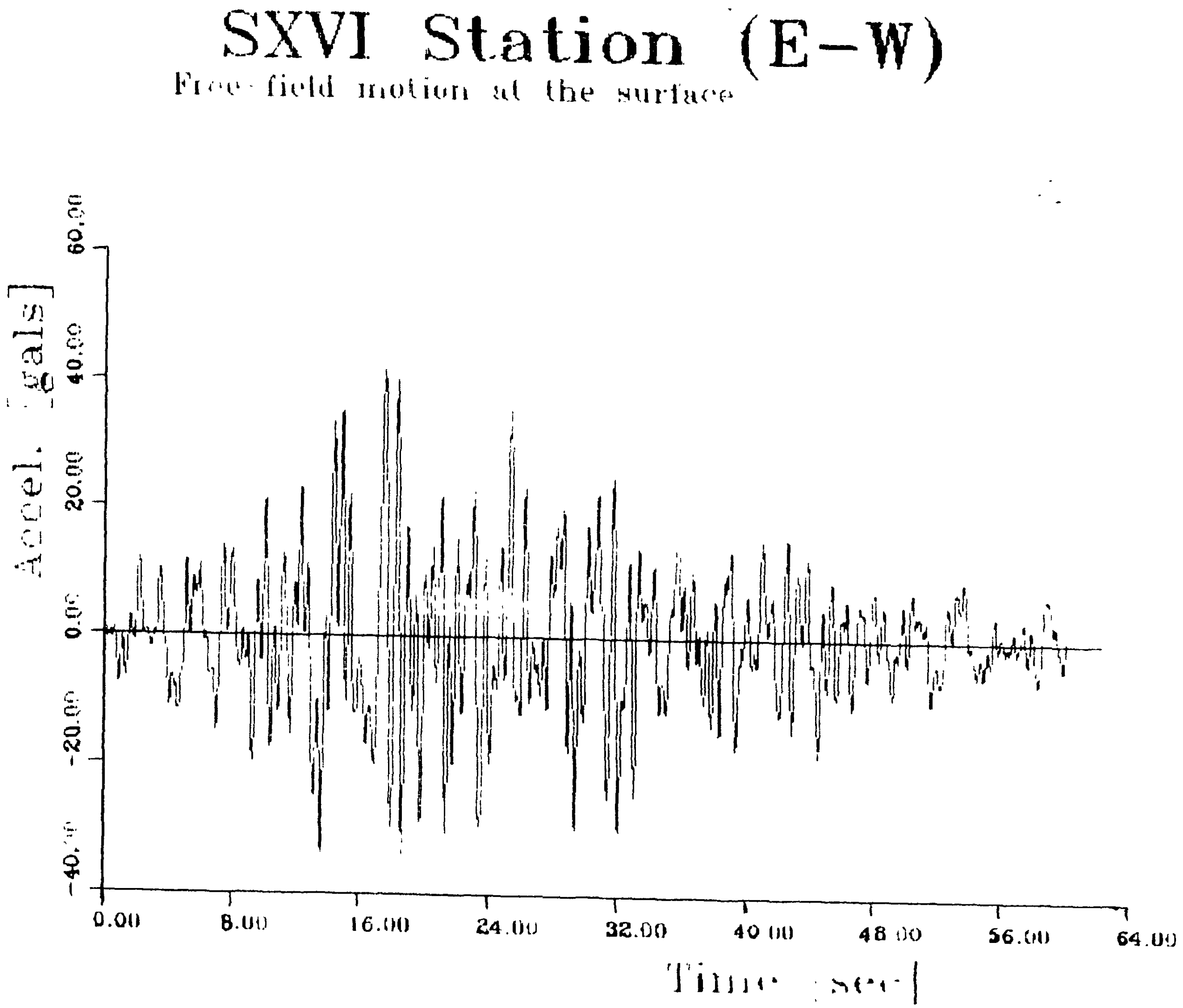
SXVI Station (E-W)
Free-field motion at the surface
Accel. [gals]
60.00
40.00
20.00
0.00
-20.00
-40.00
0.00
8.00
16.00
24.00
32.00
40.00
48.00
56.00
64.00
Time [sec]

Figure 4.16

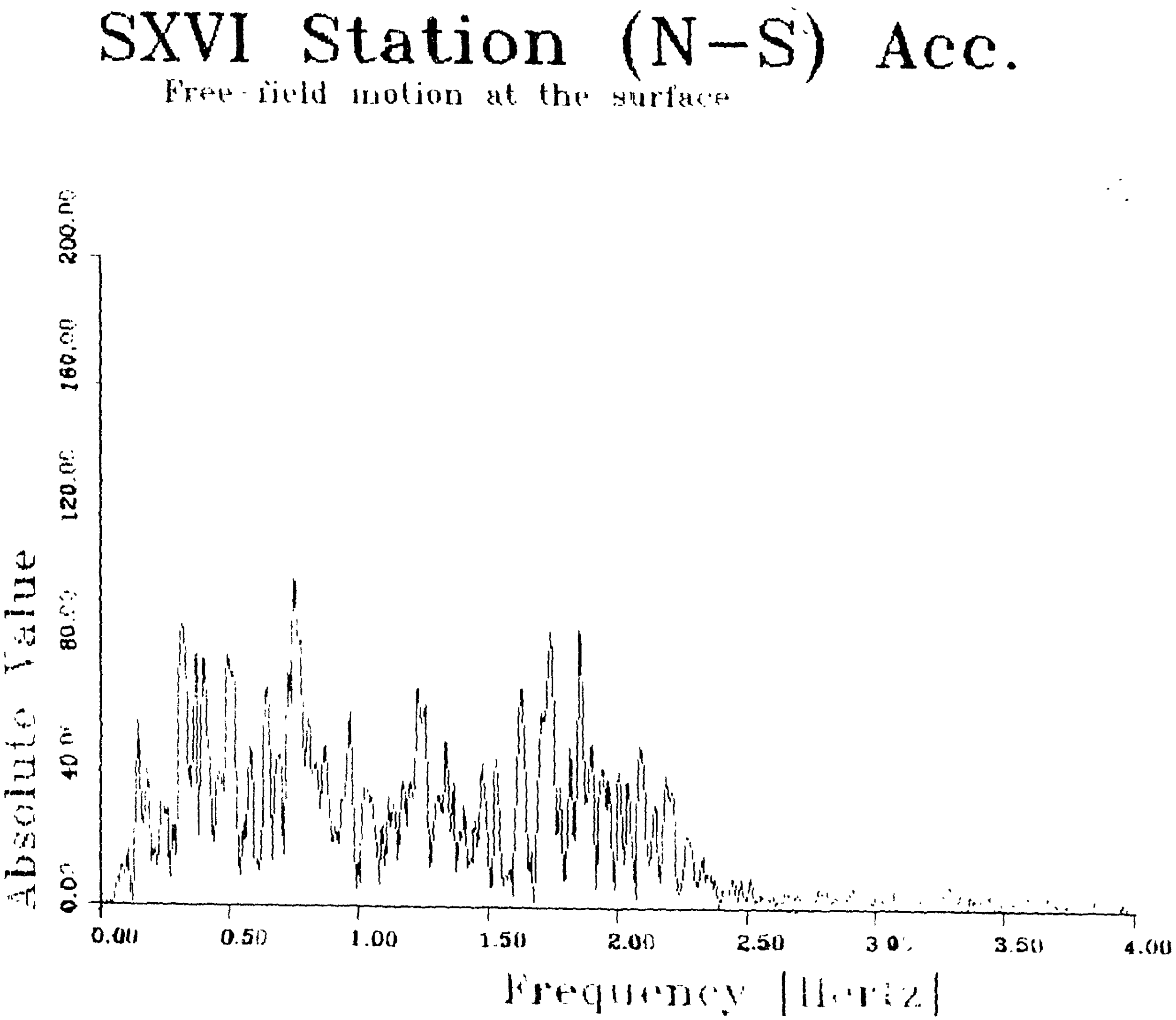
SXVI Station (N-S) Acc.
Free-field motion at the surface
Absolute Value
0.00
40.00
80.00
120.00
160.00
200.00
0.00
0.50
1.00
1.50
2.00
2.50
3.00
3.50
4.00
Frequency [Hertz]

Figure 4.17

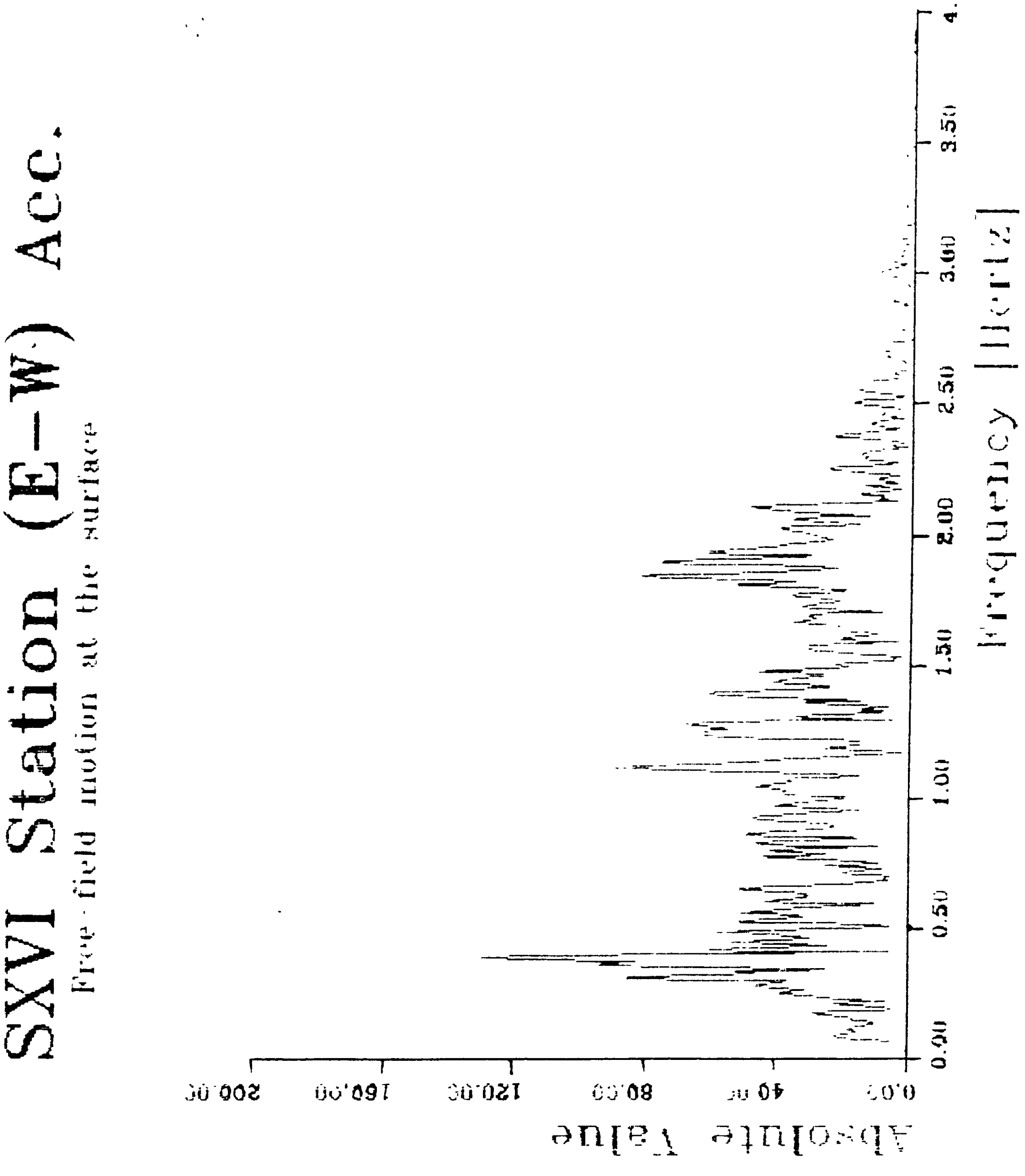
SXVI Station (E-W) Acc.
Free-field motion at the surface
Absolute Value
0.00
40.00
80.00
120.00
160.00
200.00
Frequency [Hertz]
0.00
0.50
1.00
1.50
2.00
2.50
3.00
3.50
4.00

Figure 4.18

4.3.2 Boundary Element Results

The boundary element program referred to earlier was used to study the scattering of seismic waves by the underground tunnel, and in a particular, the influence of the tunnel on the ground motion at the surface.

Figure 4.19 shows the geometry of the tunnel and soil properties used. The tunnel was idealized as a rectangular rigid box with a height of 8.3 m and a width of 9.4m; these dimensions correspond approximately to the overall dimensions of a typical section of the actual tunnel. A soil layer with a thickness of 2.5m covers the the tunnel; while the actual depth of the tunnel varies along the longitudinal axis, the value of 2.5m seems to be a representative one. The mass of the tunnel and its inertial moment were set to be equal to the mass of soil removed. Actual inertias are probably somewhat smaller, but precise values are not needed since they do not have an important effect in the response, as will be shown.

The stratum is composed of three different layers of soil: a very soft top layer extending to a depth of 31.0 m; an intermediate thin layer having a shear wave velocity almost double that of the top layer; and a third layer with properties similar to the first one. The stratum rests on top of a much stiffer soil, which in the numerical computations was idealized as a rigid boundary.

The stratum was first discretized into 14 sublayers and then into 28 sublayers; the results were then compared. While an excellent agreement was found, the final computations were nevertheless performed using the more refined model. The soil–tunnel boundary was discretized into 8 linear elements along each vertical wall

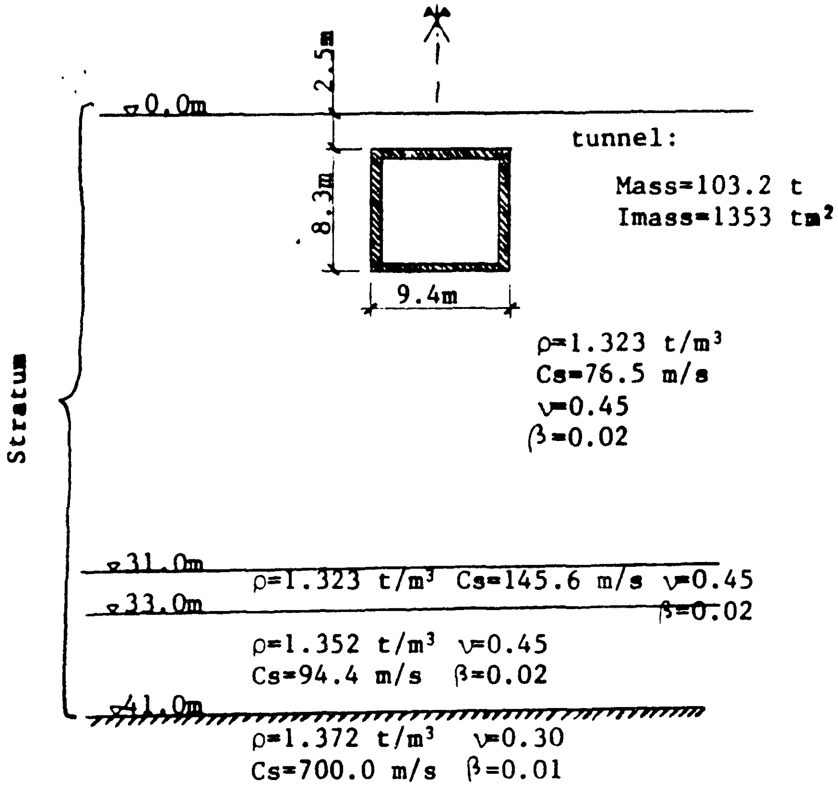

Figure 4.19 - Geometry and soil properties

and 5 constant elements along the horizontal direction. This discretization seemed to give accurate results except in the immediate vicinity of the tunnel for distances smaller than the dimensions of the boundary elements. Frequencies up to 5 Hz were considered in the computations. At a frequency of 5 Hz, the wavelength corresponding to a wave velocity of 70 m/s is 14 m, which is greater by a factor of 4 the size of the boundary elements chosen; hence, the results provided by this model should be reliable.

Three types of seismic waves were considered: SH, SV and P waves. On the other hand, when the change in rigidity between the soft soil in the stratum and the hard deposits underneath is taken into account, it becomes clear that waves arriving from underneath the stratum will refract to a nearly vertical direction; hence, it is not necessary to assume obliquely incident waves. For this reason, only vertically traveling waves were specified as input at the base of the stratum.

An in–plane situation was considered first, the seismic excitation being described by vertically propagating SV waves. In this case, the displacements are constrained in a plane perpendicular to the longitudinal axis of the tunnel, implying that only three degrees of freedom are active: horizontal and vertical displacements, and inplane rotation. The influence of the tunnel on the resulting motion at the free surface was the main objective of the analysis. Figures 4.20 and 4.21 show the absolute value of the horizontal displacement at the surface as a function of the distance from the axis of the tunnel and the frequency of the motion. Figure 4.20 shows in more detail the results in the frequency range 0–2 Hz while in figure 4.21, the results for frequencies up to 5 Hz are displayed. Comparing these results with figures 4.22 and 4.23 showing the response functions for free–field conditions (i.e., without tunnel) it can be concluded that for frequencies up to 2 Hz the presence of the tunnel does not affect the ground motion, while for higher frequencies, a substantial reduction of the

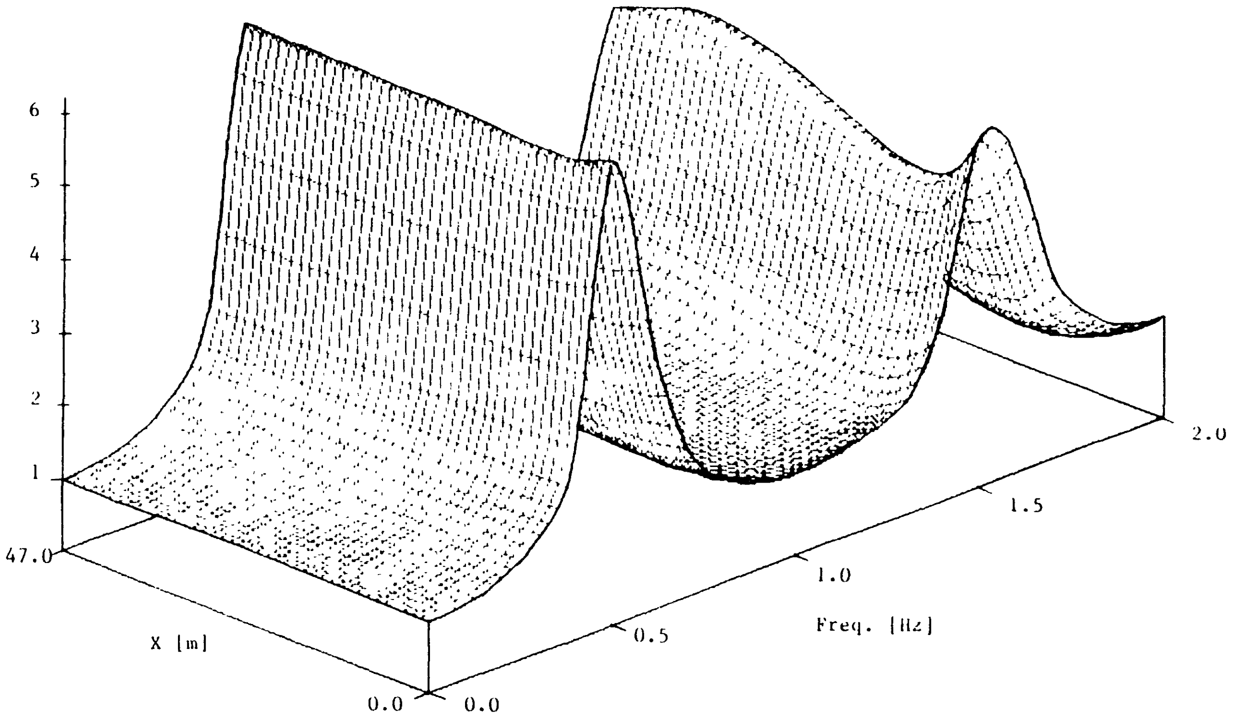

AMPLIFICATION (Hor. w. mass)

Niu=0.45 ; Freq=0.0-2.0 ; X 0-47m

Figure 4.20

AMPLIFICATION (Hor. w. mass)

Nu=0.45 ; Freq=0.0-5.0 ; X=0-47m

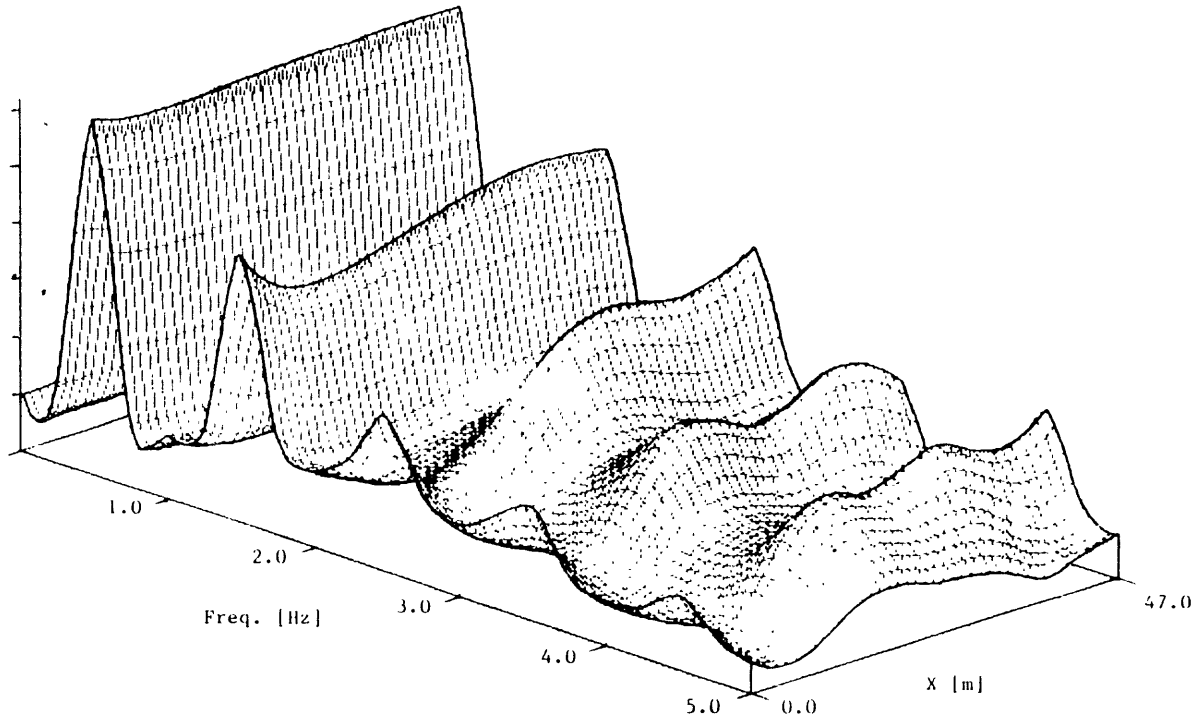

Figure 4.21

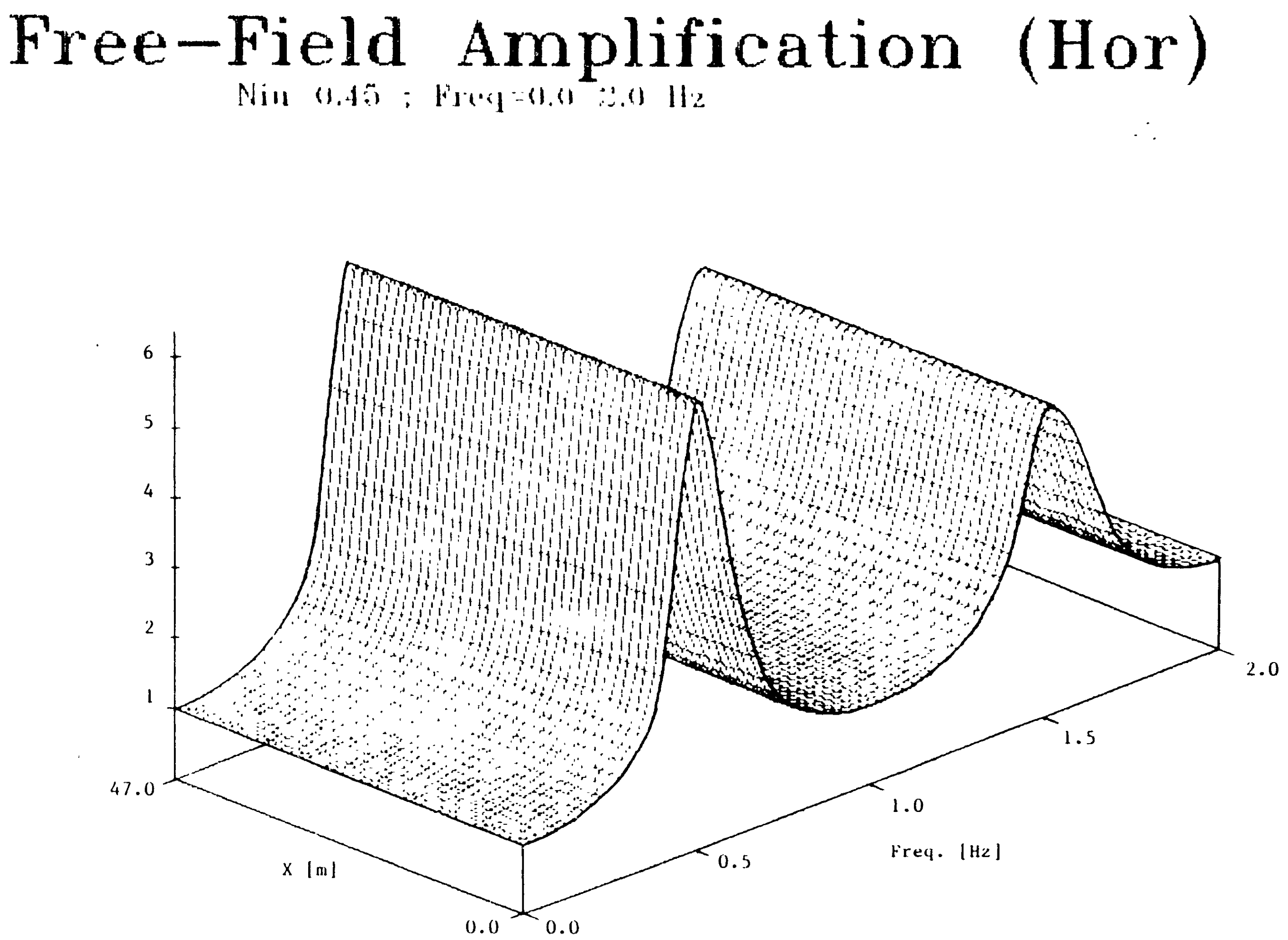
Free-Field Amplification (Hor)
Niu 0.45 ; Freq=0.0 2.0 Hz
6
5
4
3
2
1
47.0
X [m]
0.0
0.0
0.5
1.0
1.5
2.0
Freq. [Hz]

Figure 4.22

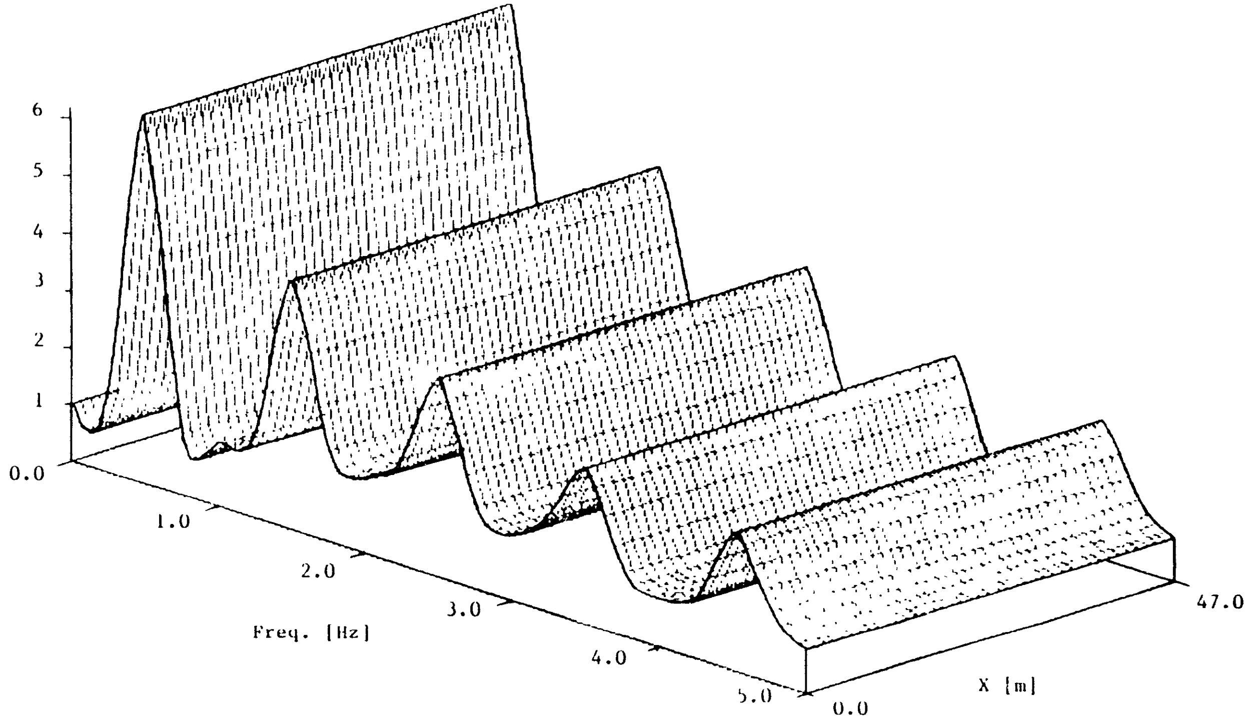

Free-Field Amplification (Hor)

Nu 0.45 ; Freq=0.0-5.0 Hz

Figure 4.23

motion arises in the vicinity of the tunnel. This can be explained intuitively considering that the maximum dimension of the tunnel along the direction of propagation of the waves is 8.3 m, which exceeds one quarter of the wavelength only for frequencies greater than $Cs/\lambda=76.5/(8.3x4) = 2.3$ Hz. At frequencies greater than this value, the soil near the tunnel deforms substantially, and because the tunnel is rigid and cannot accomodate such distortions, it follows that the displacements in the vicinity of the tunnel suffer considerable interactions.

The sensitivity of the results to the assumed mass of the tunnel was studied also, by considering the extreme case of a massless tunnel. The corresponding amplification functions for vertical SV waves are displayed in figures 4.24 and 4.25. They look very similar to figures 4.20 and 4.21, which demonstrates that the results are not very dependent on the exact mass of the tunnel.

Figures 4.26—4.29, on the other hand, show the results corresponding to a Poisson's coefficient of 0.30. In this case, the motion is more strongly affected by the presence of the tunnel because of the greater deformability of the soil. However, since the energy of the seismic motion is concentrated in a frequency band in the vicinity of the first resonant frequency of the soil, the values of the amplification functions for higher frequencies have only a minor effect on the resulting motions. Considering the high water content of the soil, a Poisson's coefficient of 0.45 seems more realistic, so that further computations will be performed using this value.

On the other hand, the rotation of the tunnel will induce vertical displacements on the surface. These displacements can attain important values at high frequencies of vibration, as is shown in figures 4.30 and 4.31. For frequencies up to 1.2 Hz, which encloses the range of interest, very small vertical displacements are induced at the

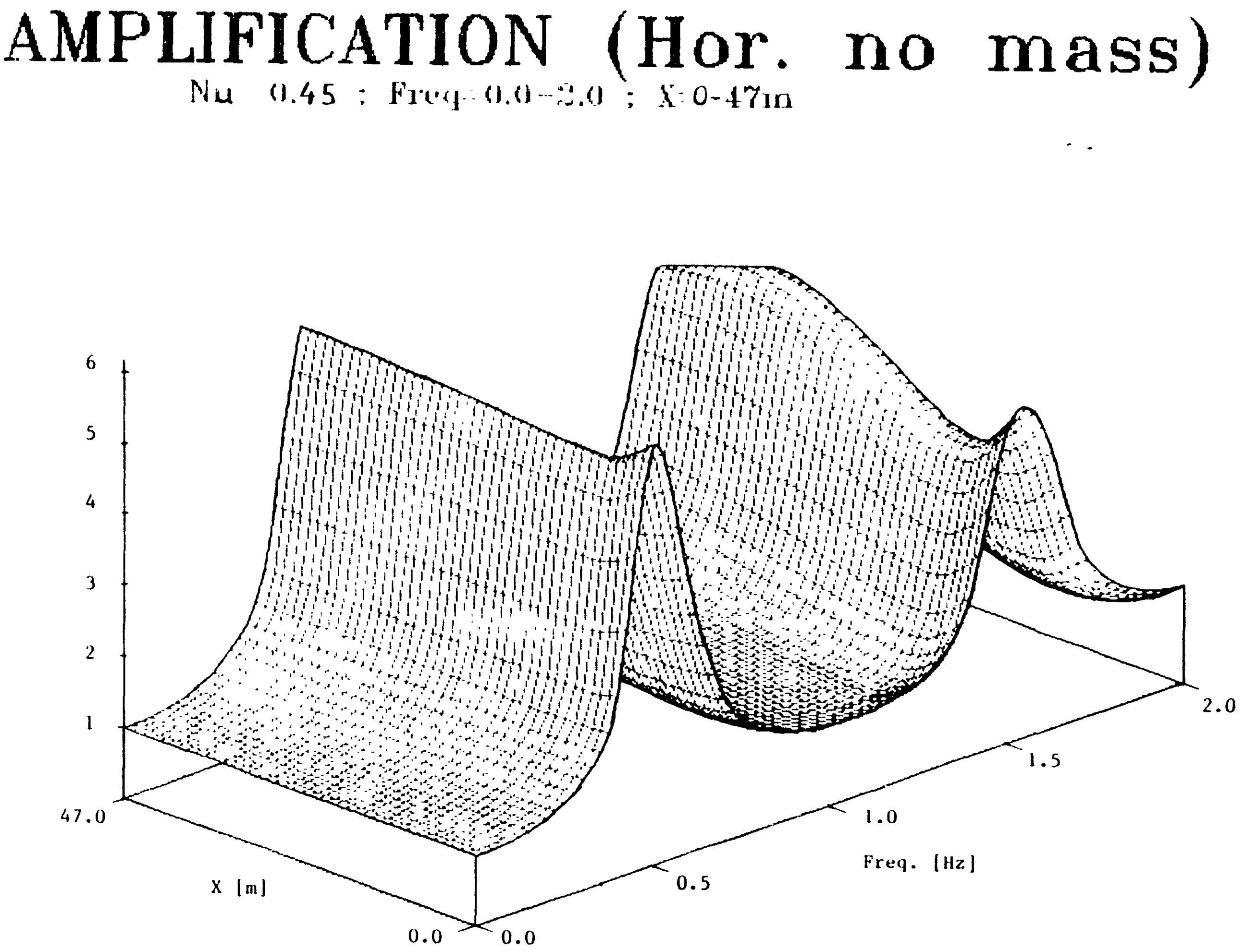

AMPLIFICATION (Hor. no mass)

Nu 0.45 ; Freq 0.0-2.0 ; X 0-47m

Figure 4.24

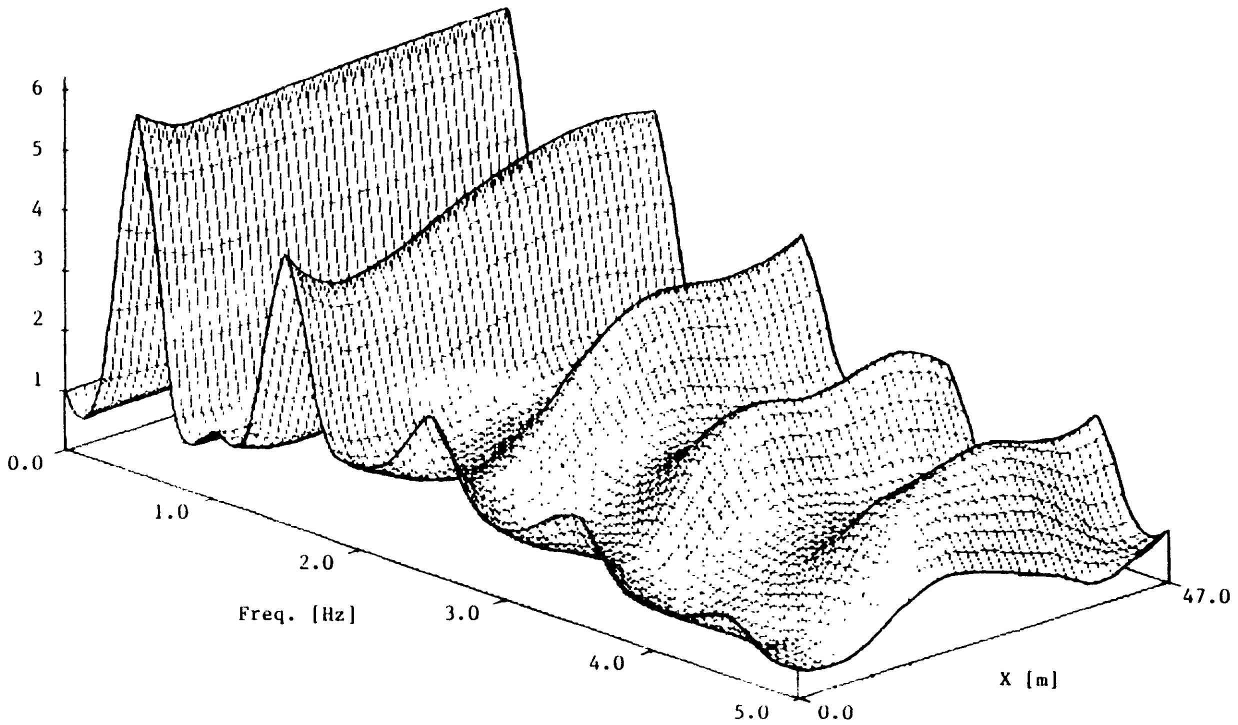

AMPLIFICATION (Hor. no mass)

Nu =0.45 ; Freq 0.0-5.0 ; X=0-47m

Figure 4.25

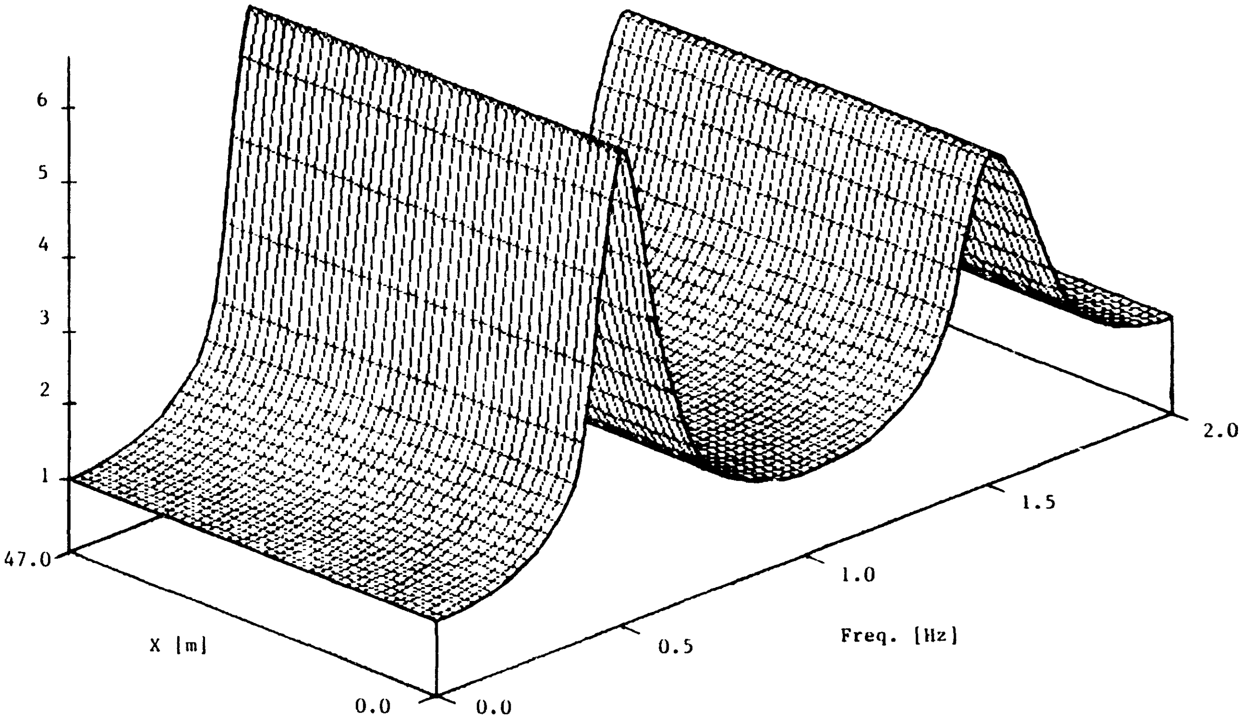

Free-Field Amplification (Hor)

Nu=0.30 ; Freq=0.0-2.0 Hz

Figure 4.26

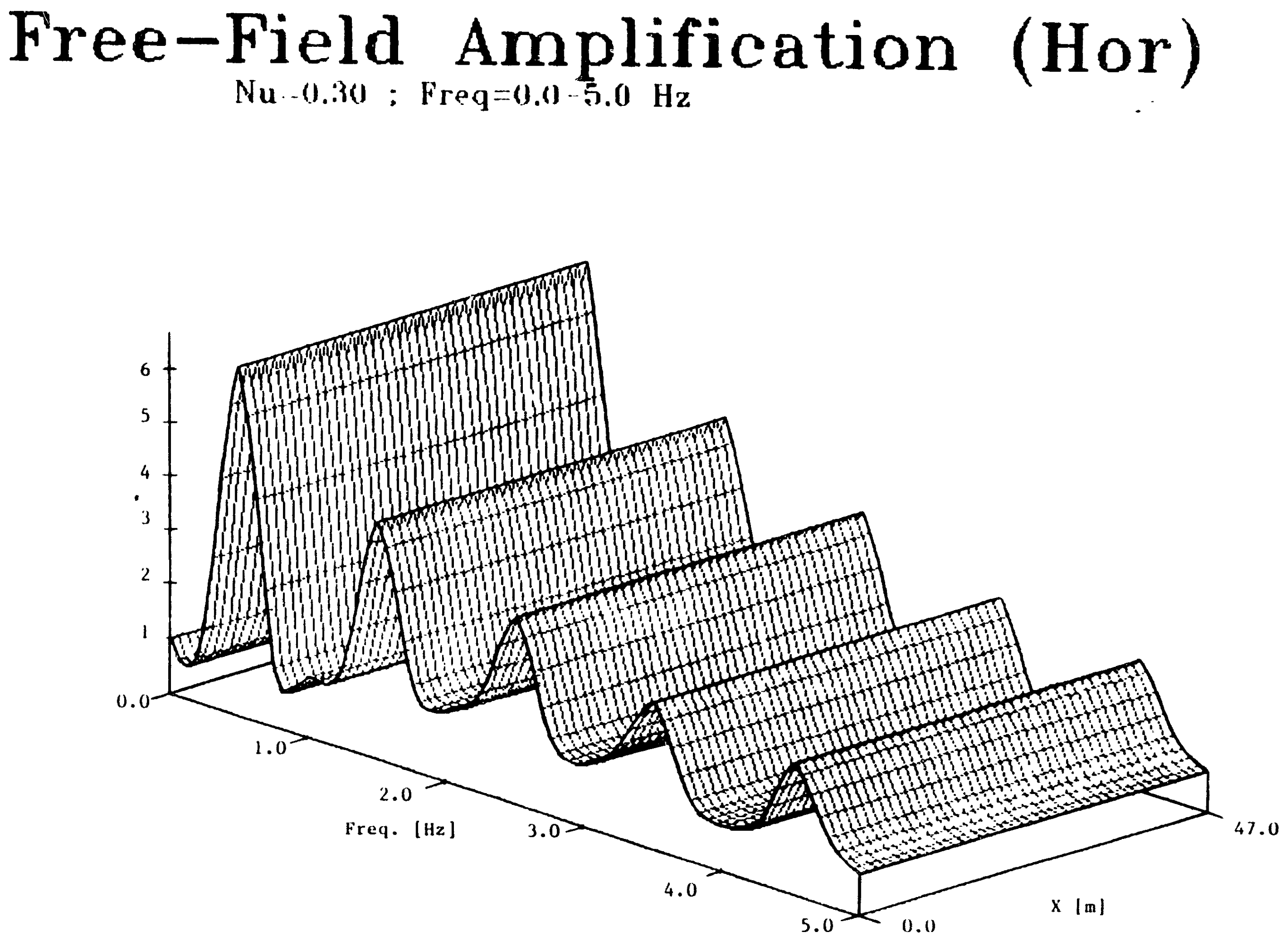
Free-Field Amplification (Hor)
Nu=0.30 ; Freq=0.0-5.0 Hz
6
5
4
3
2
1
0.0
1.0
2.0
Freq. [Hz]
3.0
4.0
5.0
0.0
X [m]
47.0

Figure 4.27

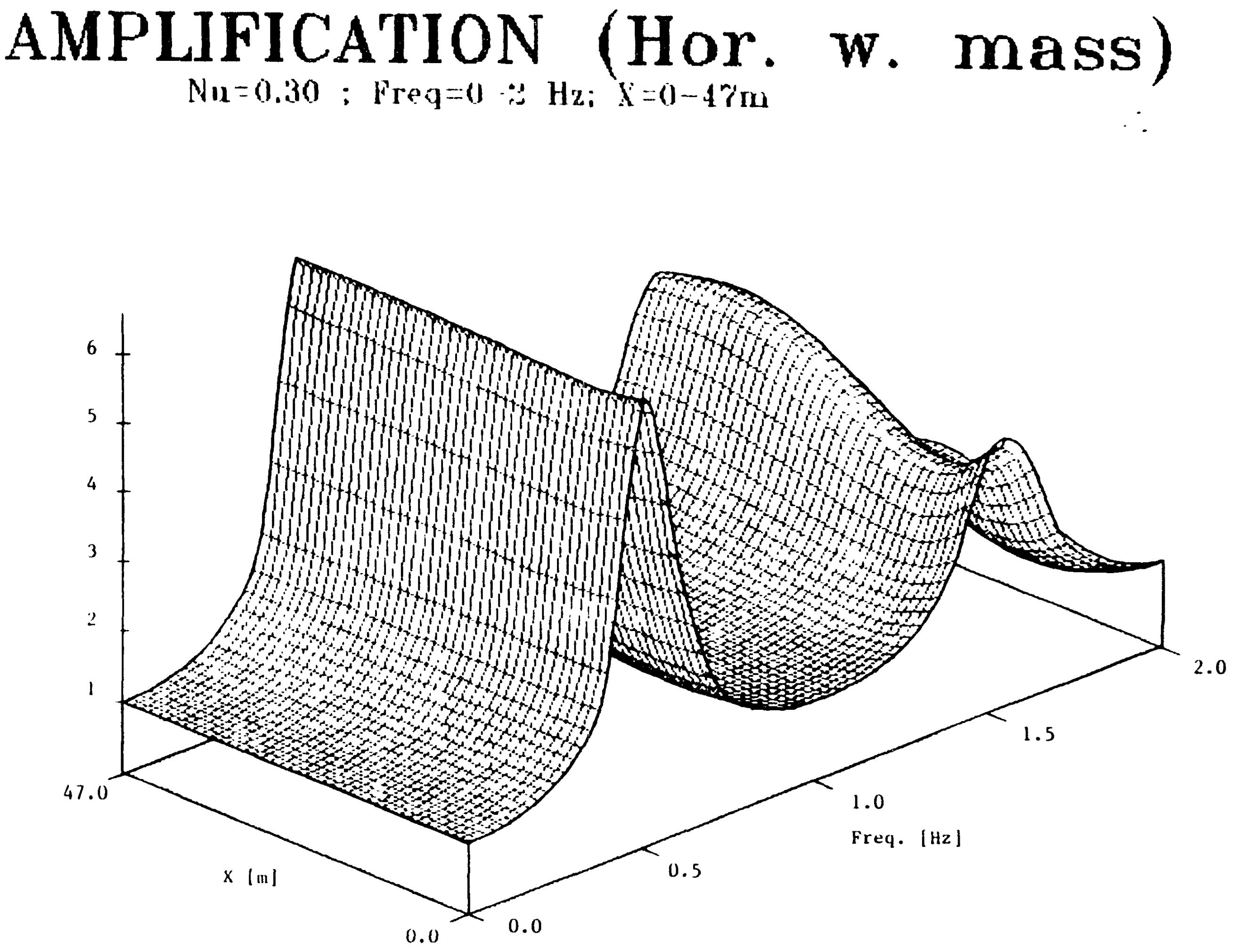
AMPLIFICATION (Hor. w. mass)
Nu=0.30 ; Freq=0-2 Hz; X=0-47m
6
5
4
3
2
1
47.0
X [m]
0.0
0.0
0.5
1.0
Freq. [Hz]
1.5
2.0

Figure 4.28

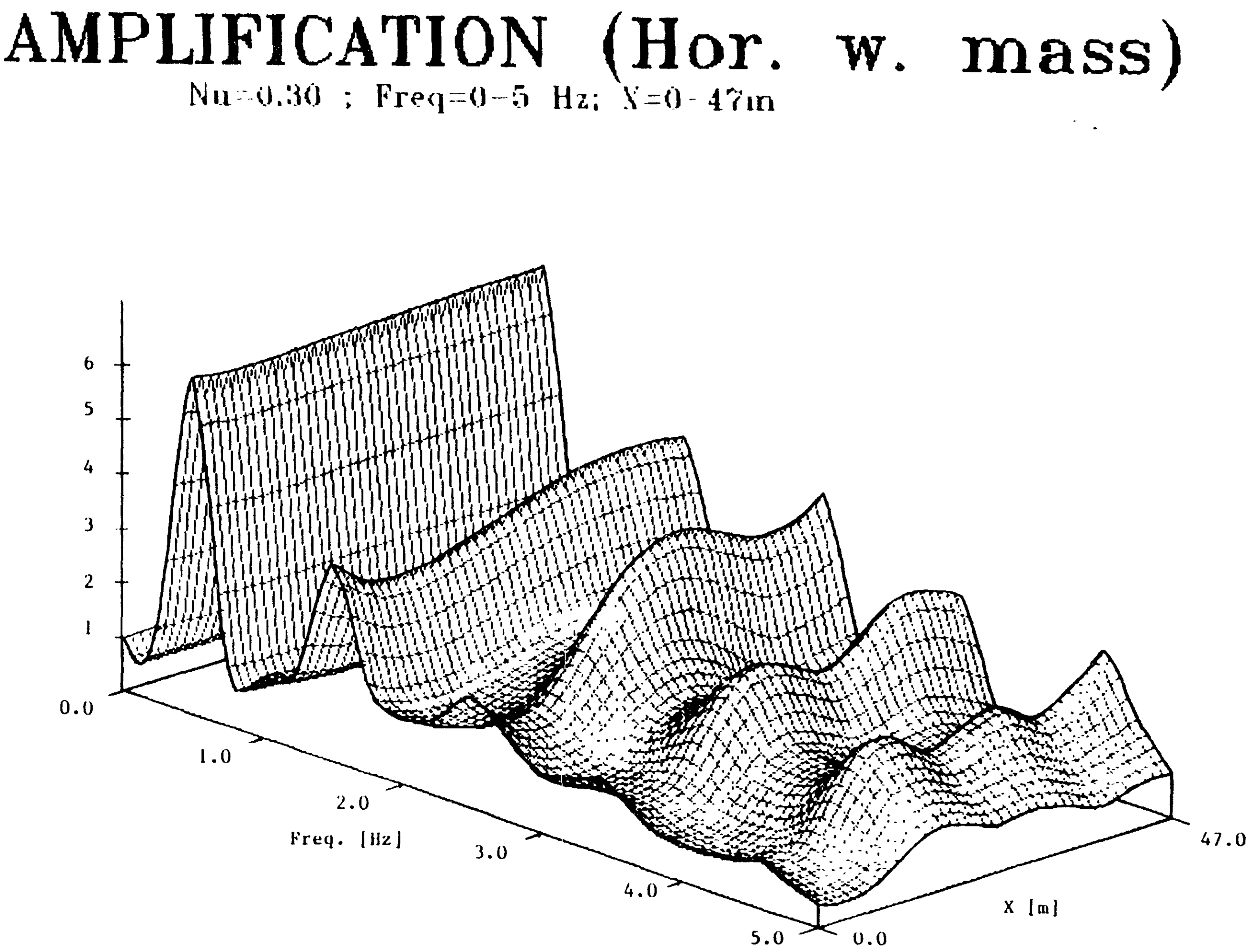
AMPLIFICATION (Hor. w. mass)
Nu=0.30 ; Freq=0-5 Hz; X=0-47m
0.0
1
2
3
4
5
6
1.0
2.0
Freq. [Hz]
3.0
4.0
5.0
0.0
X [m]
47.0

Figure 4.29

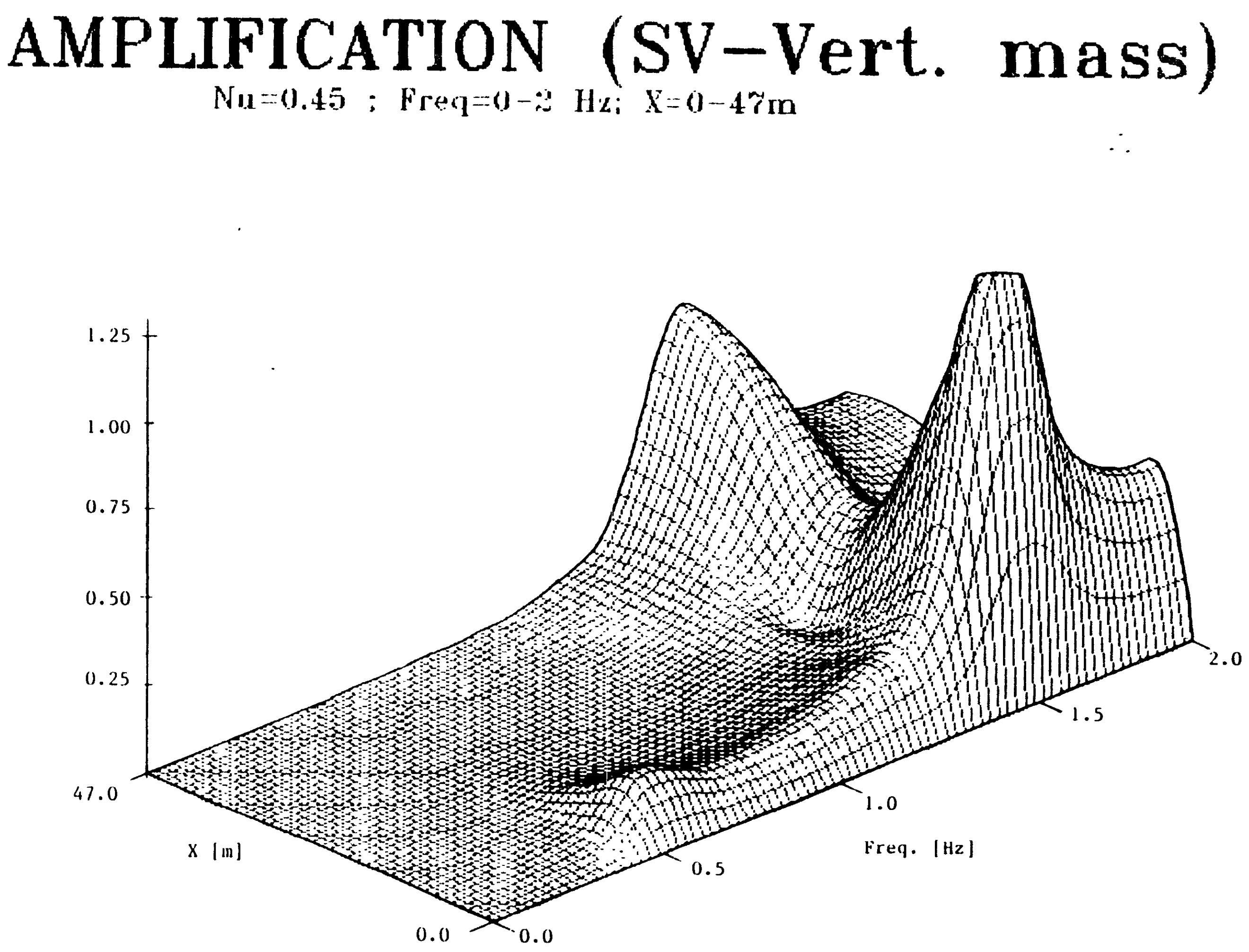

AMPLIFICATION (SV-Vert. mass)

Nu=0.45 ; Freq=0-2 Hz; X=0-47m

Figure 4.30

surface since the tunnel accommodates to the soil motions almost without rotation. For higher frequencies, especially at the natural frequencies of the stratum, larger rotations are induced in the tunnel which translate into greater vertical displacements on the surface. However, if the frequency is increased further, the highly varying displacement profile will introduce less and less rotation in the tunnel, so that the value of the corresponding vertical displacements at the surface will decrease (see fig. 4.31).

For a Poisson's coefficient of 0.45 the P wave celerity, Cp, is about 3.3 times the shear wave celerity Cs; hence the first natural mode of the stratum for vertical displacements occurs for a frequency of 3.3x0.5=1.65 Hz. Figures 4.32–4.35 correspond to vertically propagating P waves; comparing figures 4.33 and 4.35 it can be seen that for this type of waves and in the frequency range of interest, the influence of the rigid tunnel on the amplification of the seismic motion is very small. Only for frequencies on the order of 5 Hz is a substantial deamplification of the motion observed in the region adjacent to the tunnel.

A more interesting case is the excitation of the stratum by SH waves propagating vertically, with soil displacements in the longitudinal direction of the tunnel (anti–plane case). The results for this situation are displayed in figures 4.36–4.39. These figures show that, although for very low frequencies the presence of the tunnel does not produce any substantial change in the amplification of the motion, for frequencies greater than 1 Hz a substancial reduction of the motion is observed near the tunnel. Comparing this case with the one corresponding to SV waves (in–plane case), the higher attenuation in the case of SH waves can be explained by considering the fact that in the in–plane case, the tunnel can rotate to accommodate the differential displacements along the vertical propagation path of the waves, whereas for

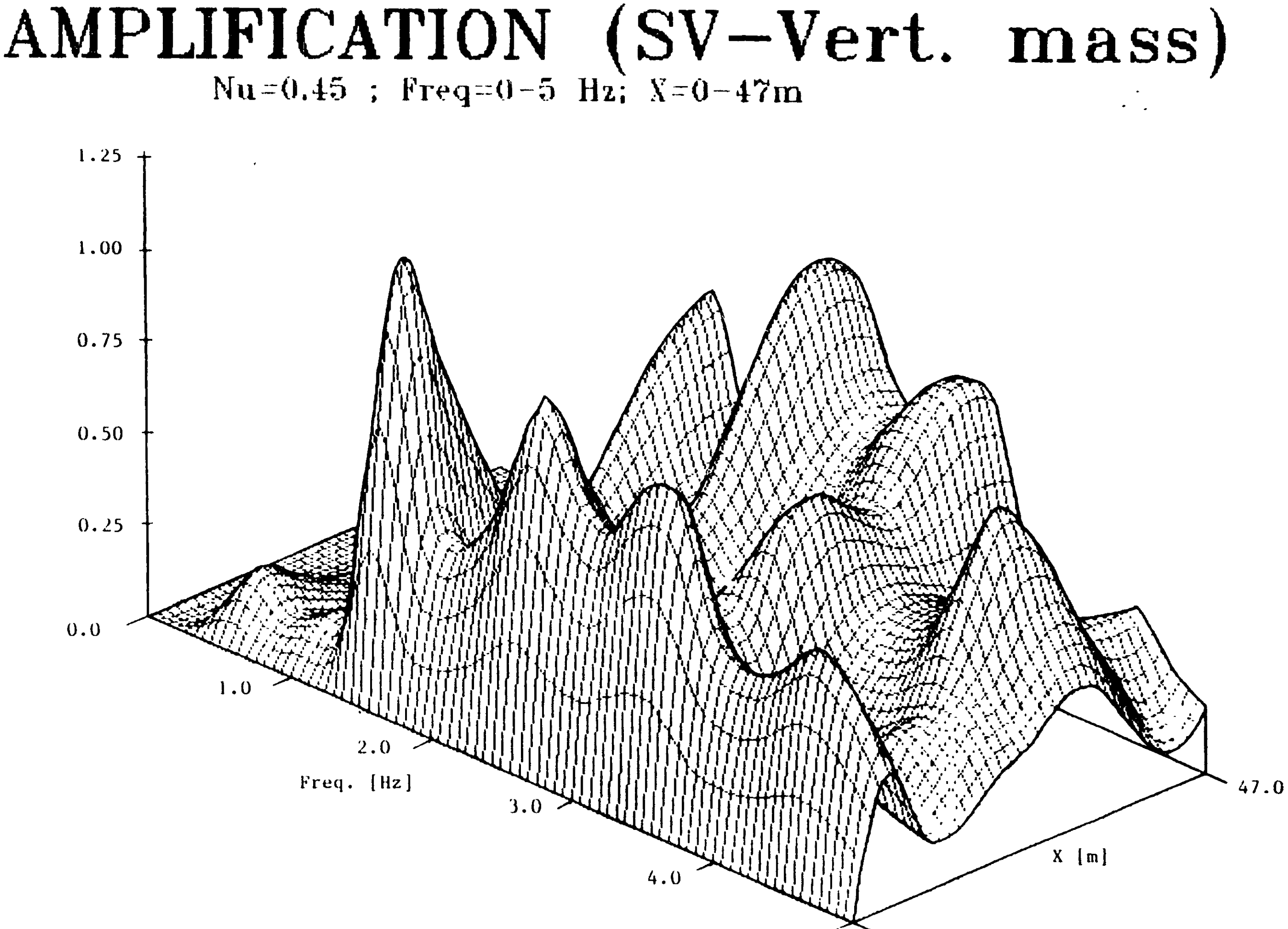
AMPLIFICATION (SV-Vert. mass)
Nu=0.45 ; Freq=0-5 Hz; X=0-47m
1.25
1.00
0.75
0.50
0.25
0.0
1.0
2.0
Freq. [Hz]
3.0
4.0
5.0
0.0
X [m]
47.0

Figure 4.31

Free-Field Amplification (Ver)

Nu=0.45 ; Freq=0.0-2.0 Hz

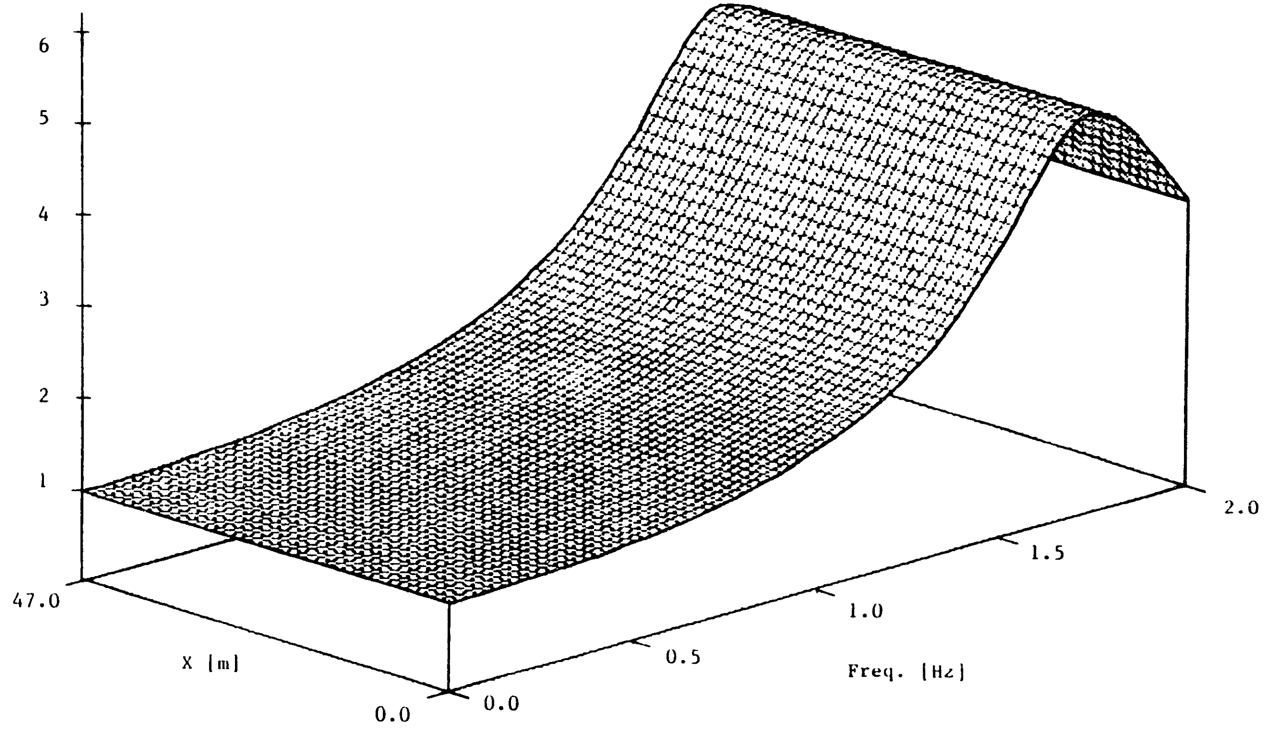

Figure 4.32

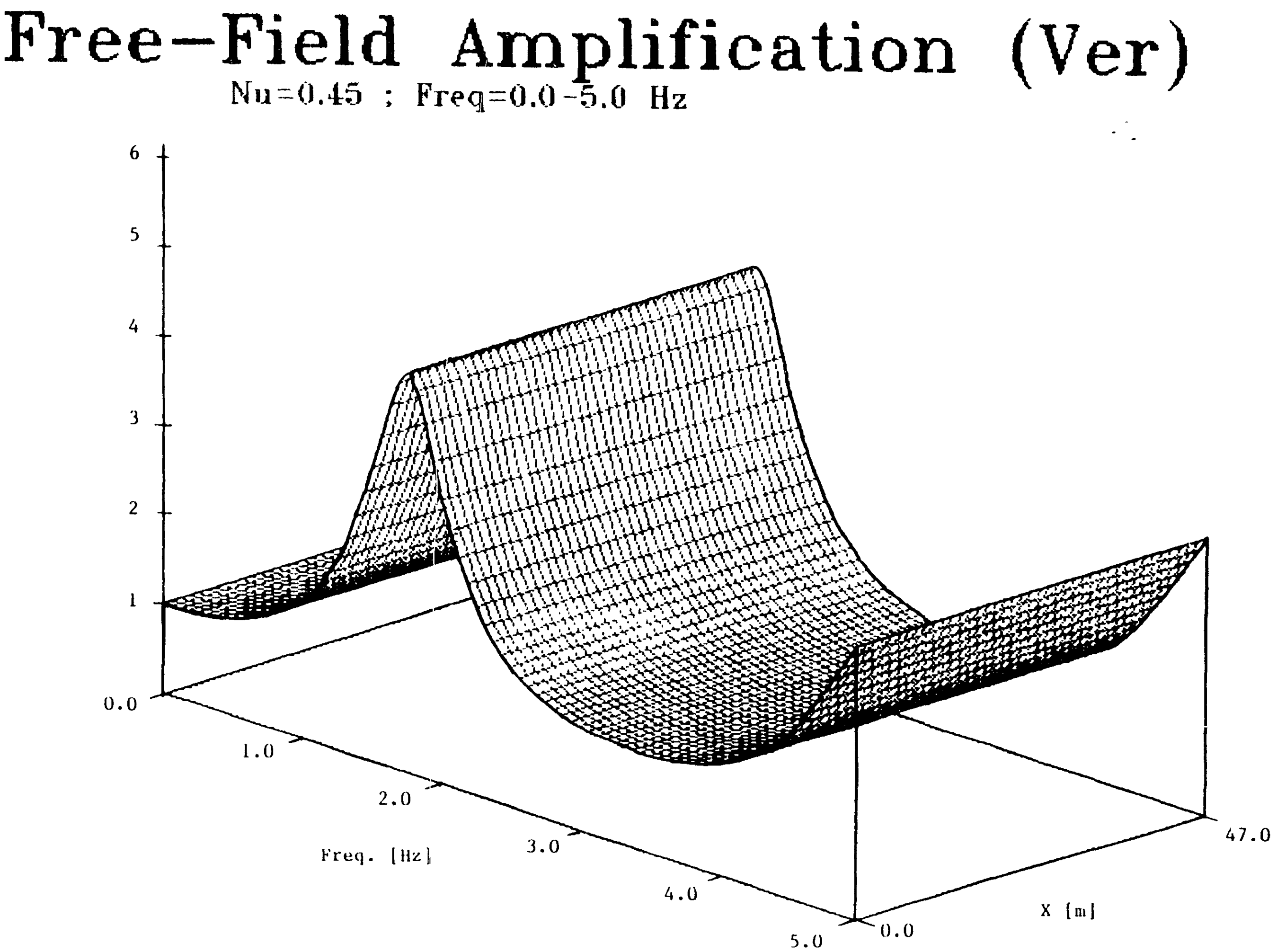
Free-Field Amplification (Ver)
Nu=0.45 ; Freq=0.0-5.0 Hz
6
5
4
3
2
1
0.0
1.0
2.0
3.0
4.0
5.0
Freq. [Hz]
0.0
47.0
X [m]

Figure 4.33

AMPLIFICATION (Ver. w. mass)

Nu=0.45 ; Freq=0-2 Hz; X=0-47m

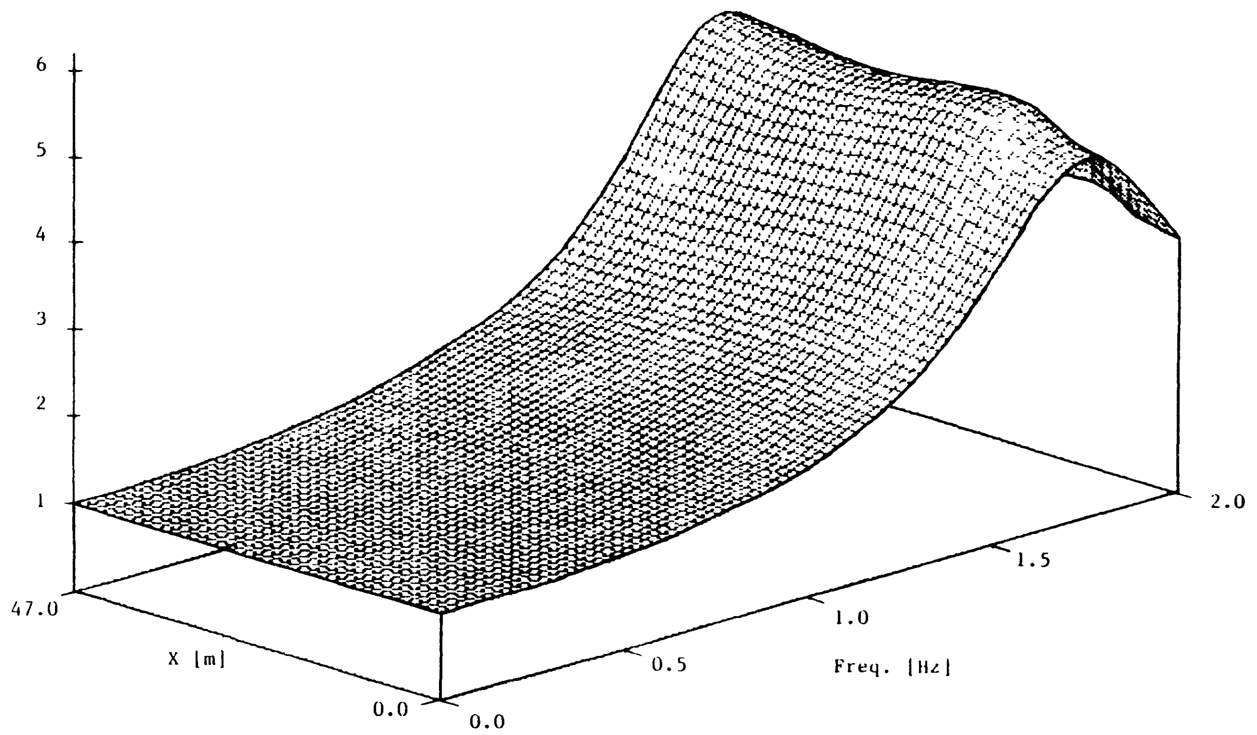

Figure 4.34

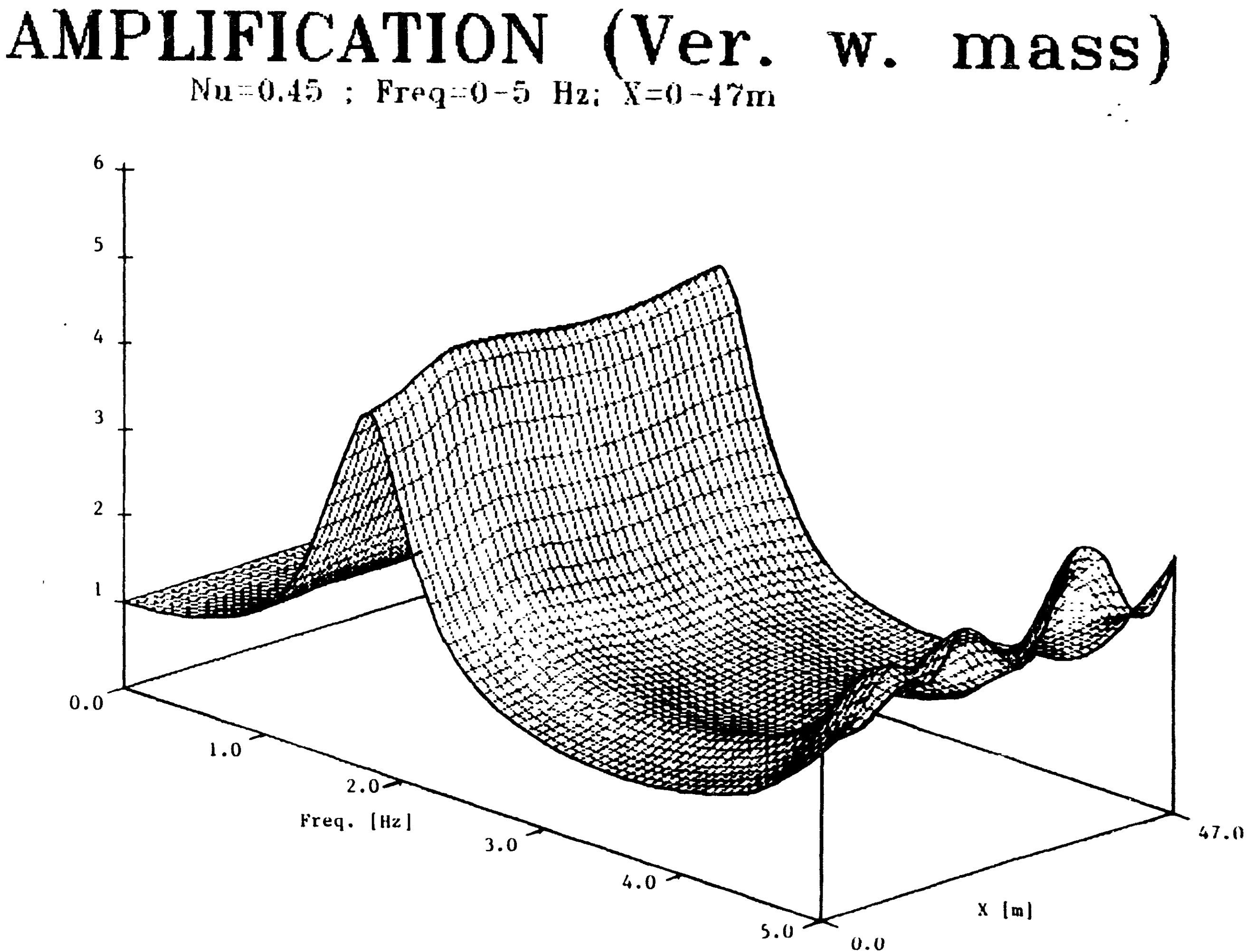
AMPLIFICATION (Ver. w. mass)
Nu=0.45 ; Freq=0-5 Hz; X=0-47m
6
5
4
3
2
1
0.0
1.0
2.0
Freq. [Hz]
3.0
4.0
5.0
0.0
X [m]
47.0

Figure 4.35

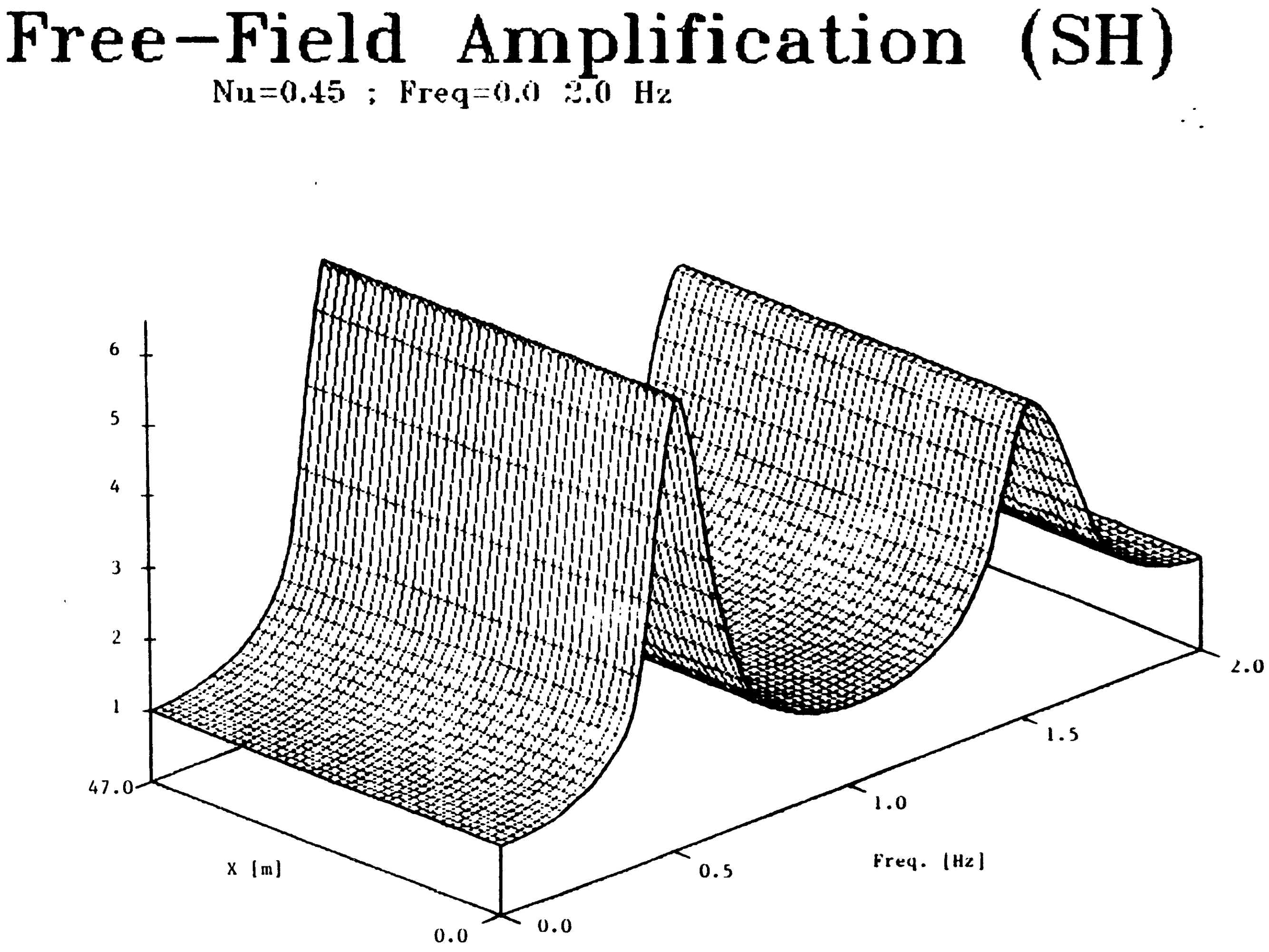
Free-Field Amplification (SH)
Nu=0.45 ; Freq=0.0 2.0 Hz
6
5
4
3
2
1
47.0
X [m]
0.0
0.0
0.5
1.0
1.5
2.0
Freq. [Hz]

Figure 4.36

Free-Field Amplification (SH)

Nu=0.45 ; Freq=0.0-5.0 Hz

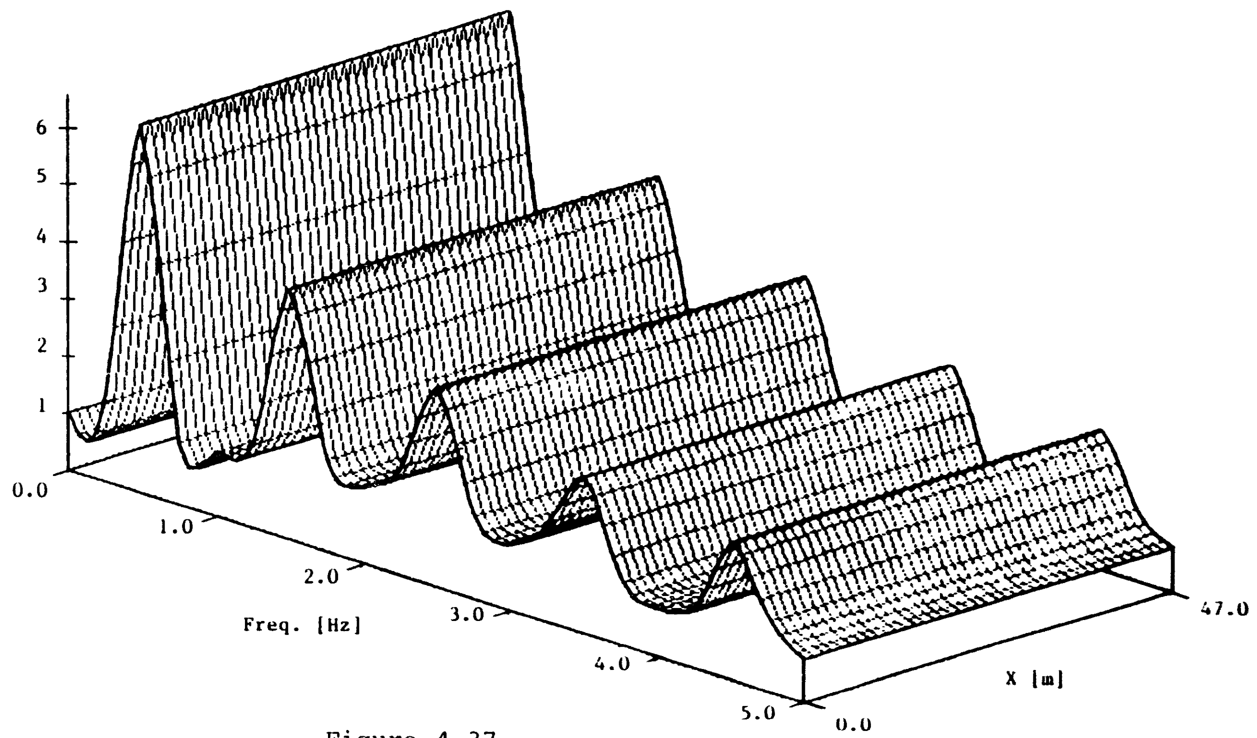

Figure 4.37

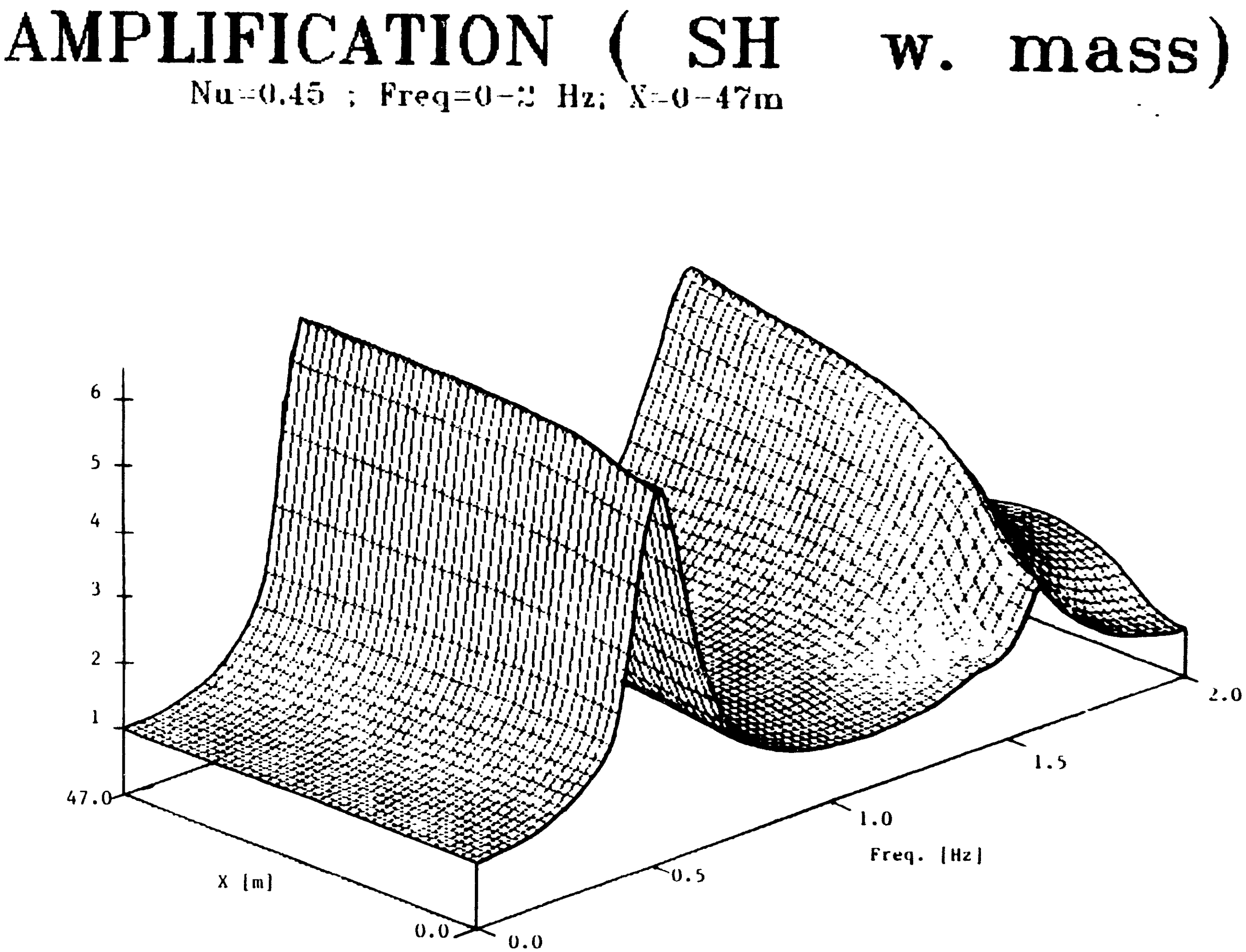
AMPLIFICATION (SH w. mass)
Nu=0.45 ; Freq=0-2 Hz; X=0-47m
6
5
4
3
2
1
47.0
X [m]
0.0
0.0
0.5
1.0
1.5
2.0
Freq. [Hz]

Figure 4.38

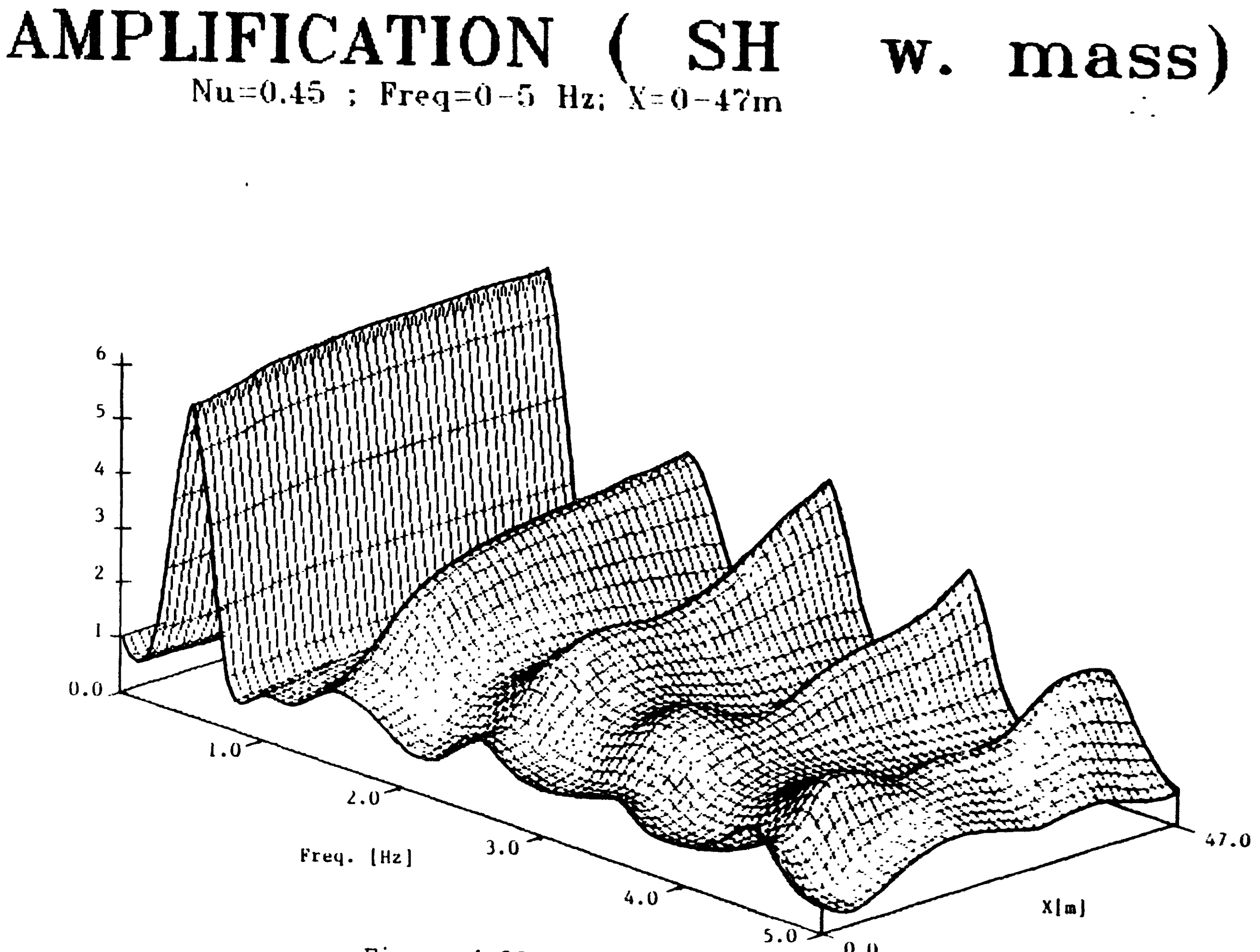
AMPLIFICATION (SH w. mass)
Nu=0.45 ; Freq=0-5 Hz; X=0-47m
6
5
4
3
2
1
0.0
1.0
2.0
3.0
4.0
5.0
Freq. [Hz]
0.0
47.0
X[m]

Figure 4.39

anti–plane motions, it cannot.

4.3.3 Ground Motion Results

In the previous section, the influence of a rigid tunnel on the seismic ground motion at the surface was studied for various wave types and frequencies of excitation. In this section we shall take into account the actual frequency content of the motions observed in order to assess the possible effects of the subway tunnel during a real earthquake. Three different observed motions are examined: the records obtained at the SCT station, Tacubaya station (TACY) and Viveros station (SXVI). The motions observed at TACY and SXVI are input at the base of the stratum at the SCT station location. An approximate measure of the maximum amplification of the motion as a function of the distance to the tunnel is obtained by computing the root mean square value of the motion on the surface, as a function of the distance to the tunnel. This is achieved by computing a normalized Root–Mean–Square (RMS) of the amplification function, T(f,x), multiplied by the amplitude of the motion at each frequency, F(f); f being the frequency of the motion and x representing the horizontal distance from the axis of the tunnel. T(f,x) corresponds to the transfer function from the base of the stratum to the surface at a distance x from the tunnel, and $T(f,\infty)$ is the same transfer function in the free–field (no tunnel present). Hence, when considering the motion recorded at the SCT station, $\frac{F(f)}{T(f,\infty)}$ represents the frequency contents of the corresponding motion observed at the base of the stratum, and in this case the following expression is used:

$$\mathrm{RMS}(x) = \sqrt{\frac{\int |T(f,x)*F(f)/T(f,\infty)|^2 \, df}{\int |F(f)|^2 \, df}} \qquad (4.1)$$

For the other motions the formula becomes:

$$\mathrm{RMS}(x)=\sqrt{\frac{\int |T(f,x)*F(f)|^2 df}{\int |T(f,\infty)*F(f)|^2 \, df}} \tag{4.2}$$

The numerator represents a measure of the severity of the motion at a distance x, while the denominator evaluates the corresponding value for the free–field situation.

The expressions in (4.1) and (4.2) are evaluated for different seismic records and types of waves. The results are displayed in figures 4.40–4.51 and show that some reduction in the amplitude of the motion is discernible near the tunnel in the case of incident shear waves. However, this reduction is very small, on the order of 4–8%, because the energy contents of the motions are concentrated in the range of 0–2 Hz, in which the tunnel does not influence significantly the surrounding motion.

When the motion observed at the TACY station is used instead as input at the base of the stratum (figs. 4.44 and 4.45), a small amplification results for points distant about 40 m of the tunnel. This is due to the higher frequency contents of this motion when compared with the one observed at the SCT station (taking deconvolution into account). For vertically incident P–waves (figs 4.46 and 4.47), the resulting motion has almost the same amplitude as in the free–field case, since only for much higher frequencies has the tunnel any significant effect.

In order to obtain a measure of the severity of the vertical component of the motion at the surface induced by the presence of the tunnel (as a result of its rotation),

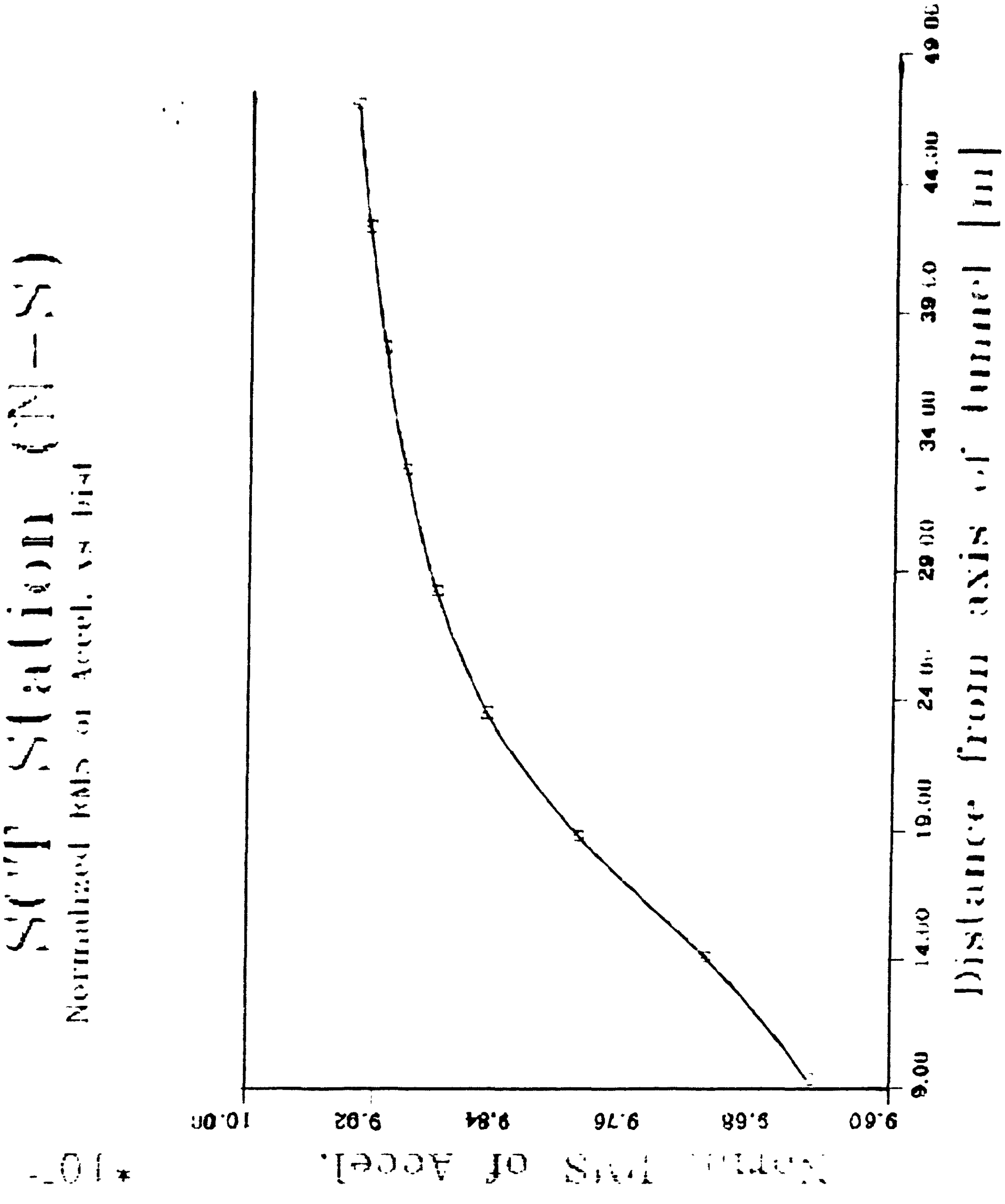
SCT Station (N-S)
Normalized RMS of Accel. vs Dist
Norm. RMS of Accel.
*10⁻¹
10.00
9.92
9.84
9.76
9.68
9.60
9.00
14.00
19.00
24.00
29.00
34.00
39.00
44.00
49.00
Distance from axis of tunnel [m]

Figure 4.40

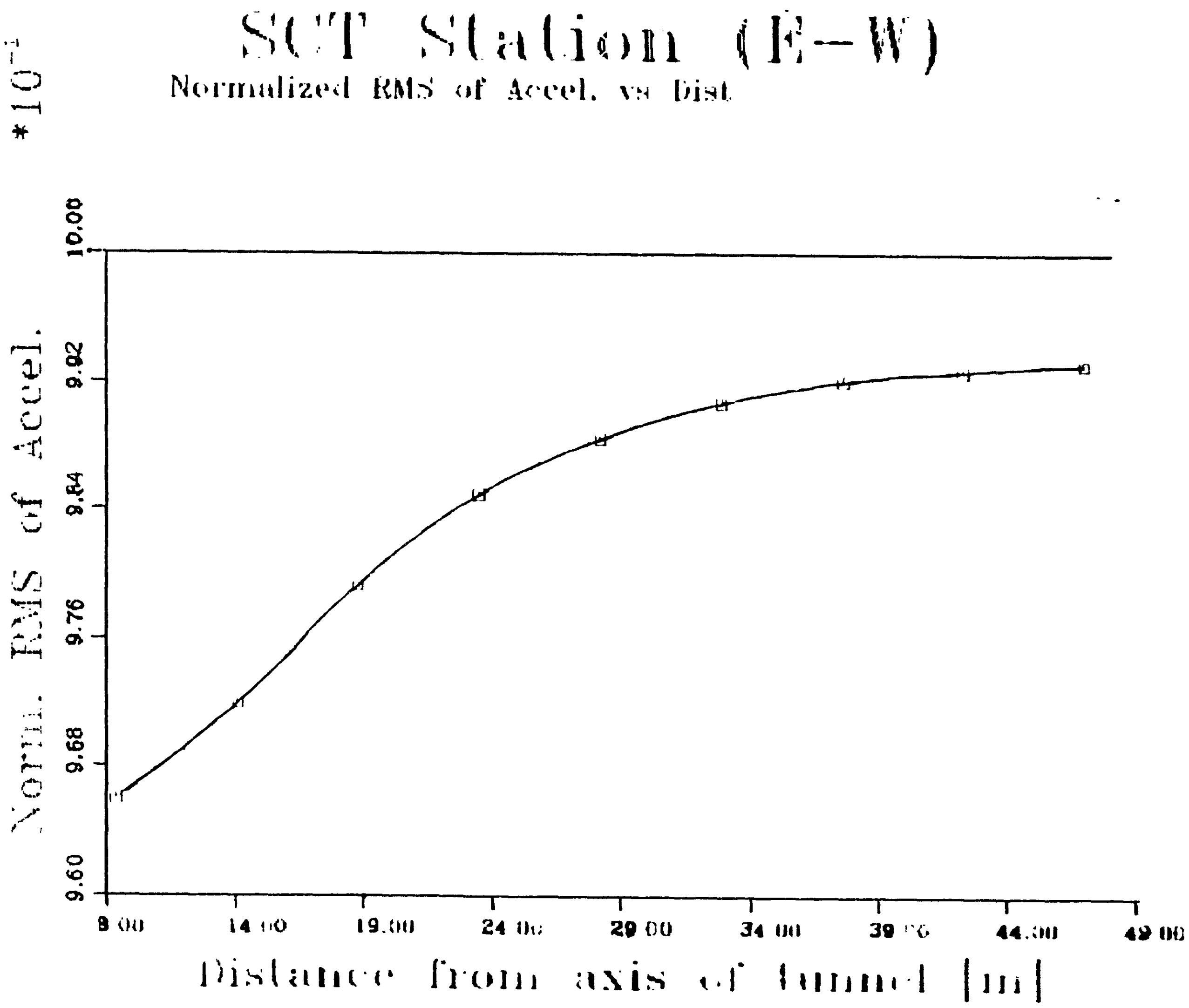
SCT Station (E-W)
Normalized RMS of Accel. vs Dist.
*10^-1
Norm. RMS of Accel.
10.00
9.92
9.84
9.76
9.68
9.60
9.00
14.00
19.00
24.00
29.00
34.00
39.00
44.00
49.00
Distance from axis of tunnel [m]

Figure 4.41

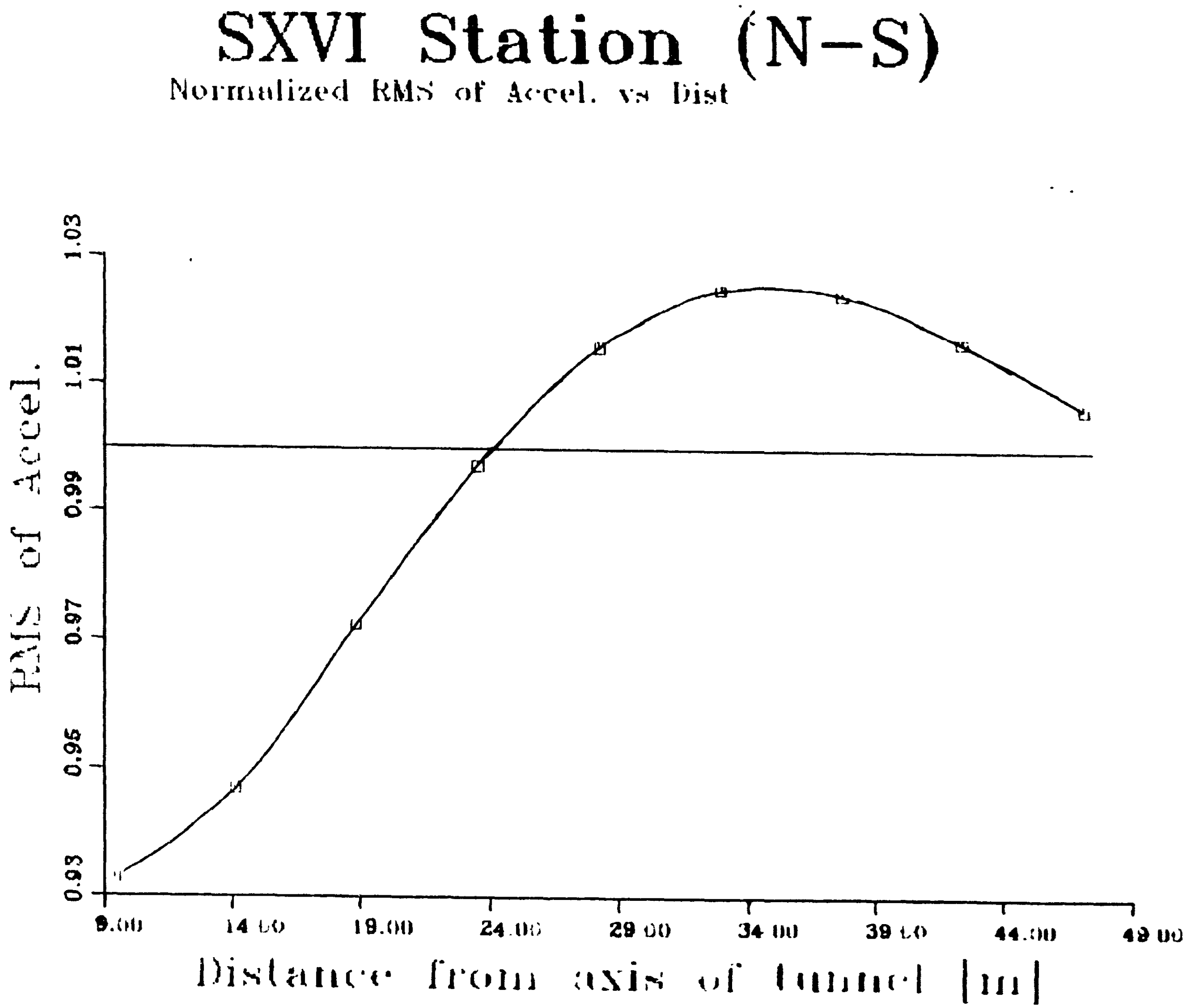
SXVI Station (N-S)
Normalized RMS of Accel. vs Dist
RMS of Accel.
1.03
1.01
0.99
0.97
0.95
0.93
9.00
14.00
19.00
24.00
29.00
34.00
39.00
44.00
49.00
Distance from axis of tunnel [m]

Figure 4.42

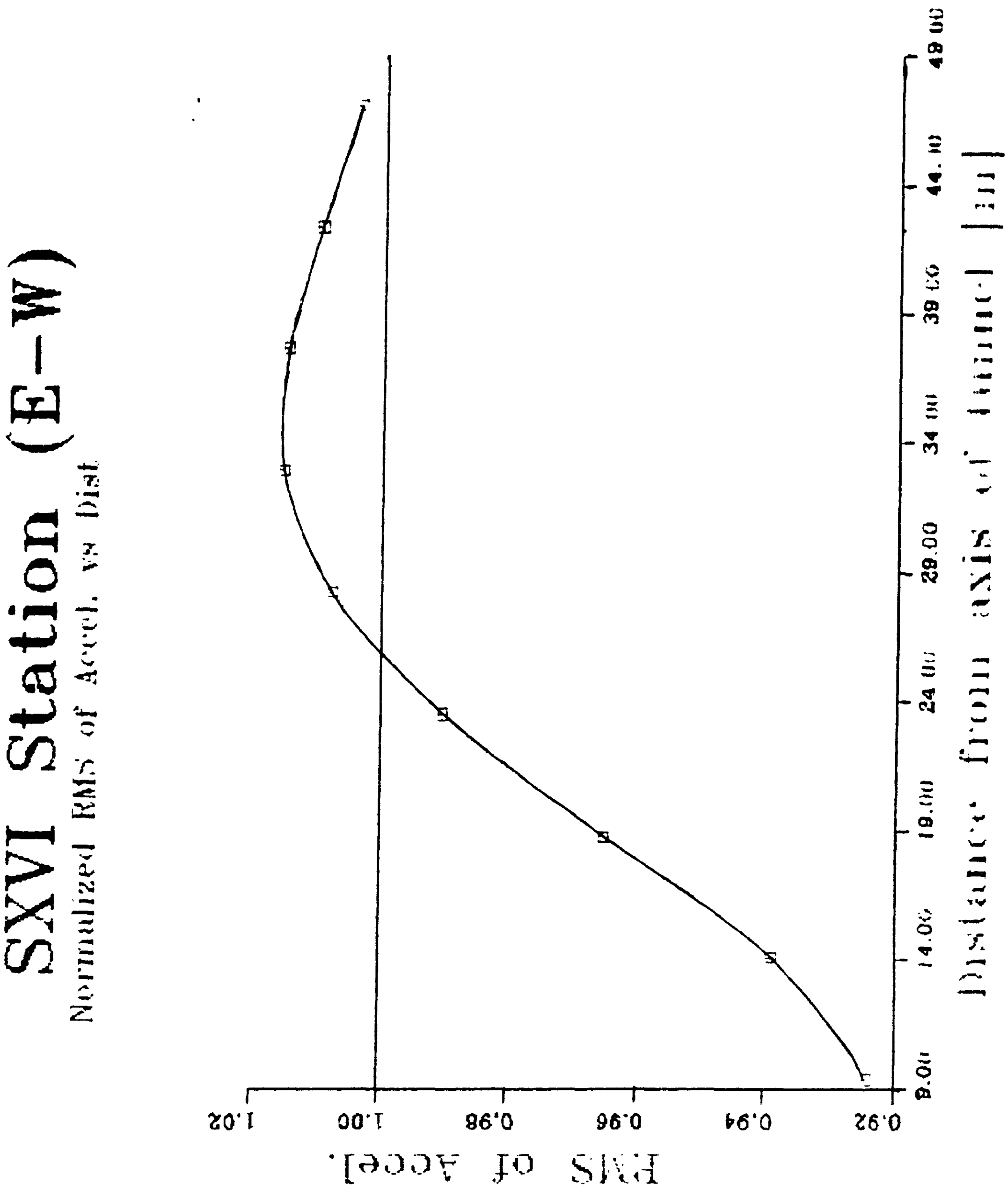

SXVI Station (E-W)
Normalized RMS of Accel. vs Dist.
RMS of Accel.
0.92
0.94
0.96
0.98
1.00
1.02
9.00
14.00
19.00
24.00
29.00
34.00
39.00
44.00
49.00
Distance from axis of tunnel [m]

Figure 4.43

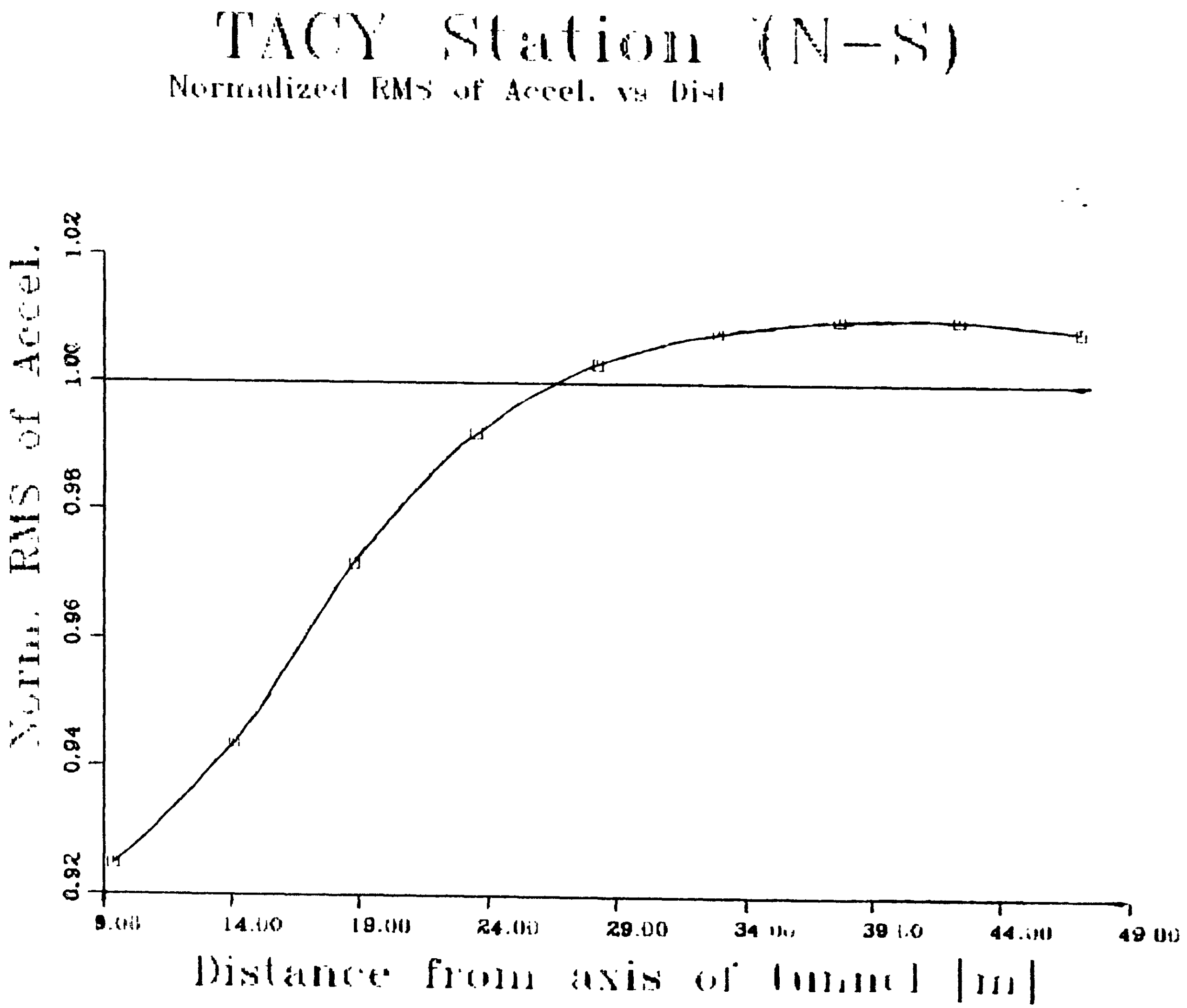
TACY Station (N-S)
Normalized RMS of Accel. vs Dist
Norm. RMS of Accel.
0.92
0.94
0.96
0.98
1.00
1.02
9.00
14.00
19.00
24.00
29.00
34.00
39.00
44.00
49.00
Distance from axis of tunnel [m]

Figure 4.44

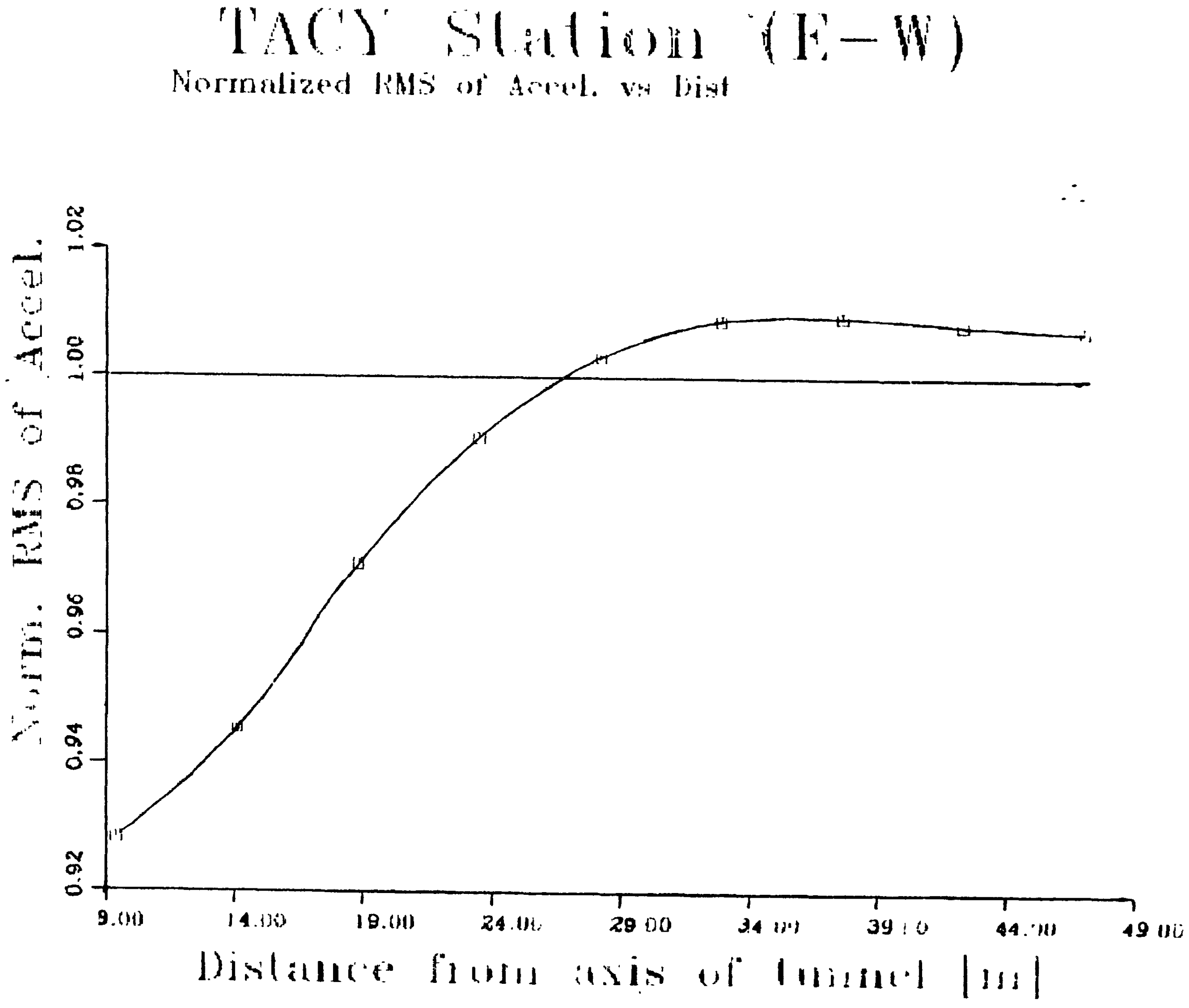
TACY Station (E-W)
Normalized RMS of Accel. vs Dist
Norm. RMS of Accel.
1.02
1.00
0.98
0.96
0.94
0.92
9.00
14.00
19.00
24.00
29.00
34.00
39.00
44.00
49.00
Distance from axis of tunnel [m]

Figure 4.45

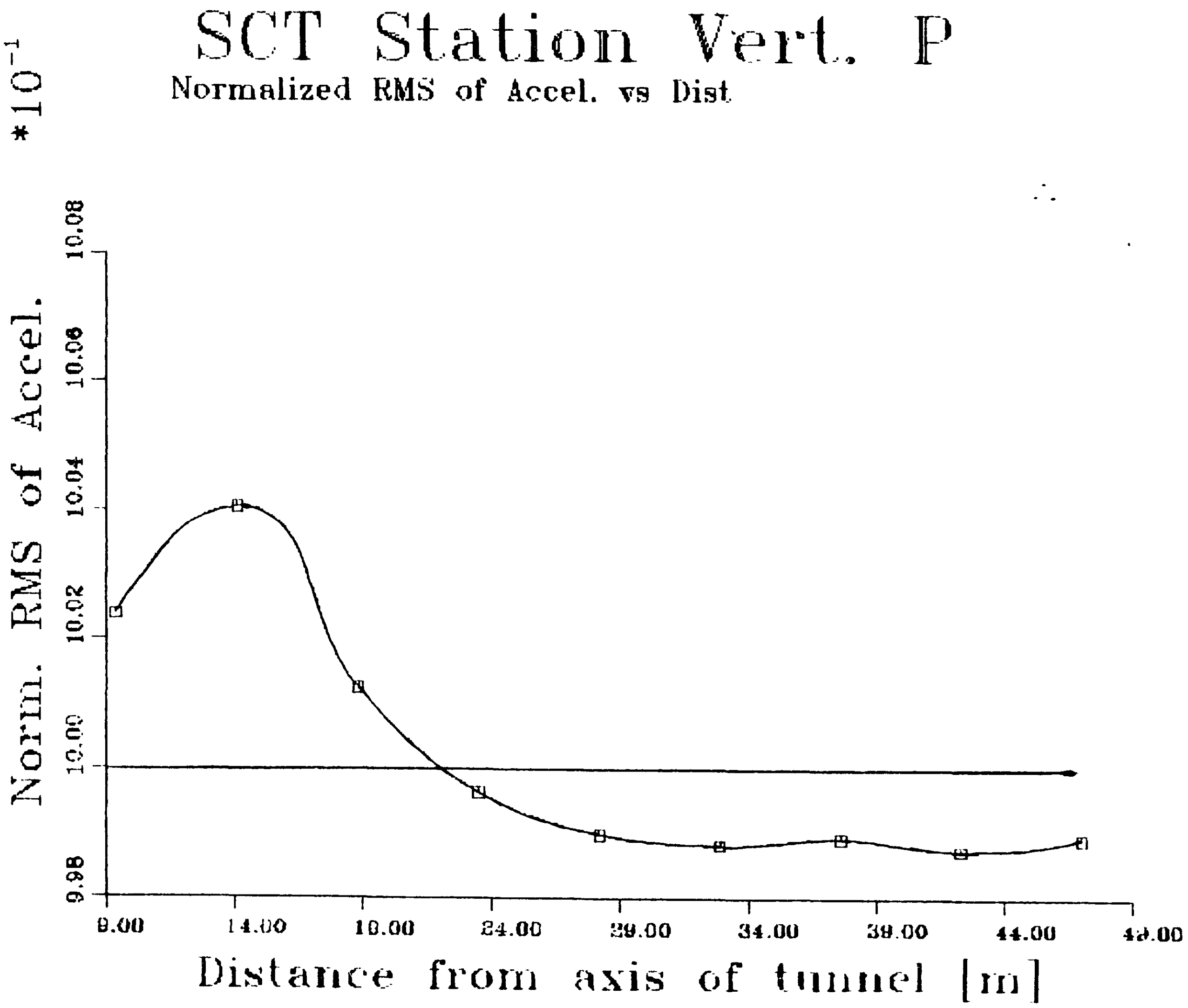
SCT Station Vert. P
Normalized RMS of Accel. vs Dist
*10^-1
Norm. RMS of Accel.
10.08
10.06
10.04
10.02
10.00
9.98
9.00
14.00
19.00
24.00
29.00
34.00
39.00
44.00
49.00
Distance from axis of tunnel [m]

Figure 4.46

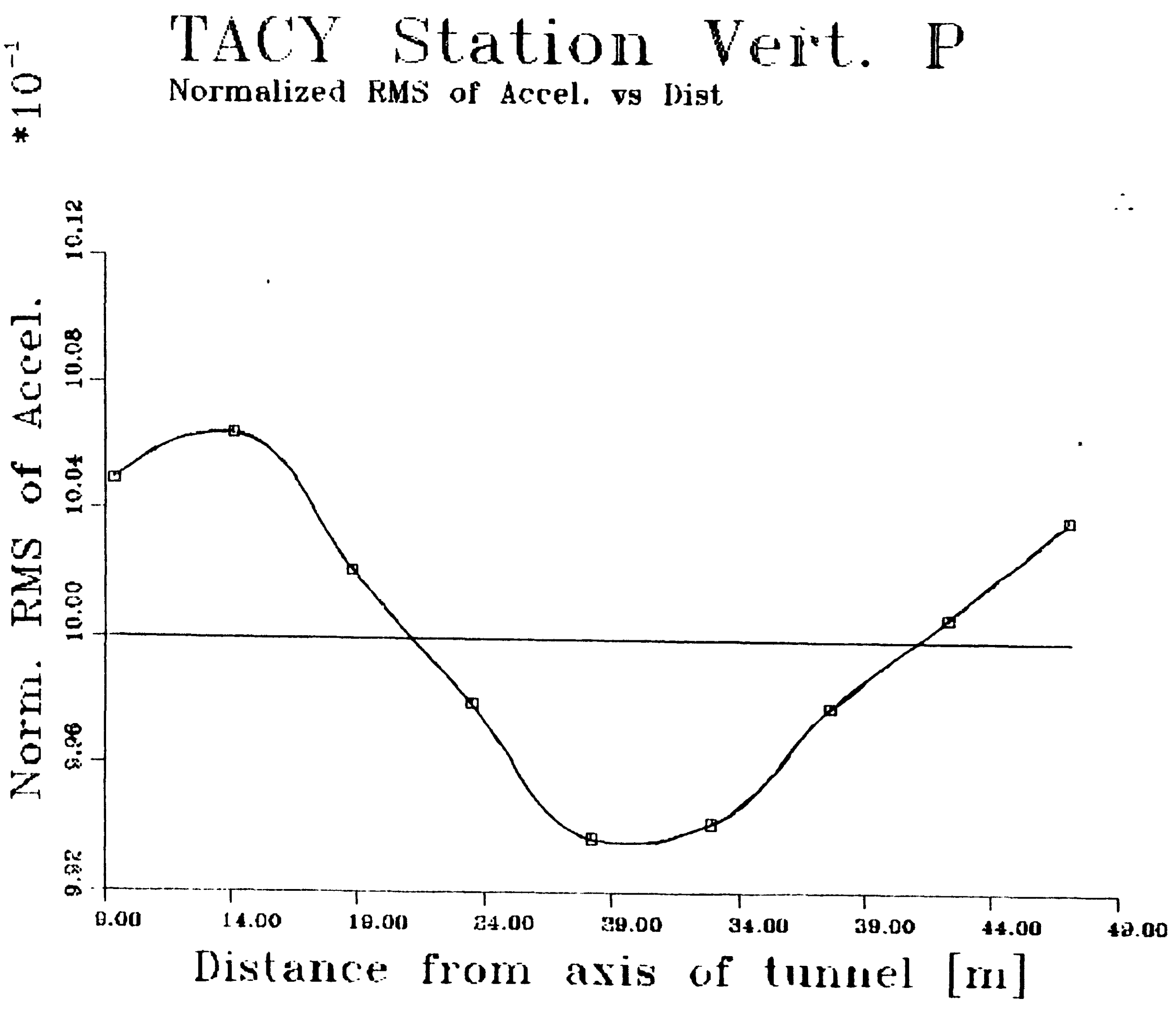
TACY Station Vert. P
Normalized RMS of Accel. vs Dist
*10^-1
Norm. RMS of Accel.
9.92
9.96
10.00
10.04
10.08
10.12
9.00
14.00
19.00
24.00
29.00
34.00
39.00
44.00
49.00
Distance from axis of tunnel [m]

Figure 4.47

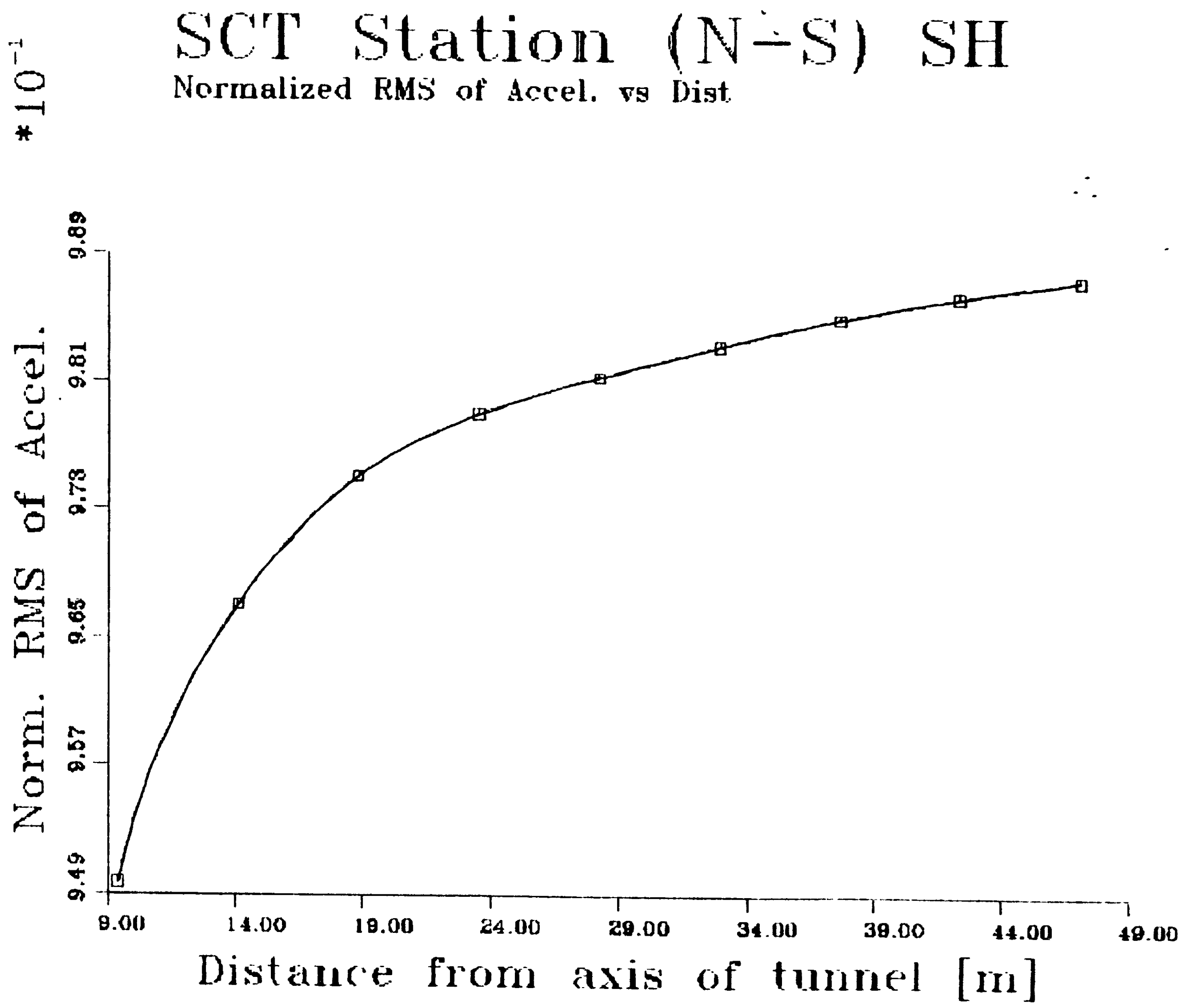
SCT Station (N-S) SH
Normalized RMS of Accel. vs Dist
*10⁻¹
Norm. RMS of Accel.
9.49
9.57
9.65
9.73
9.81
9.89
9.00
14.00
19.00
24.00
29.00
34.00
39.00
44.00
49.00
Distance from axis of tunnel [m]

Figure 4.48

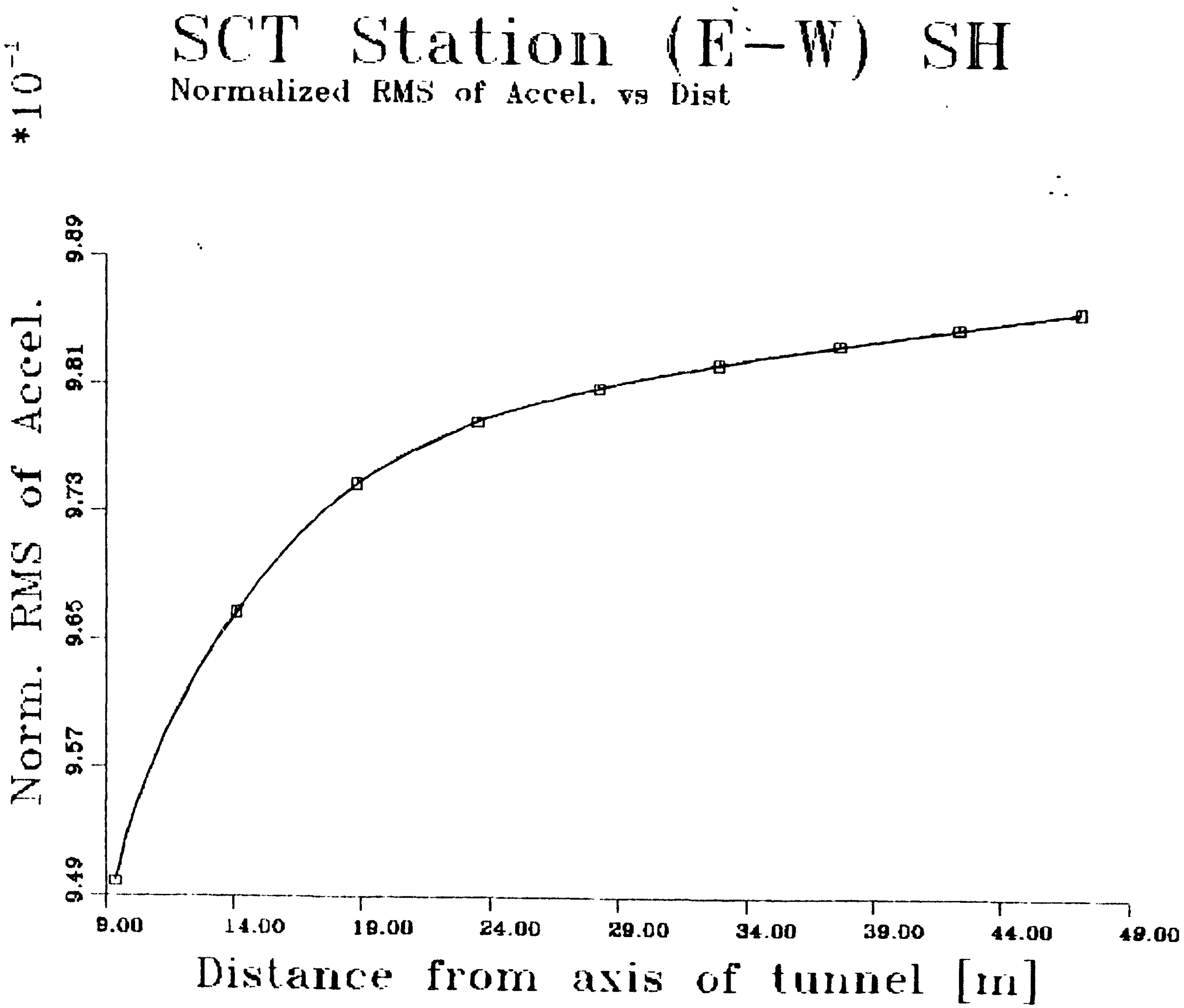
SCT Station (E-W) SH
Normalized RMS of Accel. vs Dist
*10^-1
Norm. RMS of Accel.
9.49
9.57
9.65
9.73
9.81
9.89
9.00
14.00
19.00
24.00
29.00
34.00
39.00
44.00
49.00
Distance from axis of tunnel [m]

Figure 4.49

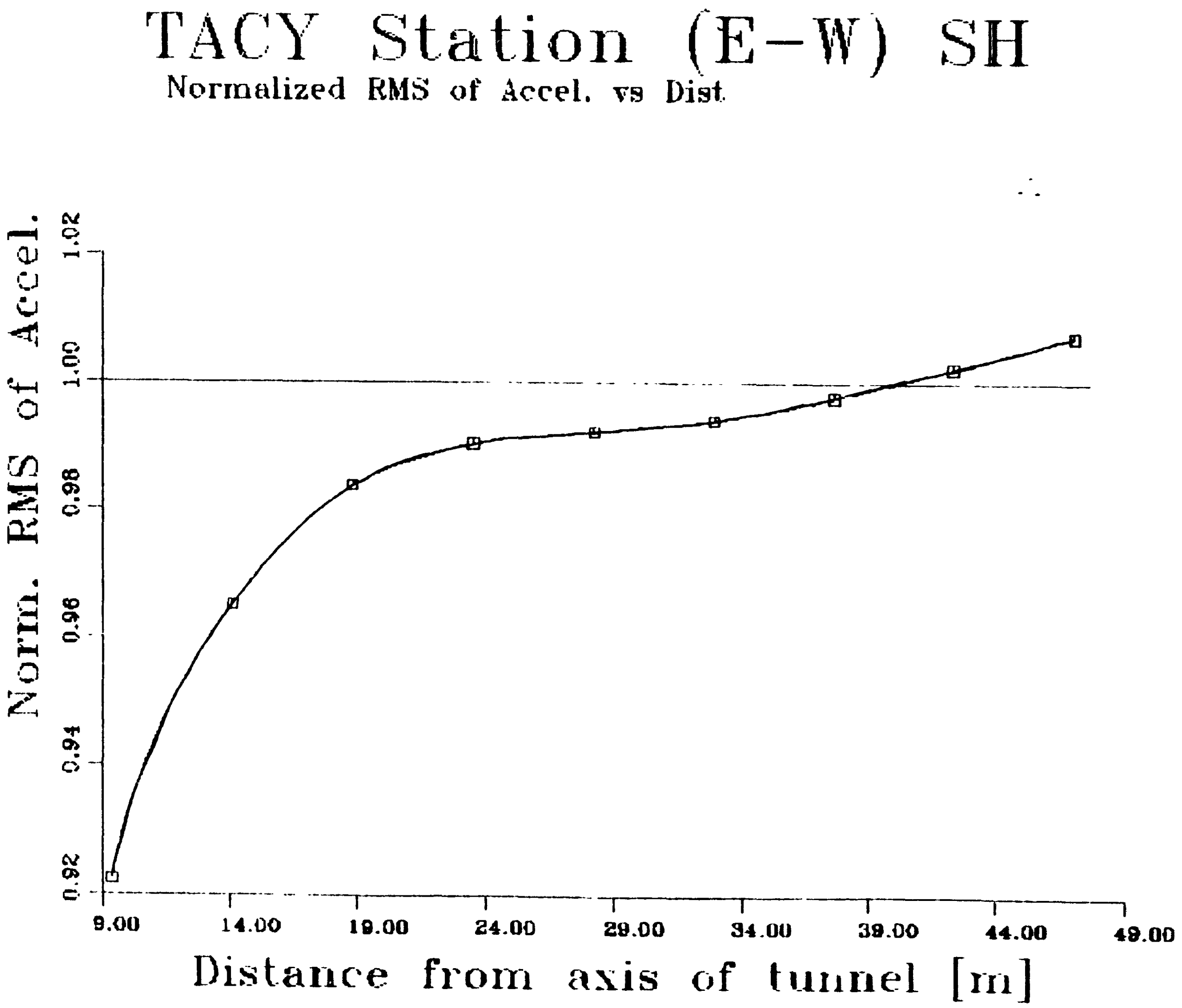
TACY Station (E-W) SH
Normalized RMS of Accel. vs Dist.
Norm. RMS of Accel.
1.02
1.00
0.98
0.96
0.94
0.92
9.00
14.00
19.00
24.00
29.00
34.00
39.00
44.00
49.00
Distance from axis of tunnel [m]

Figure 4.50

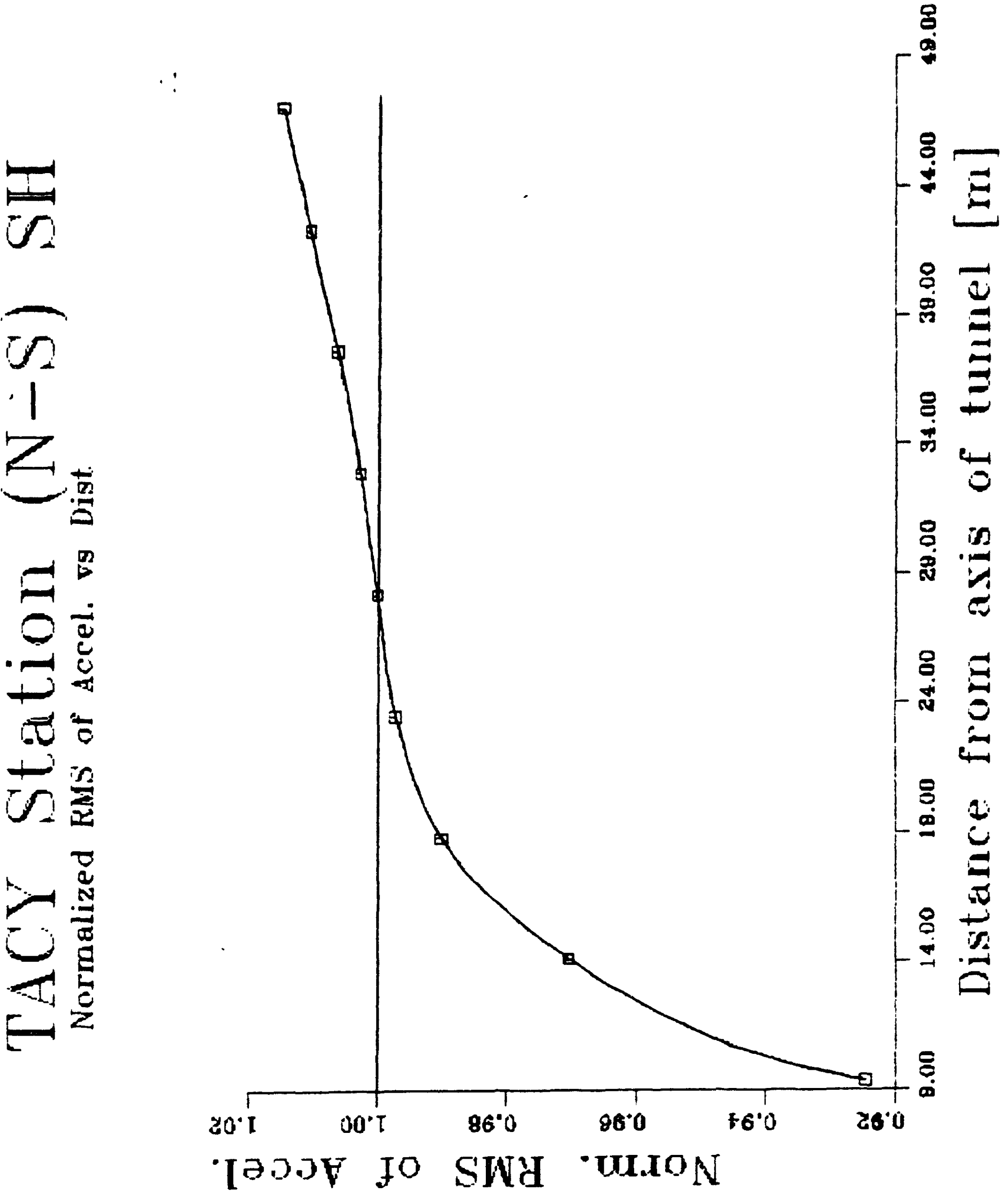
TACY Station (N-S) SH
Normalized RMS of Accel. vs Dist
Norm. RMS of Accel.
0.92
0.94
0.96
0.98
1.00
1.02
9.00
14.00
19.00
24.00
29.00
34.00
39.00
44.00
49.00
Distance from axis of tunnel [m]

Figure 4.51

formulas 4.1 and 4.2 are evaluated again for the case of vertically incident SV waves, but replacing T(f,x) by the transfer function corresponding to the vertical ccomponent, Tv(f,x). The resulting formulas give an indication of the magnitude of the vertical motion relative to the free–field horizontal motion at the surface, for a given seismic motion. Figures 4.52–4.55 show the values obtained using the seismic records at SCT and TACY stations. The vertical motion induced is maximum near the edge of the tunnel, with an intensity of about 6% of the horizontal motion if the SCT records are used; if the motion recorded at the TACY station is used instead, the resulting vertical motion is much higher, approaching 16% of the horizontal motion. This is due, again, to the higher frequency content in the motion recorded at the TACY station, which produces a more important rotation of the tunnel. The variation in magnitude of the vertical motion with distance to the tunnel could, in principle, affect nearby structures.

4.3.4 Motion Due to an Incident Wavelet

Another perspective on the effects of the underground tunnel on seismic motions can be gained by studying the scattering of waves associated with pulses of short duration and narrowly banded. A Ricker wavelet was chosen for this purpose, since it decays very rapidly both in time and frequency. Its variation in time and frequency which are given, respectively, by equations 3.29 and 3.30,are displayed on figures 3.16 and 3.17.

By convolving $F(\omega)$ with the transfer functions corresponding to the rotations induced by the tunnel, the time history of these rotations are obtained. The results are displayed in figure 4.56; it takes approximately 0.8 secs for the rotation to reach its maximum, which corresponds to the value of t_s plus the time that it takes for the wavelet to arrive at the surface ($\cong$ 0.5 sec); also, it can be seen that the tunnel executes

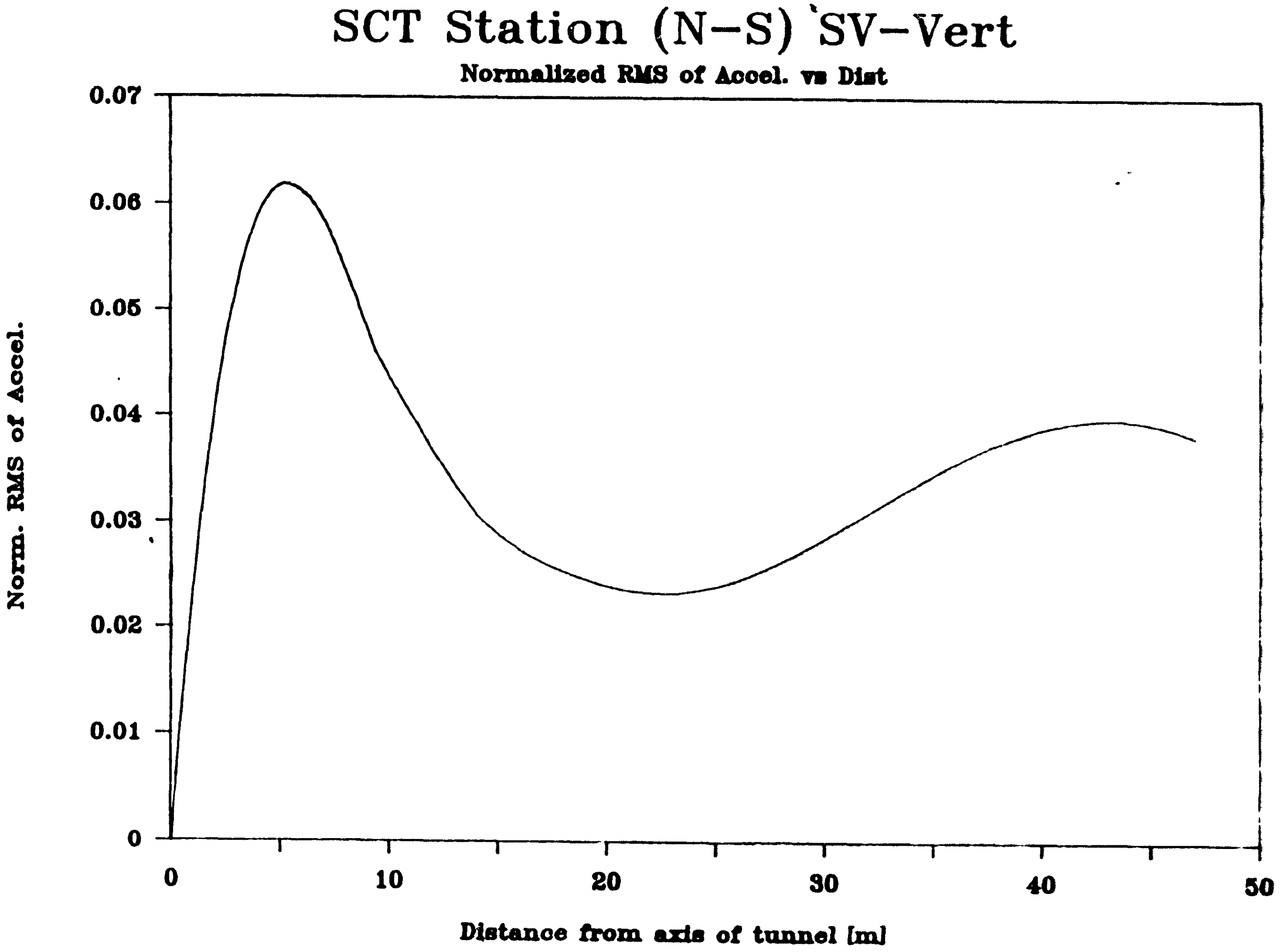
SCT Station (N-S) SV-Vert
Normalized RMS of Accel. vs Dist
Norm. RMS of Accel.
0.07
0.06
0.05
0.04
0.03
0.02
0.01
0
0
10
20
30
40
50
Distance from axis of tunnel [m]

Figure 4.52

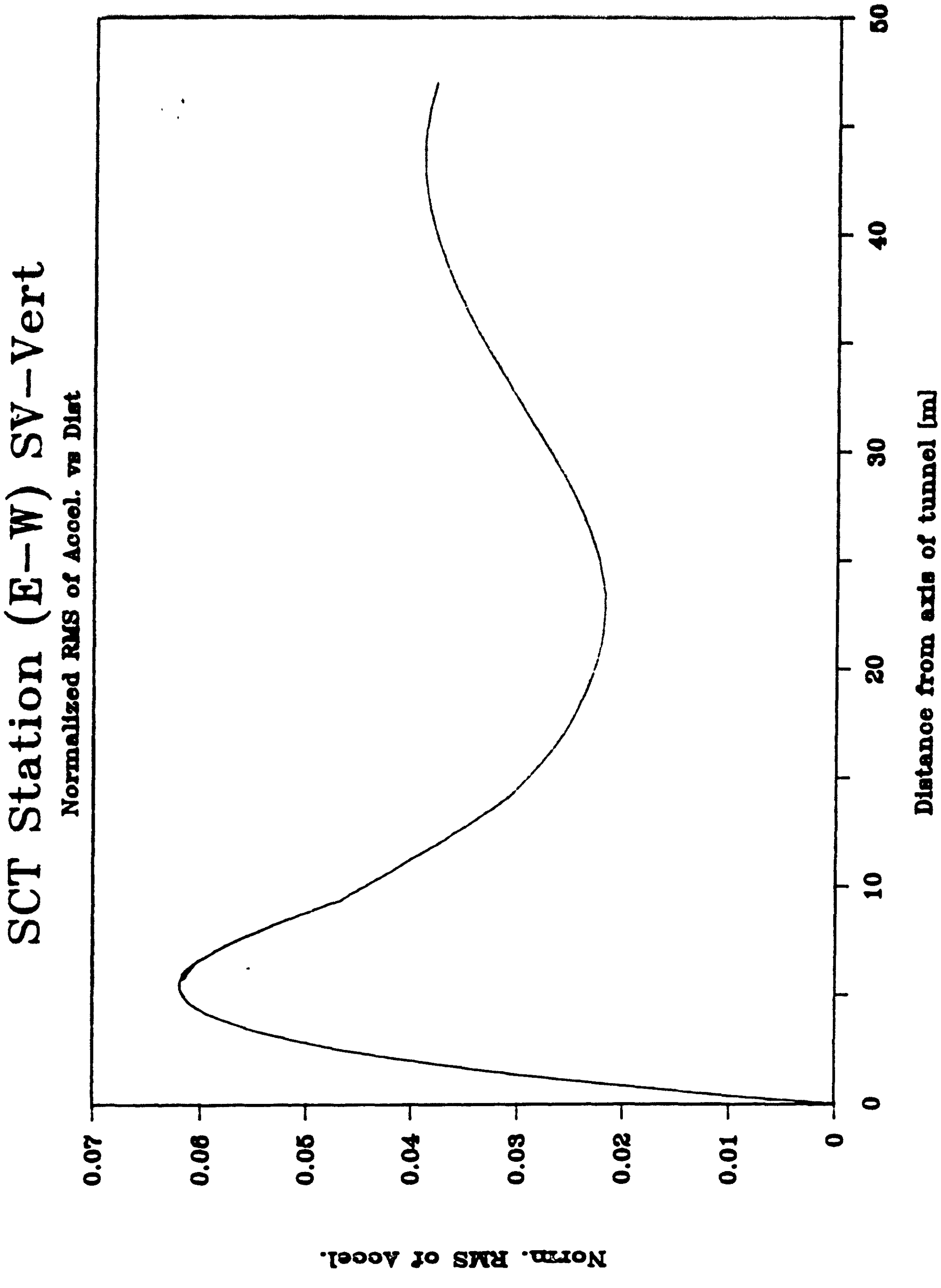
SCT Station (E—W) SV—Vert
Normalized RMS of Accel. vs Dist
Norm. RMS of Accel.
0.07
0.06
0.05
0.04
0.03
0.02
0.01
0
Distance from axis of tunnel [m]
0
10
20
30
40
50

Figure 4.53

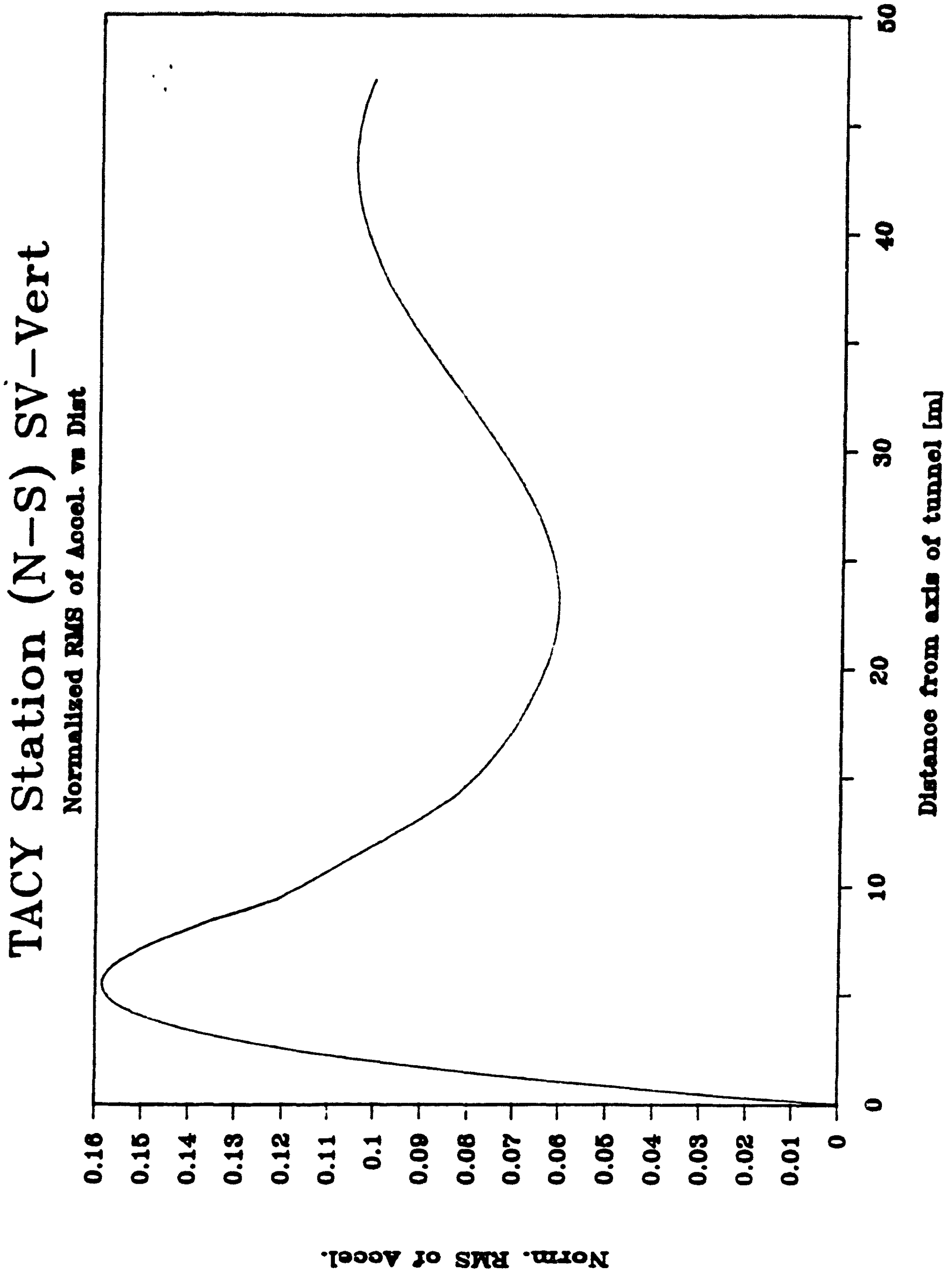
TACY Station (N-S) SV-Vert
Normalized RMS of Accel. vs Dist
Norm. RMS of Accel.
0.16
0.15
0.14
0.13
0.12
0.11
0.1
0.09
0.08
0.07
0.06
0.05
0.04
0.03
0.02
0.01
0
0
10
20
30
40
50
Distance from axis of tunnel [m]

Figure 4.54

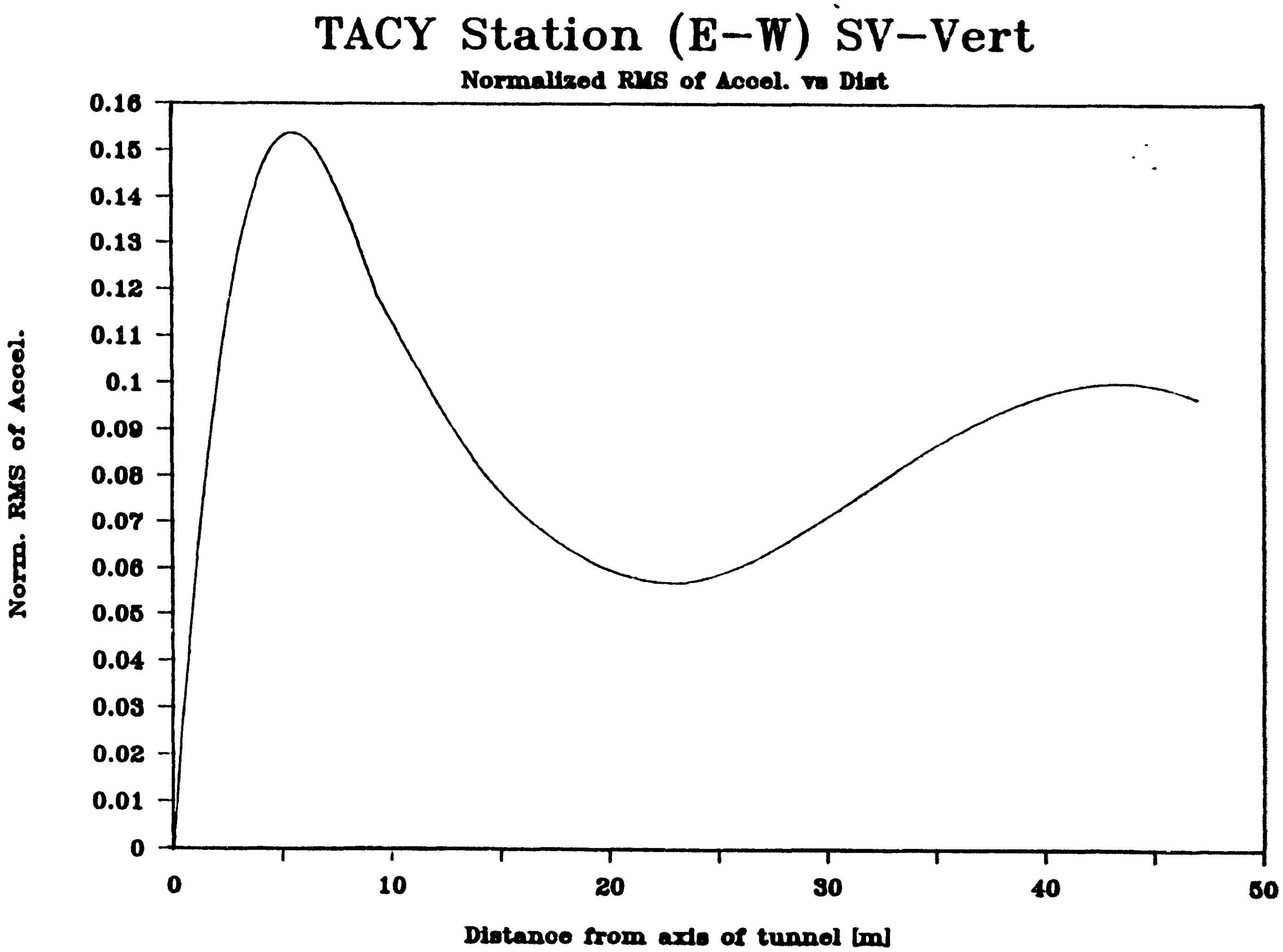
TACY Station (E–W) SV–Vert
Normalized RMS of Accel. vs Dist
Norm. RMS of Accel.
0.16
0.15
0.14
0.13
0.12
0.11
0.1
0.09
0.08
0.07
0.06
0.05
0.04
0.03
0.02
0.01
0
0
10
20
30
40
50
Distance from axis of tunnel [m]

Figure 4.55

multiple rotations, since the energy of the wavelet gets trapped in the stratum and is reflected multiple times at the surface and bottom. This motion is eventually attenuated due to the internal damping of the soil and the radiation of energy in the lateral direction. Comparing the two curves presented in figure 4.56, it can be concluded that the higher response values obtained for $t_0=1/2\pi$ are caused by the higher frequencies present in the motion for this case; these motions, however, are also attenuated more rapidly and after a certain period, the only contribution to the rotation of the tunnel comes from frequencies around 1.5 Hz. Since the Ricker wavelets for the two values of t_0 considered have about the same amplitude at this frequency, the rotations induced in both cases become very similar after some time (the two curves almost coincide for t>1.5 secs).

The rotation of the tunnel induces vertical motions at the surface that propagate away from the tunnel. Figures 4.57 and 4.58 a,b show a 3–D plot of these oscillations as a function of time and distance from the tunnel. As can be seen, the point x=0.0 does not move vertically since it is on the axis of symmetry; also, the vertical motions observed near the edge of the tunnel are very similar to the rotation of the tunnel, as expected. Concerning the propagation of the disturbances in space, they decay rapidly with distance as a result of internal damping in the soil; when the velocity of propagation of these disturbances is inferred from the plots, it is found that it approaches the shear wave celerity of the top layer, indicating that the disturbances propagate essentially as surface waves.

4.3.5 Interaction Between the Tunnel and an Embedded Foundation

In this section, the influence of the underground tunnel on nearby structures is studied by analyzing a typical situation. Figure 4.59 shows the geometry of the model

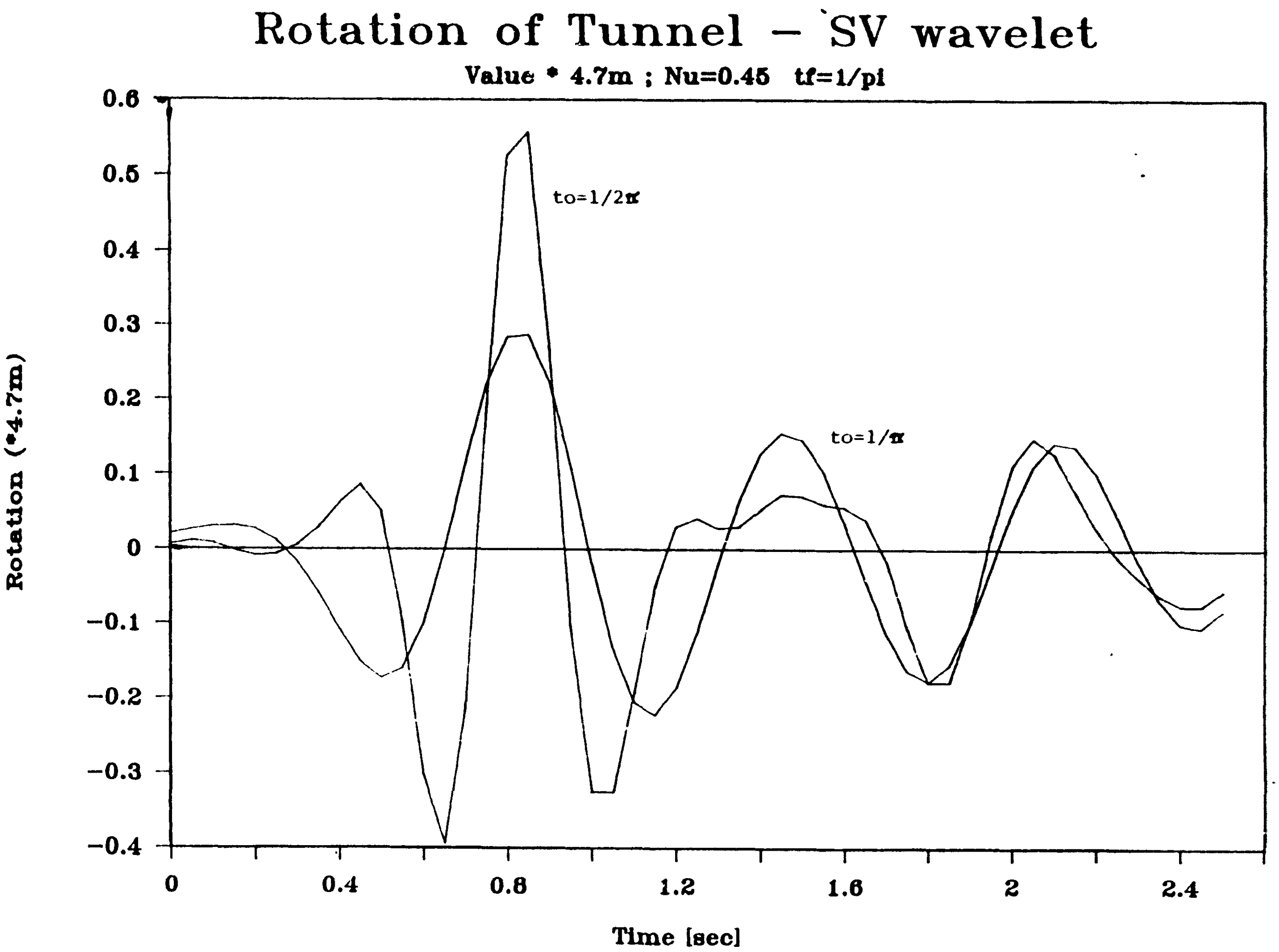
Rotation of Tunnel – SV wavelet
Value * 4.7m ; Nu=0.45 tf=1/pi
Rotation (*4.7m)
0.6
0.5
0.4
0.3
0.2
0.1
0
−0.1
−0.2
−0.3
−0.4
to=1/2π
to=1/π
0
0.4
0.8
1.2
1.6
2
2.4
Time [sec]

Figure 4.56

Vertical Motion - SV wavelet

Nu=0.45 ; t=0-2.5 sec ; X=0-47 m $t_0=1/\pi$ $t_f=1/\pi$

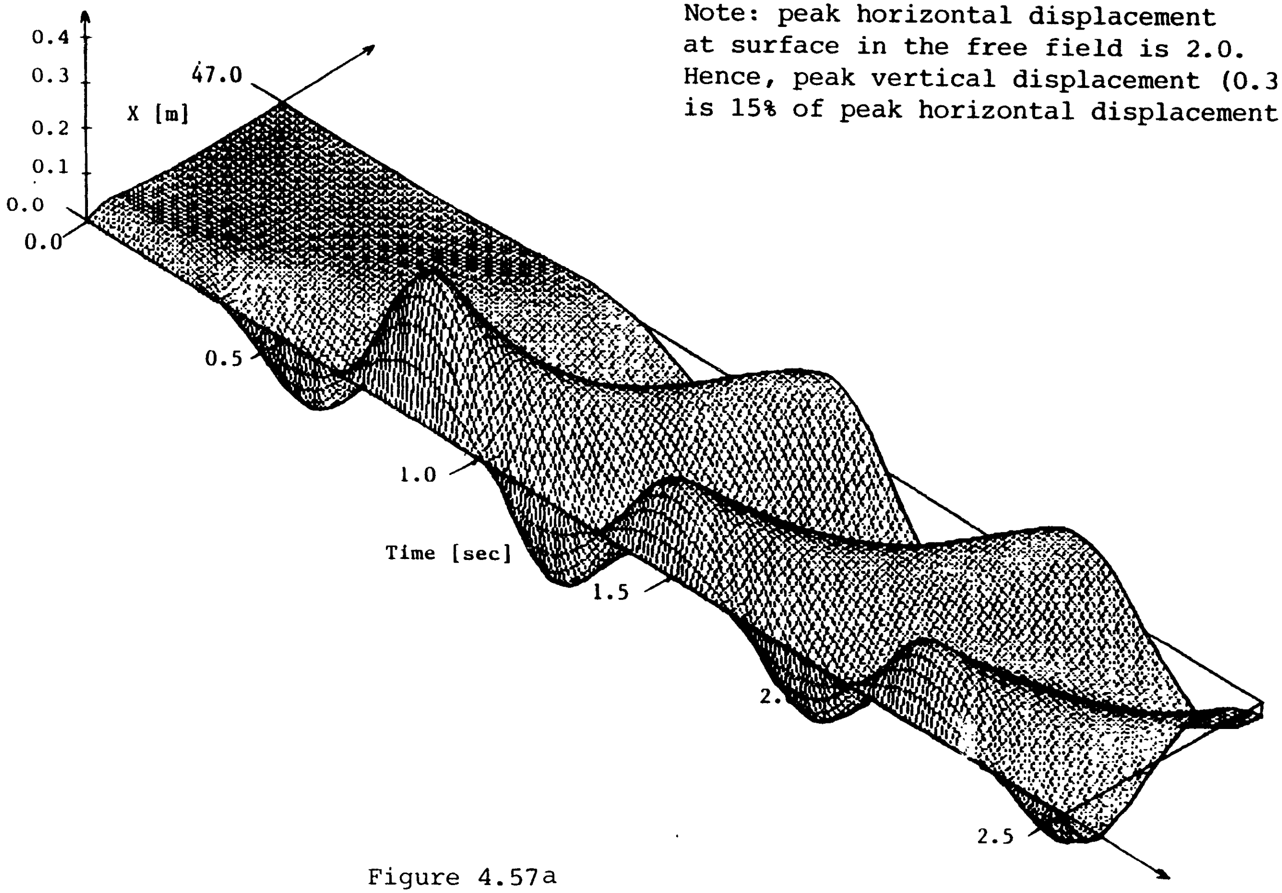

Note: peak horizontal displacement
at surface in the free field is 2.0.
Hence, peak vertical displacement (0.3)
is 15% of peak horizontal displacement.

Figure 4.57a

Vertical Motion - SV wavelet

Nu=0.45 ; t=0-2.5 sec ; X=0-47 m $t_0=1/\pi$ $t_f=1/\pi$

Note: peak horizontal displacement at surface in the free field is 2.0. Hence, peak vertical displacement (0.3) is 15% of peak horizontal displacement.

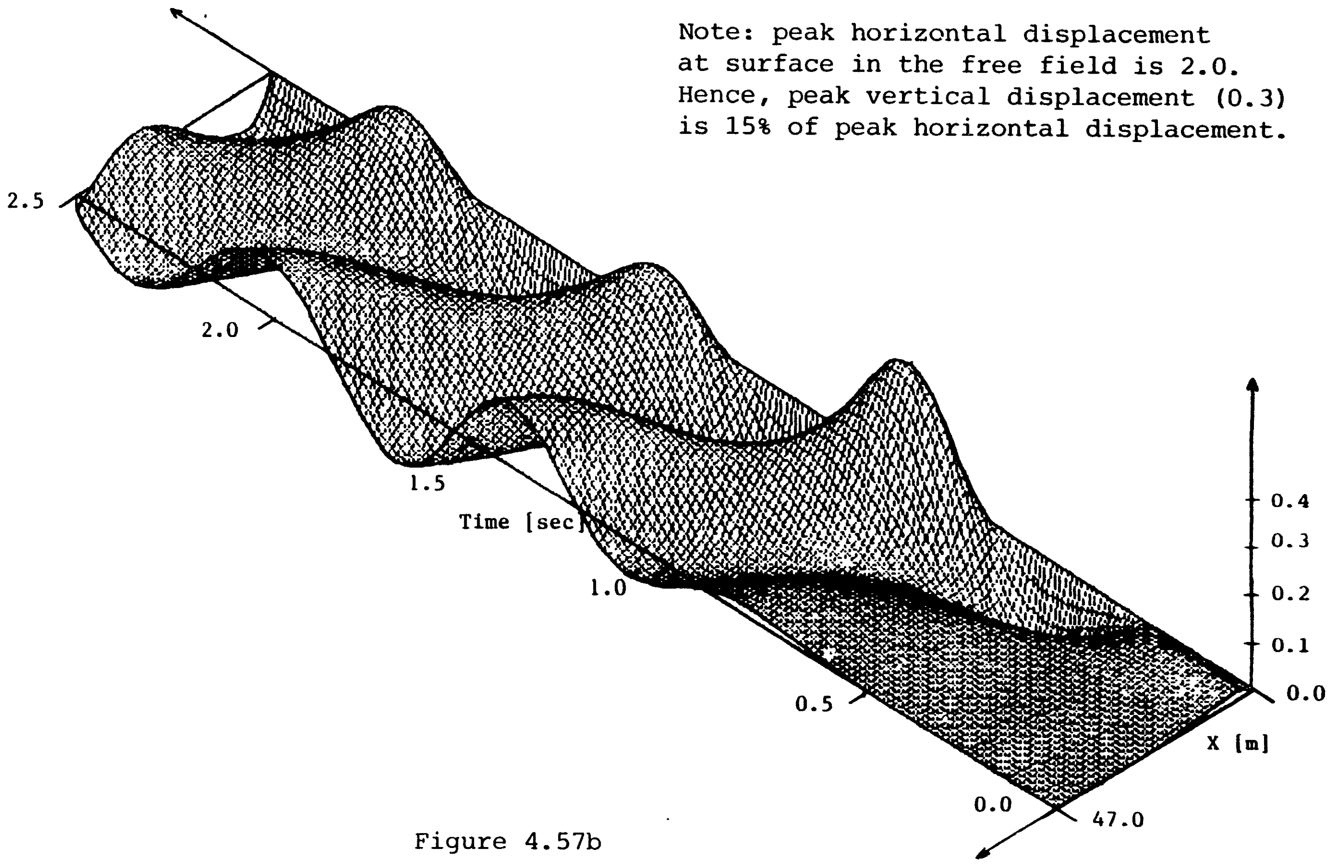

Figure 4.57b

Vertical Motion - SV wavelet

Nu=0.45 ; t=0-2.5 sec ; X=0-47 m $t_0=1/2\pi$ $t_f=1/\pi$

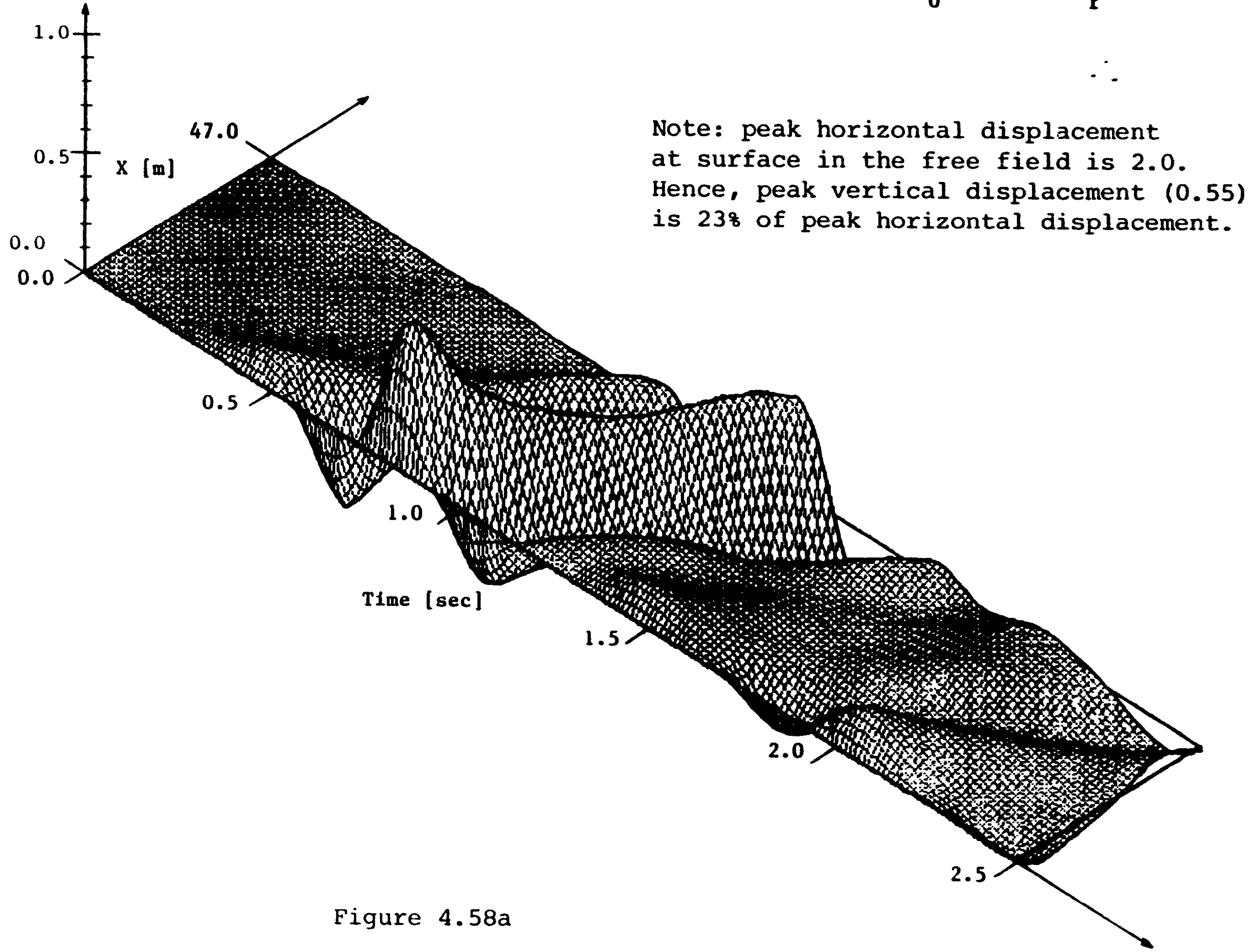

Note: peak horizontal displacement at surface in the free field is 2.0. Hence, peak vertical displacement (0.55) is 23% of peak horizontal displacement.

Figure 4.58a

Vertical Motion – SV wavelet

Nu=0.45 ; t=0–2.5 sec ; X=0–47 m $t_0=1/2\pi$ $t_f=1/\pi$

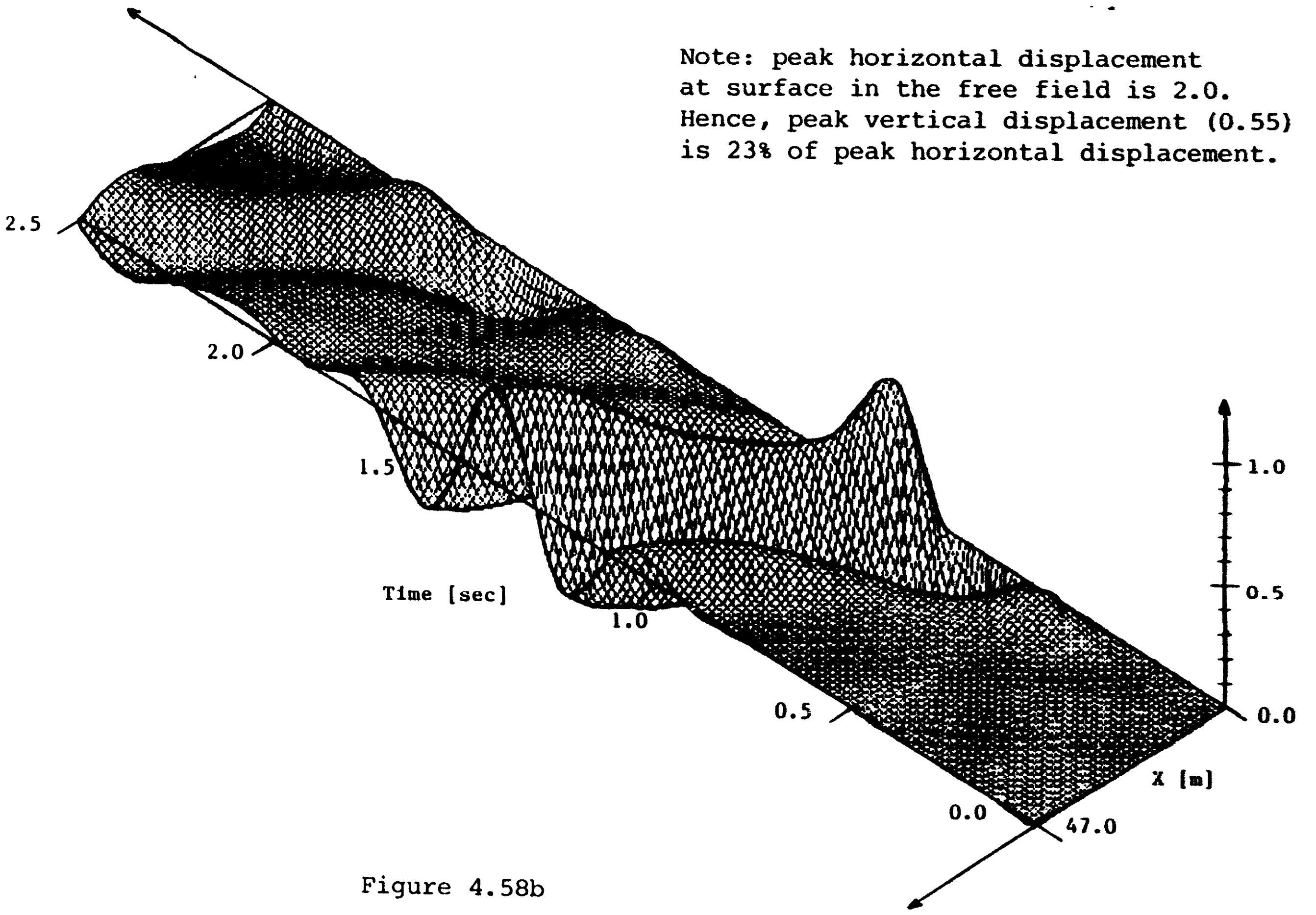

Note: peak horizontal displacement at surface in the free field is 2.0. Hence, peak vertical displacement (0.55) is 23% of peak horizontal displacement.

Figure 4.58b

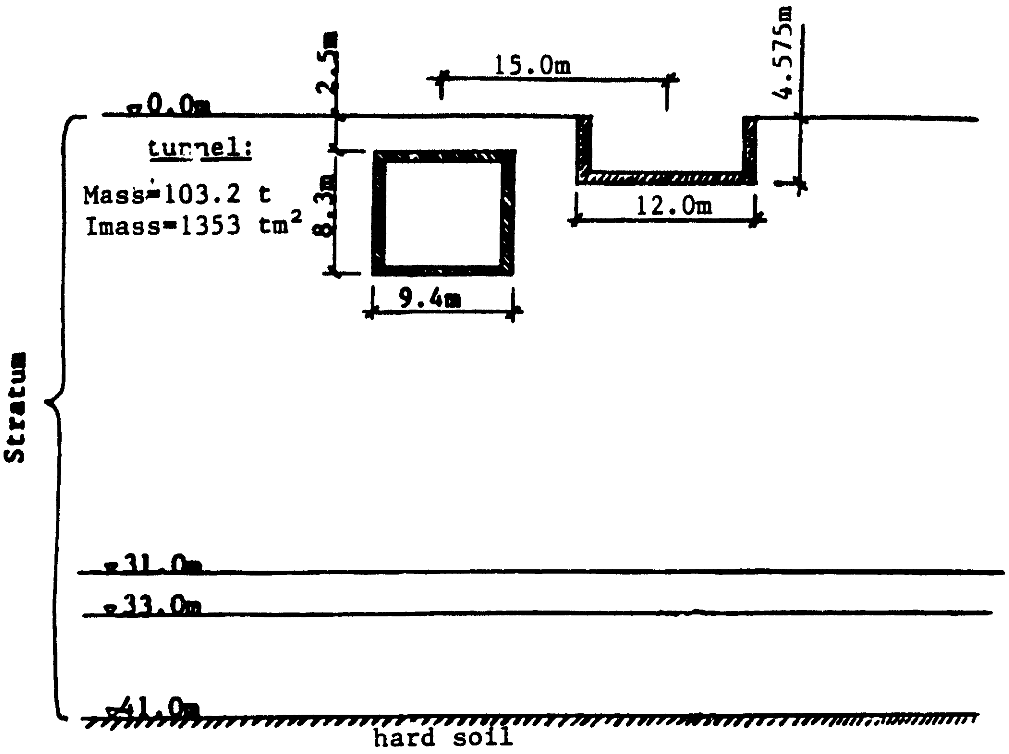
▽0.0m
2.5m
15.0m
4.575m
tunnel:
Mass=103.2 t
Imass=1353 tm²
8.3m
12.0m
9.4m
Stratum
▽31.0m
▽33.0m
▽41.0m
hard soil

Figure 4.59

chosen, a massless foundation embedded about 4.5m, situated near the tunnel, and having a width of 12m. While the majority of the structures situated in Mexico City's lakebed zone are founded on piles (either floating or endbearing), their presence is ignored in what follows in order to assess the worst scenario of a foundation without piles.

The motions of the foundation will be referred to its central point at the surface level. Vertically incident SV waves are prescribed at the base of the stratum, since we are mostly concerned with the effects of the rotation experienced by the tunnel. Frequencies up to 5 Hz are considered, even though our interest is mainly in the lower frequency range.

The motions of the embedded foundation are depicted in figures 4.60–4.62, which show the cases of a foundation with the tunnel, and without it. The presence of the tunnel influences very little the resulting horizontal displacement of the foundation for frequencies up to 2 Hz; it is only for higher frequencies that the presence of the tunnel does smooth out the variation with frequency of the horizontal displacement of the foundation. Because of symmetry, the center of the foundation would not displace vertically if it stood alone; however, the rotation of the tunnel introduces very important vertical displacements on the foundation, which attain almost 70% of the horizontal displacement at the base of the stratum for frequencies near 1.5 Hz. For lower frequencies, on the other hand, very little vertical displacement is induced in the foundation. This plot is very similar to the one showing the rotation of the tunnel, which indicates that the rotation is the direct cause of the vertical motion of the foundation. Concerning the rotation of the foundation, the presence of the tunnel has mixed effects, depending on the frequency of the motion; for frequencies near 1.5 Hz the rotation of the tunnel attenuates the rotation of the foundation since both rotations

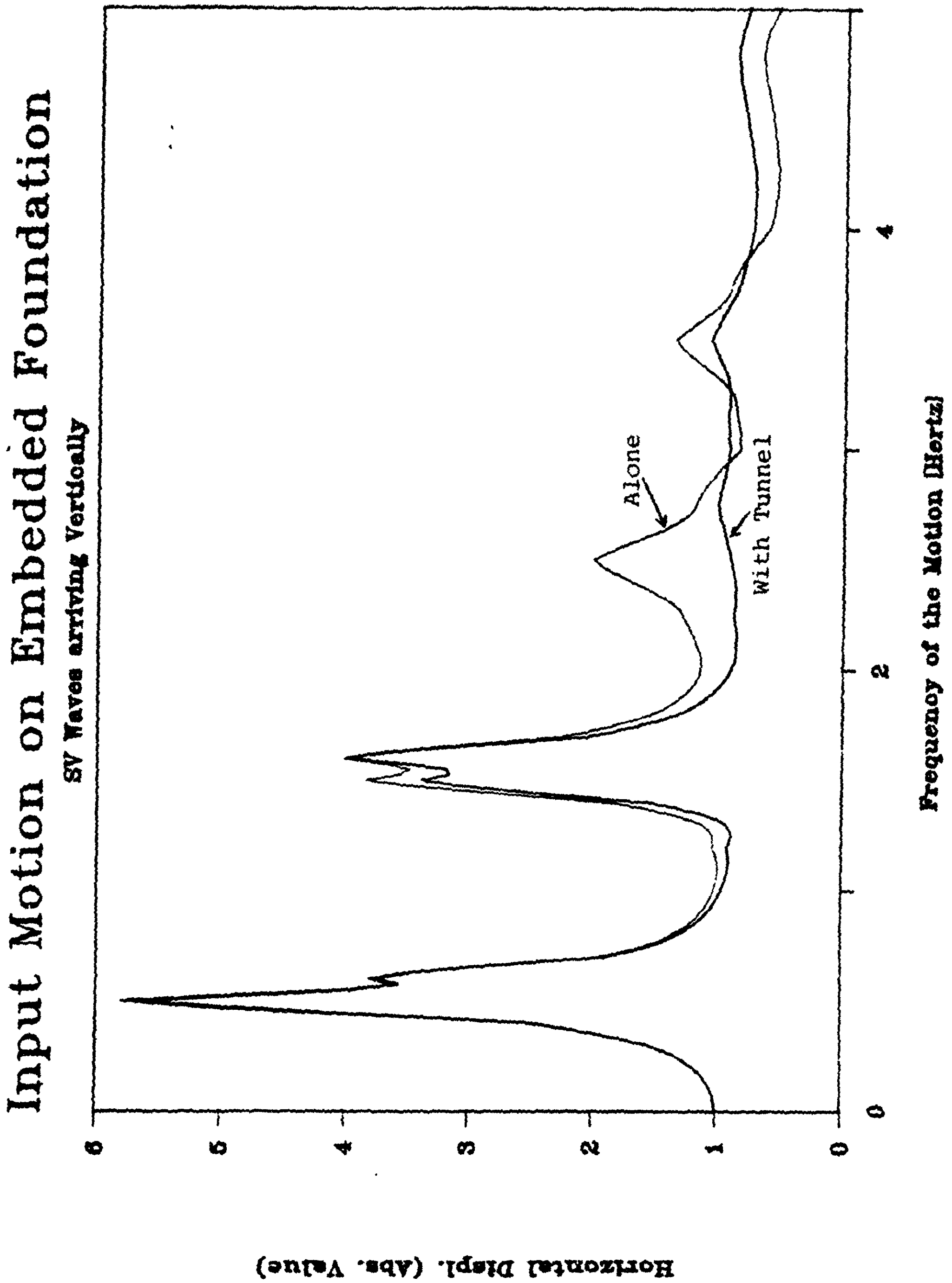
Input Motion on Embedded Foundation
SV Waves arriving Vertically
Alone
With Tunnel
0
1
2
3
4
5
6
0
2
4
Horizontal Displ. (Abs. Value)
Frequency of the Motion [Hertz]

Figure 4.60

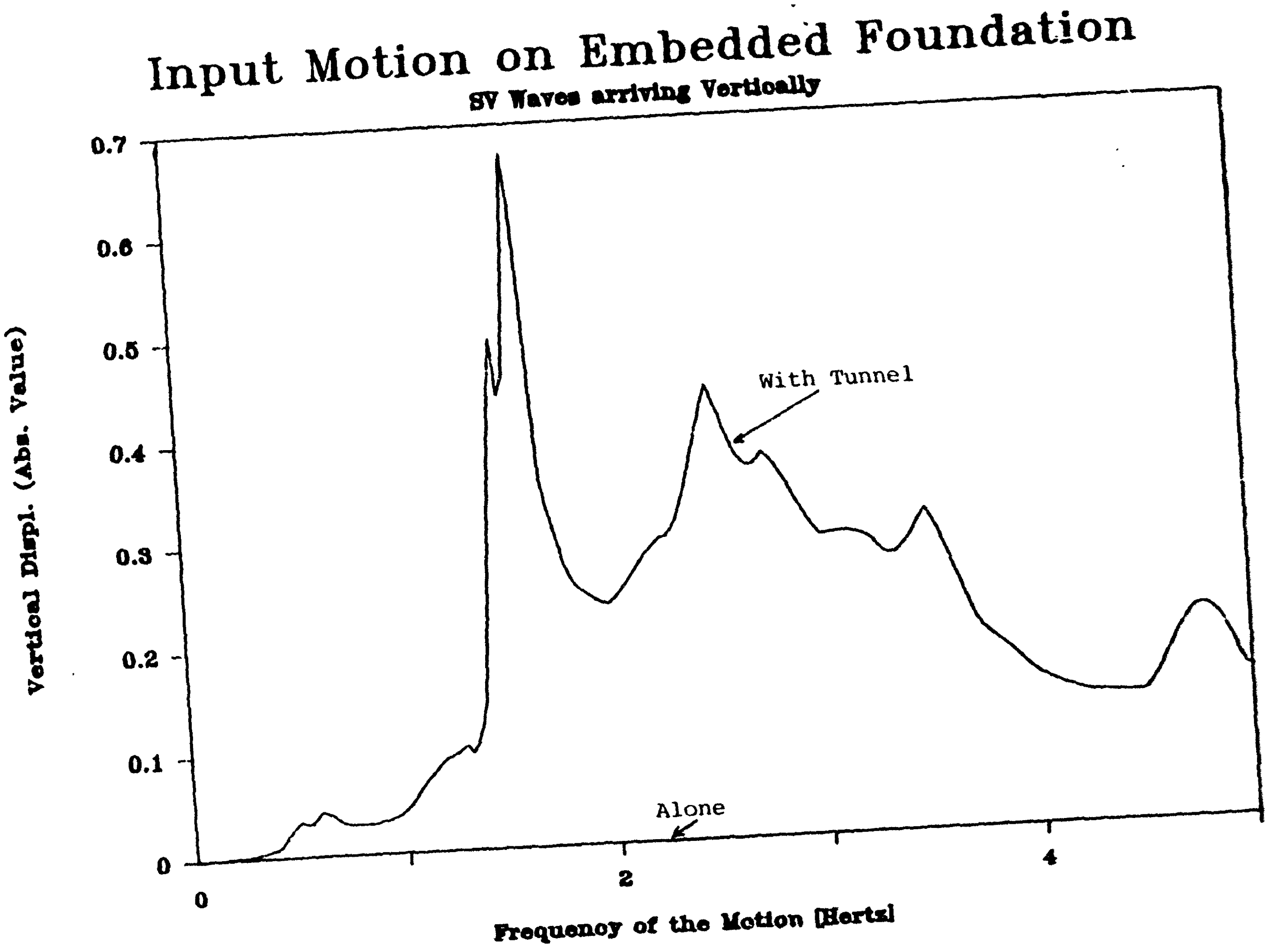
Input Motion on Embedded Foundation
SV Waves arriving Vertically
Vertical Displ. (Abs. Value)
0.7
0.6
0.5
0.4
0.3
0.2
0.1
0
With Tunnel
Alone
0
2
4
Frequency of the Motion [Hertz]

Figure 4.61

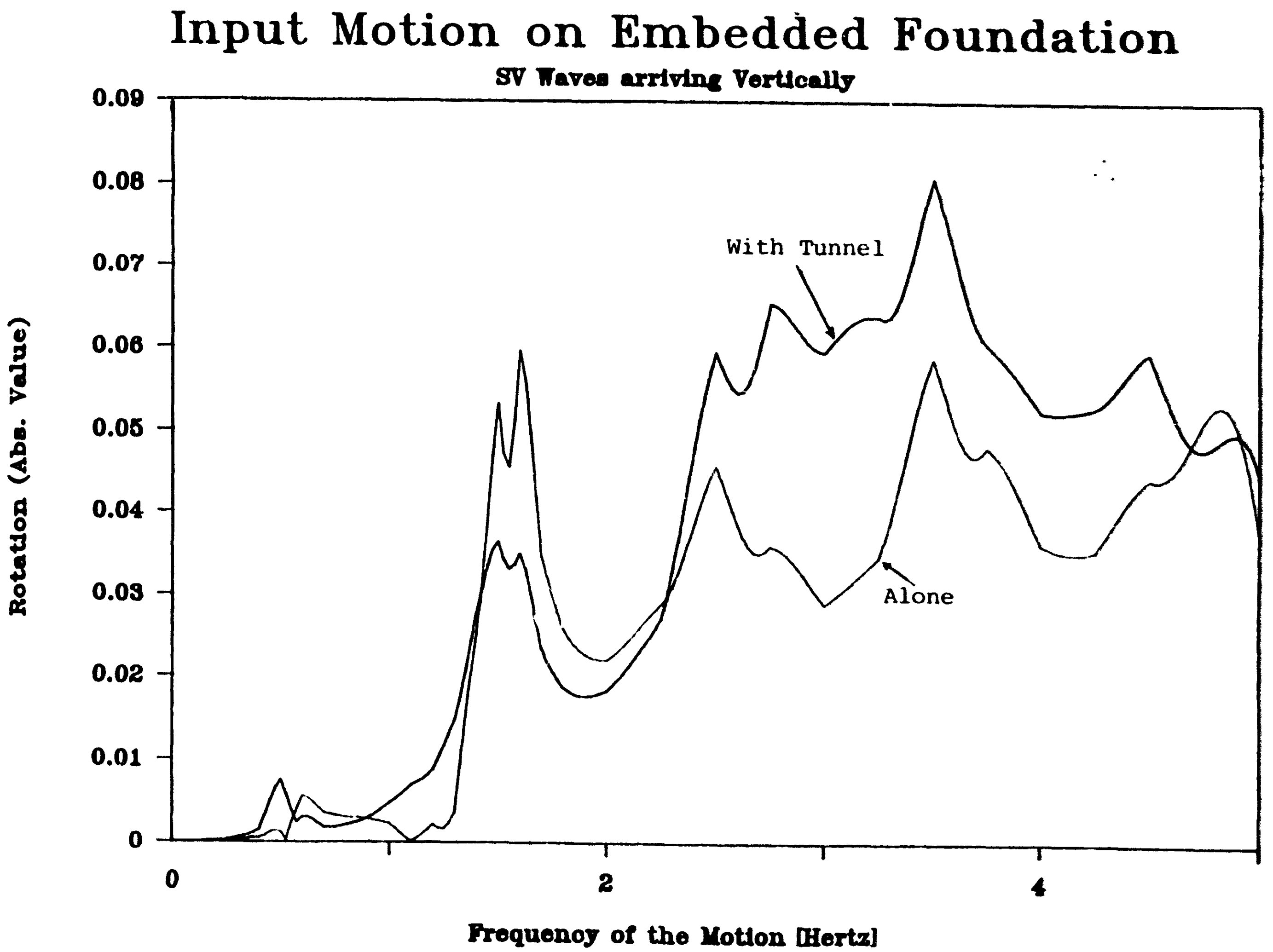
Input Motion on Embedded Foundation
SV Waves arriving Vertically
0.09
0.08
0.07
0.06
0.05
0.04
0.03
0.02
0.01
0
Rotation (Abs. Value)
With Tunnel
Alone
0
2
4
Frequency of the Motion [Hertz]

Figure 4.62

are in phase, and when the right edge of the tunnel moves up, the left edge of the foundation wants to move down; for higher frequencies (2.5–4.5 Hz) both structures rotate out of phase, so that the tunnel amplifies the rotation of the foundation. Again, in the low frequency range, both structures rotate very little so that the presence of the tunnel is not important.

4.4. Main Conclusions

This study focused on the effects of underground structures, and in particular of the subway tunnel, on the motion experienced by neighboring structures during the Mexico City earthquakes of September 1985. These effects were thought as possible explanations for the high contrast in damage intensities suffered by constructions in the lakebed zone. The records registered at several seismic stations within Mexico City, were used to obtain the frequency spectrum of the earthquakes at several locations. The horizontal ground acceleration registered in the more heavily damaged region shows a very narrow peak at a frequency of 0.5 Hz, corresponding to the first natural frequency of the underlying stratum; for higher frequencies, the energy contents of the motion is almost nil, so that the observed horizontal motion on the surface exhibits a nearly harmonic variation with time. This elicited important resonance phenomena in buildings of medium size, which in turn suffered great damage or total collapse.

The Boundary Element formulation developed was used to evaluate the effects of the subway tunnel on the motion at the ground surface and on the motions experienced by embedded foundations in the neighborhood of the tunnel. The analysis was performed for several frequencies of the motion and the results combined with the frequency spectrum of the actual seismic records, in order to obtain an overall measure of the influence of the tunnel. Both in–plane and anti–plane motions were considered. The results show that, in general, the tunnel acts as a filtering screen, attenuating somewhat the resulting motion at nearby sites for high frequency excitations. In the case of incident SV waves, the rotation of the tunnel induces important vertical displacements on the surface, which would not be present otherwise. However, in the model analyzed, only for frequencies greater than 1 Hz does the seismic waves induce important rotations in the tunnel.

It can be concluded that for the seismic motions felt in Mexico City during the earthquakes of September 1985, the interaction between underground structures and nearby foundations did not have an important effect on the levels of damage observed. This conclusion, drawn from a 2–dimensional analysis, remains valid for the 3–dimensional case, since more attenuation would be observed if the radiation damping into the third dimension was taken into consideration.

5. APPROXIMATE PROCEDURE TO ASSESS THE DYNAMIC INTERACTION OF MULTIPLE STRUCTURES SUBJECTED TO SEISMIC EXCITATIONS

5.1 Review of Past Results

The study of structure–soil–structure interaction refers to the coupling through the soil of multiple structures subjected to a dynamic excitation. This is a very complex problem requiring, in general, the use of numerical methods. Moreover, there are so many parameters to consider (geometry of the foundations and relative position, characteristics of the underground, seismic excitation, masses and dynamic characteristics of the structures) that an exhaustive study of all situations is not practical. For this reason, most studies dealing with this problem in the past have been restricted to a few typical situations, showing the effects of several structures and their response to either forced dynamic loads or seismic excitations.

Lysmer et al [31] studied the effect of two adjacent buildings on the response of a nuclear containment building subjected to a seismic excitation, with the analysis being carried out in two dimensions. The results showed a very pronounced influence of the two buildings on the peak response of the main structure, which increased by more than 100%. The structures were founded in a shallow stratum, and the two secondary buildings were located on each side of the containment structure and deeply embedded in the stratum; this may have created a box–type effect, which decreased substantially the radiation damping away from the main building, and increased its response.

Wong and Trifunac [50] investigated the effects of structure–soil–structure interaction for two or more structures subjected to obliquely incident SH–waves. The structures were idealized as vertical shear beams founded on embedded strip foundations with semi–cylindrical cross sections. Even though the analysis was two–dimensional and restricted to anti–plane motions, the results indicated that the interaction between the structures can cause noticeable changes in the amplitude of the input motions of each foundation. These effects appear to be more important for structures which are smaller and lighter than their neighboring structures. Depending on the position of the small structure relative to its neighbors and the direction of the incident seismic waves, the amplitude of its response could be altered substantially as a result of the presence of the heavier structures. If the waves were screened by the larger structure before arriving to the smaller one, the latter would tend to follow the motion of the former; however, if the waves impinge first on the small structure, then the presence of the larger structure behind it changes the displacements observed in the first structure in an erratic way (depending on the frequency of the motion).

The dynamic interaction between two embedded strip foundations for in–plane motions was studied by Chang–Liang [9] using a finite element formulation. The soil was idealized as a homogeneous viscoelastic stratum on rigid rock. The results showed that for forced vibrations, a very shallow layer of soil produces less interaction between the two foundations than a deep layer. Indeed, the secondary foundation displaced horizontally by about 50% of the motion of the excited foundation for a deep soil, but only 20% for a shallow soil. This can be explained by the fact that for very shallow strata, the energy does not radiate much laterally, which results in smaller displacements in the far–field. Furthermore, it was also found that the motion of the excited structure was not substantially affected by the presence of the other foundation, especially for rocking or vertical excitations. Rocking excitations give, in general, less cross–interaction than horizontal excitations because the moments giving rise to rocking have no net resultant; as a result, the displacement field associated with rocking decays faster with distance to the source than for swaying. Chang–Liang also analyzed the effects of the interaction for seismic excitations, considering the case of vertically propagating shear waves. The results showed that the interaction changes the natural frequencies of the systems, and depending on the frequency of the excitation, amplifications of up to 100% or attenuations of 40–60% can be observed; hence, these effects can be very important, in particular for narrow band processes.

The study of structure–soil–structure interaction in three–dimensional domains involves an enormous number of degrees of freedom to model properly the foundations and the subgrade; hence, most of these studies have been restricted to surface foundations, which simplifies greatly the computations. Of special mention are the works by Wong and Luco [49], Bielak and Coronato [7], Gonzalez [14], Kobori et al [26,27], Sarfeld and Frohlich [37] and more recently Triantafyllidis [42]; these researchers investigated the response of a passive surface foundation to the dynamic excitation of a nearby surface foundation, and the response of groups of foundations to seismic excitations. In most of these analyses, both foundations were square and the soil was taken as a homogeneous stratum or halfspace. Several cases were studied, varying the relative position of the foundations and their masses as well as the depth of the stratum. It was found that a forced vibration of one of the masses induces displacements of the same order of magnitude in the secondary mass, even for distances between the masses equal to five times their width. Another consequence of the interaction between the two foundations is the presence of vertical displacements, torsion or rocking due to horizontal loads. This result is not surprising if one considers the displacement field of the soil in the vicinity of the excited foundation and the fact that the other foundation has to accommodate to these displacements. These effects can be very important for the dynamic response of both structures.

More recently, Lin et al [30] studied the effects of dynamic interaction between two square, closely spaced, embedded foundations. In their study, these authors varied the masses of the structures, their relative position and distance, and their degree of embedment. The analysis was fully three–dimensional and the structures were founded on a homogeneous stratum of soil. The results confirmed previous works by showing that the interaction had little effect on the motion of the excited foundation; that the motion of the loaded foundation induced a substantial vibration in the passive foundation; and that these effects increased as the distances between the two foundations was made smaller. In addition, important changes were detected in the coupling terms (rotation due to an horizontal load, etc.) of the primary structure caused by the secondary structure. They observed also that when the polarization of the free field motion is not aligned with the direction defined by the two foundations, then the interaction effects are decreased. In other words, when the foundations shake in the plane defined by the two foundations, the interaction effects are more pronounced than when the shaking occurs in a transversal direction. This suggests that the results obtained from a two–dimensional analysis provide an upper bound on the total effects of the interaction, if one discards torsional motions.

In all of the works cited previously, it was shown that the interaction between multiple adjacent foundations can be a very important factor that should not be ignored in a dynamic analysis. However, as pointed out before, models that accurately take into account structure–soil–structure interaction require expensive numerical solutions. Several attempts were made to formulate simpler solutions to this problem, but usually the approximations obtained were only valid for very specific situations. Wong and Trifunac [50] used an infinite series solution in their study, which was restricted to anti–plane motions and to embedded strip foundations having a semi–cylindrical cross section. Wong and Luco [49] used an iterative procedure to solve the resulting algebraic system of equations which reduced the number of computations necessary without affecting much the accuracy of the solution. In the work by Triantafyllidis [42], the stress distribution at the foundation boundaries was approximated by Chebychev polynomials, thus reducing the total number of unknowns.

The great majority of seismic analyses deal with very idealized situations: the soil is thought of as a linear elastic and homogeneous medium; the foundation is assumed to be completely welded to the surrounding soil; the seismic excitation is highly simplified both on its frequency contents and type of waves present. In reality, however, the soil properties vary from point to point, nonlinearities are present, the contact of the foundation with the surrounding soil can exhibit complex behavior, with possible upliftings and slidings, and the actual characteristics of the seismic excitation are unpredictable. With so many uncertainties in the physical model, the results obtained in the analysis should be taken with caution, and the limitations of the model be studied by varying a few parameters and looking at their effect on the results. Hence, it is often preferable to use simple models to get an idea of the important factors dominating the behavior of the system, at least in a preliminary analysis. In this way, one can estimate the degree of interaction between several foundations. Should the results obtained by use of these approximate methods indicate the effects of structure–soil–structure interaction are not important, then the application of more sophisticated (and more expensive!) methods could be avoided. Moreover, such approximate methods would allow more frequent consideration of the dynamic interaction between foundations, even if the results were valid only in a qualitative sense. For this reason, an approximate technique for the analysis of structure–soil–structure interaction is presented in the next pages.

5.2 Response of a Group of Structures to Seismic Excitations

The response of a group of structures to seismic excitations is studied assuming an elastic behavior of the structures and soil and a complete bonding between the foundations and the surrounding soil. Since, in general, problems of this type need to be solved numerically, discretizing the model, the formulation is presented for a discrete number of degrees of freedom, and not for continuous media. In this case, the equations of motion can be written as

$$M\ddot{U} + C\dot{U} + KU = R(t) \tag{5.1}$$

where M,C, and K are respectively the mass, damping and stiffness matrices of the system; U represents the displacements vector; a superscript dot indicates differentiation with respect to time; and R(t) is the loading vector, corresponding to the imposed displacements and tractions at the boundaries.

By using the Superposition Theorem, presented by Kausel et al [24], the system of equations in 5.1 can be split into two. First, all the structures and foundations are assumed massless, and in a second step the loading is imposed as inertial forces only at the degrees of freedom of the structures. This corresponds to splitting the mass matrix into two parts

$$M = M^1 + M^2 \tag{5.2}$$

and equation 5.1 becomes

$$M^1\ddot{U}^O + C\dot{U}^O + KU^O = R(t) \tag{5.3}$$

$$M\ddot{U}^r + C\dot{U}^r + KU^r = -M^2\ddot{U}^O \tag{5.4}$$

The equivalence of equations 5.3 and 5.4 with equation 5.1 can be verified by simple addition, noting that the total displacement U is the sum of U^O and U^r. The phenomena described by equations 5.3 and 5.4 are usually referred to as Kinematic Interaction and Inertial Interaction, respectively. While several structures can be taken into account simultaneously, for the sake of simplicity and without loss of generality, in what follows the formulation is presented for the case of only two structures (see fig.5.1). We distinguish between the displacements of the soil, U_g, the displacements of the nodes on the soil–structure interfaces, U_{s_1} and U_{s_2}, and the displacements of each structure, U_1 and U_2. Equation 5.3 can be written in full as

$$\begin{bmatrix} 0 & 0 & 0 & 0 & 0 \\ 0 & 0 & 0 & 0 & 0 \\ 0 & 0 & M^1_{s_1} & 0 & M_{s_1g} \\ 0 & 0 & 0 & M^1_{s_2} & M_{s_2g} \\ 0 & 0 & M_{gs_1} & M_{gs_2} & M_g \end{bmatrix} \cdot \begin{bmatrix} \ddot{U}^O_1 \\ \ddot{U}^O_2 \\ \ddot{U}^O_{s_1} \\ \ddot{U}^O_{s_2} \\ \ddot{U}^O_g \end{bmatrix} + \begin{bmatrix} C_1 & C_{12} & C_{1,s_1} & C_{1,s_2} & 0 \\ C_{21} & C_2 & C_{2,s_1} & C_{2,s_2} & 0 \\ C_{s_{1,1}} & C_{s_{1,2}} & C_{s_1} & C_{s_1s_2} & C_{s_1g} \\ C_{s_{2,1}} & C_{s_{2,2}} & C_{s_2s_1} & C_{s_2} & C_{s_2g} \\ 0 & 0 & C_{gs_1} & C_{gs_2} & C_g \end{bmatrix} \cdot \begin{bmatrix} \dot{U}^O_1 \\ \dot{U}^O_2 \\ \dot{U}^O_{s_1} \\ \dot{U}^O_{s_2} \\ \dot{U}^O_g \end{bmatrix} +$$

$$+ \begin{bmatrix} K_1 & K_{12} & K_{1,s_1} & K_{1,s_2} & 0 \\ K_{21} & K_2 & K_{2,s_1} & K_{2,s_2} & 0 \\ K_{s_{1,1}} & K_{s_{1,2}} & K_{s_1} & K_{s_1s_2} & K_{s_1g} \\ K_{s_{2,1}} & K_{s_{2,2}} & K_{s_2s_1} & K_{s_2} & K_{s_2g} \\ 0 & 0 & K_{gs_1} & K_{gs_2} & K_g \end{bmatrix} \cdot \begin{bmatrix} U^O_1 \\ U^O_2 \\ U^O_{s_1} \\ U^O_{s_2} \\ U^O_g \end{bmatrix} = \begin{bmatrix} 0 \\ 0 \\ 0 \\ 0 \\ R(t) \end{bmatrix} \tag{5.5}$$

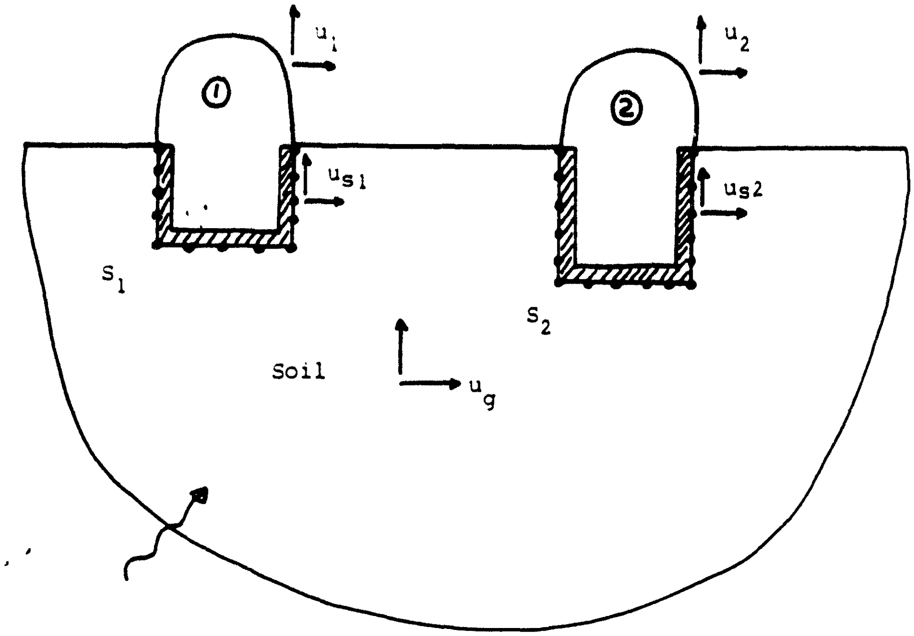

Fig. 5.1 - Degrees of freedom in the analysis of two embedded structures

Equation 5.5 is quite general, allowing for both foundations to be connected through the superstructure. Discarding (temporarily) the damping term in equation 5.5, the displacements induced in the structures can be solved in terms of the displacements at the interfaces

$$\begin{bmatrix} K_1 & K_{12} & K_{1,s_1} & K_{1,s_2} \\ K_{21} & K_2 & K_{2,s_1} & K_{2,s_2} \end{bmatrix} \begin{bmatrix} U^o_1 \\ U^o_2 \\ U^o_{s_1} \\ U^o_{s_2} \end{bmatrix} = 0$$

which gives

$$\begin{bmatrix} U^o_1 \\ U^o_2 \end{bmatrix} = - \begin{bmatrix} K_1 & K_{12} \\ K_{21} & K_2 \end{bmatrix}^{-1} \cdot \begin{bmatrix} K_{1,s_1} & K_{1,s_2} \\ K_{2,s_1} & K_{2,s_2} \end{bmatrix} \cdot \begin{bmatrix} U^o_{s_1} \\ U^o_{s_2} \end{bmatrix} = - K_t^{-1} K_{t,s} U^o_s \tag{5.6}$$

Introducing this result into equation 5.5, discarding again the coupling terms in the damping matrix between the structures and the interfaces, one obtains

$$M^1 \cdot \begin{bmatrix} \ddot{U}^o_s \\ \ddot{U}^o_g \end{bmatrix} + C^1 \cdot \begin{bmatrix} \dot{U}^o_s \\ \dot{U}^o_g \end{bmatrix} + (K^1 - K^T_{t,s} \cdot K_t^{-1} \cdot K_{t,s}) \cdot \begin{bmatrix} U^o_s \\ U^o_g \end{bmatrix} = \begin{bmatrix} 0 \\ R(t) \end{bmatrix} \tag{5.7}$$

where C^1 and K^1 correspond to the degrees of freedom for nodes at the interfaces and in the soil. (It should be noted that the term $K^T_{t,s} \cdot K_t^{-1} \cdot K_{t,s}$ in equation 5.7 contains an implicit addition of null rows and columns which are necessary to match the dimensions of K^1).

The influence of internal damping on the structures can also be incorporated, provided that relation 5.6 remains valid. This implies setting the damping terms proportional to the stiffness terms ($C_1 = \alpha K$, etc...). If this simplification is not realistic or convenient, then equation 5.5 must be solved in full.

Equation 5.4 represents the second step in the solution of the dynamic problem. Since the loading in this step is applied only to the structures, the degrees of freedom for the soil can be condensed out and just the ones for the soil–foundation interfaces are retained. After such reduction, equation 5.4 will involve only the degrees of freedom for the structures and the interfaces.

Although equations 5.4 and 5.7 are sufficiently general in that they may include coupling of the superstructures (such as in a bridge), in most cases no such coupling exists, and the structures are separate. Since the foundations are much more rigid than the surrounding soil, it may be assumed that they displace essentially as rigid bodies. In these cases, U_s can be expressed in terms of the rigid body motions of the foundations as

$$U^{o}_{s} = \begin{bmatrix} T_1 & \\ & T_2 \end{bmatrix} \cdot \begin{bmatrix} \bar{U}^{o}_{s_1} \\ \bar{U}^{o}_{s_2} \end{bmatrix} = T\,\bar{U}^{o}_{s} \tag{5.8}$$

$$\text{where } \bar{U}^{o}_{si} = [u_x\ u_y\ u_z\ \phi_x\ \phi_y\ \phi_z]^T \tag{5.9}$$

represents the rigid–body displacements of foundation i and T_i is a transformation matrix connecting the rigid–body displacements to the displacements at each node along the interface i. For example, the elements of T_i corresponding to node j are (in 3–dimensions)

$$T_{ij} = \begin{bmatrix} 1 & 0 & 0 & 0 & z-z_p & -(y-y_p) \\ 0 & 1 & 0 & -(z-z_p) & 0 & x-x_p \\ 0 & 0 & 1 & y-y_p & -(x-x_p) & 0 \end{bmatrix} \tag{5.10}$$

Since rigid body motions of the foundations do not introduce internal forces in the foundations, we have

$$K_{t,s} \cdot T = 0 \tag{5.11}$$

and equation 5.7 becomes

$$[T^T I]\, M^1 \begin{bmatrix} T\ddot{U}^o_s \\ \ddot{U}^o_g \end{bmatrix} + [T^T I] C^1 \begin{bmatrix} T\dot{U}^o_s \\ \dot{U}^o_g \end{bmatrix} + [T^T I] K^1 \begin{bmatrix} TU^o_s \\ U^o_g \end{bmatrix} = \begin{bmatrix} 0 \\ R(t) \end{bmatrix} \tag{5.12}$$

In this case, no assumptions need to be made concerning the damping matrix of the structures.

Regarding Inertial Interaction, equation 5.4 can be modified by imposing the condition that the foundation is rigid. The net effect of this kinematic constraint is a reduction in the number of degrees of freedom at the soil–structure interface to at most six dof's (3 translations and 3 rotations). The soil impedance matrix reduces then to the classical foundation stiffness matrix containing the (frequency dependent) "springs and dashpots". Since the emphasis in this section is on Kinematic Interaction, such manipulations of equation 5.4 will not be pursued further.

In the Superposition Theorem described previously, all of the structures and foundations were analyzed simultaneously. An alternative formulation is obtained if only one structure–foundation system is considered at a time, and the presence of the other structures is captures directly in the foundation stiffnesses and kinematic interaction of this structure. In other words, the other structures become "part of the soil"; mathematically speaking, the degrees of freedom for the other structures have been condensed out. This approach was used for the results presented in section 5.6, where only the first structure was assumed massless, while the other structures had mass; a dynamic condensation of the dof's of the neighboring structures was then performed.

Since the exact time variation of the seismic loading is not known, it is generally necessary to carry out analyses with different excitations. In such case, it is advantageous to formulate the equations in the frequency domain, since less computational effort is then required. An added advantage is that, arbitrary variations with frequency of the dynamic stiffnesses for the rigid foundations can be considered in the equation of motion, and that damping is not restricted to be of the viscous type. Results in the time domain can then be obtained by Inverse Fourier transformation of the frequency domain solution, after consideration is given to the frequency contents of the loading. These Fourier transformations shall be performed using the efficient fast Fourier transform algorithm.

5.3 Extension to Iguchi's Method

Iguchi [18] proposed an approximate method for the computation of the dynamic response of rigid embedded foundations to seismic motions. The method is extremely simple to implement and gives quite accurate results (see Iguchi [19] and Pais [33]). The soil–structure interaction is solved in two separate steps. First the free–field ground motion is computed, disregarding the presence of the foundation, and the displacements and tractions are computed on a fictitious surface coincident with the soil–foundation interfaces. Using these displacements, average translations and rotations of the rigid foundation are obtained by least squares, minimizing the differences between the soil displacements and those at the foundation boundary.

These rigid body displacements U_1 are obtained by computing a weighted average of the free–field displacements u^* along the interface soil–foundation, as follows

$$\overline{U} = H^{-1} \iint_s T^T u^* \, ds \tag{5.13}$$

where s corresponds to the surface of the foundation in contact with the soil;

$$\overline{U}^T = [\overline{U}_x \ \overline{U}_y \ \overline{U}_z \ \overline{\phi}_x \ \overline{\phi}_y \ \overline{\phi}_z] \tag{5.14}$$

$$u^{*T} = [u^*_x \ u^*_y \ u^*_z] \tag{5.15}$$

T, given by equation 5.10, is a transformation matrix relating the displacements of the foundation at a point <u>P</u> with coordinates (x,y,z) to the rigid body motions of the foundations, defined with respect to a reference point <u>c</u> with coordinates (x_c, y_c, z_c), and

$$H = \iint_s T^T T \, ds \tag{5.16}$$

The forces and moments corresponding to the tractions at the boundary soil–foundation are computed using the fact that the foundation is in dynamic equilibrium; hence, the inertial forces must equilibrate the boundary tractions. If the foundation is assumed massless, then the forces and moments are given by

$$\overline{F} = -\omega^2 \rho \iiint_V T^T u^* \, dv \tag{5.17}$$

$$\overline{F}^T = [\overline{f}_x \; \overline{f}_y \; \overline{f}_z \; \overline{m}_x \; \overline{m}_y \; \overline{m}_z] \tag{5.18}$$

In a second step, these forces and moments are eliminated by imposing additional displacements on the foundation. These additional displacements are obtained by multiplying the dynamic compliance matrix of the foundation $K^{d^{-1}}$ by the force vector $\overline{F}$

$$\Delta U = K^{d^{-1}} \, \overline{F} \tag{5.19}$$

The total input motions of the foundation, U_t, are then obtained by adding the displacement vectors computed in both steps

$$U_t = \overline{U} + \Delta U \tag{5.20}$$

Figure 5.2 illustrates these two steps. It can be seen that the errors in this approach arise from neglecting the global effect of the additional tractions needed at the

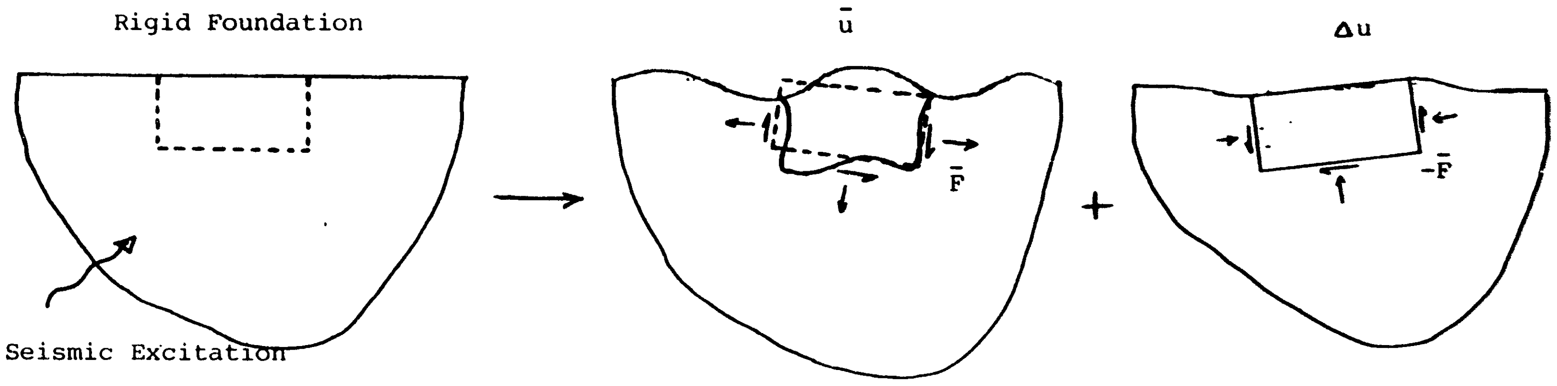

Fig. 5.2 - Iguchi's Method

boundary to make the soil displacements conform with the rigid motions of the foundation. It can be assumed that the overall effect of these additional tractions is very small since they tend to cancel each other. This would indeed happen if the soil was modelled along the boundary as a group of independent springs without coupling.

The method presented assumes that the dynamic stiffnesses of the foundation are known apriori, which restricts its use to simple configurations, such as cylindrical or rectangular foundations embedded in a halfspace. For these cases, Pais and Kausel [33] developed some approximate formulas which give with enough accuracy the values of the dynamic stiffnesses for a large range of frequencies.

If it is assumed that the foundation has a certain mass matrix M, then the forces computed in step one and the dynamic stiffnesses must be corrected as follows

$$U_t = \bar{U} + \bar{K}^{d^{-1}} \cdot (\bar{F} + \omega^2 M \bar{U}) \tag{5.21}$$

where $\bar{K}^d = K^d - \omega^2 M$

In principle, this method can be extended directly to the case where multiple foundations are considered simultaneously. Referring to figure 5.3 (which for simplicity, and without loss of generality, displays only two foundations), the average displacements and the forces and moments acting on each foundation are computed from the free–field solution, as before

$$\bar{U}_i = H_i^{-1} \iint_{S_i} A_i^T u^* \, ds_i \tag{5.22}$$

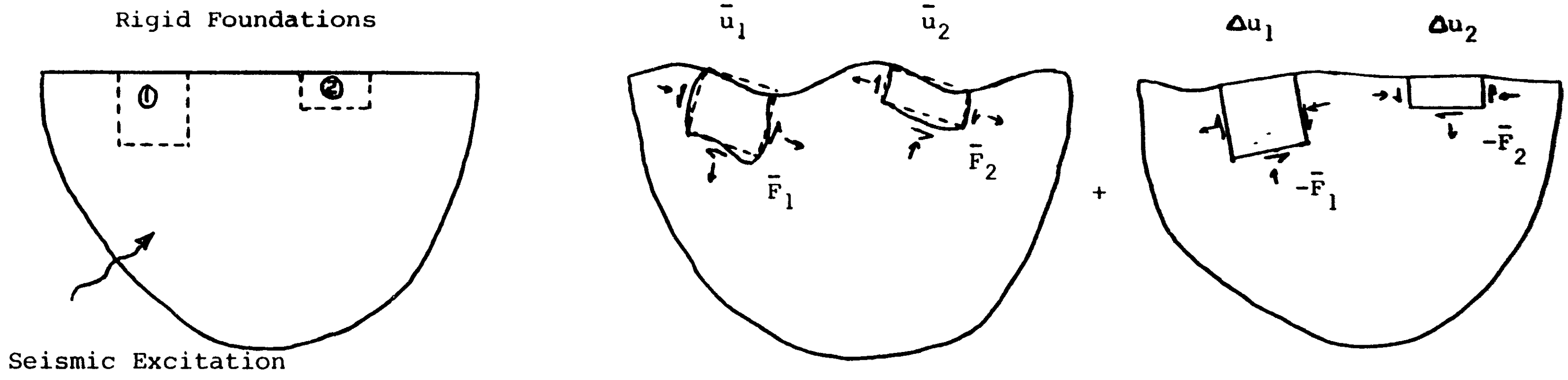

Fig. 5.3 - Iguchi's Method applied to several foundations

$$\bar{F}_i = -\omega^2\rho \iiint_{v_i} A_i^T u^* dv_i \tag{5.23}$$

where the subscript i refers to the foundation being considered.

The total displacements are obtained using a procedure similar to that used for massless foundations:

$$U_t = \begin{bmatrix} U_{1t} \\ U_{2t} \\ \vdots \end{bmatrix} = \begin{bmatrix} \bar{U}_1 \\ \bar{U}_2 \\ \vdots \end{bmatrix} + K^{d^{-1}} \left[\begin{bmatrix} \bar{F}_1 \\ \bar{F}_2 \\ \vdots \end{bmatrix} + \omega^2 M \begin{bmatrix} \bar{U}_1 \\ \bar{U}_2 \\ \vdots \end{bmatrix} \right] \tag{5.24}$$

with $\bar{K}^d$ corresponding to the global dynamic stiffness matrix of the group of foundations and M being the global mass matrix

$$\bar{K}^d = \begin{bmatrix} K^d_{11} & K^d_{12} & \cdots \\ K^d_{21} & K^d_{22} & \cdots \\ \vdots & \vdots & \ddots \end{bmatrix} - \omega^2 M \tag{5.25}$$

and

$$M = \begin{bmatrix} M_1 & & \\ & M_2 & \\ & & \ddots \end{bmatrix} \tag{5.26}$$

where K^d_{ij} are the forces and moments in foundation i corresponding to rigid motions of foundation j and M_i is the mass matrix of foundation i.

As in the case of one foundation, the errors are introduced by not taking into account the overall effect of the additional tractions required in each foundation to ensure complete compatibility. While this additional tractions have essentially no net resultant, and so have little effect on the foundation under consideration, they may nevertheless exert an important effect on neighboring foundations because of the fact that they are spatially distributed, and not point–like. As a result, some of these tractions are closer to the neighboring foundation than others and have, therefore, a greater influence. Hence, this approximation should not be used when the analysis involves very close foundations, or at least the results should be interpreted with great caution in such a case.

This approach is extremely easy to implement but there is a serious drawback in that the global dynamic stiffness matrix of the group of foundations must be known. To compute this matrix for a general situation requires complex and expensive models which would decrease the attractiveness of the approximate method described. Another approach is to try to obtain some rough estimates of the global dynamic stiffnesses and use them in equation 5.24. In this way, at least to a first approximation, some qualitative results could be obtained regarding the interaction effects of several foundations.

5.4 Dynamic Stiffnesses of Groups of Foundations

In order to be able to use Iguchi's method for finding approximate solutions for the Kinematic Interaction problem involving several embedded foundations, it is necessary to know the full dynamic stiffness matrix of the group of foundations. This section describes an approximate method for the computation of such stiffnesses as a function of the frequency of excitation ω. It will be assumed that the dynamic stiffnesses of the isolated foundations are known, or that these stiffnesses are being computed with the approximate formulae developed by Pais and Kausel [33] for cylindrical and rectangular foundations embedded in a halfspace. This approximation is described for the case of only two foundations but it can also be used for any number of foundations.

The basic approach consists in applying, one at a time, unit displacements for each of the degrees of freedom of a given foundation and evaluating approximately the displacements and generalized forces induced in the other foundation(s). Since the stiffnesses of the isolated foundations are known, the magnitude of the loads applied to them are taken equal to the stiffness terms so as to displace the foundation by one unit (assuming that the presence of the second foundation can be neglected as far as the self–stiffness is concerned). For embedded foundations the boundary tractions are forces transmitted to the soil at a certain depth. Since the displacement field due to buried forces is rather difficult to obtain, these forces will be replaced by statically equivalent surface forces distributed uniformly along the surface area of the foundation and distributed moments along the sides of the foundation. Also, to simplify further the procedure, the displacement field corresponding to a surface load will be substituted by the displacement field corresponding to a load twice as large applied to the full space. Figure 5.4 illustrates these various simplifications for the case of horizontal forces. The resulting displacements at any point in the halfspace are then computed using the full space Green's functions, which are known in closed form (see Dominguez [12]).

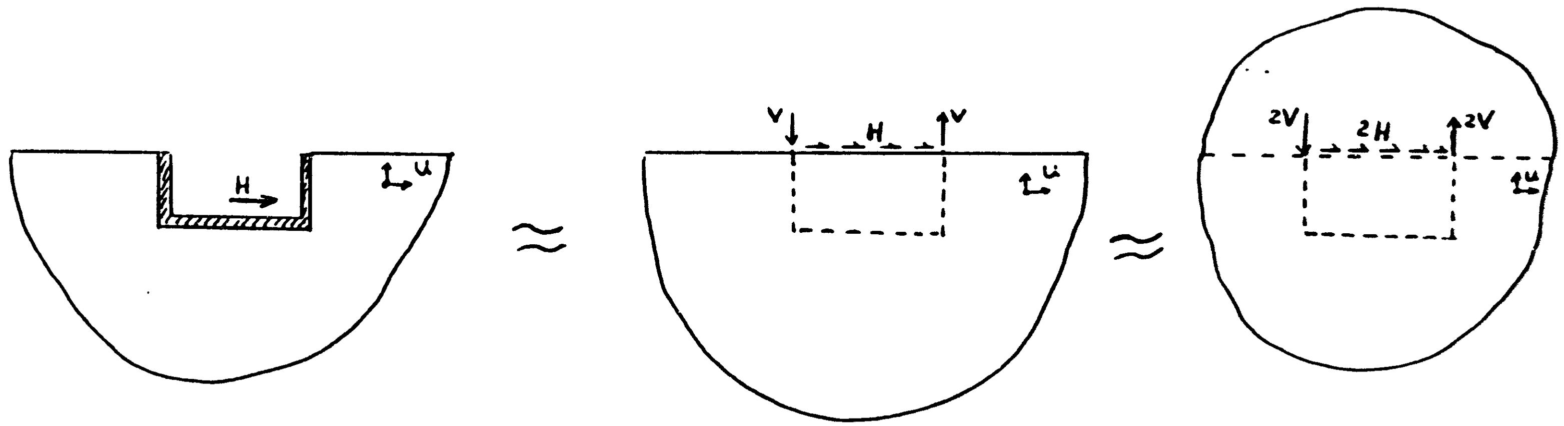

Fig. 5.4 - Assumptions in computing the displacement field

Referring to a cartesian coordinate system (1,2,3), the displacement in direction i at a point with coordinates (x_1,x_2,x_3) relative to a point where a load P with frequency ω is applied in direction j, is equal to

$$u_{ij} = \frac{1}{4\pi G}\left[\Psi \cdot \delta_{ij} - \aleph \cdot \frac{\partial r}{\partial x_i}\frac{\partial r}{\partial x_j}\right] \cdot P \tag{5.27}$$

$$\Psi = \left[1 - \frac{1}{(k_s r)^2} - \frac{i}{k_s r}\right] \cdot \frac{e^{-ik_s r}}{r} - \alpha^2\left[-\frac{1}{(k_p r)^2} - \frac{i}{k_p r}\right] \cdot \frac{e^{-ik_p r}}{r}$$

$$\aleph = \left[1 - \frac{3}{(k_s r)^2} - \frac{3i}{k_s r}\right] \cdot \frac{e^{-ik_s r}}{r} - \alpha^2\left[1 - \frac{3}{(k_p r)^2} - \frac{3i}{k_p r}\right] \cdot \frac{e^{-ik_p r}}{r}$$

where $i=\sqrt{-1}$; $r = \sqrt{x_1^2 + x_2^2 + x_3^2}$; G is the shear modulus of the soil; δ_{ij} is the Kronecker delta function; $\alpha = C_s/C_p$ (the ratio of shear wave velocity and P–wave velocity); $k_s = \omega/C_s$ and $k_p = \omega/C_p$.

Figures 5.5–5.10 display the variation of the displacement u multiplied by the distance to the load r as a function of the normalized frequency $\frac{\omega r}{C_s}$ and the angle between r and the diretion of loading θ. Both the real and imaginary parts, and the absolute value of the displacement components in the direction of the load as well as perpendicular to it are shown. It can be seen that, although the values of the displacements show some variation with frequency (and/or distance) and angle θ, these variations are smooth. Hence, when these displacements (Green's functions) will be used later as kernels in the integrals 5.28 and 5.29, it will be possible to sample the displacements at discrete points not too close to which other and still obtain accurate values for the integrals.

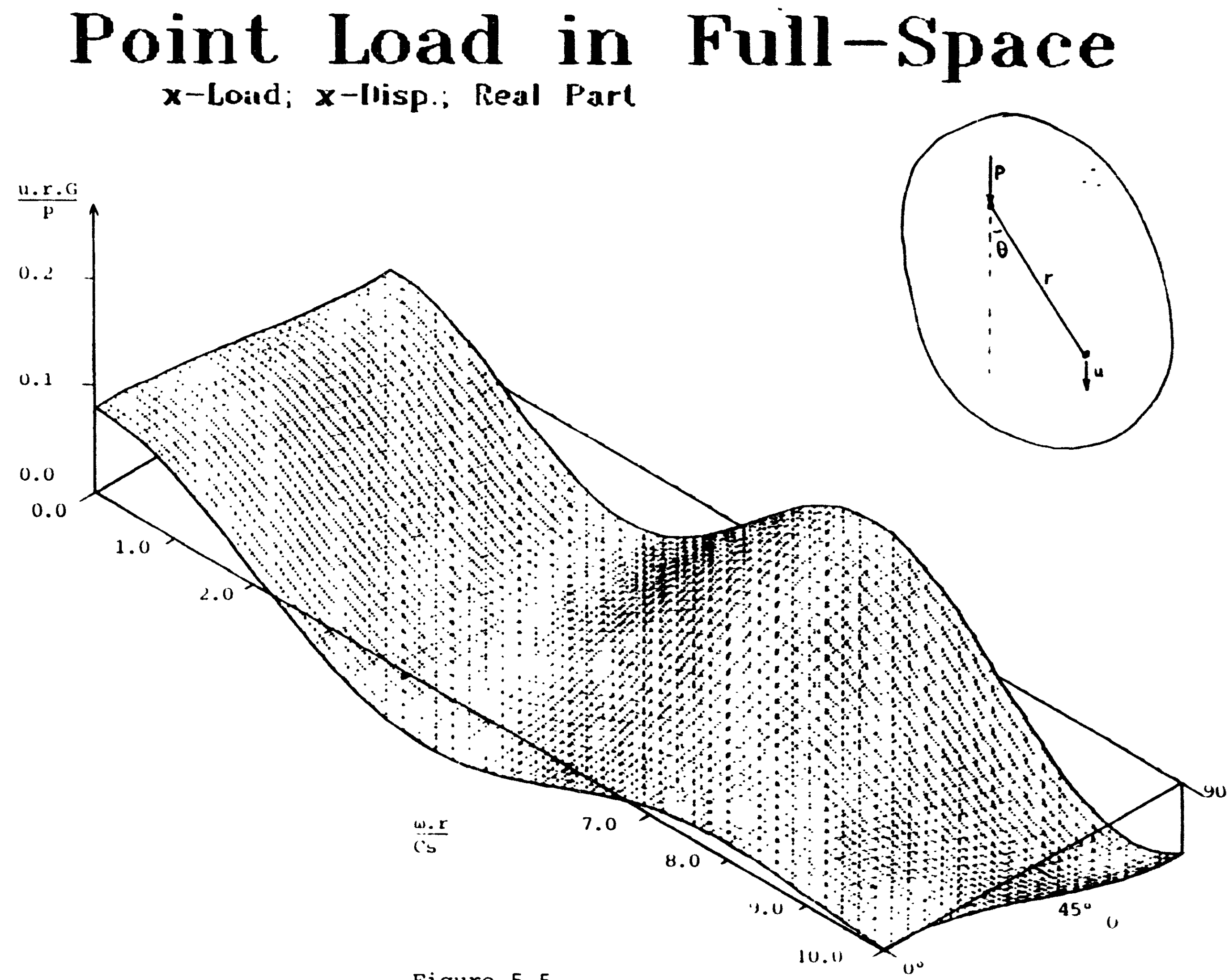
Point Load in Full-Space
x-Load; x-Disp.; Real Part
u.r.G / P
0.2
0.1
0.0
0.0
1.0
2.0
7.0
8.0
9.0
10.0
ω.r / Cs
0°
45°
θ
90°
P
θ
r
u

Figure 5.5

Point Load in Full-Space

x-Load; x-Disp.; Imag. Part

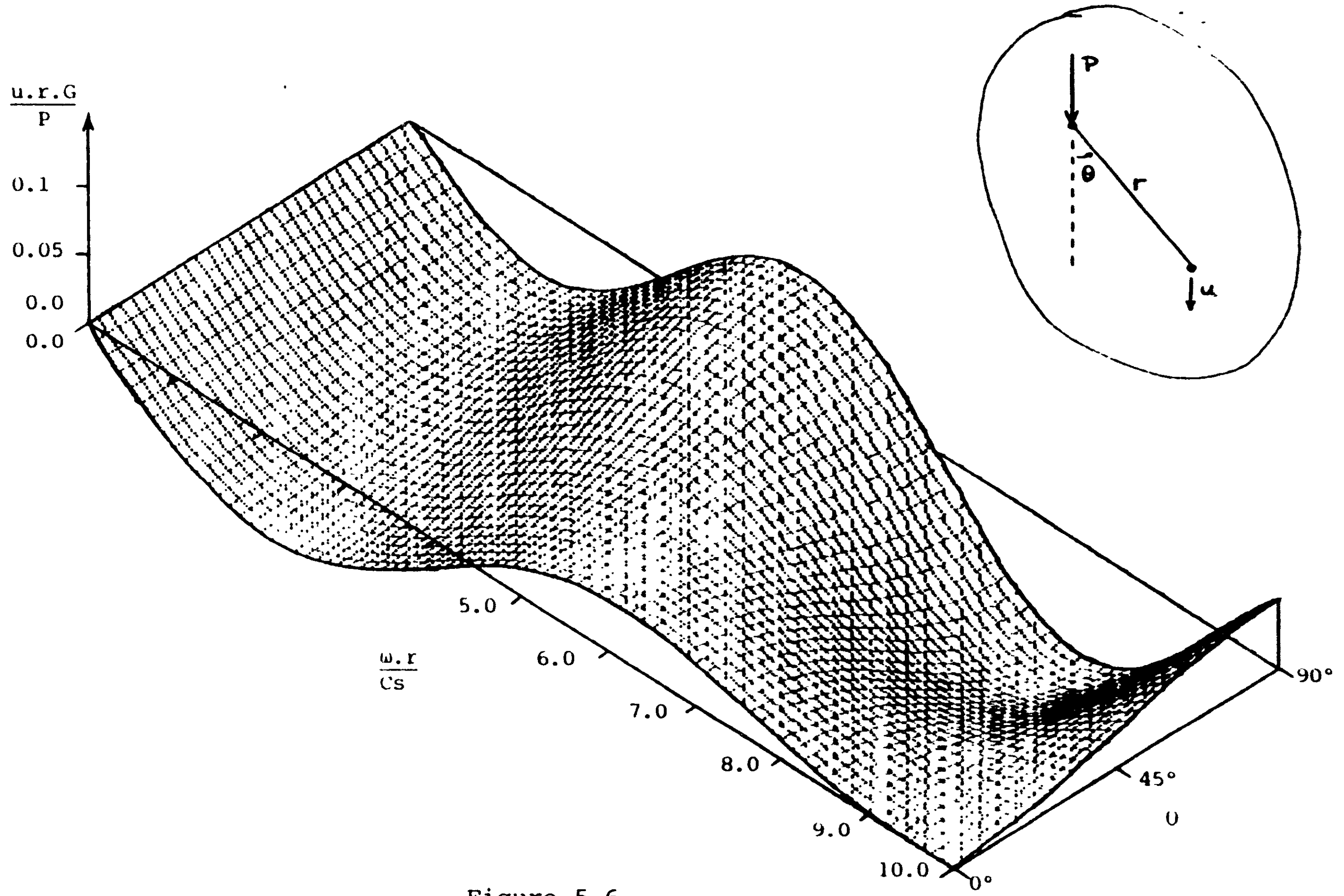

Figure 5.6

Point Load in Full-Space

x-Load; x-Disp.; Abs. Value

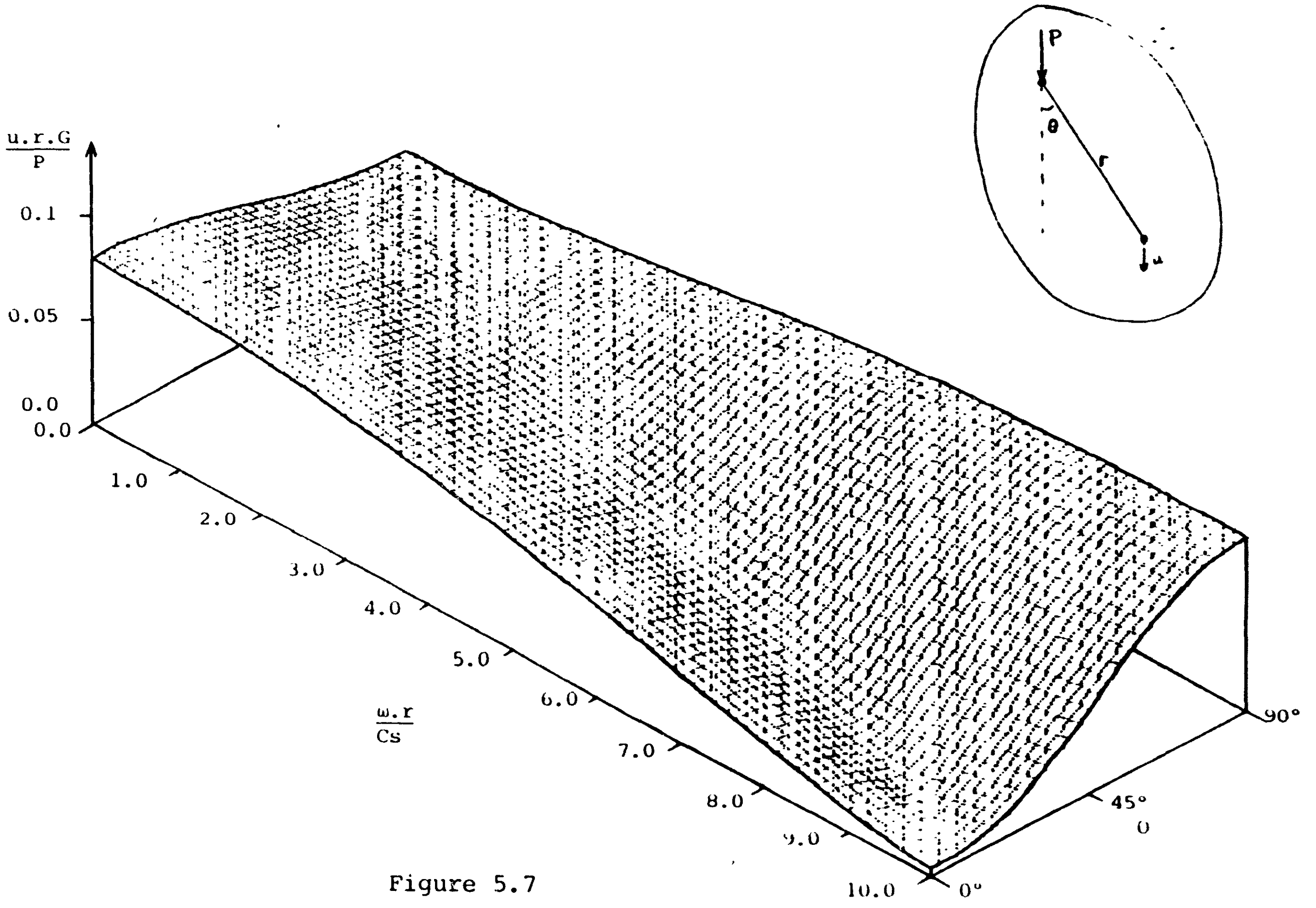

Figure 5.7

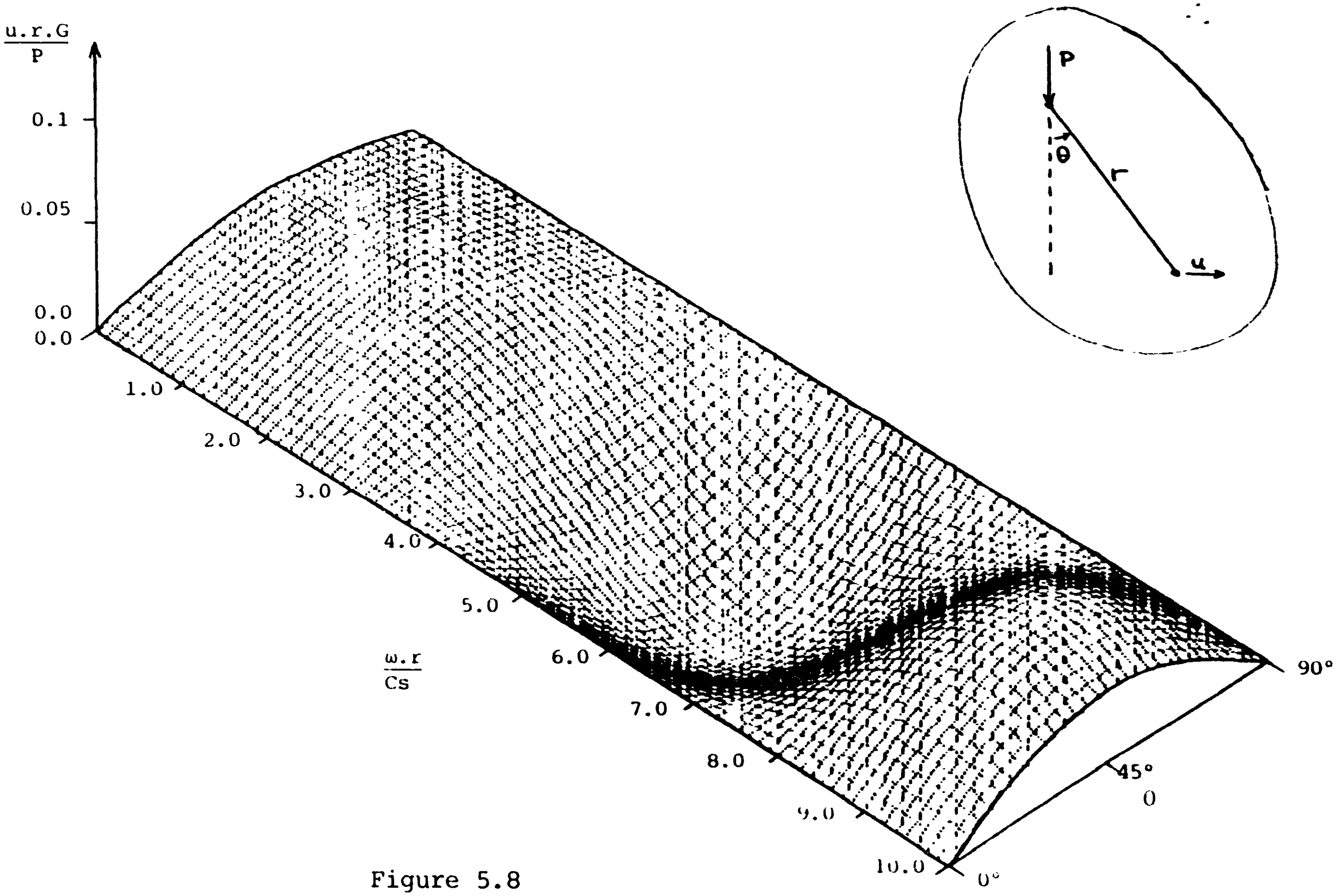

Point Load in Full-Space

x-Load; y-Disp.; Real Part

Figure 5.8

Point Load in Full-Space

x-Load; y-Disp.; Imag. Part

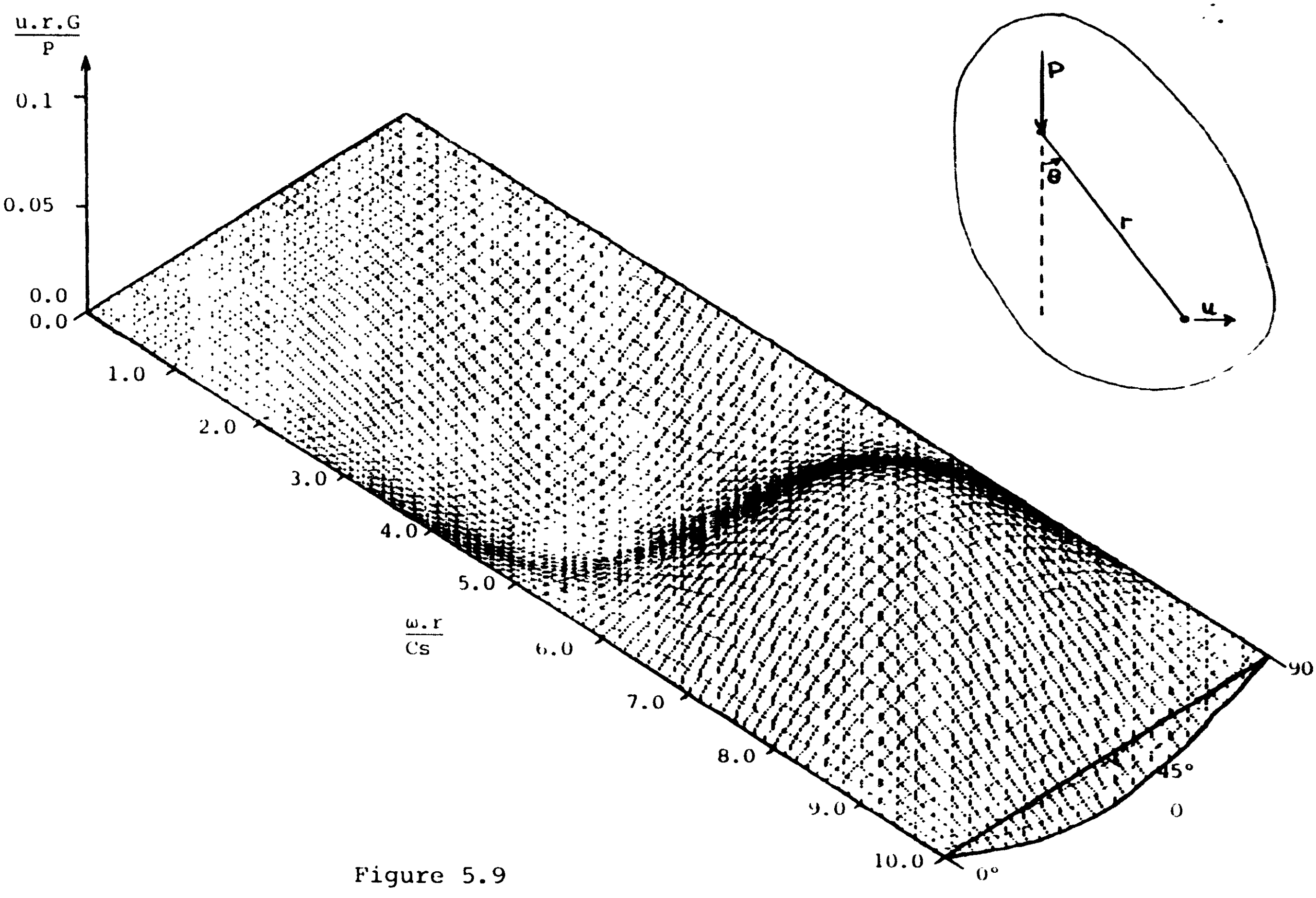

Figure 5.9

Point Load in Full-Space

x–Load; y–Disp.; Abs. Value

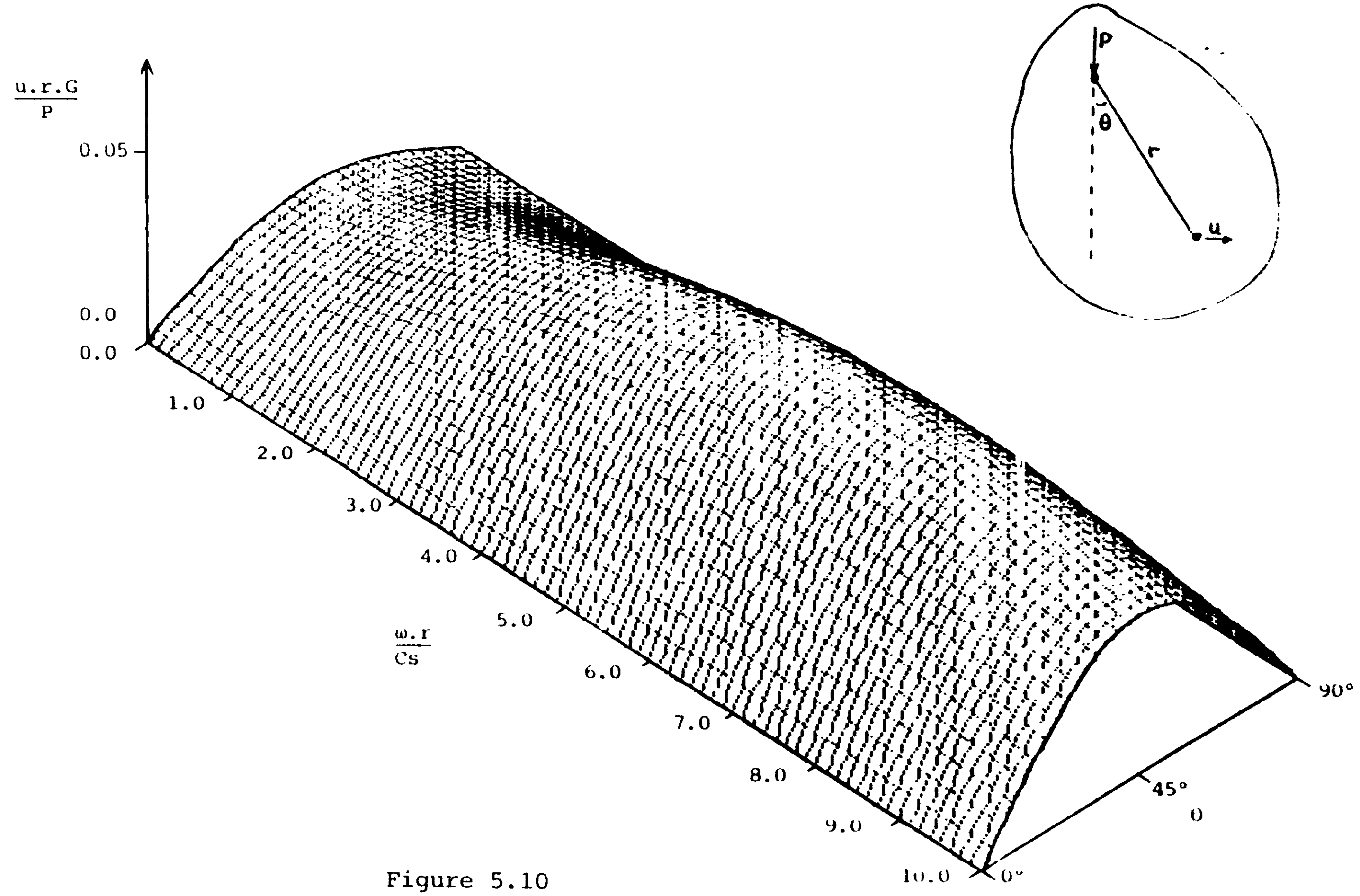

Figure 5.10

The loads corresponding to the degree of freedom being considered are then applied at discrete points at elevation z=0 over the area of the foundation (see fig. 5.4). The average rigid body motions and forces in the second foundation are then computed using an approach similar to Iguchi's method

$$U_2 = H_2^{-1} \iint_{S_2} T_2^T u^* \, dS_2 \tag{5.28}$$

$$F_2 = -\rho\omega^2 \iiint_{V_2} T_2^T u^* \, dv_2 \tag{5.29}$$

where u^* is the displacement field resulting from all the loads applied to foundation one; and T_2, H_2 are as defined in the previous section. Since, in general, these integrals can not be evaluated in closed form, they will be approximated by summations, considering a finite number of control points along the surface or volume of the excavated soil.

If the degree of freedom being considered was the horizontal displacement of foundation one, then we would have

$$U_1^T = [1 \ \ 0 \ \ 0 \ \ 0 \ \ 0 \ \ 0] \tag{5.30}$$

$$F_1^T = \left[K_{1H} \ \ 0 \ \ 0 \ \ 0 \ \ K_{1H\phi} \ \ 0\right] \tag{5.31}$$

This procedure is repeated for all rigid motions of both foundations and the displacements and forces are grouped into two matrices U and F

$$U = \begin{bmatrix} U_{11} & U_{12} \\ U_{21} & U_{22} \end{bmatrix} \tag{5.32}$$

$$F = \begin{bmatrix} F_{11} & F_{12} \\ F_{21} & F_{22} \end{bmatrix} \tag{5.33}$$

where U_{ij} and F_{ij} are the displacements and forces in foundation i due to each rigid motion of foundation j. With our choice of loads, we have that $U_{11} = U_{22} = I_6$ (the 6x6 identity matrix).

On the other hand, the stiffness matrix satisfies the following relation

$$K \cdot U = F \tag{5.34}$$

Solving for K yields

$$K = F \cdot U^{-1} \tag{5.35}$$

Because of errors of approximation while computing F and U, the resulting matrix K is not exactly symmetric. Since the true stiffness matrix must be symmetric, this condition will be enforced by substituting K by $1/2(K + K^T)$.

It is clear that the coupled dynamic stiffness matrix thus obtained is only approximate, but the method is simple to implement and very flexible, since any number of embedded foundations (and in particular rectangular and cylindrical foundations) at any relative position can be considered simultaneously. However, since the loads in this method are applied at the surface, the embedment of the foundations should be smaller than their mutual distance for meaningful results.

If, in addition, the foundations considered have mass, then the global mass matrix M can be incorporated into the stiffness matrix by simply adding to it the term $(-\omega^2 M)$.

5.5 Comparison with Numerical Results

Some comparisons with other numerical solutions were performed in order to assess the accuracy of the approximate method described in the previous sections.

First, the dynamic stiffnesses of a surface square foundation were obtained using the full space Green's functions while applying a double load. Two cases were considered: first, only four loads were applied at a distance of 0.3B from each corner (B being the halfwidth) in both directions; then, 36 equal loads were applied uniformly distributed over the surface of the foundation. The rigid displacement of the foundation was obtained by averaging the displacements at the corners, center and midpoints on each side of the foundation. Figure 5.11 shows the location of each load and control point. The variation with frequency of the vertical and horizontal stiffnesses obtained by this method is displayed in figures 5.12–5.15 for both the real part and normalized imaginary part (divided by a_0). These figures also show the more accurate solutions. It can be seen that the results obtained, while certainly crude, give a good indication of the stiffnesses of the square foundation especially in the low frequency range. For higher frequencies, it is apparent that more than 4 loads need be used since the contact stresses are more uniformly distributed over the soil–foundation interface than in the static case. These results seem to justify the validity of using the full space displacement–field with a double load to simulate the halfspace solution with a single load. It should be noted

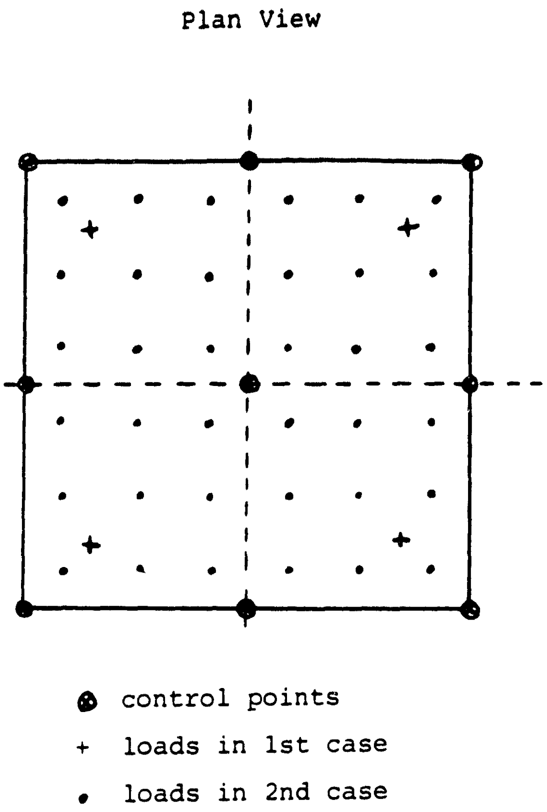

Fig. 5.11 - Location of load and control points

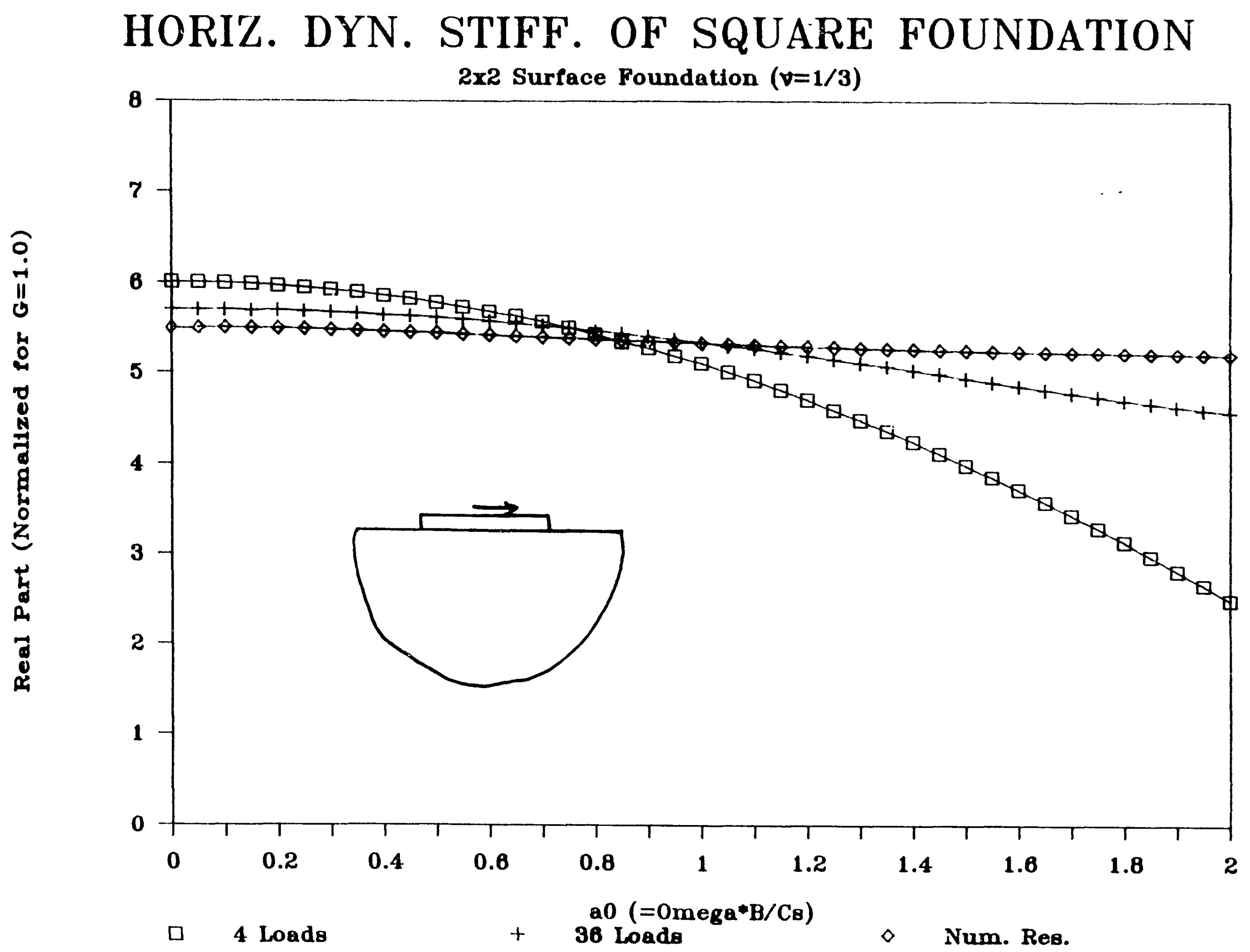
HORIZ. DYN. STIFF. OF SQUARE FOUNDATION
2x2 Surface Foundation (v=1/3)
Real Part (Normalized for G=1.0)
8
7
6
5
4
3
2
1
0
0
0.2
0.4
0.6
0.8
1
1.2
1.4
1.6
1.8
2
a0 (=Omega*B/Cs)
□ 4 Loads
+ 36 Loads
◇ Num. Res.

Figure 5.12

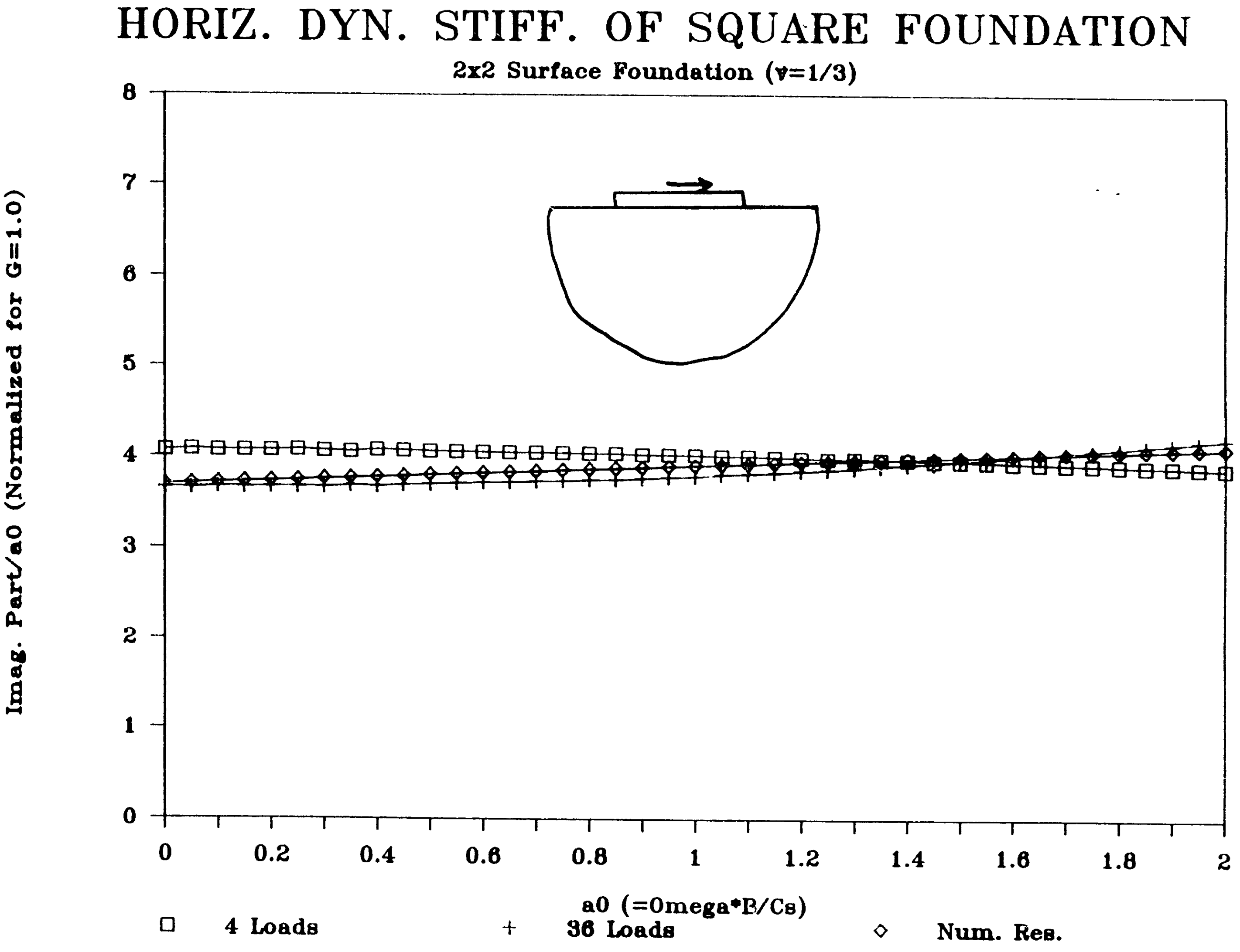
HORIZ. DYN. STIFF. OF SQUARE FOUNDATION
2x2 Surface Foundation (v=1/3)
Imag. Part/a0 (Normalized for G=1.0)
8
7
6
5
4
3
2
1
0
0
0.2
0.4
0.6
0.8
1
1.2
1.4
1.6
1.8
2
a0 (=Omega*B/Cs)
□ 4 Loads
+ 36 Loads
◇ Num. Res.

Figure 5.13

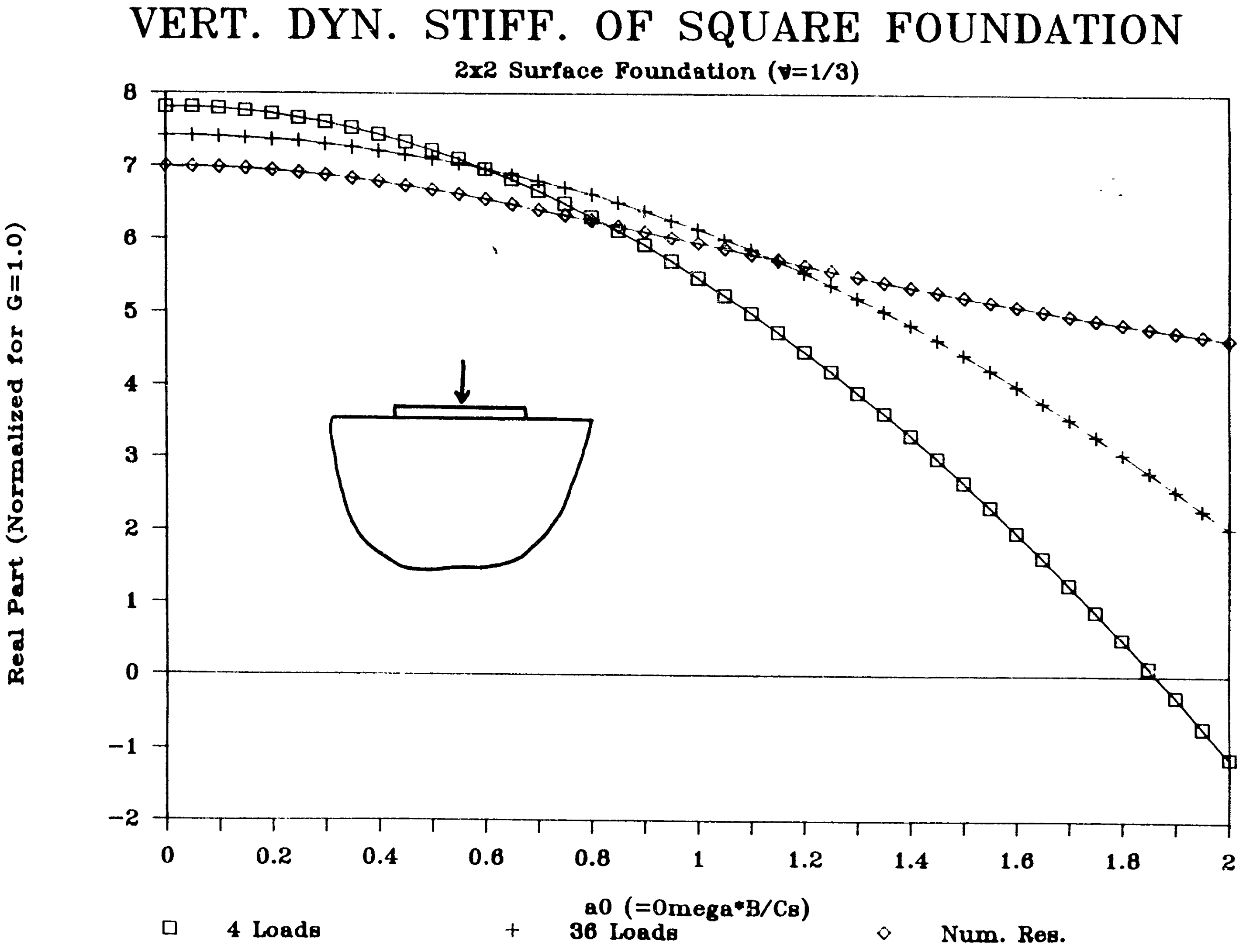
VERT. DYN. STIFF. OF SQUARE FOUNDATION
2x2 Surface Foundation (ν=1/3)
Real Part (Normalized for G=1.0)
8
7
6
5
4
3
2
1
0
−1
−2
0
0.2
0.4
0.6
0.8
1
1.2
1.4
1.6
1.8
2
a0 (=Omega*B/Cs)
□ 4 Loads
+ 36 Loads
◇ Num. Res.

Figure 5.14

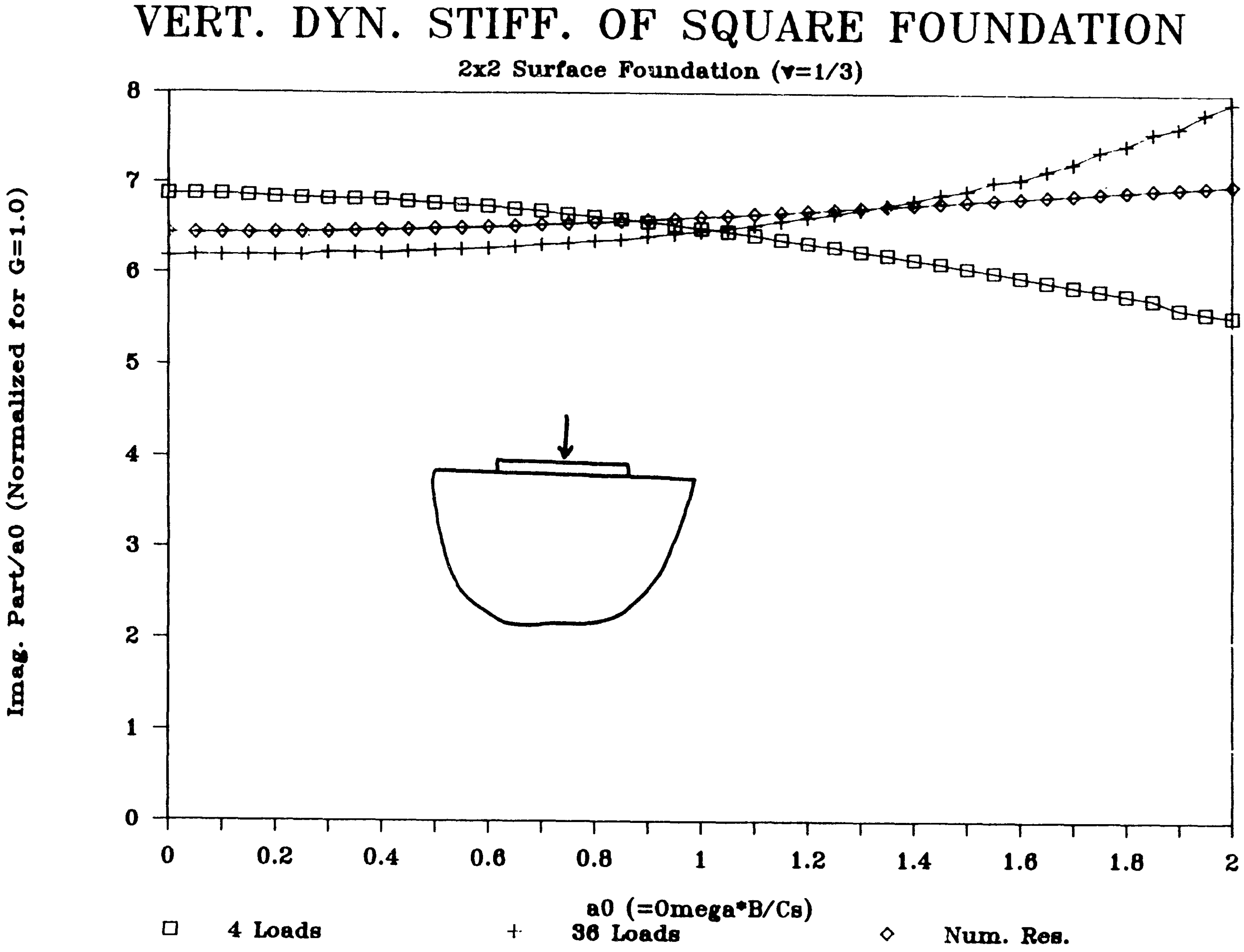
VERT. DYN. STIFF. OF SQUARE FOUNDATION
2x2 Surface Foundation (v=1/3)
Imag. Part/a0 (Normalized for G=1.0)
8
7
6
5
4
3
2
1
0
0
0.2
0.4
0.6
0.8
1
1.2
1.4
1.6
1.8
2
a0 (=Omega*B/Cs)
□ 4 Loads
+ 36 Loads
◇ Num. Res.

Figure 5.15

however, that this procedure discards the coupling between horizontal and vertical displacements at the surface, which in some cases might be important.

Unfortunately, the effects of coupling through the soil of two foundations embedded in a halfspace computed with the proposed method cannot be compared directly (as of this writing) with other numerical results published, since most of the solutions available are restricted either to surface foundations, or to foundations embedded in a stratum of finite depth. For this reason, to estimate the accuracy of the proposed method for embedded foundations, the results corresponding to two elongated rectangular foundations were compared with the results for two embedded strip footings subjected to vertically incident shear waves, obtained with the B.E. formulation developed in chapter 3. The horizontal displacement and rocking of the primary foundation are displayed in figures 5.16–5.19 for two values of the distance between the foundations and for the case of one isolated foundation. The secondary foundation was assumed to have a normalized mass equal to 1.0; this normalized mass was defined as the ratio of the mass of the foundation to the mass of the excavated soil, and its center of mass was taken at the geometric center of the excavated soil. Comparing the results obtained for rectangular foundations (using 5 loads and control points per side) with those corresponding to strip foundations, it can be seen that the effects of coupling between the foundations are qualitatively of the same magnitude, especially when the foundations are close together. If the fact is taken into account that for rectangular foundations there is radiation into the third dimension (which tends to decrease the coupling between the foundations) then the results of the comparison obtained appear to be very satisfactory. Again, the fact is stressed that the solution given by the current method is only approximate, and that the effect of coupling through the soil can be taken only in a qualitative sense. If a strong coupling is detected, then this is an indication that a more careful evaluation of this problem is warranted; on the other

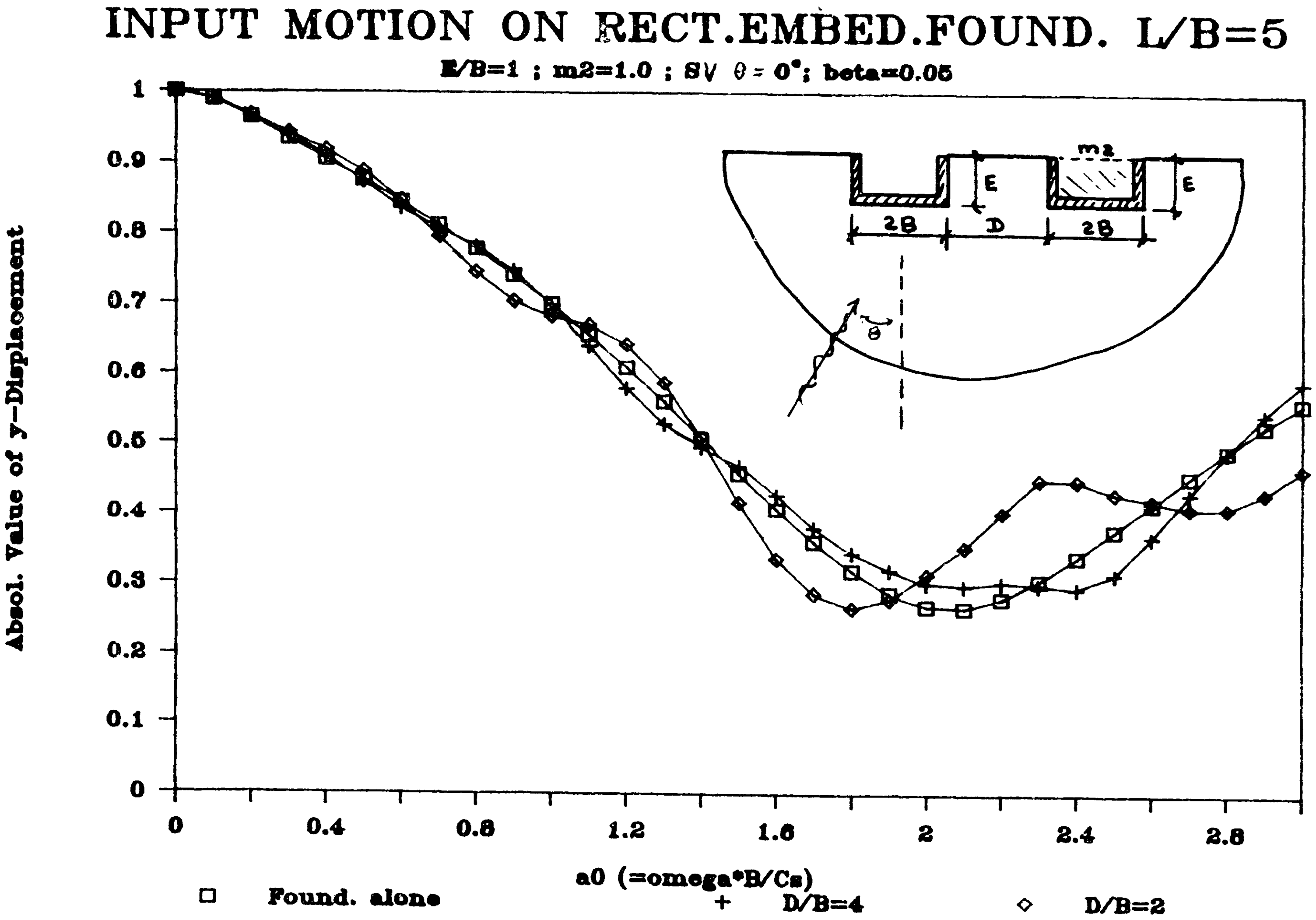
INPUT MOTION ON RECT.EMBED.FOUND. L/B=5
E/B=1 ; m2=1.0 ; SV θ = 0°; beta=0.05
Absol. Value of y-Displacement
1
0.9
0.8
0.7
0.6
0.5
0.4
0.3
0.2
0.1
0
0
0.4
0.8
1.2
1.6
2
2.4
2.8
a0 (=omega*B/Cs)
□ Found. alone
+ D/B=4
◇ D/B=2
m2
E
E
2B
D
2B
θ

Figure 5.16

INPUT MOTION ON RECT.EMBED.FOUND. L/B=5

E/B=1 ; m2=1.0 ; SV $\theta = 0°$; beta=0.05

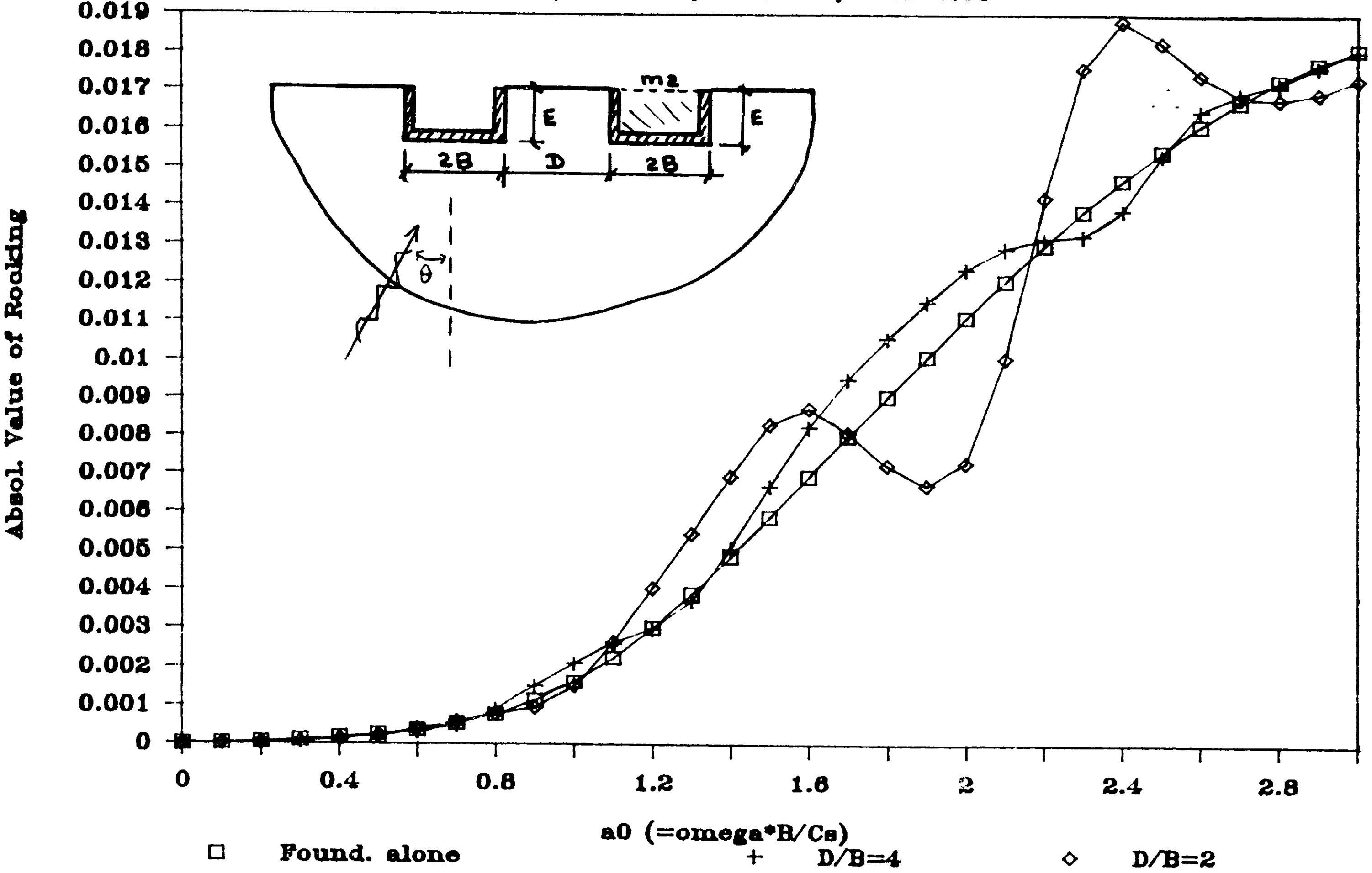

Figure 5.17

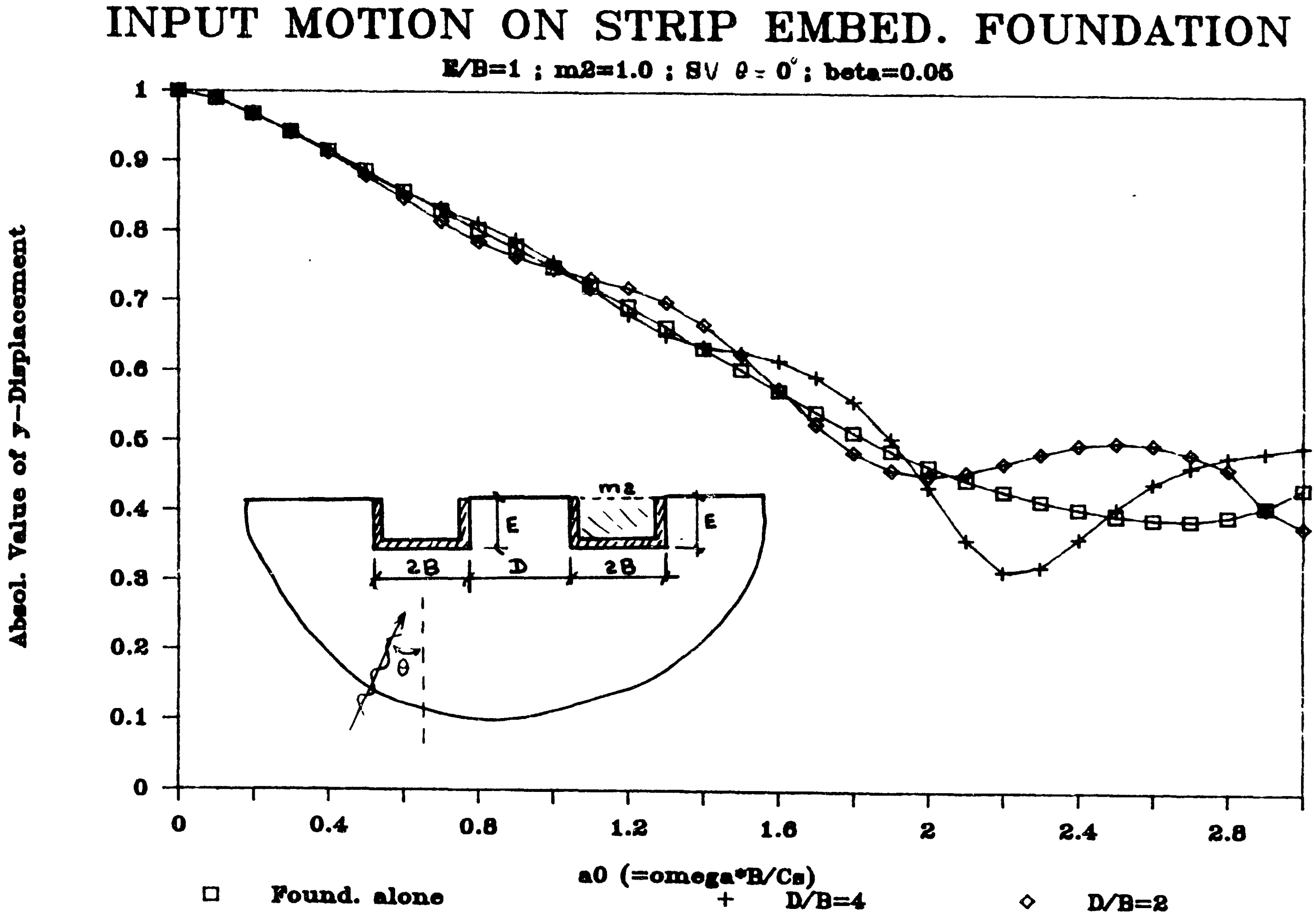
INPUT MOTION ON STRIP EMBED. FOUNDATION
E/B=1 ; m2=1.0 ; SV θ = 0° ; beta=0.05
Absol. Value of y-Displacement
1
0.9
0.8
0.7
0.6
0.5
0.4
0.3
0.2
0.1
0
0
0.4
0.8
1.2
1.6
2
2.4
2.8
a0 (=omega*B/Cs)
□ Found. alone
+ D/B=4
◇ D/B=2
m2
E
E
2B
D
2B
θ

Figure 5.18

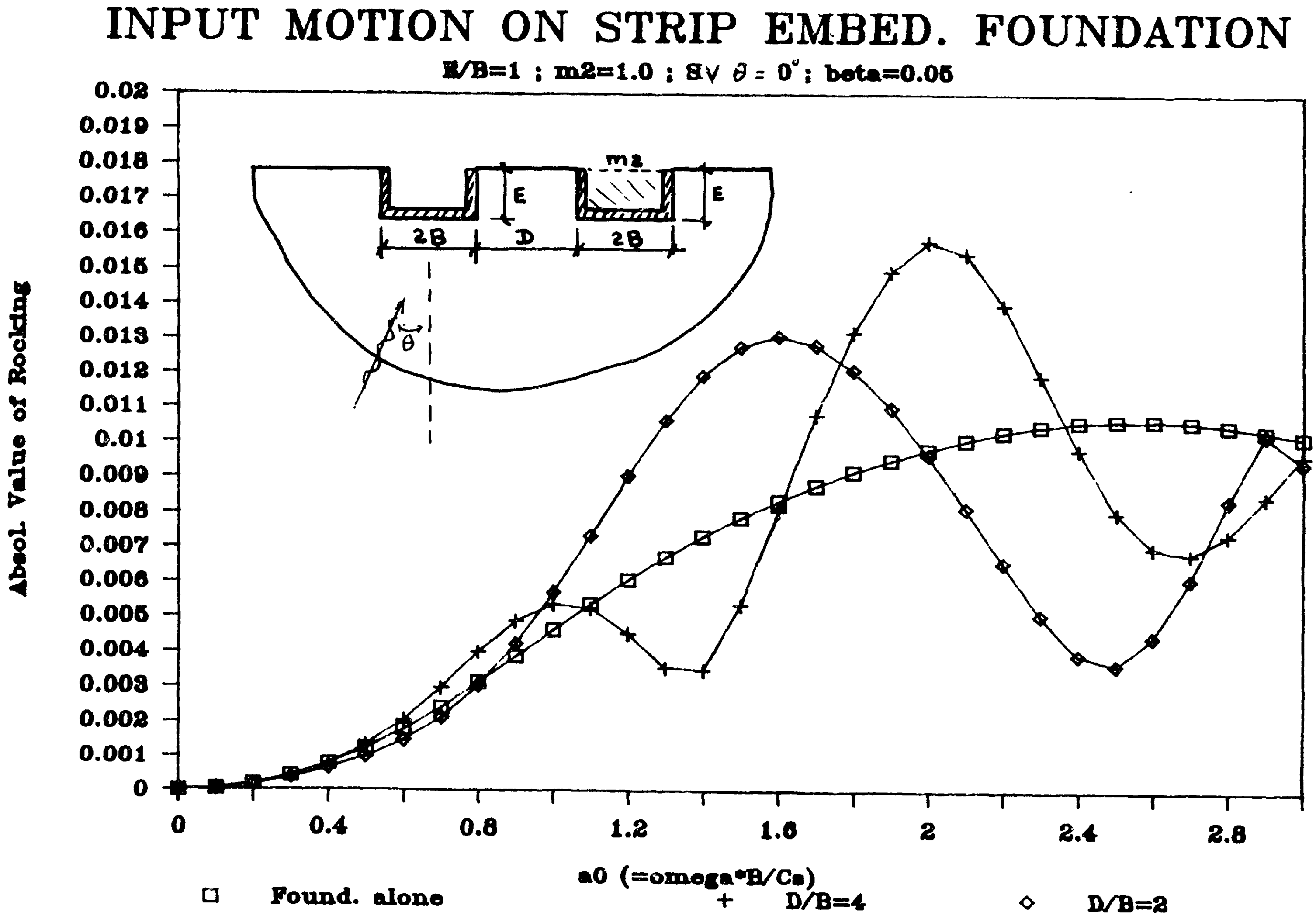
INPUT MOTION ON STRIP EMBED. FOUNDATION
E/B=1 ; m2=1.0 ; SV θ = 0°; beta=0.05
Absol. Value of Rocking
0.02
0.019
0.018
0.017
0.016
0.015
0.014
0.013
0.012
0.011
0.01
0.009
0.008
0.007
0.006
0.005
0.004
0.003
0.002
0.001
0
0
0.4
0.8
1.2
1.6
2
2.4
2.8
a0 (=omega*B/Cs)
m2
E
E
2B
D
2B
θ
□ Found. alone
+ D/B=4
◇ D/B=2

Figure 5.19

hand, if the computation indicates only weak coupling, it follows that the expense of more sophisticated analysis can be spared. In other words, the proposed procedure could be used to assess the potential of coupling through the soil without the need of complex programs.

5.6 Examples

The approximate solution described in the previous sections is used to study the effects of coupling through the soil in some typical situations. First, the global dynamic stiffness matrix of two square embedded foundations are evaluated using the procedure described in section 5.4. It is assumed that the foundation of interest (foundation one) is massless, while the second foundation has a mass that is m2 times the mass of the excavated soil. The global stiffness matrix involving both foundations is then condensed, and only the degrees of freedom of foundation one are retained. This allows to compare the stiffnesses, as seen from foundation one, with the corresponding stiffnesses for the case when this foundation is standing alone. The main differences induced by the presence of the second foundation are that the soil bonded to the neighboring foundation must vibrate as a rigid body, and that there are inertial forces associated with the mass of the second foundation and loss of such forces because of the excavation. These effects can increase or decrease the stiffness term of foundation one, depending on the frequency of vibration.

Figures 5.20–5.24 display the results obtained for several terms of the dynamic stiffness matrix. The coupling terms presented, which are zero for the case of a foundation standing alone, are normalized with respect to the square root of the corresponding diagonal terms. It can be seen that the horizontal and vertical stiffnesses are modified, especially in the low frequency range, and that the mass of the second

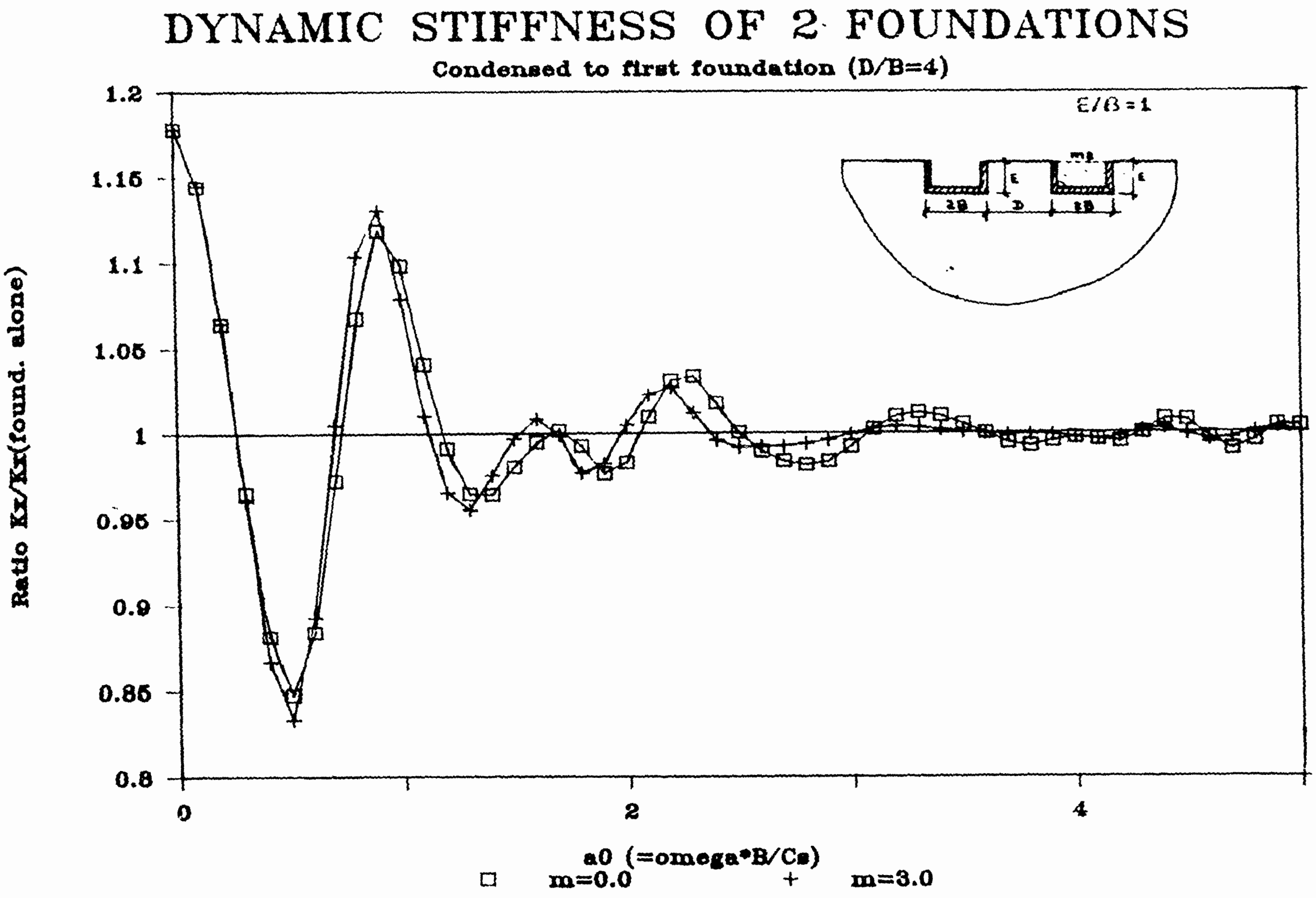
DYNAMIC STIFFNESS OF 2 FOUNDATIONS
Condensed to first foundation (D/B=4)
E/B=1
2B
D
2B
E
1.2
1.15
1.1
1.05
1
0.95
0.9
0.85
0.8
Ratio Kx/Kx(found. alone)
0
2
4
a0 (=omega*B/Cs)
□ m=0.0
+ m=3.0

Figure 5.20

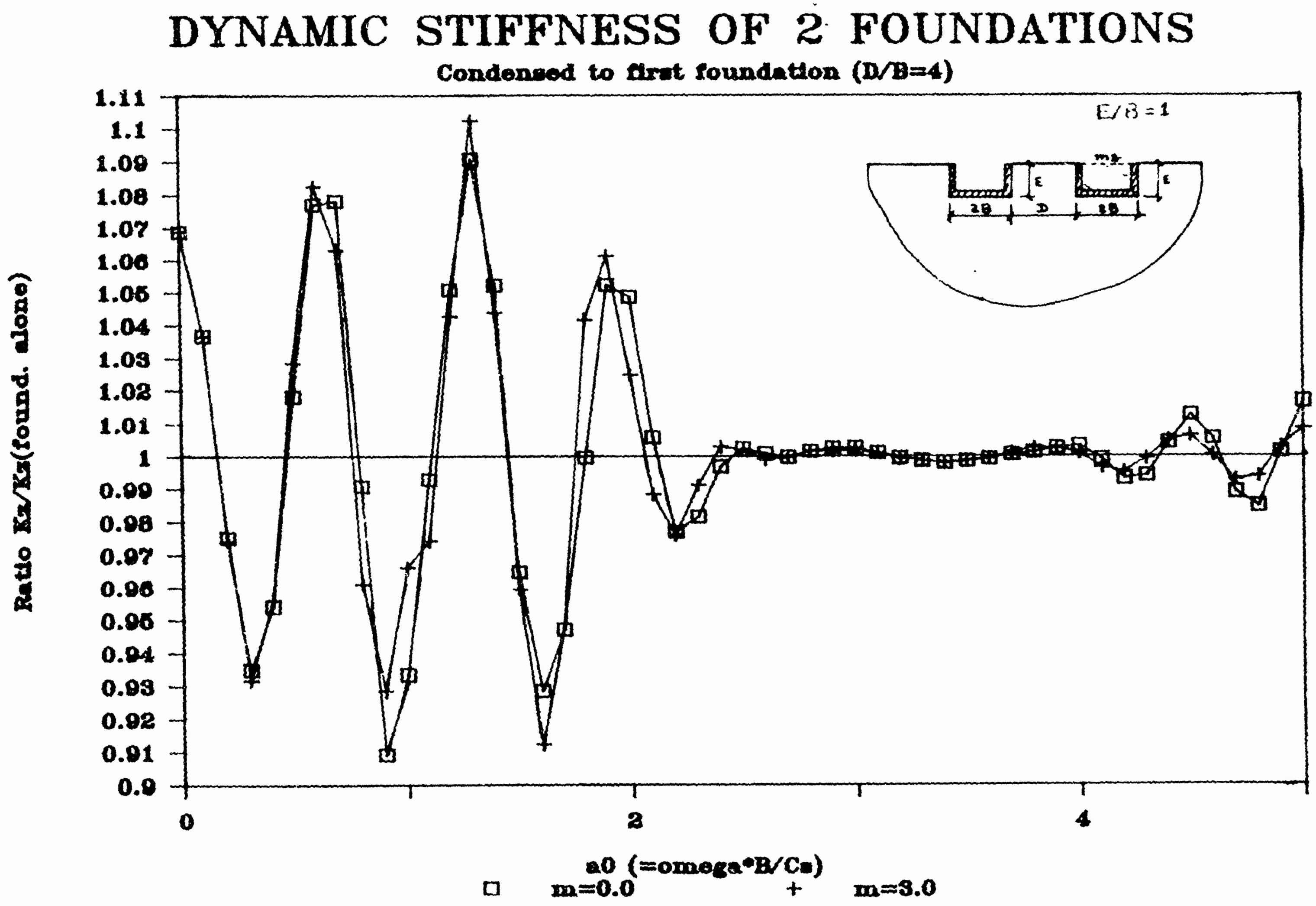
DYNAMIC STIFFNESS OF 2 FOUNDATIONS
Condensed to first foundation (D/B=4)
Ratio Kz/Kz(found. alone)
1.11
1.1
1.09
1.08
1.07
1.06
1.05
1.04
1.03
1.02
1.01
1
0.99
0.98
0.97
0.96
0.95
0.94
0.93
0.92
0.91
0.9
0
2
4
a0 (=omega*B/Cs)
□ m=0.0
+ m=3.0
E/B = 1
mB
E
E
2B
D
2B

Figure 5.21

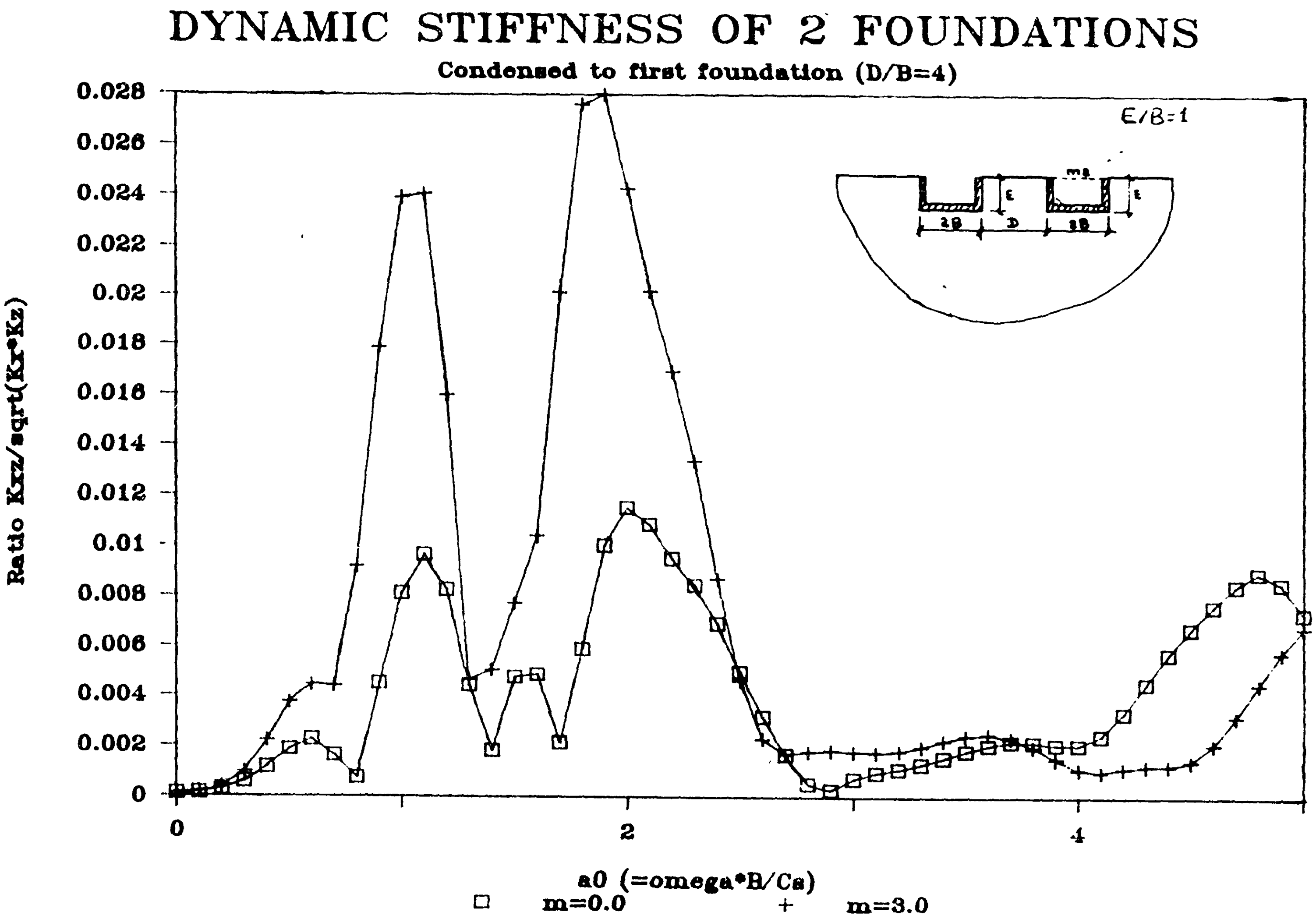
DYNAMIC STIFFNESS OF 2 FOUNDATIONS
Condensed to first foundation (D/B=4)
Ratio Kxz/sqrt(Kx*Kz)
0.028
0.026
0.024
0.022
0.02
0.018
0.016
0.014
0.012
0.01
0.008
0.006
0.004
0.002
0
0
2
4
a0 (=omega*B/Cs)
□ m=0.0
+ m=3.0
E/B=1
m2
E
E
2B
D
2B

Figure 5.22

DYNAMIC STIFFNESS OF 2 FOUNDATIONS

Condensed to first foundation (D/B=4)

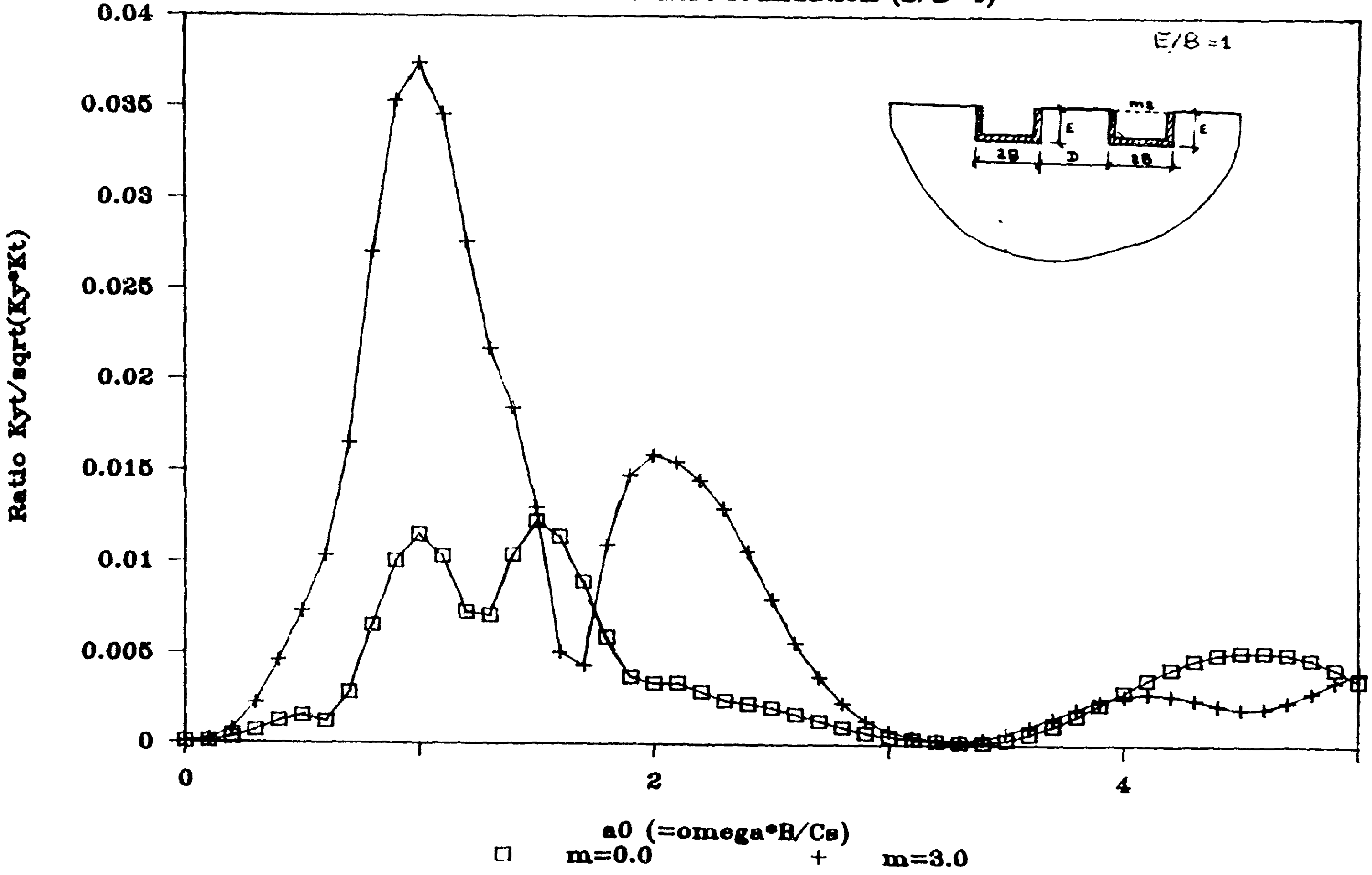

Figure 5.23

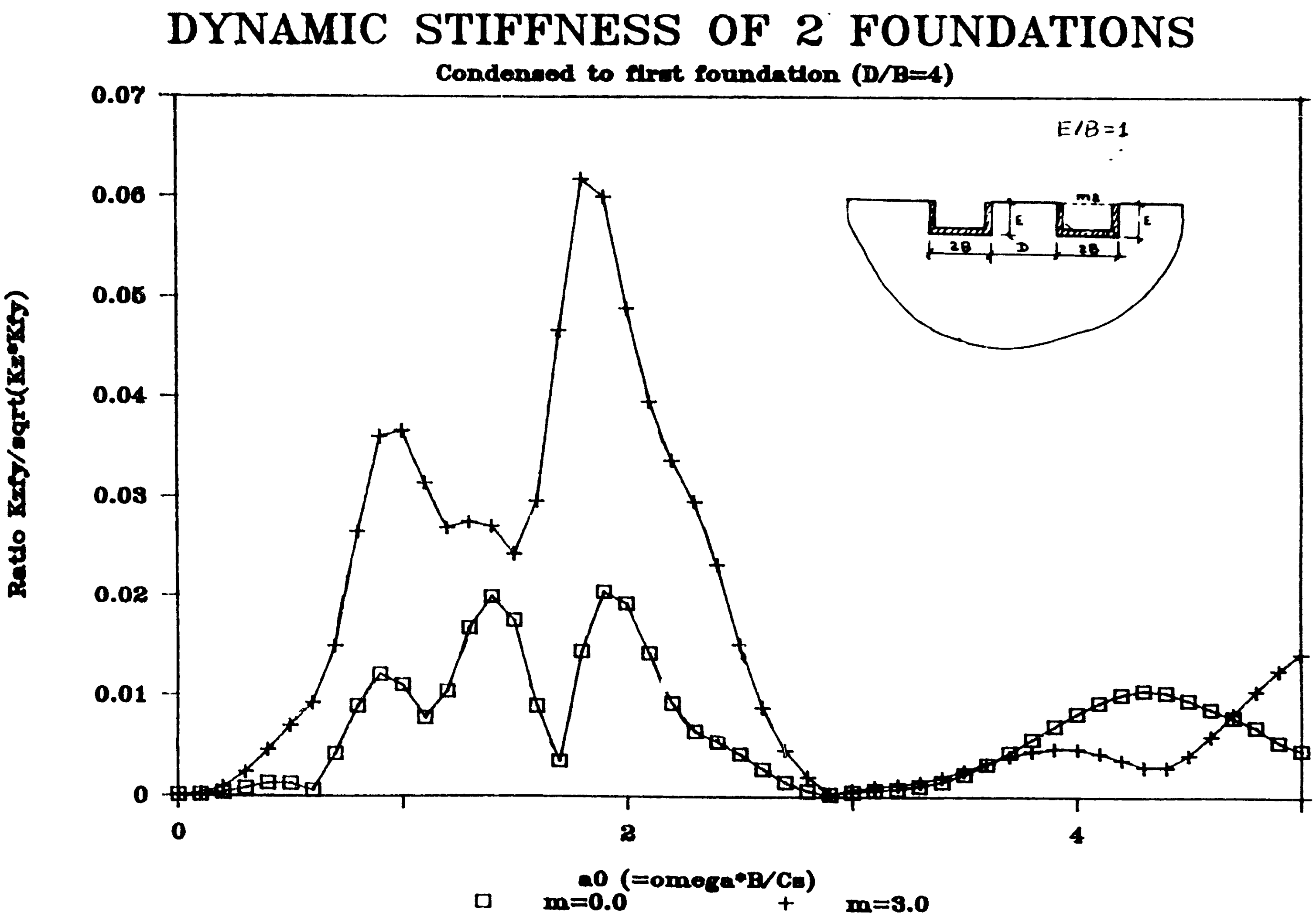
DYNAMIC STIFFNESS OF 2 FOUNDATIONS
Condensed to first foundation (D/B=4)
E/B=1
m2
E
E
2B
D
2B
Ratio Kzfy/sqrt(Kz*Kfy)
0.07
0.06
0.05
0.04
0.03
0.02
0.01
0
0
2
4
a0 (=omega*B/Cs)
□ m=0.0
+ m=3.0

Figure 5.24

foundation does not influence very much these terms. However, the coupling terms are very dependent on the mass of the second foundation, even though their normalized values are small. The peaks observed in figures 5.22–5.24 seem to coincide with frequencies for which the rotations induced in the foundation by travelling waves are higher.

The motion induced in foundation one by seismic waves is analyzed next. Three different cases are compared: the foundation standing alone; the foundation and another similar foundation present at a distance D/B=2, and having a normalized mass equal to 1.0; and a third case, similar to the second, except that the normalized mass is equal to 3.0. Three seismic motions are considered: SV waves propagating vertically; SV waves propagating at an angle of 45^{O} with respect to the vertical; and SH waves propagating horizontally. All waves travel in a vertical plane containing the x–axis. Due to symmetry, the SV waves induce only displacements in the x and z direction and rotations about the y–axis, while the SH waves induce motions in the y direction and rotations about the x (rocking) and z (torsion) axes. Figures 5.25–5.33 show the motions in foundation one for each wave type. The most pronounced effects of coupling through the soil are observed when SV waves travel vertically; these effects seem particularly important when the mass of the second foundation is increased. Somewhat different results are obtained when the SV waves travel at an angle of 45^{O}, since noticeable effects are observed only for the rotation mode. Conversely, SH waves produce very little coupling between the two foundations; this can be attributed to the fact that the motions in this case are perpendicular to the direction connecting the two foundations, and therefore, attenuate much faster in the x–direction.

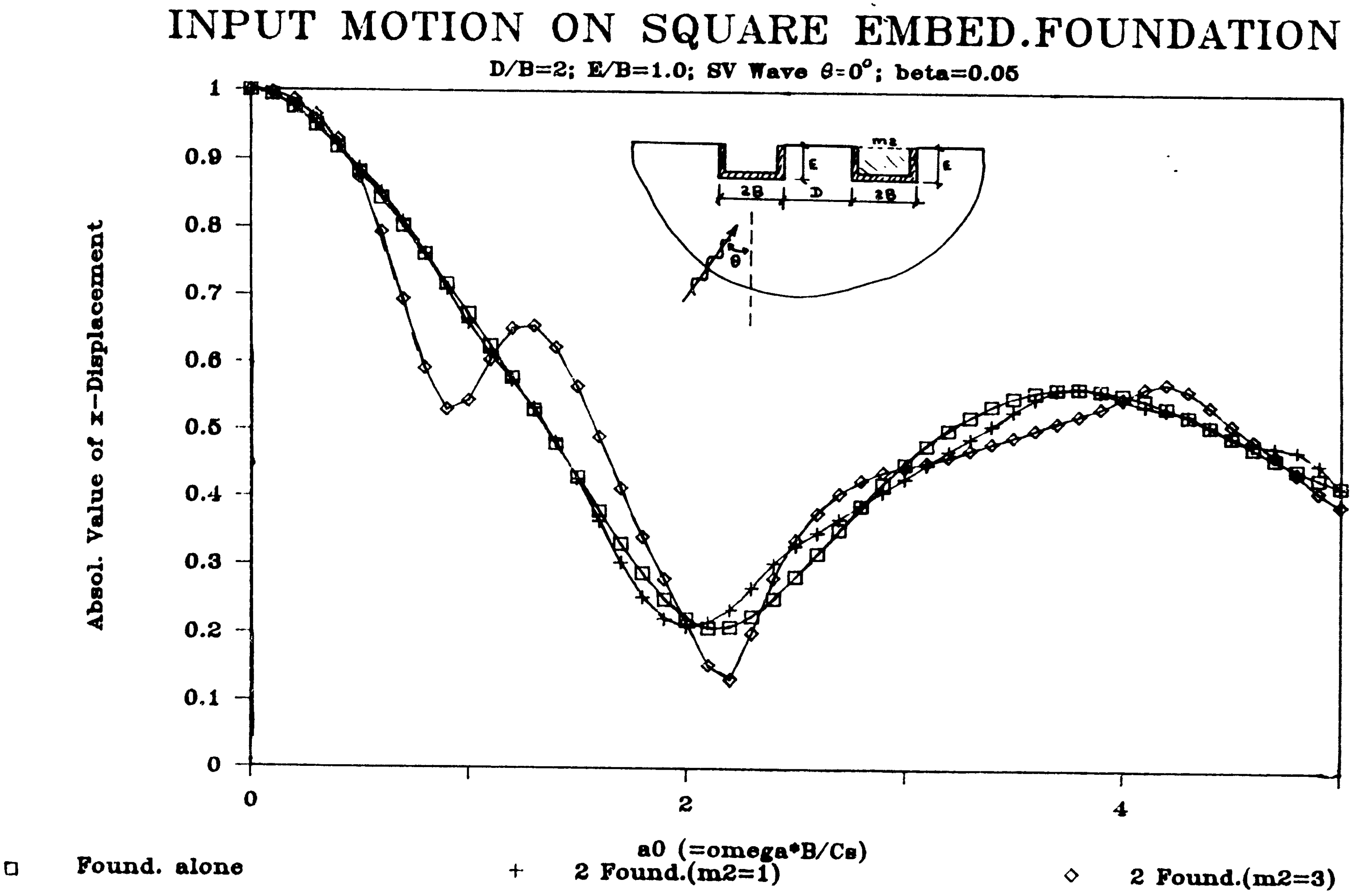
INPUT MOTION ON SQUARE EMBED.FOUNDATION
D/B=2; E/B=1.0; SV Wave θ=0°; beta=0.05
Absol. Value of x-Displacement
1
0.9
0.8
0.7
0.6
0.5
0.4
0.3
0.2
0.1
0
0
2
4
a0 (=omega*B/Cs)
□ Found. alone
+ 2 Found.(m2=1)
◇ 2 Found.(m2=3)
m2
E
2B
D
θ

Figure 5.25

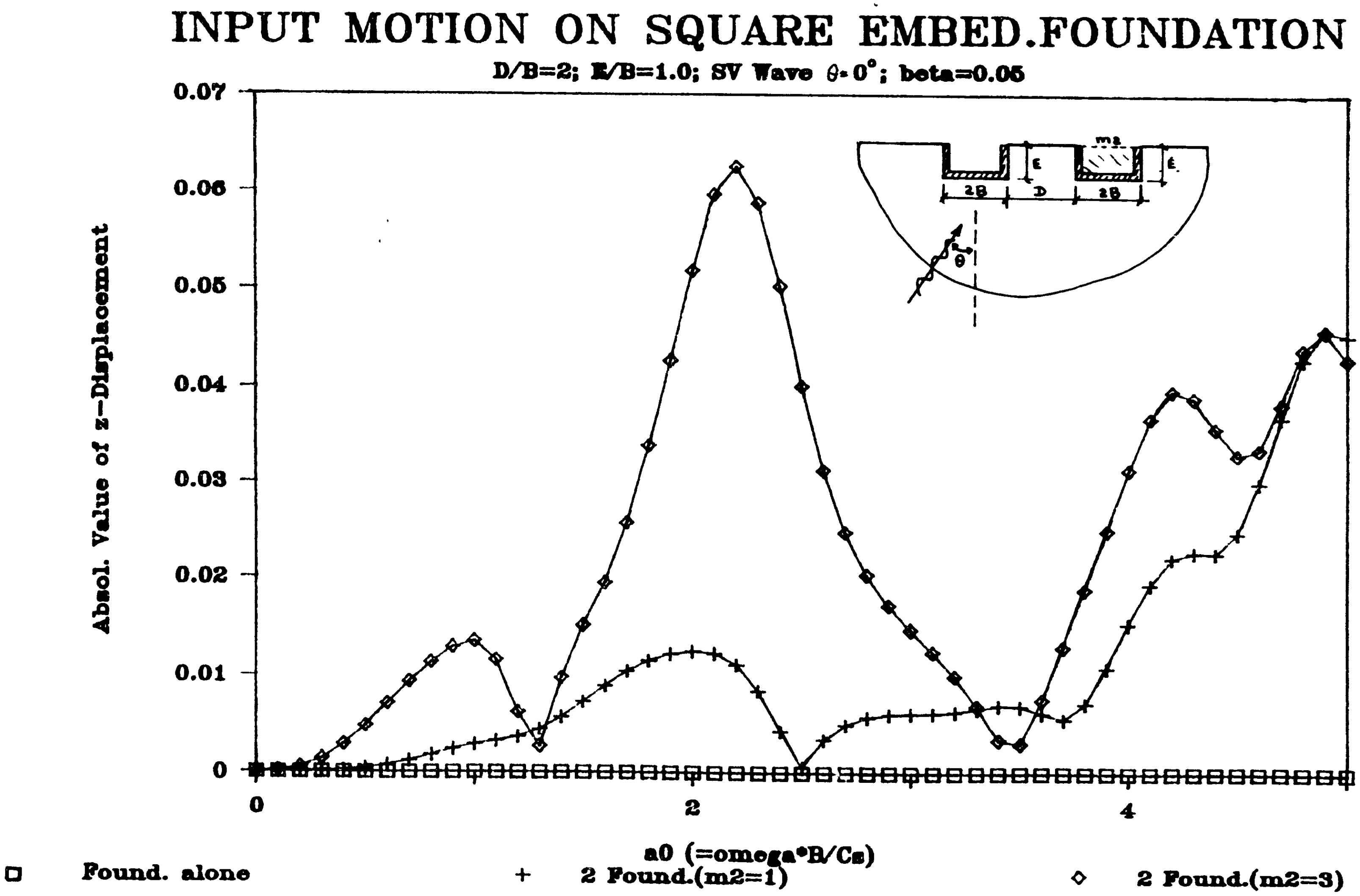
INPUT MOTION ON SQUARE EMBED.FOUNDATION
D/B=2; E/B=1.0; SV Wave θ=0°; beta=0.05
Absol. Value of z-Displacement
0.07
0.06
0.05
0.04
0.03
0.02
0.01
0
0
2
4
a0 (=omega*B/Cs)
□ Found. alone
+ 2 Found.(m2=1)
◇ 2 Found.(m2=3)
m2
E
2B
D
θ

Figure 5.26

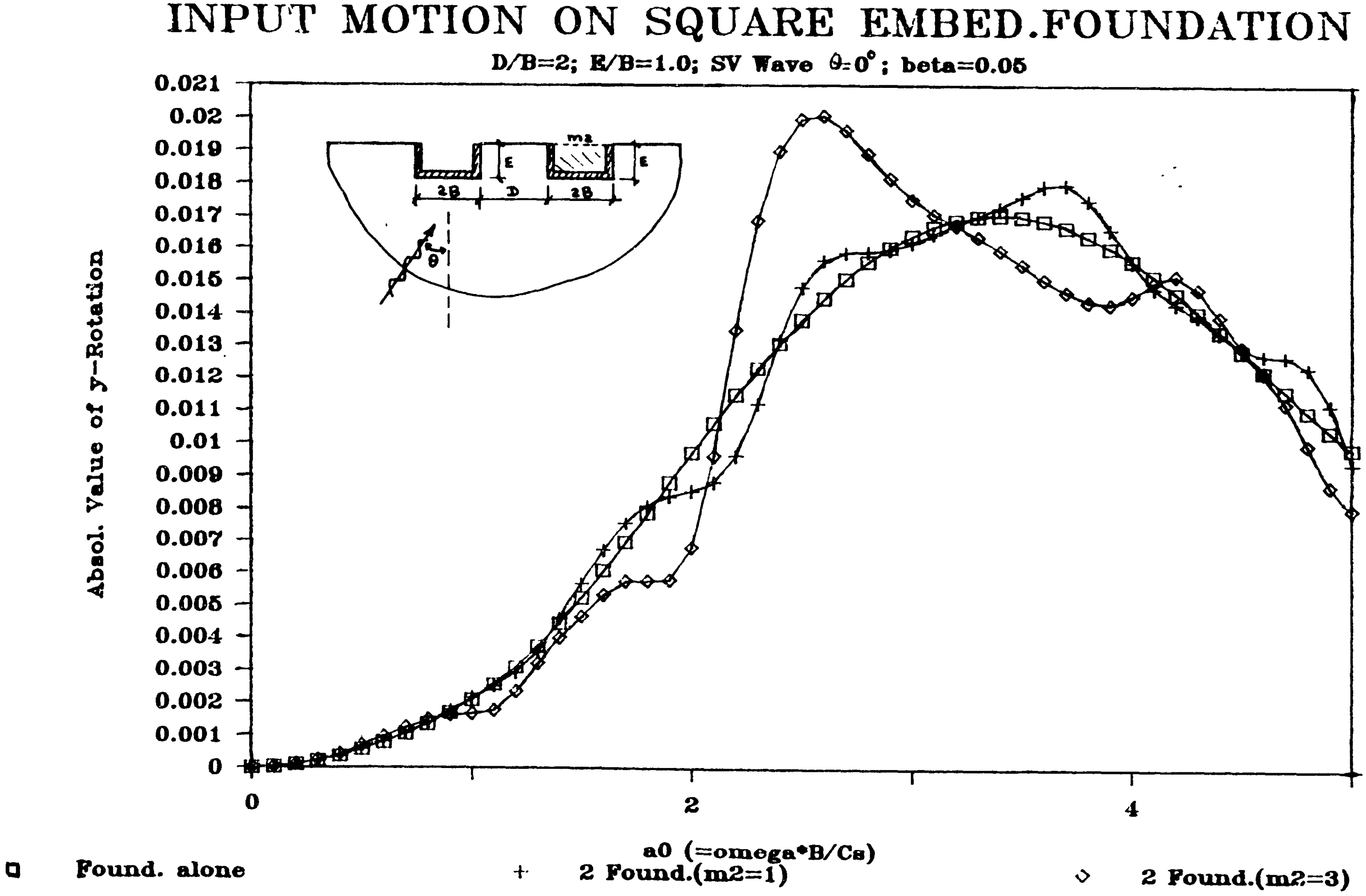
INPUT MOTION ON SQUARE EMBED.FOUNDATION
D/B=2; E/B=1.0; SV Wave θ=0°; beta=0.05
Absol. Value of y-Rotation
0.021
0.02
0.019
0.018
0.017
0.016
0.015
0.014
0.013
0.012
0.011
0.01
0.009
0.008
0.007
0.006
0.005
0.004
0.003
0.002
0.001
0
0
2
4
a0 (=omega*B/Cs)
m2
E
E
2B
D
2B
θ
□ Found. alone
+ 2 Found.(m2=1)
◇ 2 Found.(m2=3)

Figure 5.27

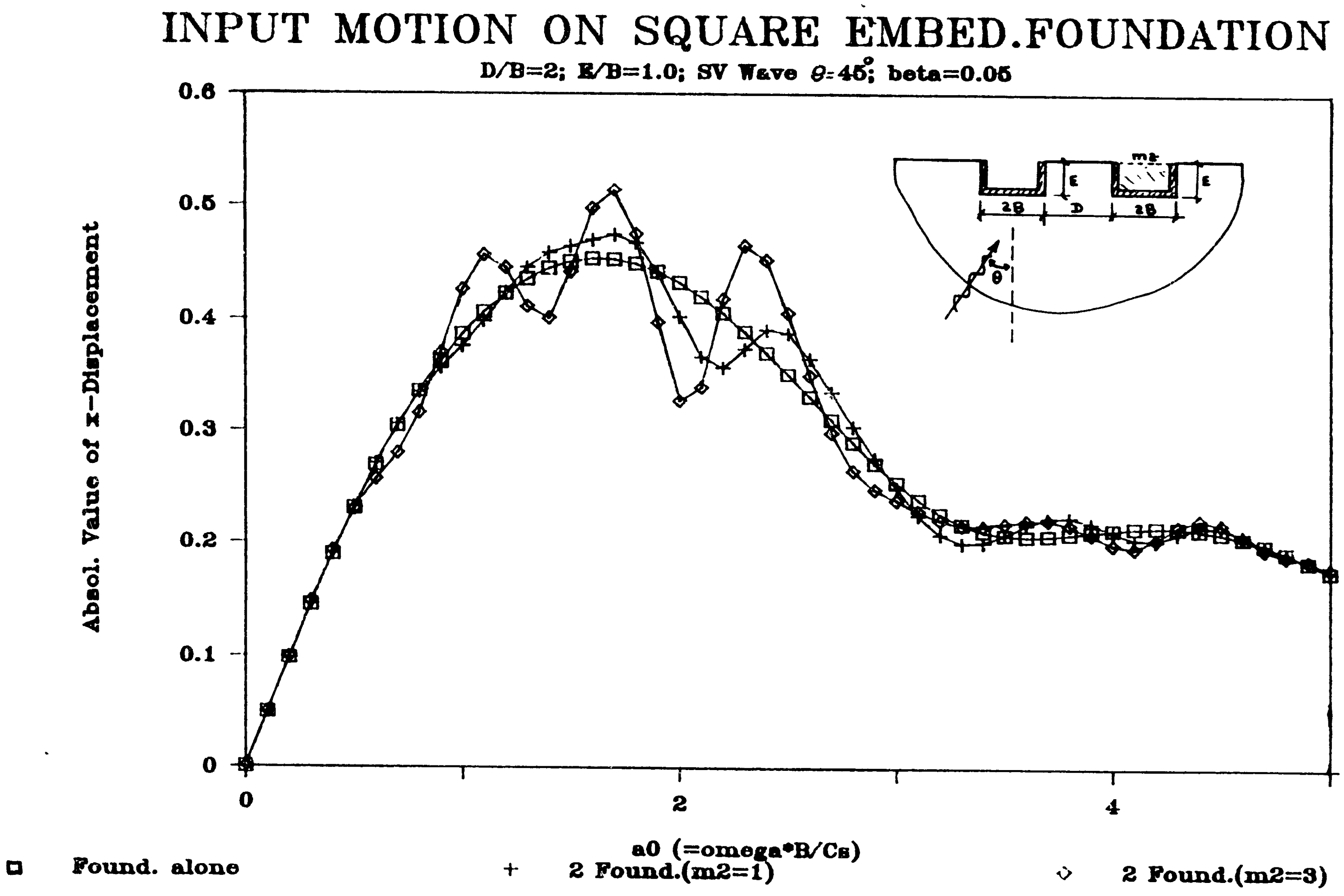
INPUT MOTION ON SQUARE EMBED.FOUNDATION
D/B=2; E/B=1.0; SV Wave θ=45°; beta=0.05
Absol. Value of x-Displacement
0.6
0.5
0.4
0.3
0.2
0.1
0
0
2
4
a0 (=omega*B/Cs)
m2
E
2B
D
θ
Found. alone
2 Found.(m2=1)
2 Found.(m2=3)

Figure 5.28

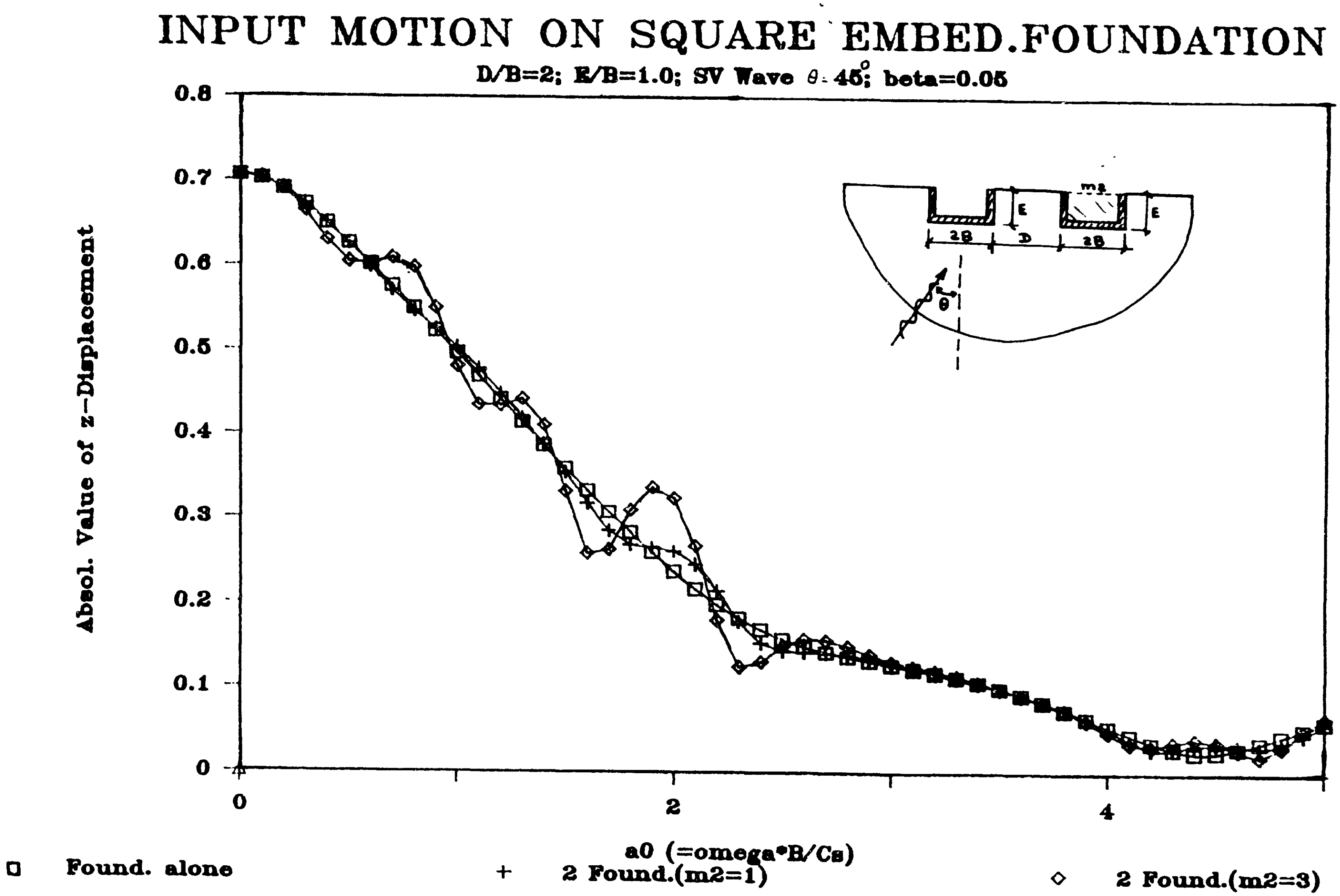
INPUT MOTION ON SQUARE EMBED.FOUNDATION
D/B=2; E/B=1.0; SV Wave θ=45°; beta=0.05
Absol. Value of z-Displacement
0.8
0.7
0.6
0.5
0.4
0.3
0.2
0.1
0
0
2
4
a0 (=omega*B/Cs)
m2
E
2B
D
2B
E
θ
□ Found. alone
+ 2 Found.(m2=1)
◇ 2 Found.(m2=3)

Figure 5.29

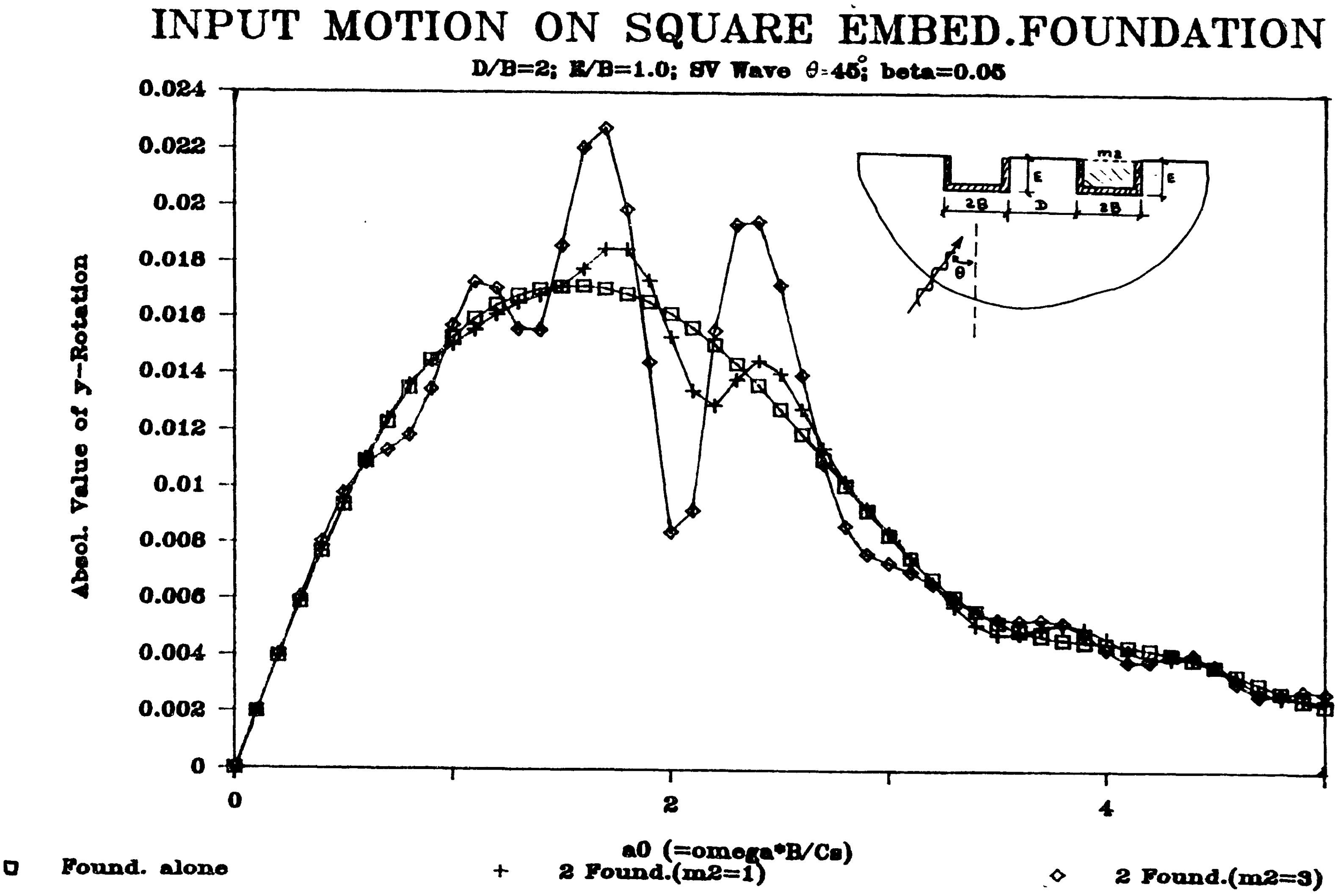
INPUT MOTION ON SQUARE EMBED.FOUNDATION
D/B=2; E/B=1.0; SV Wave θ=45°; beta=0.05
Absol. Value of y-Rotation
0.024
0.022
0.02
0.018
0.016
0.014
0.012
0.01
0.008
0.006
0.004
0.002
0
0
2
4
a0 (=omega*B/Cs)
2B
D
2B
E
E
m2
θ
Found. alone
2 Found.(m2=1)
2 Found.(m2=3)

Figure 5.30

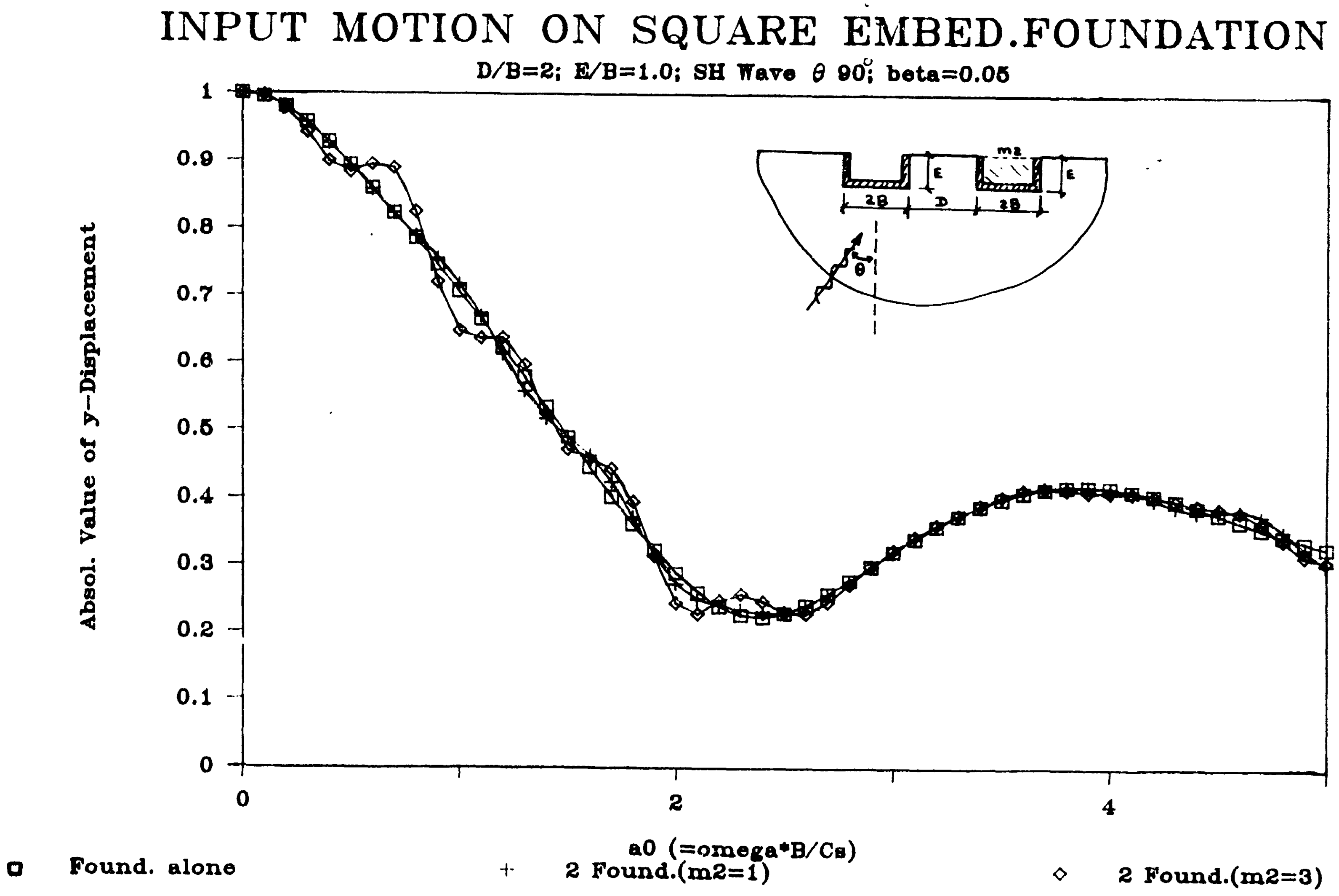
INPUT MOTION ON SQUARE EMBED.FOUNDATION
D/B=2; E/B=1.0; SH Wave θ 90°; beta=0.05
Absol. Value of y-Displacement
1
0.9
0.8
0.7
0.6
0.5
0.4
0.3
0.2
0.1
0
0
2
4
a0 (=omega*B/Cs)
m2
E
2B
D
θ
□ Found. alone
+ 2 Found.(m2=1)
◇ 2 Found.(m2=3)

Figure 5.31

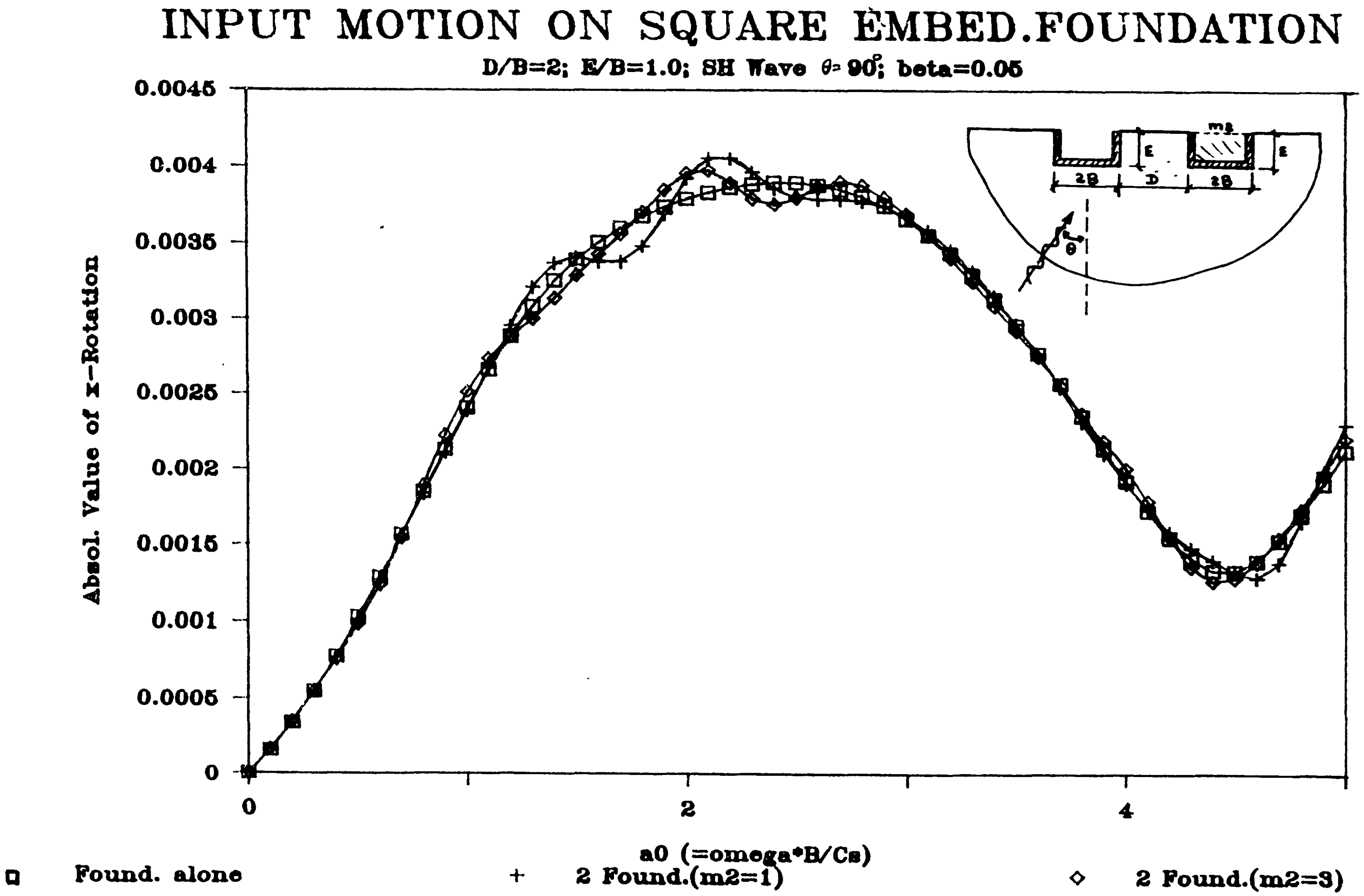
INPUT MOTION ON SQUARE EMBED.FOUNDATION
D/B=2; E/B=1.0; SH Wave θ= 90°; beta=0.05
Absol. Value of x-Rotation
0.0045
0.004
0.0035
0.003
0.0025
0.002
0.0015
0.001
0.0005
0
0
2
4
a0 (=omega*B/Cs)
Found. alone
2 Found.(m2=1)
2 Found.(m2=3)
m2
E
E
2B
D
2B
θ

Figure 5.32

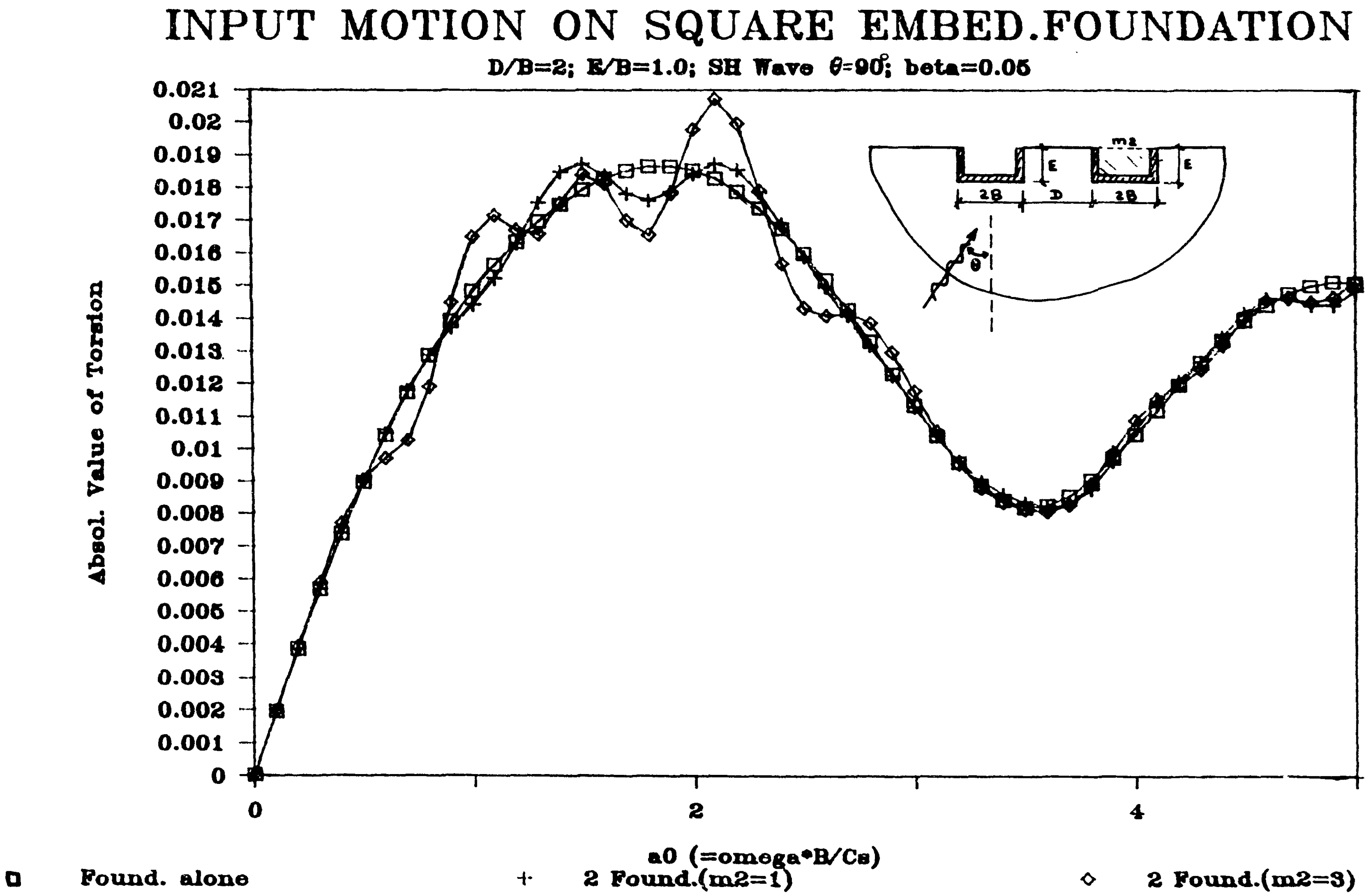
INPUT MOTION ON SQUARE EMBED.FOUNDATION
D/B=2; E/B=1.0; SH Wave θ=90°; beta=0.05
Absol. Value of Torsion
0.021
0.02
0.019
0.018
0.017
0.016
0.015
0.014
0.013
0.012
0.011
0.01
0.009
0.008
0.007
0.006
0.005
0.004
0.003
0.002
0.001
0
0
2
4
a0 (=omega*B/Cs)
m2
E
E
2B
D
2B
θ
□ Found. alone
+ 2 Found.(m2=1)
◇ 2 Found.(m2=3)

Figure 5.33

Interesting results are also obtained when considering incident waves with a prescribed Power Spectrum and computing the Response Spectra for a 1–dof structure supported by foundation one. The Response Spectra are obtained using the approximate formulas given by Der Kiureghian [25] which in turn are based on a probability distribution derived by Vanmarcke [44] for the time to first–exceedance of a given level by a stochastic process. This approach was used by Pais and Kausel [33], who describe in more detail the formulas used in the computation of Response Spectra from Power Spectra. Examples of Response Spectra are presented in figures 5.35–5.38, which show the influence of coupling through the soil as a function of the natural frequency of the structure and the mass of the second foundation. These spectra were obtained considering incident waves with an acceleration Power Spectrum given by

$$S_{\ddot{u}_g} = \begin{cases} \dfrac{f^4}{0.5 + f^4}(1-f^2/64)\, S_0 & f \le 7\text{Hz} \\ 0 & f \ge 7\text{Hz} \end{cases} \tag{5.36}$$

where f (in Hertz) represents the frequency of the motion. Also, damping of the structure is assumed to be 5% of critical, and the duration of the earthquake is 100 secs.

This function is displayed in figure 5.34 for the case $S_0=1$. Note that in the low frequency range, $S_{\ddot{u}_g}$ varies at least as f^4 (or ω^4), so that the associated displacement Power Spectrum $S_{u_g} = \frac{1}{\omega^4} S_{\ddot{u}_g}$ does not become unbounded as f approaches zero. The cross–coupling for the two foundations can either increase or decrease the maximum displacement recorded at the top of the first structure, depending on its natural frequency. As would be expected, these differences are more pronounced when the second foundation is heavier, and when the incident waves propagate vertically.

These results illustrate how the simple approximation developed can be used to estimate the influence of coupling through the soil of multiple structures. By varying the parameters of the model, namely the seismic excitation or the masses of the structures, several cases can be analyzed and some qualitative conclusions drawn concerning the most unfavorable situations.

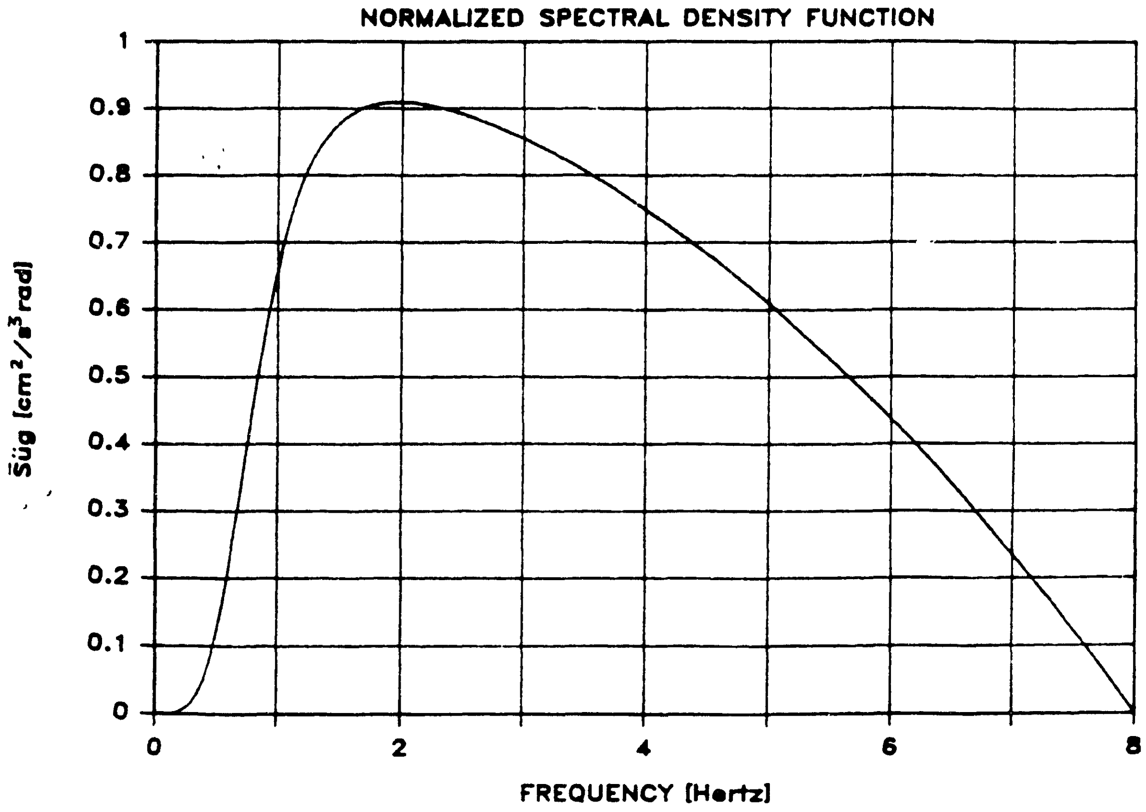
NORMALIZED SPECTRAL DENSITY FUNCTION
S̄üg [cm²/s³ rad]
1
0.9
0.8
0.7
0.6
0.5
0.4
0.3
0.2
0.1
0
0
2
4
6
8
FREQUENCY [Hertz]

Figure 5.34

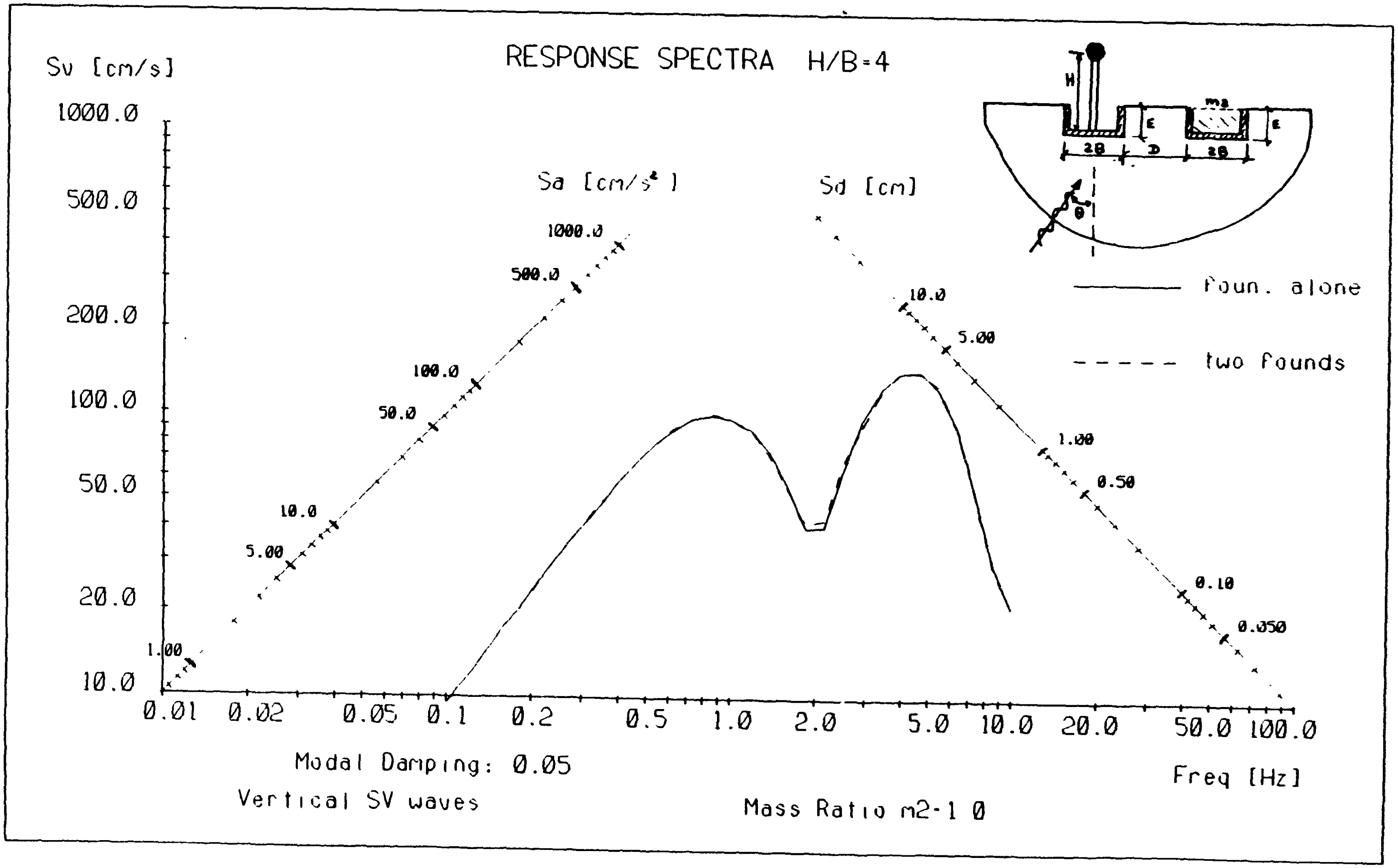
RESPONSE SPECTRA H/B=4
Sv [cm/s]
1000.0
500.0
200.0
100.0
50.0
20.0
10.0
Sa [cm/s²]
1000.0
500.0
100.0
50.0
10.0
5.00
1.00
Sd [cm]
10.0
5.00
1.00
0.50
0.10
0.050
H
E
2B
D
ms
θ
foun. alone
two founds
0.01
0.02
0.05
0.1
0.2
0.5
1.0
2.0
5.0
10.0
20.0
50.0
100.0
Freq [Hz]
Modal Damping: 0.05
Vertical SV waves
Mass Ratio m2-1 0

Figure 5.35

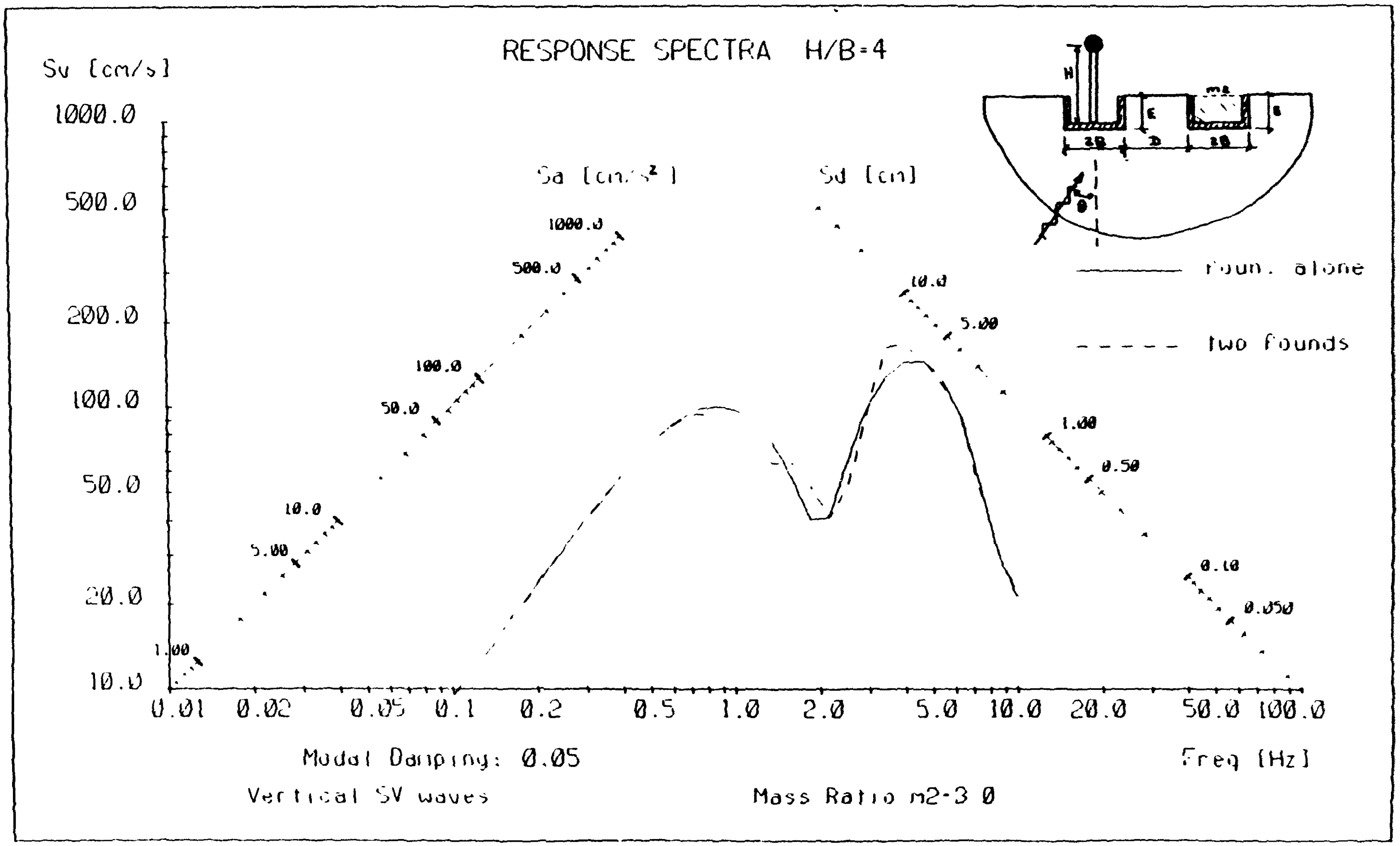
RESPONSE SPECTRA H/B=4
Sv [cm/s]
1000.0
500.0
200.0
100.0
50.0
20.0
10.0
Sa [cm/s²]
1000.0
500.0
100.0
50.0
10.0
5.00
1.00
Sd [cm]
10.0
5.00
1.00
0.50
0.10
0.050
Foun. alone
Two founds
H
E
D
2B
m2
θ
0.01
0.02
0.05
0.1
0.2
0.5
1.0
2.0
5.0
10.0
20.0
50.0
100.0
Freq [Hz]
Modal Damping: 0.05
Vertical SV waves
Mass Ratio m2-3 0

Figure 5.36

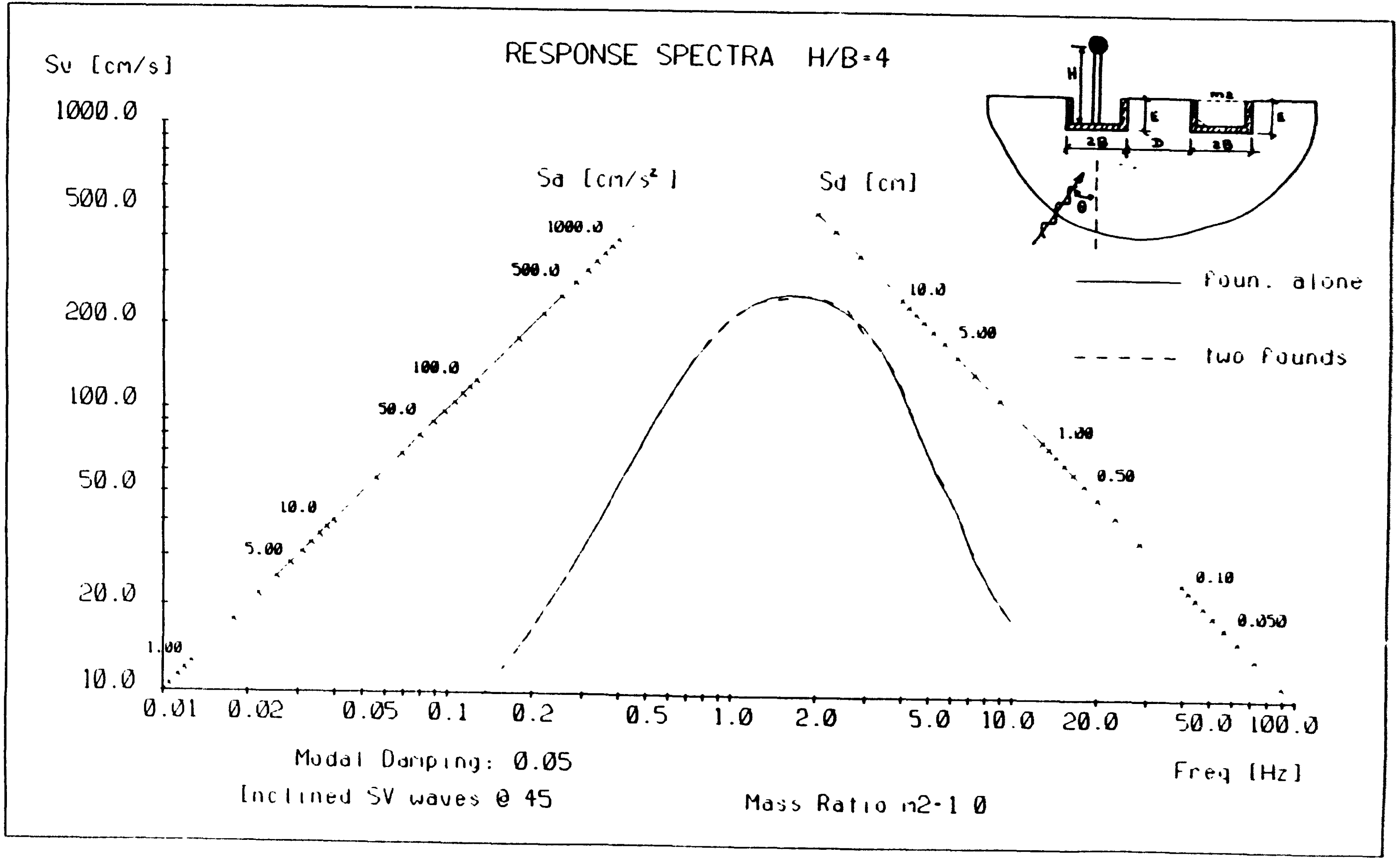
RESPONSE SPECTRA H/B=4
Sv [cm/s]
1000.0
500.0
200.0
100.0
50.0
20.0
10.0
Sa [cm/s²]
1000.0
500.0
100.0
50.0
10.0
5.00
1.00
Sd [cm]
10.0
5.00
1.00
0.50
0.10
0.050
Foun. alone
Two founds
H
E
D
2B
m2
θ
0.01
0.02
0.05
0.1
0.2
0.5
1.0
2.0
5.0
10.0
20.0
50.0
100.0
Freq [Hz]
Modal Damping: 0.05
Inclined SV waves @ 45
Mass Ratio m2-1 0

Figure 5.37

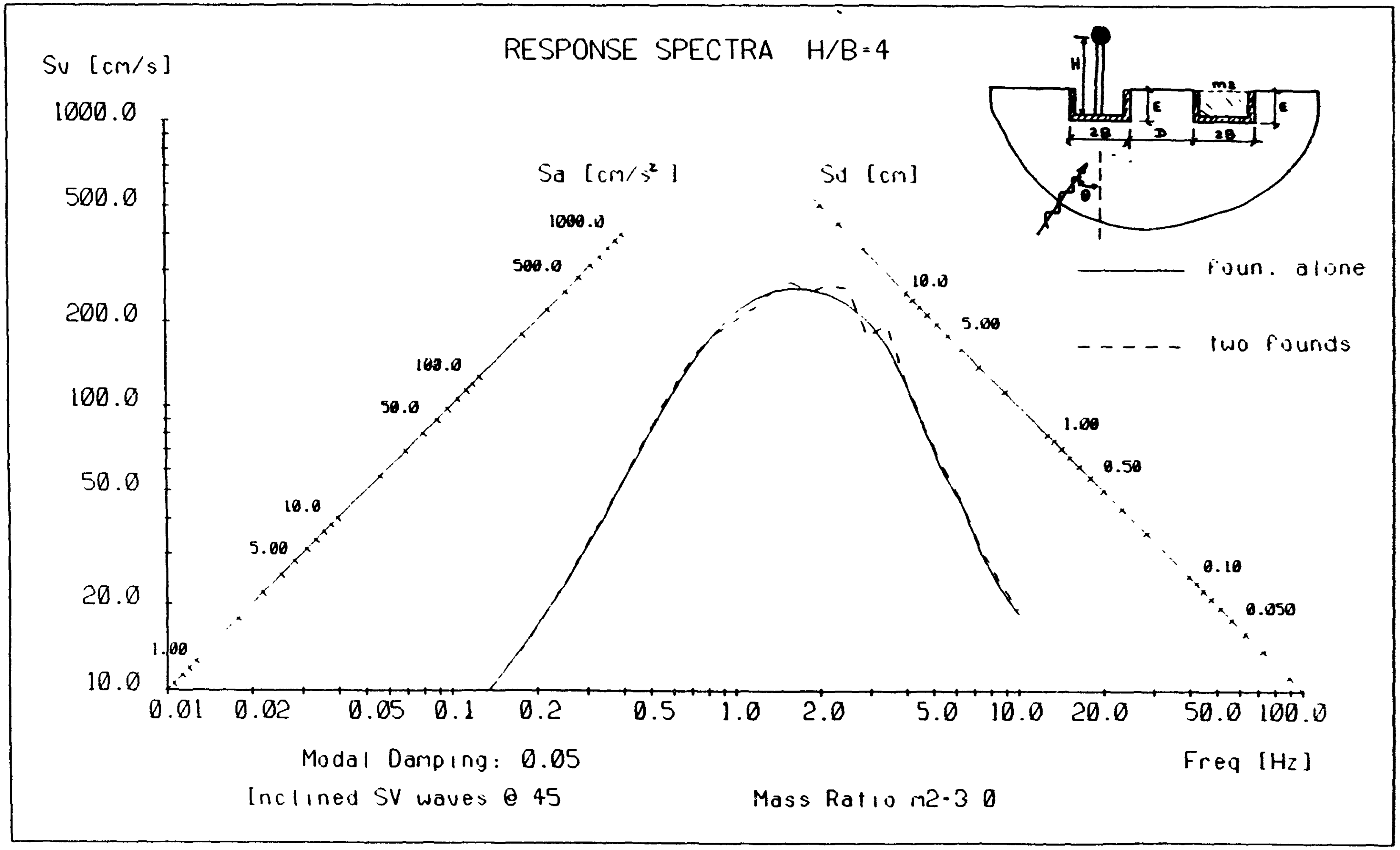
RESPONSE SPECTRA H/B=4
Sv [cm/s]
1000.0
500.0
200.0
100.0
50.0
20.0
10.0
Sa [cm/s²]
1000.0
500.0
100.0
50.0
10.0
5.00
1.00
Sd [cm]
10.0
5.00
1.00
0.50
0.10
0.050
H
m2
E
2B
D
θ
foun. alone
two founds
0.01
0.02
0.05
0.1
0.2
0.5
1.0
2.0
5.0
10.0
20.0
50.0
100.0
Freq [Hz]
Modal Damping: 0.05
Inclined SV waves @ 45
Mass Ratio m2=3.0

Figure 5.38

6. CONCLUSIONS

This work focused on the dynamic response of multiple foundations and buried structures to seismic waves, and on the influences (or "coupling") that these various structures exert on each other.

A Boundary Element formulation was developed to study dynamic problems involving several rigid foundations and tunnels embedded in a layered halfspace. This procedure is formulated in the frequency domain, and uses very efficient approximate Green's functions developed by Kausel and Peek [22]. These functions represent the displacement field produced by a unit load applied at some point inside the domain, and can be evaluated in closed form without numerical integrations. The approximation consists in subdividing each layer of soil into several sublayers, and assuming a linear variation of the displacements across each sublayer. The effect of the halfspace is introduced by a paraaxial approximation suggested by Seale [39]. To reduce the number of equations, the formulation was restricted to two dimensions, considering both in–plane and anti–plane motions. Comparisons were then performed with corresponding solutions obtained using the finite element method, and excellent agreements were found.

When applying the Boundary Element method to wave propagation problems in non–convex domains, the solution can exhibit noncausal behavior; this means that a dynamic excitation at a given point produces responses at other points before the time it takes the fastest waves to travel thereto. Such observed responses are certainly not physically possible, and result from errors introduced by the discretization of the boundary integral. Hence, a study of the causality of the response for certain classes of problems gives an indication of the accuracy of a given Boundary Element formulation. The case of an open trench was analyzed using the method described, and the results compared with a time–domain boundary element solution. It was found that the frequency domain results obey causality in every case while the results obtained with the available time–domain model did not. This is a consequence of having constrained the displacements to vary piecewise linearly along the vertical direction; as a result, the boundary elements satisfy exactly the boundary conditions along vertical planes. Hence, the formulation developed is especially well suited for problems involving non–convex boundaries, such as the analysis of embedded foundations and tunnels.

The earthquakes that struck Mexico City in September 1985 produced very heavy structural damage, especially in the downtown zone. Even though the severity of the seismic motion felt at the surface, and the concentration of its energy near the fundamental natural frequency of the underlying stratum, certainly contributed to the great damages sustained, some concerns were raised about the influence of underground structures, namely the subway tunnel, on the vibration of nearby structures. The subgrade in the downtown area consists of very soft sediments having a high water content and low shear wave velocities; therefore, soil–structure interaction can be expected to be very important for large structures. The boundary element method developed was used to study this problem. The influence of the subway tunnel on the motion observed at the surface was analyzed for various frequencies considering vertically incident P, SV and SH waves. These results were then convolved with the frequency contents of the records obtained during the earthquake so as to obtain a measure of the disturbances on the seismic motions caused by the presence of the tunnel. It was found that the underground tunnel in Mexico City did not have a significant influence on the severity of the motions observed, since their energy was concentrated at low frequencies for which the associated wavelengths are large in comparison to the dimensions of the tunnel. Hence, the tunnel experience mostly translations, and only very little rotation.

Chapter 5 describes an approximate procedure to evaluate the interaction between multiple foundations subjected to seismic excitations. The method is very simple to implement and can be used for situations involving several cylindrical and rectangular foundations embedded in a halfspace. Some comparisons with the results obtained by more accurate methods, namely the boundary element method developed, show a good qualitative agreement. Hence, the procedure proposed seems to be ideally suited for the preliminary assessment of cross–coupling effects in systems involving multiple foundations.

REFERENCES

1. Antes, H. and Estorff, O. von, 1986: "Dynamic Soil–Structure Interaction by BEM in the Time and Frequency Domain," pp. 5.5–33 to 5.5–40, Vol. 2, Proc. 8th European Conf. on Earthquake Engineering, Lab. Nac. Eng. Civil, Lisbon, Portugal.

2. Antes, H. and Estorff, O. von, 1987: "On Causality in Dynamic Response Analysis by Time–Dependent Boundary Element Methods," Earthqu. Engng & Struct. Dynamics (to be published).

3. Antes, H. and Estorff, O. von, 1987: "The Effect of Non–Convex Boundaries on Time Domain Boundary Element Solutions," Proc. 9th Conf. BEM87, Stuttgart.

4. Apsel, R.J., 1979: "Dynamic Green's Functions for Layered Media and Applications to Boundary–Value Problems" – PhD Thesis, Univ. of California at San Diego

5. Banerjee, P.K. and Butterfield, R., 1981: Boundary Element Methods in Engineering Science, McGraw–Hill, London.

6. Beskos, D.E., 1987: "Boundary Element Methods in Dynamic Analysis" – ASME, Applied Mechanics Reviews, Vol. 40, No. 1, Jan.

7. Bielak, J. and Coronato, J.A., 1981: "Response of Multiple–Mass Systems to Nonvertically Incident Seismic Waves", Vol. II, pp. 801–804, Proceedings of Int. Conf. on Recent Advances in Geotechnical Earthquake Engineering and Soil Dynamics, St. Louis, USA, 1981, University of Missuri–Rolla.

8. Bouchon, M.,1981: "A simple method to calculate Green's functions for elastic layered media," Bull. Seism. Soc. Am., Vol. 71, pp. 959–971.

9. Chang–Liang, V., 1974: "Dynamic Response of Structures in Layered Soils" – Report No. R74–10. MIT Dept. of Civil Engineering, Cambridge, Massachusetts.

10. Clough, R.W. and Penzien, J., 1975: Dynamics of Structures, McGraw–Hill, New York.

11. Dominguez, J., 1978: "Dynamic Stiffness of Rectangular Foundations" – Report No. R78–20, MIT, Cambridge, Massachusetts.

12. Domingues, J. and Abascal, R., 1984: "On Fundamental Solutions for the Boundary Integral Equations Method in Static and Dynamic Elasticity," Engineering Analysis, Vol. 1, No. 3, pp. 128–134.

13. Gazetas, G., 1983: "Analysis of Machine Foundation Vibrations", State of the Art" – International Journal of Soil Dynamics and Earthquake Eng., Vol. 2, No. 1, pp. 2–42.

14. Gonzalez, J.J., 1977: "Dynamic Interaction Between Adjacent Structures" – Report No. R77–30, MIT Dept. of Civil Engineering, Cambridge, Massachusetts.

15. Graffi, D., 1947: "Sul Teorema di Reciprocita nella Dinamica dei Corpi Elastici," Mem. Accad. Sci. Bologna, Vol. 18, pp. 103–109.

16. Haddon, R.A.W., 1986: "Exact Evaluation of the Response of a Layered Elastic Medium to an Explosive Point Source using Leaking Modes," Bull. Seism. Soc. Amer., Vol. 76, No. 6, pp. 1755–1775.

17. Haskell, N.A., 1953: "The dispersion of surface waves on multilayered media," Bull. Seism. Soc. Am., Vol. 43, pp. 17–34.

18. Iguchi, M., 1982: "An Approximate Analysis of Input Motions for Rigid Embedded Foundations" – Trans. of Architectural Inst. of Japan, No. 315, May, pp. 61–75.

19. Iguchi, M., 1984: "Earthquake Response of Embedded Cylindrical Foundations to SH and SV Waves" – Proceedings of the 8th World Conference on Earthquake Engineering (San Francisco).

20. Kausel, E., 1981: "An Explicit Solution for the Green's Functions for Dynamic Loads in Layered Media," M.I.T. Research Report R81.113, Order No. 699, Department of Civil Engineering.

21. Kausel, E. and Roesset, J.M., 1981: "Stiffness Matrices for Layered Soils" – Bull. Seism. Soc. Amer., Vol. 71, No. 6, pp. 1743–1761.

22. Kausel, E. and Peek, R., 1982: "Dynamic Loads in the Interior of a Layered Stratum: an Explicit Solution" – Bull. Seism. Soc. Amer., Vol. 72, No. 5, pp. 1459–1481.

23. Kausel, E. and Peek, R. 1982: "Boundary Integral Method for Stratified Soils" – Report No. R82–50, MIT Dept. of Civil Engineering, Cambridge, Massachusetts.

24. Kausel, E., Whitman, R.V., Morray, J.P. and Elsabee, F., 1978: "Spring method for embedded foundations," Nuclear Eng. and Design, Vol. 48, pp. 377–392.

25. Kiureghian, A., 1980: "Structural Response to Stationary Excitation" – Journal of the Eng. Mech. Division, ASCE, Vol. 106, No. EM6, Dec., pp. 1195–1213.

26. Kobori, T. and Kusakabe K., 1978: "Dynamic Cross–Interaction Between Two Embedded Structures," Proc. 5th Japan Earthquake Engineering Symposium, Tokyo, pp. 521–528.

27. Kobori, T., Minai, R. and Kusakabe K., 1973: "Dynamic Characteristics of Soil–Structure Cross–Interaction System, I", Bull. of the Disaster Prevention Research Institute, Kyoto University, Vol. 22, pp. 111–151.

28. Kotake, N., 1987: "On the Response of Foundations to Travelling Waves" – MS Thesis, MIT Dept. of Civil Engineering, Cambridge, Massachusetts.

29. Lee, T.H. and Wesley, D.A., 1973: "Soil–structure interaction of nuclear reactor structures considering through soil coupling between adjacent structures," Nuclear Eng. Des., Vol.24, pp. 374–387.

30. Lin, H.T., Roesset, J.M., and Tassoulas, J.C., 1987: "Dynamic Interaction between Adjacent Foundations" – Earthquake Eng. and Struc. Dynamics, Vol. 15, pp. 323–343.

31. Lysmer, J., Seed, H.B., Udaka, T., Hwang, R.N. and Tsai, C.F., 1975: "Efficient finite element analysis of seismic soil structure interaction," Report No. EERC 75–34, Earthquake Engineering Research Center, University of California, Berkeley, CA.

32. MacCalden, P.B. and Matthiesen, R.B., 1973: "Coupled Response of Two Foundations," Fifth World Conference on Earthquake Engineering, Rome.

33. Pais, A. and Kausel, E., 1985: "Stochastic Response of Foundations" – Report No. R85–6, MIT Dept. of Civil Engineering, Cambridge, Massachusetts.

34. Roesset, J.M. and Resendiz, D. – "Soil–Structure Interaction in Mexico City During the 1985 Earthquakes" – in "The Mexico Earthquakes–1985, Factors Involved and Lessons Learned," proceedings of the ASCE International Conference in Mexico City, Sept. 1986, edited by Cassaro, M.A. and Romero, E.M..

35. Roesset, J.M., Whitman, R.V. and Dobry, R., 1973: "Modal Analysis for Structures with Foundation Interaction" – Journal of the Struc. Division, ASCE, Vol. 99, No. ST3, March, pp. 394–416.

36. Romo, M.P. and Seed, H.B. – "Analytical Modelling of Dynamic Soil Response in the Mexico Earthquake of 1985" – in "The Mexico Earthquakes–1985, Factors Involved and Lessons Learned," proceedings of the ASCE International Conference in Mexico City, Sept. 1986, edited by Cassaro, M.A. and Romero, E.M..

37. Sarfeld, W. and Frohlich, K.–C., 1980: "Dynamische Wechselwirkung von Gebauden und Fundamenten auf dem elastisch–isotropen Halbraum," Bauingenieur, Vol. 55, pp. 419–426.

38. Savidis, S.A. and Richter, T., 1977: "Dynamic interaction of rigid foundations," Proc. 9th Int. Conf. Soil Mech. Found. Eng., Vol., Vol. 2, pp. 369–374.

39. Seale, S.H.,, 1985: "Dynamic Loads in Layered Halfspaces" – PhD Thesis, MIT, Cambridge, Massachusetts.

40. Tassoulas, J.L., 1981: "Elements for the Numerical Analysis of Wave Motions in Layered Media" – Report No. R81–2, MIT Dept. of Civil Engineering, Cambridge, Massachusetts.

41. Thomson, W.T., 1950: "Transmission of elastic waves through a stratified soil medium," Journal Appl. Phys., Vol. 21, pp. 89–93.

42. Triantafyllidis, T., 1987: "Some Aspects of the Dynamic Subsoil–Coupling Between Circular and Rectangular Foundations," Ground Motion and Engineering Seismology, Developments in Geotechnical Engineering, Vol. 44, A.S. Cakmak (editor).

43. Triantafyllidis, T, and Dasgupta, B. 1988: "The Causality of the Boundary Element Method in Elastodynamics," Soil Dynamics and Earthquake Engineering (to be published).

44. Vanmarcke, E.H., 1975: "On the Distribution of the First–passage Time for Normal Stationary Random Processes" – Journal of Applied Mech., Vol. 42, Mar., pp. 215–220.

45. Waas, G., 1972: "Analysis Method for Footing Vibrations through Layered Media" – PhD Thesis, Univ. of California, Berkeley.

46. Warburton, G.B., Richardson, J.D. and Webster, J.J., 1971: "Forced vibrations of two masses on an elastic half space," Journal of Applied Mech., ASME, Vol. 38, pp. 148–156.

47. Wilson, J.C. and Jennings P.C., 1985: "Spatial Variation of Ground Motion Determined from Accelerograms Recorded on a Highway Bridge," Bull. Seism. Soc. Amer., Vol. 75, No. 6, pp. 1515–1533.

48. Wolf, J., 1985: Dynamic Soil–Structure Interaction, Prentice–Hall, Inc.

49. Wong, H.L. and Luco, J.E., 1986: "Dynamic Interaction between Rigid Foundations in a Layered Half–Space," Soil Dyn. and Earthq. Eng., Vol. 5, No. 3, pp. 149–158.

50. Wong, H.L. and Trifunac, M.D., 1975: "Two Dimensional, Antiplane, Building–Soil–Building Interaction for Two or More Buildings and for Incident Plane SH–Waves," Bull. Seism. Soc. Am., Vol. 65, No. 6, pp. 1863–1885.

51. Report on the Investigation of the Earthquake in Mexico (Sept. 19, 1985)", June 1986, Tokyo Metropolitan Government.

APPENDIX A

Thin–Layer Method

Consistent forces at the interfaces:

The finite element method is applied by requiring the approximate solution to satisfy the principle of virtual displacements (PVD) for virtual fields consistent with the displacement expansions chosen. The PVD can be written as:

$$\iiint_v \delta\epsilon_{ij}\,\overline{\sigma}_{ij}\,dV = -\iiint_v \delta u_i(\rho\ddot{\overline{u}}_i - b_i)dV + \iint_S \delta u_i\overline{t}_i dS \tag{A.1}$$

where the superscript bar denotes an approximate solution and the double dot represents a second derivative with respect to time.

Noting that $\delta\epsilon_{ij} = \frac{1}{2}(\delta u_{i,j} + \delta u_{j,i})$ and integrating by parts the left hand side of equation A.1, the following is obtained:

$$\iint_S \delta u_i(\alpha_{\nu j}\overline{\sigma}_{ij} - \overline{t}_i)dS - \iiint_v \delta u_i(\overline{\sigma}_{ij,j} + b_i - \rho\ddot{\overline{u}}_i)dV = 0 \tag{A.2}$$

$\alpha_{\nu j}$ being the j coordinate of the outwards unit normal to the surface S.

The calculation of the approximate stiffness matrices will be illustrated for in–plane motions. Assume a solution in the wave number domain k in which $u = U(z)\,e^{-ikx}$. Hence, $\frac{\delta}{\delta x} = -ik$.

An isolated sublayer extending between interfaces m and m+1, with the coordinates' axes defined as indicated is shown below

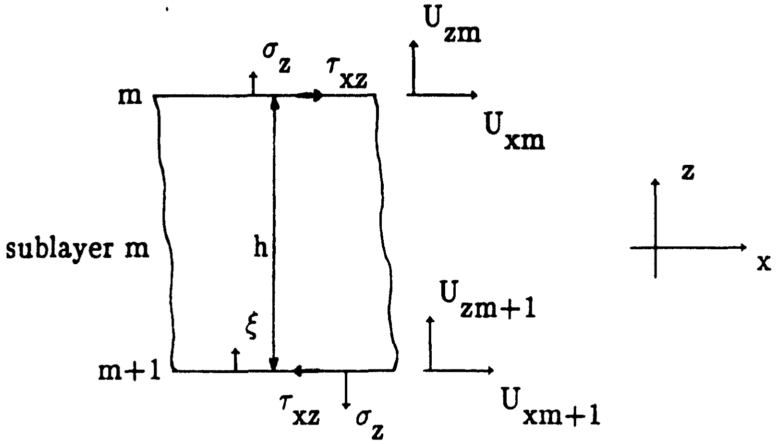

at m, $\xi = 1$; at m+1, $\xi = 0$; $\frac{\partial}{\partial z} = \frac{1}{h}\frac{\partial}{\partial \xi}$

The stresses are given by:

$$\sigma_z = [(\lambda+2G)\frac{\partial U_z}{\partial z} - ik\lambda U_x] \tag{A.3}$$

$$\tau_{xz} = G[-ikU_z + \frac{\partial U_x}{\partial z}] \tag{A.4}$$

Inside the sublayer the displacements are given by

$$\begin{bmatrix} U_x \\ U_z \end{bmatrix} = \mathbf{N} \cdot \mathbf{U} \tag{A.5}$$

$$\text{where } \mathbf{N} = \begin{bmatrix} \xi & \cdot & 1\text{-}\xi & \cdot \\ \cdot & \xi & \cdot & 1\text{-}\xi \end{bmatrix} \quad \text{and} \quad \mathbf{U} = \begin{bmatrix} U_{xm} \\ U_{zm} \\ U_{xm+1} \\ U_{zm+1} \end{bmatrix}$$

Introducing this expansion in the equations for the stresses, we get

$$\sigma_z = \left\{ \frac{\lambda + 2G}{h} \left[\cdot\ 1\ \cdot\ -1 \right] - ik\lambda \left[\xi\ \cdot\ 1-\xi\ \cdot \right] \right\} \cdot \mathbf{U} \tag{A.6}$$

$$\tau_{xz} = G \left\{ -ik \left[\cdot\ \xi\ \cdot\ 1-\xi \right] + \frac{1}{h} \left[1\ \cdot\ -1\ \cdot \right] \right\} \cdot \mathbf{U} \tag{A.7}$$

Equation (A.2) can be written as

$$\delta U_i^T \cdot \left[\iint_S \mathbf{N}^T (\alpha_{\nu j} \overline{\sigma}_{ij} - \overline{t_i}) dS - \iiint_v \mathbf{N}^T (\overline{\sigma}_{ij,j} + b_i - \rho \ddot{\overline{u_i}}) dV \right] = 0 \tag{A.8}$$

Since we require this equation to hold for arbitrary δU_i , the term in brackets should equal zero. In this case, the boundary S is represented by the top and bottom interfaces (m and m+1) and the integral over the volume becomes an integral over ξ. Also $b_i = 0$ if no distributed loadings are prescribed. For harmonic motion $\ddot{\overline{u}} = -\omega^2 \overline{u}.$ Hence

$$\left\{ \mathbf{N}^T \cdot \left(\left[\alpha_{\nu j} \overline{\sigma}_{ij} \right] - \overline{t_i} \right) \right\} \Big|_{m+1}^{m} = \int_0^1 \mathbf{N}^T \cdot \left(\sigma_{ij,j} + \rho \omega^2 \overline{u_i} \right) d\xi \tag{A.9}$$

or

$$\begin{bmatrix} P_{xm} \\ P_{zm} \\ P_{xm+1} \\ P_{zm+1} \end{bmatrix} = \begin{bmatrix} \tau_{xzm} \\ \sigma_{zm} \\ -\tau_{xzm+1} \\ -\sigma_{zm+1} \end{bmatrix} - \left\{ h\int_0^1 \mathbf{N}^T \cdot \begin{bmatrix} -k^2\xi(\lambda+2G) & -ik\frac{\lambda+G}{h} & -k^2(1-\xi)(\lambda+2G) & -ik\frac{-\lambda-G}{h} \\ -ik\frac{\lambda+G}{h} & -k^2\xi G & -ik\frac{-\lambda--G}{h} & -k^2(1-\xi)G \end{bmatrix} \cdot d\xi - \rho\omega^2 h\int_0^1 \mathbf{N}^T\mathbf{N}\, d\xi \right\} \cdot \mathbf{U} \qquad \text{(A.10)}$$

Evaluating the above integrals and changing the result so that the vertical components of P and U are multiplied by i ($i=\sqrt{-1}$), we obtain:

$$\mathbf{P}_m = (\mathbf{A}_m k^2 + \mathbf{B}_m k + \mathbf{G}_m - \omega^2 \mathbf{M}_m) \cdot \mathbf{U}_m \qquad \text{(A.11)}$$

with $\mathbf{A}_m = \frac{h}{6}\begin{bmatrix} 2(\lambda+2G) & & \lambda+2G & \\ & 2G & & G \\ \lambda+2G & & 2(\lambda+2G) & \\ & G & & 2G \end{bmatrix}$; $\mathbf{B}_m = \frac{1}{2}\begin{bmatrix} & \lambda-G & & -(\lambda+G) \\ \lambda-G & & \lambda+G & \\ & \lambda+G & & -(\lambda-G) \\ -(\lambda+G) & & -(\lambda-G) & \end{bmatrix}$

$$\mathbf{G}_m = \frac{1}{h}\begin{bmatrix} G & & -G & \\ & \lambda+2G & & -(\lambda+2G) \\ -G & & G & \\ & -(\lambda+2G) & & (\lambda+2G) \end{bmatrix} \text{ and } \mathbf{M}_m = \frac{\rho h}{6}\begin{bmatrix} 2 & & 1 & \\ & 2 & & 1 \\ 1 & & 2 & \\ & 1 & & 2 \end{bmatrix} \qquad \text{(A.12)}$$

For the anti–plane case, we obtain similarly:

$$\mathbf{A}_m = \frac{h}{6}\begin{bmatrix} 2G & G \\ G & 2G \end{bmatrix} ; \mathbf{B}_m = 0 ; \mathbf{G}_m = \frac{1}{h}\begin{bmatrix} G & -G \\ -G & G \end{bmatrix} \text{ and } \mathbf{M}_m = \frac{\rho h}{6}\begin{bmatrix} 2 & 1 \\ 1 & 2 \end{bmatrix} \qquad \text{(A.13)}$$

Internal damping

An internal damping of the hysteretic type can be incorporated in the dynamic stiffness matrices by using the Correspondence Principle. In the present formulation, this is achieved by multiplying the Lame constants λ and G by $(1+2i\beta)$, where β is the fraction of critical damping. The complex moduli thus obtained are

$$\lambda^c = \lambda(1+2i\beta) \tag{A.14}$$

$$G^c = G(1+2i\beta) \tag{A.15}$$

and it suffices to substitute λ and G by their complex counterparts in the matrices A_m, B_m and G_m.

APPENDIX B

Green's Functions

The Green's functions are obtained using the solution proposed by Kausel and Peek [22] and extended to layered halfspaces by Seale [39]. This solution requires the spectral decomposition of the dynamic stiffness matrix, which requires in turn the solution of a quadratic eigenvalue problem. The displacements are then computed as a summation over all the natural modes of the system.

Evaluation of Green's functions

The quadratic eigenvalue problem can be written as:

$$(\mathbf{A}k_j^2 + \mathbf{B}k_j + \mathbf{G} - \omega^2\mathbf{M})\phi_j = 0 \tag{B.1}$$

where **A**, **B**, **G** and **M** are assembled using the sublayer matrices given in appendix A.

The solution for this eigenproblem results in 4N eigenvalues for the in–plane case and 2N for anti–plane motions (N being the total number of sublayers). Half of these eigenvalues correspond to motions that decay with distance from the source or propagate away from it; the other half corresponding to the opposite. We keep only the former modes, since these are the ones that satisfy the variation and boundedness condition at infinity. This is accomplished by choosing the eigenvalues with a negative imaginary part or, for real eigenvalues, the positive ones.

Since our analysis is 2–D we will study separately the in–plane and anti–plane situations. We will follow the solution algorithm as described in [20].

in–plane case

Rearranging all matrices and vectors by considering first the x components and then the z components, and defining $\mathbf{C}=\mathbf{G}-\omega^2\mathbf{M}$, the eigenvalue problem can be written as

$$k_j^2\overline{\mathbf{A}}\mathbf{z}_j + \overline{\mathbf{C}}\mathbf{z}_j = 0 \qquad \text{(B.2a)}$$

or

$$y_j^T\overline{\mathbf{A}}k_j^2 + y_j^T\overline{\mathbf{C}} = 0 \qquad \text{(B.2b)}$$

$$\text{where } \overline{\mathbf{A}} = \begin{bmatrix} A_x & \\ B_{xz}^T & A_z \end{bmatrix} \quad \overline{\mathbf{C}} = \begin{bmatrix} C_x & B_{xz} \\ & C_z \end{bmatrix} \quad z_j = \begin{bmatrix} \phi_{xj} \\ k_j\phi_{zj} \end{bmatrix} \quad y_j = \begin{bmatrix} k_j\phi_{xj} \\ \phi_{zj} \end{bmatrix}$$

Premultiplying equation B.2a by y_i^T, post multiplying equation B.2b by z_j and subtracting the two equations, the following orthogonality conditions are found:

$$y_i^T\overline{\mathbf{A}}\mathbf{z}_j = 0 \quad i\neq j \ ; \ \neq 0 \quad i=j \qquad \text{(B.3a)}$$

$$y_i^T\overline{\mathbf{C}}\mathbf{z}_j = 0 \quad i\neq j \ ; \ \neq 0 \quad i=j \qquad \text{(B.3b)}$$

Defining

$$\mathbf{Y} = \{y_j\} = \begin{bmatrix} \Phi_x\mathbf{K} \\ \Phi_z \end{bmatrix}; \ \mathbf{Z} = \{z_j\} = \begin{bmatrix} \Phi_x \\ \Phi_z\mathbf{K} \end{bmatrix}; \ \mathbf{K} = \text{diag}\ \{k_j\} \quad j=1, \ldots, 2N$$

equations B.2 can be written in matrix form as

$$\bar{A}ZK^2 + \bar{C}Z = 0 \tag{B.4a}$$

or

$$\bar{A}^T YK^2 + \bar{C}^T Y = 0 \tag{B.4b}$$

The following normalization of the eigenvectors is chosen

$$Y^T \bar{A}Z = K \tag{B.5}$$

which implies $Y^T \bar{C}Z = -K^3$

Let us now consider the solution of the dynamic equilibrium equation in the wave–number domain

$$(\bar{A}k^2 + \bar{C})\bar{U}^* = \bar{P}^* \tag{B.6}$$

where $\bar{U}^* = \begin{bmatrix} \bar{U}_x \\ k\bar{U}_z \end{bmatrix}$ $\bar{P}^* = \begin{bmatrix} \bar{P}x \\ k\bar{P}_z \end{bmatrix}$ k being the horizontal wave number of the load and displacements.

Premultiplying equation B.6 by Y^T and introducing $ZZ^{-1}=I$, we obtain

$$Y^T(\bar{A}k^2 + \bar{C})ZZ^{-1}\bar{U}^* = Y^T\bar{P}^* \tag{B.7}$$

Considering the normalization relations this equation becomes

$$(Kk^2 - K^3)\, Z^{-1}\bar{U}^* = Y^T\bar{P}^* \tag{B.8}$$

which can easily be solved for $\bar{U}^*$ since the matrix in parenthesis is diagonal

$$\bar{U}^* = Z(Kk^2 - K^3)^{-1}Y^T\bar{P}^* \tag{B.9}$$

or, in extended form

$$\begin{bmatrix} \bar{U}_x \\ k\bar{U}_z \end{bmatrix} = \begin{bmatrix} \phi_x \\ \phi_z K \end{bmatrix} (Kk^2 - K^3)^{-1} \begin{bmatrix} K\phi_x^T & \phi_z^T \end{bmatrix} \begin{bmatrix} \bar{P}_x \\ k\bar{P}_z \end{bmatrix} \tag{B.10}$$

hence

$$\begin{bmatrix} \bar{U}_x \\ \bar{U}_z \end{bmatrix} = \begin{bmatrix} \phi_x D\phi_x^T & k\phi_x K^{-1} D\phi_z^T \\ \frac{1}{k}\phi_z KD\phi_x^T & \phi_z D\phi_z^T \end{bmatrix} \begin{bmatrix} \bar{P}_x \\ \bar{P}_z \end{bmatrix} \tag{B.11}$$

with $D = (k^2I - K^2)^{-1}$ (I representing the identity matrix)

Since the dynamic stiffness matrix is symmetric, its inverse must also be. Hence

$$k\phi_x K^{-1} D\phi_z^T = \frac{1}{k}(\phi_z KD\phi_x^T) = \frac{1}{k}\phi_x DK\phi_z^T \tag{B.12}$$

$$\text{or } \phi_x(k^2K^{-1}D - KD)\phi_z = 0 \quad \text{(since } KD=DK) \tag{B.13}$$

Noting that $(k^2I - K^2)D = I$ we obtain

$$\phi_x K^{-1}\phi_z^T = 0 \tag{B.14}$$

anti–plane case

A similar procedure gives for the anti–plane case

$$\overline{U}_y = \Phi_y D_L \Phi_y^T \overline{P}_y \tag{B.15}$$

$D_L = (k^2 I - K_L^2)^{-1}$ $K_L = \mathrm{diag}\{k_j\}$ $j=1,\ldots N$ the eigenvalues corresponding to anti–plane motion

and $\Phi_y = [\phi_{yj}]$

Transformation of the results to spatial coordinates

To obtain the displacements corresponding to a point load, the previous results have to be Fourier transformed back to the spatial coordinate x.

The Spatial Fourier transform of a point load located at x=0 is equal to unity for all wave numbers

$$P = \delta(x) \quad ; \quad \int_{-\infty}^{\infty} \delta(x) e^{ikx} dx = 1 \tag{B.16}$$

Hence, to find the displacements corresponding to a point load, it suffices to Fourier invert the relations in equation B.11 and B.15. The only function of k present in these relations are D_j and kD_j/k_j ($D_j = (k^2 - k_j^2)^{-1}$), which need to be inverted

$$I_1 = \frac{1}{2\pi}\int_{-\infty}^{\infty} \frac{e^{-ikx}}{k^2 - k_j^2} dk = \frac{e^{-ik_j|x|}}{2ik_j} \tag{B.17}$$

$$I_2 = \frac{1}{2\pi}\int_{-\infty}^{\infty} \frac{k}{k_j} \frac{e^{-ikx}}{k^2-k_j^2} dk = \frac{e^{-ik_j|x|}}{2ik_j} \mathrm{sng}(x) \tag{B.18}$$

where $\mathrm{sng}(x) = \begin{cases} 1 & x \geq 0 \\ -1 & x < 0 \end{cases}$

Calling $E_{|x|} = \mathrm{diag}\left\{e^{-ik_j|x|}\right\}$ and removing an implicit factor "i" from the z components of U and $\overline{P}$(introduced into the formulation so as to attain symmetry in the dynamic stiffness matrix), equations B.11 and B.15 become

in–plane

$$\begin{bmatrix} U_x \\ U_z \end{bmatrix} = \frac{1}{2i} \begin{bmatrix} \phi_x E_{|x|} K^{-1} \phi_x^T & i\phi_x E_{|x|} K^{-1} \phi_z^T \, \mathrm{sgn}(x) \\ -i\,\phi_z K^{-1} E_{|x|} \phi_x^T \, \mathrm{sgn}(x) & \phi_z E_{|x|} K^{-1} \phi_z^T \end{bmatrix} \begin{bmatrix} \overline{P}_x \\ \overline{P}_z \end{bmatrix} \tag{B.19}$$

where $E_{|x|}$ and K contain the in–plane modes (Rayleigh modes).

anti–plane

$$U_y = \frac{1}{2i} \phi_y E_{|x|} K_L^{-1} \phi_y^T \overline{P}_y \tag{B.20}$$

where $E_{|x|}$ and K_L contain the anti–plane modes (Love modes).

APPENDIX C

Evaluation of Consistent Tractions on Vertical and Horizontal Planes

In the boundary element formulation developed, only vertical and horizontal boundaries are considered. Along vertical planes, the boundary elements are assumed to have a linear variation of displacements between nodes; moreover, these nodes are located at the interfaces between the sublayers; in horizontal planes, on the other hand, the elements have piecewise constant displacements, and have one node in the middle of each element. For best results, if there are elements in different horizontal planes (interfaces) that overlap one another (i.e., if the shadow of elements in one plane is cast onto elements below), then these elements are taken of the same size, and their nodes are place in the same vertical line.

The nodal tractions at the boundary are obtained from the displacements. Because of the vertical discretization, the procedure to obtain consistent nodal tractions is not evident and will be illustrated here.

in–plane case

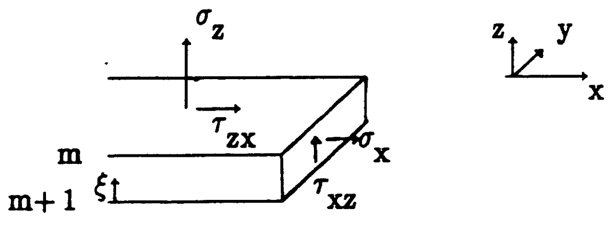

The figure above shows the sign convention for the stresses and coordinate axes in this case.

vertical planes

Using the stress–strain relations, we have

$$\begin{bmatrix}\sigma_x\\ \tau_{xz}\end{bmatrix} = \left[\begin{bmatrix}\lambda+2G & \\ & G\end{bmatrix}\frac{\delta}{\delta x} + \begin{bmatrix} & \lambda\\ G & \end{bmatrix}\frac{\delta}{\delta z}\right]\cdot\begin{bmatrix}u_x\\ u_z\end{bmatrix} \tag{C.1}$$

The tractions at the boundary are given by

$$\begin{bmatrix}t_x\\ t_z\end{bmatrix} = \begin{bmatrix}\sigma_x\\ \tau_{xz}\end{bmatrix}\mathrm{sng}(n_x) \tag{C.2}$$

$\mathrm{sng}(n_x)$ being equal to the cosine between the outward normal to the boundary and the x axis

$$\text{Since } u = \begin{bmatrix}u_x\\ u_z\end{bmatrix} = \begin{bmatrix}\xi & \cdot & 1-\xi & \cdot\\ \cdot & \xi & \cdot & 1-\xi\end{bmatrix}\cdot\begin{bmatrix}U_{xm}\\ U_{zm}\\ U_{xm+1}\\ U_{zm+1}\end{bmatrix} = \mathbf{N}\cdot\begin{bmatrix}U_m\\ U_{m+1}\end{bmatrix} \tag{C.3}$$

$$\frac{\delta}{\delta z}u = \frac{\delta}{\delta z}\mathbf{N}\cdot\begin{bmatrix}U_m\\ U_{m+1}\end{bmatrix} = \frac{1}{h}\begin{bmatrix}1 & 0 & -1 & 0\\ 0 & 1 & 0 & -1\end{bmatrix}\cdot\begin{bmatrix}U_m\\ U_{m+1}\end{bmatrix} = \mathbf{F}\cdot\begin{bmatrix}U_m\\ U_{m+1}\end{bmatrix} \tag{C.4}$$

In order to find the consistent nodal tractions, we need to multiply the stresses by $\mathbf{N}^T$ and evaluate the integrals over the sublayer thickness.

The result is

$$\begin{bmatrix} T_m \\ T_{m+1} \end{bmatrix} = \left(A_m \frac{\delta}{\delta x} + D_m\right) \cdot \begin{bmatrix} U_m \\ U_{m+1} \end{bmatrix} \mathrm{sgn}(n_x) \qquad \text{(C.5)}$$

where $T_m = \begin{bmatrix} T_{xm} \\ T_{zm} \end{bmatrix}$ represents the nodal tractions, A_m is as given in appendix A and D_m is equal to

$$D_m = \frac{1}{2} \begin{bmatrix} 0 & \lambda & 0 & -\lambda \\ G & 0 & -G & 0 \\ 0 & \lambda & 0 & -\lambda \\ G & 0 & -G & 0 \end{bmatrix} \qquad \text{(C.6)}$$

To evaluate $\frac{\delta}{\delta x} \begin{bmatrix} U_m \\ U_{m+1} \end{bmatrix}$ one just substitutes in equation B.19 $E_{|x|} = \mathrm{diag}\left\{e^{-ik_j|x|}\right\}$ by $E_{|x|} = \mathrm{diag}\left\{-ik_j e^{-ik_j|x|}\mathrm{sgn}(x)\right\}$. It should be noted that σ_x due to a vertical load or τ_{xz} due to an horizontal load exhibit a discontinuity at x=0 (change in sign); hence, at x=0 these stresses are taken as null. This formulation shows the contribution of one sublayer to the nodal tractions; if the boundary extends to adjacent sublayers, their contribution must be added as well. When the load is applied to the same node where the tractions are computed, then one can consider the load to be just inside the domain and sum one unit to the corresponding diagonal element of matrix A of the BEM equation.

horizontal planes

The tractions on horizontal planes are obtained by considering only one sublayer. The sublayer chosen can either be the one just on top, or the one below;

identical results are obtained in both cases. The only difference is the singular term that arises when the load is applied to the same node where the traction is computed; this singular term can be computed either using the sublayer that is inside the domain (which means that the concentrated force is the real one being applied to the soil), or from the ficticious layer that extends outside the domain (in this last case, the concentrated force computed is applied to the outer layer and to obtain the corresponding real force applied to the soil one should subtract the computed force from 1, since these two forces equilibrate the external unit load).

We begin with the relation in the wave–number domain, equation 2.10 (considering only the top two rows of the l.h.s.).

$$\begin{bmatrix} \bar{T}_{xm} \\ i\bar{T}_{zm} \end{bmatrix} = \begin{bmatrix} \bar{\tau}_{m} \\ i\bar{\sigma}_{m} \end{bmatrix} \mathrm{sng}(n_z) = K_m \cdot \begin{bmatrix} \begin{bmatrix} \bar{U}_{xm} \\ i\bar{U}_{zm} \end{bmatrix} \\ \begin{bmatrix} \bar{U}_{xm+1} \\ i\bar{U}_{zm+1} \end{bmatrix} \end{bmatrix} \cdot \mathrm{sng}(n_z) \qquad \text{(C.7)}$$

where $K_m = A_m k^2 + B_m k + G_m - \omega^2 M_m$, is the dynamic stiffness matrix of sublayer m.

$$\text{But} \quad \begin{bmatrix} \bar{U}_x \\ i\bar{U}_z \end{bmatrix} = \begin{bmatrix} \phi_x D \phi_x^T & k\phi_x K^{-1} D \phi_z^T \\ k\phi_z D K^{-1} \phi_x^T & \phi_z D \phi_z^T \end{bmatrix} \cdot \begin{bmatrix} \bar{P}_x \\ i\bar{P}_z \end{bmatrix} \qquad \text{(C.8)}$$

where $D = (k^2 I - K^2)^{-1}$ and the off diagonal terms can be substituted by $\frac{1}{k}\phi_x D K \phi_z^T$ and its transpose.

Since we are considering the top of a sublayer, sng(nz)=1 and we will drop it.

<u>horizontal loads</u>

Considering an horizontal load at the interface n

$$\bar{P}_x = \begin{bmatrix} 0 \\ \vdots \\ 0 \\ 1 \\ 0 \\ \vdots \\ 0 \end{bmatrix} \begin{matrix} \\ \\ \\ \longleftarrow \text{n interface} \\ \\ \\ \\ \end{matrix} \qquad \text{(C.9)}$$

$$\text{at the } m^{th} \text{ interface } \begin{bmatrix} \bar{U}_{xm} \\ i\bar{U}_{zm} \end{bmatrix} = \begin{bmatrix} \sum_j \phi_{xm,j} \dfrac{1}{k^2-k_j^2} \phi_{xn,j} \\ \sum_j \phi_{xm,j} \dfrac{k_j}{k} \dfrac{1}{k^2-k_j^2} \phi_{xn,j} \end{bmatrix} \qquad \text{(C.10)}$$

where j represents the natural mode of the system and the summation extends over all the modes (j=1, ,.., 2N)

hence

$$\begin{bmatrix} \bar{T}_{xm} \\ i\bar{T}_{zm} \end{bmatrix} = (A_m k^2 + B_m k + G_m - \omega^2 M_m) \cdot \begin{bmatrix} \sum_j \phi_{xm,j} \dfrac{1}{k^2-k_j^2} \phi_{xn,j} \\ \sum_j \phi_{zm,j} \dfrac{k_j}{k} \dfrac{1}{k^2-k_j^2} \phi_{xn,j} \\ \sum_j \phi_{xm+1,j} \dfrac{1}{k^2-k_j^2} \phi_{xn,j} \\ \sum_j \phi_{zm+1,j} \dfrac{k_j}{k} \dfrac{1}{k^2-k_j^2} \phi_{xn,j} \end{bmatrix} \qquad \text{(C.11)}$$

Taking into account the fact that $\sum_j k_j \phi_{zn,j}\phi_{xn,j} = \sum_j \frac{1}{k_j}\phi_{zn,j}\phi_{xn,j} = 0$ and substituting $A_m k^2 = A_m(k^2 - k^2) + A_m k_j^2$ and $B_m k = B_m k_j \frac{k}{k_j}$, we get after inverse Fourier transforming the non–zero terms:

$$\begin{bmatrix} T_{xm} \\ iT_{zm}\cdot \mathrm{sng}(x) \end{bmatrix} = \delta(x)\, A_m \sum_j \begin{bmatrix} \phi_{xm,j} \\ 0 \\ \phi_{xm+1,j} \\ 0 \end{bmatrix} \phi_{xn,j} +$$

$$+ \sum_j K_m(k_j)\, \frac{1}{2ik_j} e^{-ik_j|x|} \cdot \begin{bmatrix} \phi_{xm,j} \\ \phi_{zm,j} \\ \phi_{xm+1,j} \\ \phi_{zm+1,j} \end{bmatrix} \phi_{xn,j} \tag{C.12}$$

where $K_m(k_j) = A_m k_j^2 + B_m k_j + G_m - \omega^2 M_m$

<u>vertical loads</u>

Considering a vertical load at the interface n

$$\overline{P}_z = \begin{bmatrix} 0 \\ \vdots \\ 0 \\ 1 \\ 0 \\ \vdots \\ 0 \end{bmatrix} \longleftarrow \text{n interface} \tag{C.13}$$

and using an approach as before, the tractions are obtained as follows

$$\begin{bmatrix} T_{xm} \cdot \mathrm{sng}(x) \\ iT_{zm} \end{bmatrix} = i\delta(x)\, A_m \sum_j \begin{bmatrix} 0 \\ \phi_{zm\,,\,j} \\ 0 \\ \phi_{zm+1,j} \end{bmatrix} \phi_{zn,j} +$$

$$+ \sum_j K_m(k_j)\, \frac{1}{2ik_j} e^{-ik_j|x|} \,.\, \begin{bmatrix} \phi_{xm\,,\,j} \\ \phi_{zm\,,\,j} \\ \phi_{xm+1,j} \\ \phi_{zm+1,j} \end{bmatrix} \phi_{zn,j} \qquad \text{(C.14)}$$

In order to find the corresponding nodal tractions, it is necessary to multiply the second term in equations C.12 and C.14 by the length of the boundary element , since we consider constant displacement elements. Also, the integration of the singular term is straight forward, sufficing to integrate the delta function, which gives one. Since the matrix A_m is not diagonal, the contribution of the singularity extends along the same vertical to adjacent interfaces.

<u>anti–plane case</u>

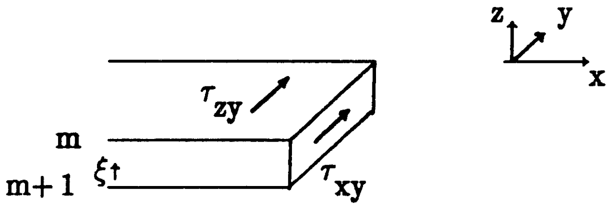

The figure above shows the sign convention for the stresses and coordinate axes in this case.

vertical planes

Using the same approach as for the in–plane case the nodal tractions are given by

$$T_{ym} = A_m \frac{\delta}{\delta x} \begin{bmatrix} U_{ym} \\ U_{ym+1} \end{bmatrix} \mathrm{sgn}(n_x) \tag{C.15}$$

To evaluate $\frac{\delta}{\delta x} \begin{bmatrix} U_{ym} \\ U_{ym+1} \end{bmatrix}$ one just substitutes in equation B20 $E_{|x|} = \mathrm{diag}\left\{e^{-ik_j|x|}\right\}$ by $E_{|x|} = \mathrm{diag}\left\{-ik_j e^{-ik_j|x|} \mathrm{sgn}(x)\right\}$.

horizontal planes

Following a procedure that is similar to that used for the in–plane case, one obtains (for $\mathrm{sng}(n_z)=1$)

$$T_{ym}=\delta(x)A_m\sum_j \begin{bmatrix} \phi_{ym\,,\,j} \\ \phi_{ym+1,j} \end{bmatrix} \phi_{yn,j}+\sum_j K_m(k_j)\frac{1}{2ik_j}e^{-ik_j|x|} \begin{bmatrix} \phi_{ym\,,\,j} \\ \phi_{ym+1,j} \end{bmatrix} \phi_{yn,j} \tag{C.16}$$

In order to get the nodal traction, it is necessary to multiply the second term of T_{ym} by the length of the boundary element, and add the singular term if the horizontal coordinates in the element contain the horizontal position of the load.